Deformation, Light, Electrical and Magnetic Fields in Soft Matter

by

Amir Hossein Rahmati

A dissertation submitted to the Department of Mechanical Engineering,
Cullen College of Engineering
in partial fulfillment of the requirements for the degree of

Doctor of Philosophy
in Mechanical Engineering

Chair of Committee: Pradeep Sharma, Professor
Committee Member: Yashashree Kulkarni, Professor
Committee Member: Kalyana Nakshatrala, Associate Professor
Committee Member: Theocharis Baxevanis, Assistant Professor
Committee Member: Shailendra Joshi, Assistant Professor

University of Houston
May 2022

Abstract

One of the "holy grails" of soft multifunctional materials is to design a material that is simultaneously capable of (i) large deformation under the application of a moderate external stimuli such as an electric or magnetic field and (ii) generating appreciable electric field under the application of moderate forces. Such soft materials enable applications that range from sensors, actuators, artificial muscles, self-powered biomedical devices, soft robotics to energy harvesting. In this dissertation, we focus on three different aspects of the design of soft multifunctional materials:

(1) Use of immobile embedded charges (called electrets) to obtain an emergent piezoelectric or flexoelectric response in a soft material Specifically, we show the underlying mechanisms for the weak apparent piezoelectric effect in flexure mode of electret beams and how to appropriately design such structures for energy harvesting applications.

(2) Imagine a material that will produce electricity via a contactless, wireless signal. Further, we hope that this material is capable of large deformation reminiscent of soft robots. This would all be possible if soft magnetoelectric materials were available; paving the way for applications such as remote drug delivery, wireless energy harvesting, multiple state memories among others. Here, for the first time, using the concept of hard magnetic soft matter in combination with electrets, we design and create a soft magnetoelectric material that exhibits an extremely strong, self-biased magnetoelectric effect. Further, using programmable pattern of deposition of magnetic dipoles and charges, we report a giant magnetoelectric coefficient in an ultra-soft deformable material that retains its strength even under infinitesimal external fields and at low frequencies.

(3) Liquid crystal elastomers are an interesting class of soft materials that combine the elasticity of rubber with the ordered structure and mobility of liquid crystals. In this work, we present a nonlinear theory to couple mechanics, electrical fields and light in nematic liquid crystal elastomers. In particular, we incorporate the effect of photomechanical coupling and flexoelectricity.

Table of Contents

List of Figures

Chapter 1

Overview

Inspired by nature, scientists have been attempting to develop soft materials and systems that can undergo large deformations and safely interact with living organisms [27, 28]. As a result, over the last two decades, the nascent field of soft robotics has begun to come of age [29]. The progress in this field has led to development of robots which can roll [30], jump [31], elongate [32], squeeze [33] and climb [34]. These advancement would not have been possible without soft materials. In addition to robotics, soft materials find applications in stretchable and wearable electronics [35], tissue engineering [36], health monitoring devices [37], surgical devices [38], biomedical implants [39], large deformation sensors [40] and actuators [41], and energy harvesting [42]. In addition to softness, the material has to be responsive to an expedient stimulus for many of these applications. The focus of this dissertation is to engineer new functionalities into soft materials that facilitates the generation of electricity under the application of mechanical forces, magnetic fields and light. The outline of the dissertation is as follows and we have provided motivation and context within each chapter so that all the chapters are largely self-contained.

Chapter 2 and 3 focus on the design of apparent piezoelectric materials through the use of embedded immobile charges called electrets.

In Chapter 4 and 5, we present the design of a material that leads to arguably the world record for the highest (emergent) magnetoelectricity in a *soft* material. While our focus was on the theoretical and computational work, with the help of our experimental collaborators, we are able to show proof of the key concepts proposed by our theory and also an excellent agreement with experimental characterization. In Chapter 6, we present a novel theory that links the phenomenon of flexoelectricity, light and deformation in liquid crystal elastomers. Our theoretical and computational examples illustrate how light may be used to harvest electrical energy.

Chapter 2

Nonlinear Bending Deformation of Soft Electrets and Prospects for Engineering Flexoelectricity and Transverse Piezoelectricity

Soft materials that exhibit electromechanical coupling are an important element in the development of soft robotics, flexible and stretchable electronics, energy harvesters, sensor and actuators. Truly *soft* natural piezoelectrics essentially do not exist and typical dielectric elastomers, predicated on electrostriction and the Maxwell stress effect, exhibit only a one-way electromechanical coupling. Extensive research however has shown that soft *electrets* i.e. materials with embedded *immobile* charges and dipoles, can be artificially engineered to exhibit a rather large piezoelectric-like effect. Unfortunately, this piezoelectric effect—large as it may be—is primarily restricted to an electromechanical coupling in the longitudinal direction or what is referred colloquially as the d_{33} piezoelectric coefficient. In sharp contrast, the transverse piezoelectric property (the so-called d_{31} coefficient) is rather small. This distinction has profound implications since these soft electrets exhibit negligible electromechanical coupling under bending deformation. As a result, the typically engineered soft electrets are rendered substantively ill-suited for energy harvesting as well as actuation/sensing of flexure motion that plays a critical role in applications like soft robotics. In this work, we analyze nonlinear bending deformation of a soft electret structure and examine the precise conditions that may lead to a strong emergent piezoelectric response under bending. Furthermore, we show that non-uniformly distributed dipoles and charges in the soft electrets lead to an apparent electromechanical response that may be ambiguously and interchangeably interpreted as either transverse piezoelectricity or *flexoelectricity*. We suggest pragmatic routes to engineer a large transverse piezoelectric (d_{31}) and flexoelectric coefficient in soft electrets. Finally, we show that in an appropriately designed soft electret, even a *uniform* external electric field can induce *curvature* in the structure thus enabling

its application as a bending actuator.

2.1 Introduction

One of the "holy grails" of soft multifunctional materials is to design a material that is simultaneously capable of (i) large deformation under the application of a moderate electric field[1], (ii) generating appreciable electric field under the application of moderate forces, and (iii) (specifically) exhibit the features embodied in (i)-(ii) for bending deformation. Such soft materials with a pronounced electromechanical coupling enable applications that range from sensors [43], actuators [44], artificial muscles [45], self-powered biomedical devices [46], soft robotics [28] to energy harvesting [47, 48, 49]. The reader is referred to the following reviews and references therein for an overview [44, 50, 28, 51, 47, 52, 53, 54].

The simplicity of the aforementioned requirements is somewhat deceptive. Piezoelectric materials deform when subjected to electrical stimuli and vice-versa, but the hard crystalline ones such as lead zirconium titanate (PZT), that exhibit a strong electromechanical coupling, are not capable of large deformations. Piezoelectric polymers like Polyvinylidene Fluoride (PVDF) do not exhibit strong electromechanical coupling (when compared to the crystalline piezoelectrics) and, with an elastic modulus in the range of 1 GPa, are not really that soft [55]. Dielectric elastomers are an alternative to piezoelectrics. They are capable of large deformation but require imposition of rather high voltage. In a remarkable work, Keplinger et al. [56] demonstrated an areal increase of nearly 1700% for an acrylic membrane. However, dielectric elastomers operate via the mechanism of Maxwell stress and/or electrostriction[2]. In dielectric elastomers, due to the Maxwell stress effect or electrostriction, an electric field exerts a force proportional to E^2 where E is the applied electric field. This force is somewhat small unless an appropriately large voltage difference is imposed. Even then, only soft dielectrics such as elastomers (with an elastic modulus of 1 MPa or less) deform appreciably for practically feasible applied electric fields. Most importantly,

[1] –or other stimuli of interest such as magnetic fields, temperature among others

[2] In this work we will not distinguish between the Maxwell stress effect and electrostriction since they are mathematically similar and this distinction does not impact the central message of our work. For further discussion on this topic, see [57, 58, 59]

electrostriction is a one-way coupling i.e. an electric field will produce deformation but a mechanical stress will not induce any electricity—unlike in piezoelectric materials. Due the absence of this converse effect, energy harvesting is not easily possible unless creative design augmentations are made[3]. Additionally, the quadratic dependence of the deformation on electric fields implies that upon reversal of the applied voltage, the deformation will not reverse.

Another alternative are soft electrets. Therein, (typically) polymer foams are impregnated with *immobile* charges and dipoles [62, 63, 64]. Both experimental and theoretical work has shown that electrets exhibit a rather large apparent piezoelectricity. Remarkably, an apparent (*longitudinal*) piezoelectric coefficient[4] as high as 1200 pC/N–six times that of PZT– has been measured in polypropylene foams [65]. Charge stability is a concern in electrets and their application is restricted to room temperature where the trapped charges tend to stabilize for sufficiently long times to enable engineering applications.

Bending deformation, in the context of piezoelectrics, dielectric elastomers and electrets, must be specifically highlighted which represents a unique challenge. Conversion of a mechanical motion into electricity (i.e. energy harvesting) is a key application area for multifunctional soft materials and is most facile under bending-type deformation as opposed to simple compression or stretching. Further, a variety of sensing and actuation contexts, including soft robotics, require flexure motion[5]. Bending deformation yields lower reso-

[3]cf. [60, 61] for further details. Also, a somewhat deeper consideration will reveal that their approach for energy harvesting from dielectric elastomers can be considered as a special form of electrets where the charges reside on the surfaces.

[4]There are several equivalent ways to parametrize the piezoelectric property viz. as relation between the electric displacement and stress or polarization or strain; among others. In a widely used formalism, the electric displacement vector $\mathbf{D}$ is related to stress tensor σ through the third order piezoelectric tensor d_{ijk} ($D_i \sim d_{ijk}\sigma_{jk}$). Odd order tensors can only exist in non-centrosymmetric crystal structures and therefore piezoelectricity is restricted to only a limited set of materials. Furthermore, symmetry considerations for typical piezoelectric materials allows for only six independent components for the property tensor (out of the maximum possible 27). The electric displacement in the poling direction of material D_3 can be correlated to three normal stresses σ_{11}, σ_{22} and σ_{33} using contracted notation for piezoelectric coefficients: $D_3 \sim d_{31}\sigma_{11} + d_{32}\sigma_{22} + d_{33}\sigma_{33}$. The d_{33} (longitudinal) piezoelectric coefficient is important when both deformation (or stress) and polarization (or electric displacement) are in the poling direction (thickness direction in this chapter) and d_{31} plays a pivotal role when the stress and electric displacement are in perpendicular direction with respect to each other.

[5]There are several interesting uses of bending based energy generators from electromechanical coupling e.g. from the natural contractile and relaxation motions of the heart, lung, and diaphragm for self-powered wearable and implantable biomedical devices [46] or to harvest wind energy by using a piezoelectric flag [66]. Examples of sensors and actuators include micromotors [67], micropumps [68], robots [69] and cooling fans [70].

nance frequencies and larger attainable strain which is especially advantageous for small size generators with limited environmental mechanical forces [71, 72].

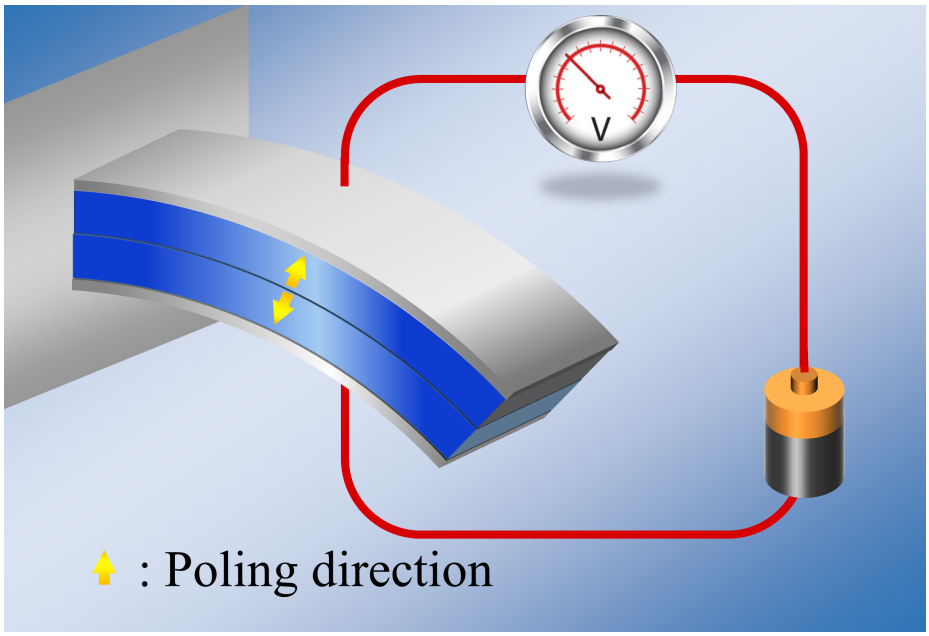

Figure 2.1: Bending piezoelectric actuator is based on the so-called d_{31} piezoelectric effect. Typically, this actuator is made of two layers of piezoelectric materials with opposite poling directions.

The preceding paragraph underscores the importance of bending deformation, however, the following issues are notable:

1. Naive bending of a typical piezoelectric material will generate negligible electricity. The reason is simple. Assuming the neutral axis to be centered in the cross-section of the structural element, the polarization above the neutral line due to tension is expected to substantively cancel the polarization below the neutral axis due to compressive strains. Accordingly, bending piezoelectric devices are nearly always bimorphs. We remark that the bending piezoelectric device is based on the d_{31} piezoelectric effect (or transverse piezoelectricity) which is defined as the linear coupling between deformation in axial direction and electric field in thickness direction. The working principle of bending piezoelectric actuator is shown in Fig. 2.1 where two layers of piezoelectric film with oppositely poled directions are attached to each other. An ex-

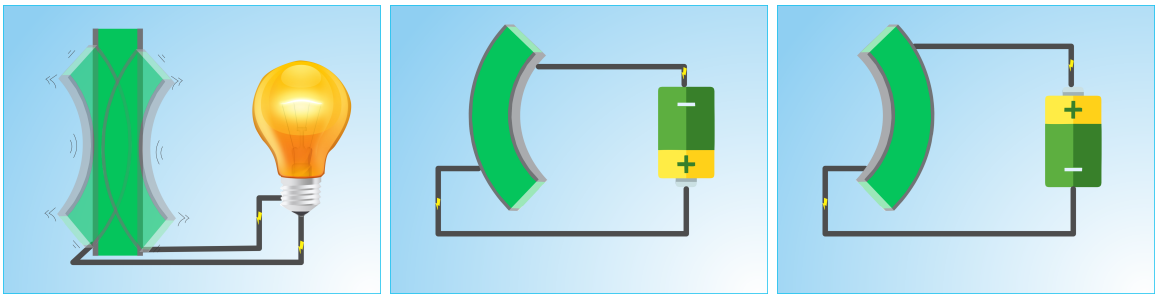

(a) (b) (c)

Figure 2.2: (a) Electrical energy may be harvested from bending deformation of a material with suitable form of electromechanical coupling, (b) and (c) The flexure actuator functionality of an electromechanical material.

ternally applied electric field creates a positive strain in one of the films and a negative one in the other; resulting therefore in the flexure of the entire structure.

2. Special arrangements are also required to ensure bending actuation of dielectric elastomers under an electric field.The application of an electric field on a dielectric elastomer thin film structure will simply compress the film in its thickness direction. As an example of an approach to induce flexure, He and coworkers [73] used pre-stretched films. Of course, as already indicated earlier, since the Maxwell stress effect/electrostriction are a one-way electromechanical coupling, sensing and energy harvesting is not easily possible.

3. Since electrets exhibit an apparent piezoelectricity—and a rather large one at that—they would appear to be a viable solution. Unfortunately, this is not the case. As well-articulated by the experimental papers [64, 3] , the emergent piezoelectricity of electrets is largely restricted to the longitudinal direction i.e. a large d_{33} piezoelectric coefficient but a very small value for d_{31} piezoelectric coefficient is reported. This shortcoming ensures that bending/harvesting is not easily possible[6].

[6]There is an interesting and singular exception to the low d_{31} reports for electrets. Zhang et al. [1] explored a rather special microstructure which did exhibit a notable d_{31} piezoelectric coefficient however a clear quantitative explanation was not presented. In due course, we will attempt to rationalize their results based on our developed models.

4. It is germane here to allude to another type of electromechanical coupling mechanism that has generated much attention in recent years—*flexoelectricity*. In this phenomenon, a strain gradient generates electrical polarization[7]. Various experiments have confirmed the existence of flexoelectricity in different materials including soft polymers [74, 75], hard crystalline ceramics [76, 77] and biological membranes [78, 79]. Furthermore, several review articles have recently summarized theoretical and experimental activities in this topic [80, 81, 82, 83, 84, 85]. In addition, several numerical studies have been preformed to analyze flexoelectric behavior of materials. Thai et al. [86] presented an approach to construct a numerical framework which can account for both flexoelectricity and the Maxwell stress effects in finite deformation and also can treat material interfaces effectively. Ghasemi et al. [87] presented a topology optimization of flexoelectric composites to enhance electromechanical performance. Since bending is in fact the most suitable form of strain gradient that can elicit a flexoelectric response, flexoelectricity could be considered as a reliable mechanism for bending based electro-mechanical devices. However, the effect is rather weak, and very large strain gradients (or extreme bending curvatures) are required for the flexoelectric effect to be significant. Only at nano-scale feature size is this effect considerable where a large strain gradient is easily achievable. However, we note that in the converse flexoelectric effect, an electric field *gradient* is required to create curvature and uniform electric field will not bend the material [83].

With the preceding paragraphs as the appropriate context, the following questions motivate the current work:

1. What are the theoretical underpinnings for the small value of transverse piezoelectricity (d_{31} coefficient) in typical electret foams?

2. Based on a suitable theoretical model, what are the physical and quantitative insights to engineer a large transverse piezoelectric coefficient in electrets?

[7]Flexoelectricity is characterized through the linear relation between polarization $\mathbf{P}$ and strain gradient $\nabla\mathbf{S}$ mediated by a fourth order flexoelectric tensor $\mathbf{f}$ such that $P_i \sim f_{ijkl}\frac{\partial S_{jk}}{\partial X_l}$).

3. Is it possible to create an electret structure that will directly couple curvature to uniformly imposed electric fields and vice-versa? This is not possible in piezoelectrics and dielectric elastomers

4. As well-established, embedding charges and dipoles in soft materials lead to an emergent piezoelectric response. Directly relevant to the preceding question, can embedding charges and dipoles lead to an emergent flexoelectricity as well?

To answer the afore-posed questions, in this chapter, we rigorously analyze the nonlinear deformation of soft electrets under in-plane deformation. We provide insights into the reasons underlying the marginal d_{31} effect in conventional soft electrets under an in-plane stretch. Using the developed theoretical framework, we propose design guidelines to create a substantial emergent d_{31} in electrets such that electrical energy is harvested from flexure (Fig. 2.2(a)). Specifically we determine the emergent piezoelectric and flexoelectric coefficients. Intriguingly, we also are able to demonstrate that with appropriate design of charge and dipole placements in electrets, bending can be directly induced with the application of a *uniform* electric field—(Figs. 2.2(b) and 2.2(c)).

The chapter is organized as follows. In section 2.2, a general theoretical framework for nonlinear electrostatics of deformable media is summarized in a form suitable for the present work. In section 2.3, we present an analysis of conventional soft electrets under in-plane deformation to understand the experiments showing a small d_{31} effect. Bending behavior of soft dielectrics is presented in section 2.4 and several physically meaningful design scenarios are discussed in section 2.5.

2.2 General theoretical framework

There are numerous, essentially equivalent, ways that electrostatics of deformable continua may be formulated [88, 89, 90, 91, 92, 93, 94, 95, 96, 57, 58]. In this work, we have favored the exposition by Liu[97] who has also compared the various formulations that exist in the literature.

Let Ω_R be a continuum deformable body in the reference configuration. This body is located in an ambient medium such that body and ambient medium occupy domain V_R. Thermodynamic state of the body is described by deformation $\boldsymbol{\chi} : \Omega_R \to \mathbb{R}^3$ (which maps material points $\mathbf{X}$ from the reference configuration to the spatial points $\mathbf{x}$ in the current configuration Ω) and polarization $\widetilde{\mathbf{P}} : \Omega_R \to \mathbb{R}^3$. Deformation and polarization outside of the body are zero. Moreover, the gradient, divergence and curl operators in the current configuration are denoted by "grad", "div" and "curl", respectively. Gradient in the reference configuration is denoted by "∇". The deformation gradient tensor is defined as $\mathbf{F} = \nabla\chi$ and the Jacobian is $J = \det \mathbf{F}$.

Maxwell's equations in the current configuration take the following familiar form

$$\operatorname{curl} \mathbf{e} = \mathbf{0}, \quad \operatorname{div} \mathbf{d} = \rho_e, \quad \mathbf{d} = \epsilon_0 \mathbf{e} + \mathbf{p} \qquad \text{in} \quad V, \tag{2.1}$$

where $\mathbf{e}$, $\mathbf{d}$, $\mathbf{p}$ and ρ_e are the true electric field, the electric displacement, the polarization, and the external charge density in the current configuration, respectively. Also, ϵ_0 denotes the electric permittivity of the ambient medium. From the first of Eq.(2.1), we can define a scalar electric potential $\xi : \Omega_R \to \mathbb{R}$, such that $\mathbf{e} = -\text{grad}\xi$. Composition map can be used to denote $\mathbf{e}$, $\mathbf{d}$ and $\mathbf{p}$ in the reference configuration

$$\mathbf{E} = \mathbf{e} \circ \boldsymbol{\chi}, \quad \mathbf{D} = \mathbf{d} \circ \boldsymbol{\chi} \quad \text{and} \quad \mathbf{P} = \mathbf{p} \circ \boldsymbol{\chi}. \tag{2.2}$$

In addition we define the nominal electric displacement $\widetilde{\mathbf{D}}$, the nominal electric field $\widetilde{\mathbf{E}}$ and the nominal polarization $\widetilde{\mathbf{P}}$ as

$$\widetilde{\mathbf{E}} = \mathbf{F}^T \mathbf{E}, \quad \widetilde{\mathbf{D}} = J\mathbf{F}^{-1}\mathbf{D} \quad \text{and} \quad \widetilde{\mathbf{P}} = J\mathbf{P}. \tag{2.3}$$

Maxwell's equations in the reference configuration can then be derived to be

$$\nabla \cdot \widetilde{\mathbf{D}} = \widetilde{\rho_e} \quad \text{and} \quad \widetilde{\mathbf{D}} = -\epsilon_0 J\mathbf{C}^{-1}\nabla\xi + \mathbf{F}^{-1}\widetilde{\mathbf{P}} \qquad \text{in} \quad V_R, \tag{2.4}$$

where $\widetilde{\rho_e} = J\rho_e \circ \boldsymbol{\chi}$ for volume electric charge density and for surface charge density, J

should be replaced with the surface Jacobian.

The total free energy of the system is written as[8]

$$\mathcal{F}[\boldsymbol{\chi}, \widetilde{\mathbf{P}}] = \int_{\Omega_R} \psi[\mathbf{X}; \mathbf{F}, \widetilde{\mathbf{P}}] + \int_V \frac{\epsilon_0}{2} |\mathbf{e}|^2 + \int_{\Gamma_D} \xi_b \widetilde{\mathbf{D}} \cdot \mathbf{n_R} - \int_{S_N} \widetilde{\mathbf{t}}^{\mathbf{e}} \cdot \boldsymbol{\chi}, \tag{2.5}$$

where $\psi : \mathbb{R}^3 \times \mathbb{R}^{3\times 3} \times \mathbb{R}^3 \to \mathbb{R}$ is the internal energy function of the body Ω_R and $\mathbf{n}_R$ is the unit normal to the boundary ∂V_R. Also, $\xi_b : \Gamma_D \to \mathbb{R}$ and $\widetilde{\mathbf{t}}^e : \partial S_N \to \mathbb{R}^3$ are the imposed boundary potential and traction (dead load), respectively, applied on the surfaces Γ_D and S_N (Fig. 2.3). In addition, as it is shown in Fig. 2.3, Dirichlet boundary condition $\boldsymbol{\chi} = \boldsymbol{\chi}_b$ ($\boldsymbol{\chi}_b : S_D \to \mathbb{R}^3$) and Robin boundary condition $\widetilde{\mathbf{D}} \cdot \mathbf{n}_R = D_b$ ($D_b : \Gamma_R \to \mathbb{R}$) are imposed on the surfaces S_D and Γ_R, respectively.

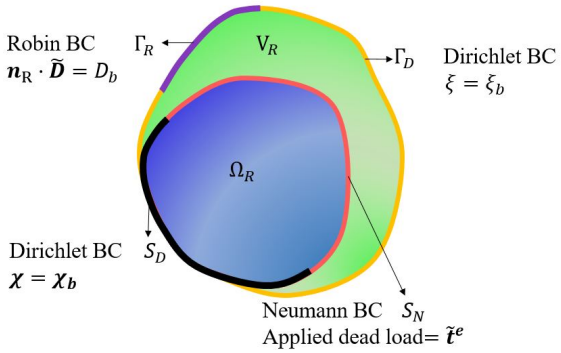

Figure 2.3: Continuum deformable body in the reference configuration and applied boundary conditions.

Based on the principle of minimum free energy, the equilibrium state of the system is the state that minimizes the free energy of the system subject to the constraint imposed by the Maxwell's equations

$$\min\{\mathcal{F}[\boldsymbol{\chi}, \widetilde{\mathbf{P}}] : (\boldsymbol{\chi}, \widetilde{\mathbf{P}}) \in \mathcal{S} \quad \text{and} \quad (\boldsymbol{\chi}, \widetilde{\mathbf{P}}) \quad \text{satisfies (2.4)}\}, \tag{2.6}$$

[8]We emphasize that the domain of the second integral on the right hand side of Eq.(2.5) is not reference configuration. We can write this term in the reference configuration as

$$\int_V \frac{\epsilon_0}{2} |\mathbf{e}|^2 = \int_{V_R} \frac{\epsilon_0}{2} \nabla\xi \cdot J\mathbf{C}^{-1} \nabla\xi.$$

where $\mathcal{S}$ is the admissible set of functions over which the minimization is performed

$$\mathcal{S} = \{(\boldsymbol{\chi}, \widetilde{\mathbf{P}}) | \quad \boldsymbol{\chi} \in C^2(\Omega_R; \mathbb{R}^3), \quad \int_{\Omega_R} |\widetilde{\mathbf{P}}|^2 < +\infty\}. \tag{2.7}$$

Equilibrium equations of the system are the Euler-Lagrange equations associated with (2.6) which may be derived using standard variational calculus. Imposing boundary conditions $\boldsymbol{\chi} = \boldsymbol{\chi}_b$ on S_D, $\xi = \xi_b$ on Γ_D and $\widetilde{\mathbf{D}} \cdot \mathbf{n}_R = D_b$ on Γ_R, following system of governing equations and natural boundary condition should be solved simultaneously to determine the equilibrium state of the system:

$$\mathbf{F}^{-T}\nabla\xi + \frac{\partial\psi}{\partial\widetilde{\mathbf{P}}} = \mathbf{0} \qquad \text{in} \quad \Omega_R, \tag{2.8a}$$

$$\nabla \cdot (-\epsilon_0 J\mathbf{C}^{-1}\nabla\xi + \mathbf{F}^{-1}\widetilde{\mathbf{P}}) = \widetilde{\rho}_e \qquad \text{in} \quad V_R, \tag{2.8b}$$

$$\nabla \cdot \left(\widetilde{\boldsymbol{\Sigma}} + \widetilde{\boldsymbol{\Sigma}}^{MW}\right) = \mathbf{0} \qquad \text{in} \quad \Omega_R, \tag{2.8c}$$

$$\nabla \cdot \widetilde{\boldsymbol{\Sigma}}^{MW} = \mathbf{0} \qquad \text{in} \quad V_R \backslash \Omega_R \tag{2.8d}$$

$$\text{and} \qquad \left(\widetilde{\boldsymbol{\Sigma}} + \widetilde{\boldsymbol{\Sigma}}^{MW}\right) \cdot \mathbf{n}_R - \widetilde{\mathbf{t}}^e = \mathbf{0} \qquad \text{on} \quad S_N, \tag{2.8e}$$

where $\widetilde{\boldsymbol{\Sigma}}$ is given as

$$\widetilde{\boldsymbol{\Sigma}} = \frac{\partial\psi}{\partial\mathbf{F}}, \tag{2.9}$$

and $\widetilde{\boldsymbol{\Sigma}}^{MW}$ is the Piola-Maxwell stress

$$\widetilde{\boldsymbol{\Sigma}}^{MW} = -\frac{\epsilon_0}{2} J|\mathbf{E}|^2\mathbf{F}^{-T} + \mathbf{E} \otimes \widetilde{\mathbf{D}}. \tag{2.10}$$

We chose the following form of the internal energy density function

$$\psi[\mathbf{X}; \mathbf{F}, \widetilde{\mathbf{P}}] = W^{elast}(\mathbf{F}) + \frac{|\widetilde{\mathbf{P}}|^2}{2J(\epsilon - \epsilon_0)}, \tag{2.11}$$

where W^{elast} is the strain energy function and can be chosen to appropriately model the constitutive nature of the materials being examined. Also, ϵ is electric permittivity of material. Substituting Eq.(2.11) into equilibrium equations and writing all of the quantities

in the current configuration, we have

$$\text{grad}\xi + \frac{\mathbf{p}}{\epsilon - \epsilon_0} = \mathbf{0} \qquad \text{in} \quad V, \tag{2.12a}$$

$$\text{div}\,\mathbf{d} = \rho_e \qquad \text{in} \quad \Omega, \tag{2.12b}$$

$$\text{div}(\boldsymbol{\sigma} + \boldsymbol{\sigma}'^{MW}) = \mathbf{0} \qquad \text{in} \quad \Omega, \tag{2.12c}$$

$$\text{div}\,\boldsymbol{\sigma}^{MW} = \mathbf{0} \qquad \text{in} \quad V \backslash \Omega \tag{2.12d}$$

$$\text{and} \qquad (\boldsymbol{\sigma} + \boldsymbol{\sigma}'^{MW}) \cdot \mathbf{n} - \mathbf{t}^e = \mathbf{0} \qquad \text{on} \quad S_n, \tag{2.12e}$$

where $\boldsymbol{\sigma}$, $\boldsymbol{\sigma}'^{MW}$ and $\boldsymbol{\sigma}^{MW}$ are the Cauchy stress, Maxwell stress inside the body and Maxwell stress outside the body, respectively, and are given by

$$\boldsymbol{\sigma} = \frac{1}{J}\frac{\partial W^{elast}}{\partial \mathbf{F}}\mathbf{F}^T, \tag{2.13}$$

$$\boldsymbol{\sigma}'^{MW} = \mathbf{e} \otimes \mathbf{d} - \frac{\epsilon}{2}(\mathbf{e} \cdot \mathbf{e})\mathbf{I} \tag{2.14}$$

$$\text{and} \qquad \boldsymbol{\sigma}^{MW} = \mathbf{e} \otimes \mathbf{d} - \frac{\epsilon_0}{2}(\mathbf{e} \cdot \mathbf{e})\mathbf{I}. \tag{2.15}$$

2.3 A model to explain low d_{31} effect in conventional electrets

As already alluded to earlier, there has been compelling experimental indication for large value of (apparent) longitudinal piezoelectric coefficient d_{33} in electret foams[3]. Theoretically also, Deng et al. [98, 99] have derived how the Maxwell stress, elastic heterogeneity and the presence of pre-existing charges or dipoles conspire to lead to this emergent longitudinal piezoelectric effect. We also remark that recently, Liu and Sharma [100] have presented a homogenization theory for the effective properties of electrets. In this section, we examine a paradigmatical model of the conventionally fabricated electrets to explain the experimentally observed low values of emergent transverse piezoelectric coefficient d_{31} [3]. To do so, we analyze the in-plane stretching of the representative electret configuration shown in Fig. 2.4. This electret consists of two different materials on top and bottom which

are referenced with subscripts "t" and "b", respectively. Let $\mathbf{X} = X\mathbf{e}_X + Y\mathbf{e}_Y + Z\mathbf{e}_Z$ be representation of points in the Lagrange coordinates while points in Euler coordinates are denoted by $\mathbf{x} = x\mathbf{e}_x + y\mathbf{e}_y + z\mathbf{e}_z$. The domains of these two materials are

$$\Omega_{R_b} = \{(X,Y,Z) \in \mathbb{R}^3 : -H \leq X \leq \alpha H, |Y| \leq L, |Z| \leq W\} \quad \text{and} \tag{2.16a}$$

$$\Omega_{R_t} = \{(X,Y,Z) \in \mathbb{R}^3 : \alpha H < X \leq H, |Y| \leq L, |Z| \leq W\}, \tag{2.16b}$$

where $|\alpha| < 1$ is a constant that parametrizes the interface between the two materials.

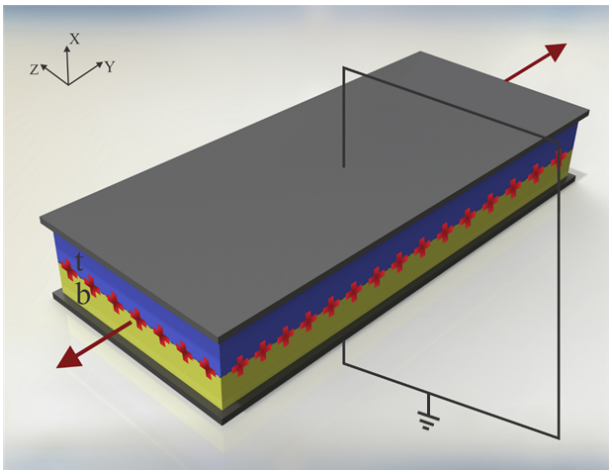

Figure 2.4: Dielectric made of two different layers with embedded external charges under in-plane tension and short circuit boundary condition.

A layer of external charges with surface charge density q is inserted at the interface $X = \alpha H$. As shown in Fig. 2.4, the two-material film is stretched in the Y direction[9]. Assuming plane-strain deformation, the deformation in Z direction vanishes. In what follows, we will refer to X and Y directions, respectively, as the thickness and in-plane directions. In the present case, the deformation in both these directions is uniform and the deformation gradient for both layers is given by

$$\mathbf{F} = \lambda_1 \mathbf{e}_x \otimes \mathbf{e}_X + \lambda_2 \mathbf{e}_y \otimes \mathbf{e}_Y + \mathbf{e}_z \otimes \mathbf{e}_Z, \tag{2.17}$$

[9]We remark that in the presently defined coordinate system, the longitudinal piezoelectric coefficient will be defined by examining the electric response in the X-direction in response to mechanical loading in the X-direction—as discussed in the theoretical models of Deng et al. [98, 99]

where λ_1 and λ_2 are, respectively, the stretches in the thickness and in-plane direction. The incompressibility constraint ($J = \lambda_1\lambda_2 = 1$) implies that $\lambda_2 = \frac{1}{\lambda_1}$. For the ease of notation, in what follows, we drop the subscript 1 and write $\lambda_1 = \lambda$ here and henceforth. In order to explore the implication of incompressibility constraint, we add one more term to the total free energy of the system given in Eq.(2.5)

$$\int_{\Omega_R} -\mathcal{L}_a(J-1), \tag{2.18}$$

where $\mathcal{L}_a$ is a Lagrange multiplier. Also, Ω_R may be replaced with Ω_{R_t} or Ω_{R_b} to derive the equilibrium equations for each of the layers. Due to this modification of free energy, Eq.(2.9) and (2.13) are updated as

$$\widetilde{\mathbf{\Sigma}} = \frac{\partial \psi}{\partial \mathbf{F}} - \mathcal{L}_a J \mathbf{F}^{-T}, \tag{2.19}$$

$$\text{and} \qquad \boldsymbol{\sigma} = \frac{1}{J}\frac{\partial W^{elast}}{\partial \mathbf{F}}\mathbf{F}^T - \mathcal{L}_a \mathbf{I}. \tag{2.20}$$

To model the mechanical behavior of the materials, we choose the incompressible neo-Hookean constitutive law and accordingly, the internal energy W^{elast} may be expressed as

$$W^{elast} = \frac{\mu}{2}(\text{tr}(\mathbf{F}^T\mathbf{F}) - 3), \tag{2.21}$$

where μ is the shear modulus. We remark that the choice of this particular hyperelastic constitutive model is not central to the main conclusions of this chapter.

Two mechanically compliant electrodes are attached to the top and bottom surfaces of the electret structure and a short circuit electrical boundary condition is imposed (Fig. 2.4) to facilitate the definition of an apparent piezoelectric coefficient in response to mechanical stimulus. The objective is to determine the induced dielectric displacement as a result of the applied mechanical deformation or stress. The geometry of the structure and deformation assumptions ensures that the considered problem is essentially one-dimensional in nature with the electric field that varies only in the thickness direction. From Eq.(2.12a) and (2.1)

we have

$$\mathbf{p} = (\epsilon - \epsilon_0)\mathbf{e}, \quad \mathbf{d} = \epsilon\mathbf{e} \quad \text{and} \quad \mathbf{e} = -\frac{d\xi}{dx}\mathbf{e}_x. \tag{2.22}$$

Substituting Eq.(2.22) and (2.21) into (2.8) and using Eq.(2.11), equilibrium equations for each layer become:

$$\frac{\mathrm{d}}{\mathrm{d}X}\Big[\mu_i\left(\lambda - \frac{1}{\lambda^3}\right) - \frac{\mathcal{L}_a}{\lambda} + \frac{\epsilon_i}{2\lambda^3}\left(\frac{\mathrm{d}\xi}{\mathrm{d}X}\right)^2\Big] = 0 \tag{2.23a}$$

$$\text{and} \qquad \frac{\mathrm{d}}{\mathrm{d}Y}\Big[-\mathcal{L}_a\lambda - \frac{\epsilon_i}{2\lambda}\left(\frac{\mathrm{d}\xi}{\mathrm{d}X}\right)^2\Big] = 0, \tag{2.23b}$$

and the boundary conditions are given as

$$\left[\mu_i\left(\lambda - \frac{1}{\lambda^3}\right) - \frac{\mathcal{L}_a}{\lambda} + \frac{\epsilon_i}{2\lambda^3}\left(\frac{\mathrm{d}\xi}{\mathrm{d}X}\right)^2\right]\Bigg|_{X=\alpha H}^{X=\gamma_i H} = 0 \tag{2.24a}$$

$$\text{and} \qquad \left[-\mathcal{L}_a\lambda - \frac{\epsilon_i}{2\lambda}\left(\frac{\mathrm{d}\xi}{\mathrm{d}X}\right)^2 - \widetilde{t}_i^e\right]\Bigg|_{Y=-L}^{Y=L} = 0, \tag{2.24b}$$

for $i = b$ and t. $\gamma_b = -1$ and $\gamma_t = 1$. $\widetilde{\mathbf{t}}_i^e = \widetilde{t}_i^e\mathbf{e}_Y$ is the imposed traction (dead load) applied to each layer on the surfaces $|Y| = L$. As evident from the Maxwell's equations, the electric field is homogeneous within each layer. Therefore, eliminating $\mathcal{L}_a$ from system of equations (2.23), using boundary conditions (2.24), the equilibrium equation for each layer reduces to:

$$\mu_i\left(\lambda^4 - 1\right) + \epsilon_i\left(\frac{\mathrm{d}\xi}{\mathrm{d}X}\right)^2 + \lambda\widetilde{t}_i^e = 0 \qquad \text{for} \quad i = b, t. \tag{2.25}$$

Given the short circuit boundary condition, the electric potential on the top and bottom surfaces remains zero and the electric potential at the interface is considered to be equal to an unknown value V, where V will be determined using the interface condition. Using these values for electric potential at boundaries and solving the Maxwell equation (2.12b) for each layer, electric potential difference is derived as

$$\frac{\mathrm{d}\xi}{\mathrm{d}x} = \begin{cases} -\frac{V}{h_t} & \text{for the layer at the top,} \\ \frac{V}{h_b} & \text{for the layer at the bottom,} \end{cases} \tag{2.26}$$

where $h_t = \lambda(1-\alpha)H$ and $h_b = \lambda(1+\alpha)H$ are the deformed thicknesses of top and bottom layers, respectively. Considering the fact that surface charge density q in the reference configuration will change to λq in the current configuration, the interface condition is used to determine V

$$\epsilon_t \frac{V}{h_t} + \epsilon_b \frac{V}{h_b} = \lambda q. \tag{2.27}$$

Using Eq.(2.27) and substituting Eq.(2.26) into (2.25), the traction in each layer required to maintain this deformation can be determined. We note that the electric displacement in each layer is also homogeneous and, d_t and D_t are identified such that for the layer at the top we have $\mathbf{d} = d_t \mathbf{e}_x$ and $\widetilde{\mathbf{D}} = D_t \mathbf{e}_X$. Substituting Eq.(2.26) into Eq.(2.22) we obtain

$$d_t = \frac{\epsilon_t \lambda q h_b}{\epsilon_t h_b + \epsilon_b h_t}. \tag{2.28}$$

D_t is derived substituting Eq.(2.28) into Eq.(2.3)

$$D_t = \frac{q}{1 + \frac{\epsilon_b(1-\alpha)}{\epsilon_t(1+\alpha)}}. \tag{2.29}$$

In order to measure the d_{31} piezoelectric coefficient of an actual piezoelectric material, an in-plane stretch similar to what is shown in Fig. 4 is applied. The piezoelectric coefficient can then be determined by measuring the change in the electric displacement in the thickness direction, D_X, in response to the applied in-plane normal tractions where the following constitutive relation for piezoelectricity is used[10] [101, 102]

$$D_i = \epsilon_{ij} E_j + d_{ijk} \Sigma_{jk}, \tag{2.30}$$

where D_i, ϵ_{ij}, E_j, d_{ijk} and Σ_{jk} are, respectively, components of the electric displacement, dielectric tensor, electric field, piezoelectric tensor and stress tensor. Using contracted notation and considering material symmetry $d_{31} = d_{32}$, Eq.(2.30) reduces to $D_X = d_{31}(\Sigma_{YY} + \Sigma_{ZZ})$ in absence of external electric field and in presence of normal in-plane

[10] We remark that this constitutive relation is based on linearized theories of piezoelectricity which do to consider the incompressibility constraint. To connect our work as closely as possible to constitutive equations what experimentalists are likely to use, we employ (2.30) in this work.

stresses. We can therefore determine the piezoelectric coefficient by measuring the change in the electric displacement in response to the applied loading. Analogously, in the case of the electret structure under consideration, we use the same notion to define an apparent piezoelectric coefficient

$$d_{31}^{app} = \frac{d(D_t^f - D_t^i)}{d\lambda} \left(\frac{d\langle \Sigma_{YY} + \Sigma_{ZZ} \rangle}{d\lambda} \right)^{-1}, \tag{2.31}$$

where $D_t^f = D_t$ is the electric displacement after deformation and determined in Eq.(2.29) and $D_t^i = D_t|_{\widetilde{\mathbf{t}}^e=0}$ is the electric displacement in the absence of an externally applied loading. In what follows, for any parameter f, we define $\langle f \rangle = \frac{1}{2H} \int_{-H}^{H} f(X) dX$. As evident from Eq.(2.29), in our considered electret structure (which is representative of conventionally fabricated electrets), $D_t^f - D_t^i$ is zero. Therefore, the emergent d_{31}^{app} piezoelectric coefficient is also zero. This is to be contrasted with the derivation for the large d_{33}^{app} coefficient obtained for soft electrets [98]. Physically, when a mechanical load in thickness direction is applied to the electret structure being considered, deformation distributes non-uniformly. This non-uniformity of deformation results in an appreciable value for the d_{33}^{app} piezoelectric coefficient. The material inhomogeneity is central to enable non-uniform deformation and the consequent non-zero d_{33}^{app} coefficient. This fact it is reflected in the expression[11] [98, 99] for d_{33}^{app}

$$d_{33}^{app} = -\frac{2qH_tH_b\epsilon_t\epsilon_b}{3(\epsilon_tH_b + \epsilon_bH_t)^2}\left(\frac{1}{\mu_t} - \frac{1}{\mu_b}\right). \tag{2.32}$$

In short, as long as deformation is non-uniformly distributed inside the material ($\mu_t \neq \mu_b$) a non-zero d_{33}^{app} is predicted. However under in-plane stretch, the deformation is almost uniform everywhere in the electret.

The simple derivation in this section explains the root cause for low d_{31}^{app} coefficient and highlights that, to obtain a non-zero transverse piezoelectric response, a non-homogeneous deformation in the thickness direction must be engineered. This observation and our model also suggests the reason for a non-trivial d_{31} effect for electret polymer films observed by Zhang et al. [1]. They showed that electrets made of fluoroethylene propylene films with

[11] We remark in passing that Deng et al. [98, 99] defined the apparent piezoelectric coefficient in a slightly different manner but to within a trivial scaling factor, the physics is identical.

charged *parallel-tunnel* voids can have a very large d_{31}. Based on our developed model, we speculate that the reason for this large piezoelectric coefficient is the specific design that they used which permits large deformation in the voids while polymer sections remain almost undeformed. For more clarification, consider Fig. 2.5(a) which shows a polymer foam with two *parallel-tunnel* voids in its undeformed configuration. Under an in-plane loading, the film undergoes a deformation similar to what is shown in Fig. 2.5(b). The shape of voids alter significantly, but there is almost no deformation in the polymer sections and deformation in distributed non-uniformly between air voids and polymer sections leading therefore to a large bending piezoelectric effect.

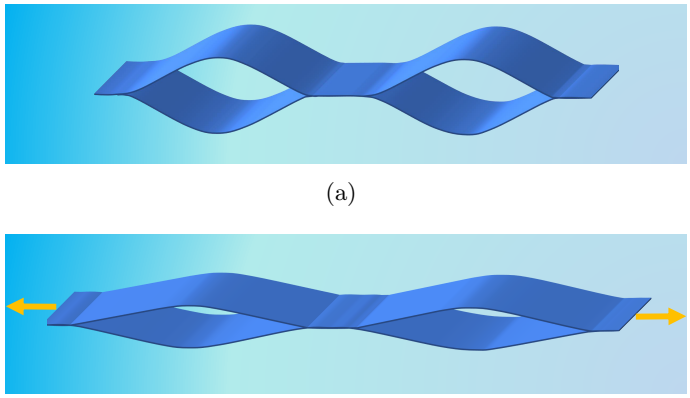

(a)

(b)

Figure 2.5: Cross-section of a specif electret polymer film fabricated by Zhang et al. [1] (a) Undeformed configuration (b) Deformed configuration.

2.4 Flexure behavior of soft electrets

A non-trivial d_{31} piezoelectric coefficient is essential for a strong electromechanical response under flexure. To enable the design of electrets, and armed with insights from the preceding section, we perform a nonlinear analysis of the bending deformation of an electret structure. To our knowledge, there is no such analysis in the literature. Specifically we will consider both soft electret structure made of a single homogeneous material as well as composite electrets with two different materials. Specifically, we will, to a large extent possible, carry out a fully three-dimensional analysis as opposed to using the kinematics of a beam theory. Retaining the complexity of treating a three-dimensional object will allow us to

show that the change in thickness (which is not captured in conventional beam theories) plays a crucial role in the nonlinear bending deformation of soft electrets. To distinguish between our analysis and a beam-type consideration, we will often refer our considered structure as a "block" rather than a "beam". We remark here that in the purely mechanical context, flexure of a three-dimensional block was first analyzed by Rivlin [103]. Our work is its generalization to the electromechanical case.

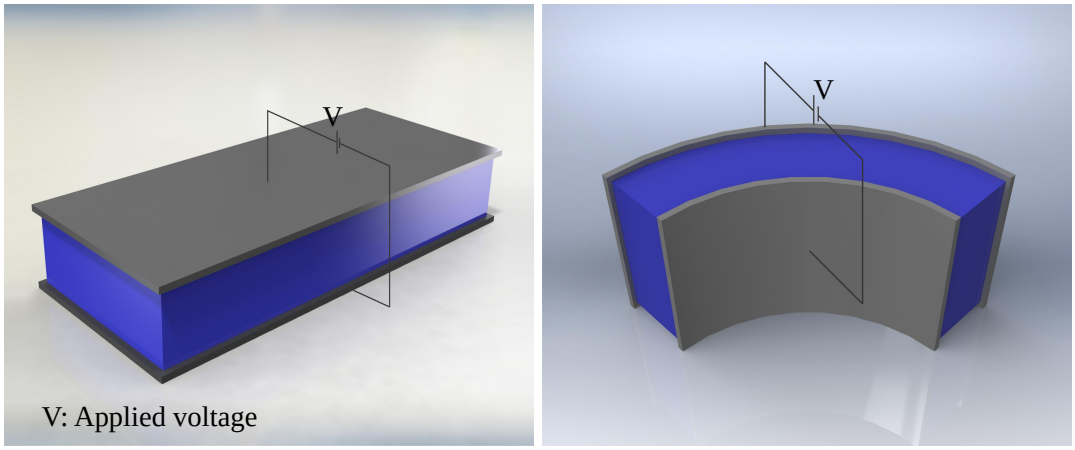

(a) (b)

Figure 2.6: Soft dielectric block under bending deformation and external electric field: (a) reference configuration (b) current configuration.

2.4.1 Bending of a homogeneous dielectric block under an external electric field

In order to elucidate the shortcomings of conventional soft dielectrics as a bending sensor and actuator, we first analyze the nonlinear flexure problem of a homogeneous dielectric block that is *not* an electret i.e without embedded charges or dipoles. The reference and current configurations are shown in Fig. 2.6 where the three-dimensional representation of the block is due to the fact that we don't treat our structure as a "beam". The block in the reference configuration is denoted by

$$\Omega_R = \{(X, Y, Z) \in \mathbb{R}^3 : |X| \leq H, |Y| \leq L, |Z| \leq W\}, \tag{2.33}$$

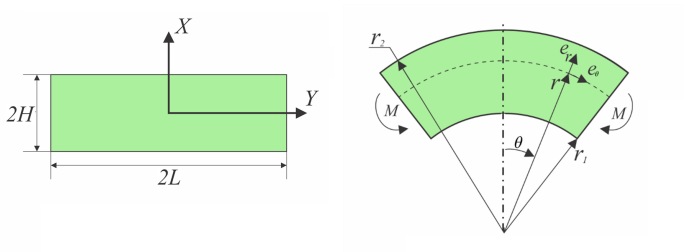

(a) (b)

Figure 2.7: Schematic of the coordinate systems used in the reference and current configurations. (a) Cartesian coordinates are used in the undeformed block. (b) A cylindrical coordinate based is employed for the deformed block.

where H, L and W are the block's geometrical dimensions. As shown in Fig. 2.7, the Cartesian coordinate bases $\{\mathbf{e}_X, \mathbf{e}_Y, \mathbf{e}_Z\}$ are used to denote material points $\mathbf{X}$. The cylindrical polar coordinates $\{\mathbf{e}_r, \mathbf{e}_\theta, \mathbf{e}_z\}$ are employed to identify points in the current configuration. To describe bending of the block, we follow the approach presented by Rivlin [103] who addressed the corresponding (purely) mechanical problem. The complete nonlinear boundary value problem (even in the purely mechanical case) is quite difficult. To simplify matter, we make the following kinematic assumption that the set of all material points initially located at any plane normal to $\mathbf{e}_X$ are deformed to a set of points located in a curved cylindrical surface with constant radius and, similarly, the set of all material points initially located at any plane normal to $\mathbf{e}_Y$ are deformed to a set of points located in a plane with constant θ and there is no deformation in the Z-direction (See Fig. 2.7).

A general deformation in the cylindrical coordinates can be expressed as

$$\mathbf{x} = r(X)\mathbf{e}_r + z(Z)\mathbf{e}_z, \tag{2.34}$$

where $\mathbf{e}_r = \mathbf{e}_r(\theta)$ and $\theta = \theta(Y)$. From Eq.(2.34), the deformation gradient is

$$\mathbf{F} = \frac{dr(X)}{dX}\mathbf{e}_r \otimes \mathbf{e}_X + r(X)\frac{d\theta(Y)}{dY}\mathbf{e}_\theta \otimes \mathbf{e}_Y + \frac{dz(Z)}{dZ}\mathbf{e}_z \otimes \mathbf{e}_Z. \tag{2.35}$$

Imposing incompressibility constraint $J = 1$ to the aforementioned class of deformation

requires r, θ and z to obey the following relations

$$r(X) = \sqrt{2AX + B}, \qquad \theta(Y) = \frac{Y}{A} \quad \text{and} \quad z(Z) = Z, \tag{2.36}$$

where A and B are unknown constants. We identify $r_1 = r(-H)$ and $r_2 = r(H)$. Associated with these deformations, we can write the deformation gradient as

$$\mathbf{F} = \frac{A}{r}\mathbf{e}_r \otimes \mathbf{e}_X + \frac{r}{A}\mathbf{e}_\theta \otimes \mathbf{e}_Y + \mathbf{e}_z \otimes \mathbf{e}_Z. \tag{2.37}$$

Similar to the stretch problem in section 2, we employ the incompressible neo-Hookean constitutive law given in Eq.(2.21) and therefore the Cauchy stress $\boldsymbol{\sigma}$ in the dielectric is given as

$$\boldsymbol{\sigma} = \mu \mathbf{F}\mathbf{F}^T - \mathcal{L}_a \mathbf{I}. \tag{2.38}$$

Ignoring non-radial components of electric field for simplicity and using Eq.(2.1) and (2.12a), electric displacement and polarization can be written in terms of the electric potential as follows:

$$\mathbf{p} = (\epsilon - \epsilon_0)\mathbf{e}, \quad \mathbf{d} = \epsilon \mathbf{e} \quad \text{and} \quad \mathbf{e} = -\frac{d\xi}{dr}\mathbf{e}_r. \tag{2.39}$$

Consequently, Maxwell's equations and the boundary conditions in the absence of external charges but with the block subjected to a potential difference are

$$\begin{cases} -\frac{1}{r}\frac{d}{dr}\left(\epsilon r \frac{d\xi}{dr}\right) = 0, \\ \xi(r_1) = 0 \qquad \text{and} \qquad \xi(r_2) = V. \end{cases} \tag{2.40}$$

Electric field in the current configuration is determined by solving (2.40):

$$\mathbf{e} = -\frac{V}{r}\frac{1}{\log \frac{r_2}{r_1}}\mathbf{e}_r. \tag{2.41}$$

Having electric field, we can calculate Maxwell stress from (2.14). Then total stress is obtained as

$$\boldsymbol{\sigma} + \boldsymbol{\sigma}'^{MW} = \sigma^*_{rr}\mathbf{e}_r \otimes \mathbf{e}_r + \sigma^*_{\theta\theta}\mathbf{e}_\theta \otimes \mathbf{e}_\theta + \sigma^*_{zz}\mathbf{e}_z \otimes \mathbf{e}_z - \mathcal{L}_a \mathbf{I}, \tag{2.42}$$

where

$$\begin{aligned} \sigma^*_{rr} &= \mu\frac{A^2}{r^2} + \frac{\epsilon}{2}\left(\frac{d\xi}{dr}\right)^2, \\ \sigma^*_{\theta\theta} &= \mu\frac{r^2}{A^2} - \frac{\epsilon}{2}\left(\frac{d\xi}{dr}\right)^2, \\ \text{and} \qquad \sigma^*_{zz} &= -\frac{\epsilon}{2}\left(\frac{d\xi}{dr}\right)^2. \end{aligned} \tag{2.43}$$

Equilibrium equation (2.12c) in the radial direction can be written as:

$$\frac{d\sigma^*_{rr}}{dr} - \frac{d\mathcal{L}_a}{dr} + \frac{1}{r}\left(\sigma^*_{rr} - \sigma^*_{\theta\theta}\right) = 0. \tag{2.44}$$

To simplify the solution, we express A and B in terms of r_1 and r_2. Using equations $r_1 = r(-H)$, $r_2 = r(H)$ and Eq.(2.36) we have

$$A = \frac{r_2^2 - r_1^2}{4H} \quad \text{and} \qquad B = \frac{r_2^2 + r_1^2}{2}. \tag{2.45}$$

To solve the equilibrium equation, we impose the following boundary conditions:

$$\mathbf{t}_r = \left(\boldsymbol{\sigma}^* - \mathcal{L}_a\mathbf{I}\right)\mathbf{e}_r = \mathbf{0} \qquad \text{at} \quad r = r_1 \quad \text{and} \quad r = r_2, \tag{2.46a}$$

$$M = \int_{r_1}^{r_2} r(\sigma^*_{\theta\theta} - \mathcal{L}_a)dr, \tag{2.46b}$$

where M is the bending moment over unit width of the block and $\mathbf{t}_r$ is the surface traction for the surface with unit normal $\mathbf{e}_r$.

Integrating Eq.(2.44) and using first Eq. of (2.46a), the Lagrange multiplier $\mathcal{L}_a$ can be determined to be

$$\mathcal{L}_a = \sigma^*_{rr} + \int_{r_1}^{r} \frac{1}{\hat{r}}\left(\sigma^*_{rr}(\hat{r}) - \sigma^*_{\theta\theta}(\hat{r})\right) d\hat{r}. \tag{2.47}$$

For future expedience, we also introduce the radial stretch λ and radius ratio Λ:

$$\lambda = \frac{|r_2 - r_1|}{2H}, \quad \Lambda = \frac{r_2}{r_1}. \tag{2.48}$$

With the relation for the Lagrange multiplier at hand, using relations (2.45) and (2.48), we can solve the second boundary condition in (2.46a) for λ. With the substitution of the stretch in Eq.(2.46b), all quantities can be expressed in closed-form in terms of Λ. The

stretch and bending moment can then be derived to be:

$$\lambda^4 = \frac{16\Lambda^2}{(\Lambda+1)^4} - \frac{(\Lambda-1)^2}{(\Lambda+1)^2\log^2(\Lambda)}\frac{\epsilon V^2}{\mu H^2}, \tag{2.49}$$

$$\text{and} \qquad M = \frac{2H^2\mu\left(\Lambda^4 - 4\Lambda^2\log(\Lambda) - 1\right)}{\left(\Lambda^2-1\right)^2}. \tag{2.50}$$

We introduce $\bar{\kappa} = \frac{r_2 - r_1}{r_1}$ as a representation for the curvature. Curvature $\bar{\kappa}$ will be positive if $r_2 > r_1$ and vice-versa. The ratio Λ in (2.48) can be easily related to curvature through relation:

$$\Lambda = 1 + \bar{\kappa}. \tag{2.51}$$

From the nonlinear relation (2.49), we observe that the stretch depends on both the curvature and the applied electric field. However, the bending moment is independent of the applied potential difference and the effect of electric field on curvature emerges *only* through a change of thickness. If the thickness in the deformed configuration remains unchanged from the reference configuration, then the electric field will not have any impact on curvature since curvature bending moment relation (2.50) is independent of the electric field.

In many practical applications, thickness of the film is much smaller than the radius of curvature even when the film undergoes large deformation. In such a case, $|\bar{\kappa}| \ll 1$. This condition is also valid for thick blocks under small deformations. It is therefore instructive to linearize (2.50) and (2.49) for the cases with $|\bar{\kappa}| \ll 1$. Ignoring higher order terms, stretch and bending moment can then be expressed as

$$\mu\left(\lambda^4 - 1\right) = -\epsilon\left(\frac{V}{2H}\right)^2 + o(\bar{\kappa}), \tag{2.52}$$

$$\text{and} \qquad M = \frac{4}{3}H^2\mu\bar{\kappa} + o(\bar{\kappa}). \tag{2.53}$$

We remark that in the flexure problem discussed in this section as well as the stretch problem discussed in section 2.3, in absence of mechanical loading, deformation is only caused by the applied electrical field. Since there is no kinematic constraint against the change of thickness in the models used for both the bending and stretch problems, the derived change of thickness in response to the applied electrical field should be the same for both models.

Indeed, Eq.(2.52) is exactly the same as (2.25) when the applied traction is zero. Also, several other interesting conclusions may be drawn by a careful consideration of Eq.s (2.52) and (2.53):

1. Equation (2.52) is independent of curvature $\bar{\kappa}$ and the external electric field is the *only* reason for the change of thickness.

2. Equation (2.53) is independent of V. Although the value of $\bar{\kappa}$ depends on the thickness of the block in the deformed configuration, and alteration in the external electric field will change the thickness and consequently curvature but ignoring the effect of external electric field on the thickness of the block will lead to the complete de-correlation of the curvature of the film and the external electric field.

3. Even if we account for the change of the thickness due to external field and its effect on the curvature, their relation is *quadratic* (see Eq.(2.52)). This observation implies that a change in the direction of the electric field will not change the direction of deformation thus limiting the application of ordinary soft dielectrics as bending actuators.

4. Equation (2.53) shows that in the absence of bending moment ($M = 0$) curvature $\bar{\kappa}$ is zero. This, in turn, signifies that no matter how large the applied electric field, flexure will not ensue in absence of an applied mechanical bending moment.

These aforementioned points emphasize that ordinary soft dielectrics are unsuitable, at least if used naively, as bending sensors and actuators. We will show in the next section that electrets offer a rather rich set of avenues to tweak flexure response of soft dielectrics.

2.4.2 Bending deformation of a homogeneous block with embedded charges—an electret

We now turn our attention to the problem that is at the heart of the central goal of the manuscript. We reconsider the nonlinear flexure problem of a soft dielectric block but now

containing a distributed (and embedded) *immobile* layer of charge[12]. We consider such a layer of charge with surface density q to be located at the plane $X = X_{ch}$ in the reference configuration (Fig. 2.8) where $X_{ch} = \alpha H$ and α is an indicator of the position of the charge layer. This parameter can take values between -1 and 1. The plane containing electric charges will deform to a curved surface with the radius $r = r_{ch}$. The total charge inside the dielectric is conserved and with that, the charge density in the current (deformed) configuration may be expressed as

$$\rho_e = q\frac{A}{r_{ch}}\delta\left(r - r_{ch}\right), \tag{2.54}$$

where $\delta(\cdot)$ is the one-dimensional Dirac delta function and A was defined earlier in Eq.(2.36).

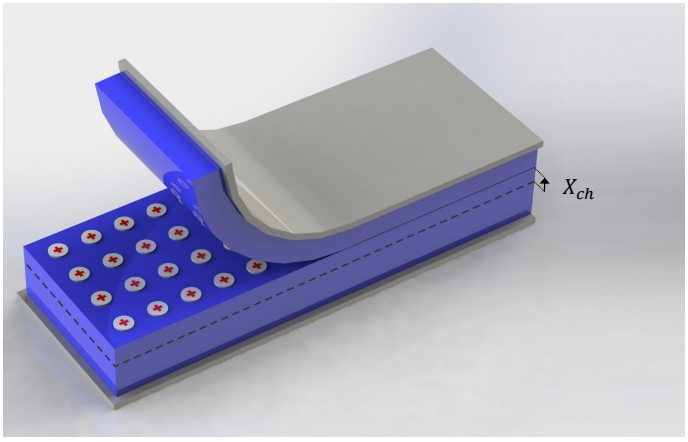

Figure 2.8: A layer of charges is embedded in a soft dielectric.

Invoking the premise that the electric field only exists in the radial direction, using (2.12a) and (2.12b), and employing the short circuit boundary condition, the electric field in the current configuration is obtained as

$$\mathbf{e} = \frac{qA}{\epsilon r}\left(\mathcal{H}(r - r_{ch}) - \frac{\log\left(\frac{r_2}{r_{ch}}\right)}{\log\left(\frac{r_2}{r_1}\right)}\right)\mathbf{e}_r, \tag{2.55}$$

[12] As typically understood in electrets, the charges and dipoles are immobile in the sense that they do not flow in the time scale (and temperature regime) of interest but do convect with deformation. Depending on the material properties, electret configuration and ambient temperature, discharge can occur on a time scale varying from days to decades [104, 64].

where $\mathcal{H}(\cdot)$ is the Heaviside step function. We defer for now the discussion on the influence of external voltage and the actuator mode application of this structure. As done in prior sections, the stretch can be evaluated analytically in terms of the radius ratio Λ and other properties of the dielectric block

$$\lambda^4 = \frac{16\Lambda^2}{(1+\Lambda)^4\left(1+\bar{q}_0^2 C_{11}\right)}, \tag{2.56}$$

where $\bar{q}_0 = \frac{q}{\sqrt{\epsilon\mu}}$. The coefficients C_{ij} depend on Λ and α and their complete expressions are recorded in Appendix 2.7.1. The bending moment necessary to maintain the desired deformation in terms of radius ratio using (2.46b) is

$$M = \frac{2H^2\mu\left(\Lambda^4 - 4\Lambda^2\log(\Lambda) - 1 + \bar{q}_0^2 C_{12}\right)}{\left(\Lambda^2-1\right)^2 + \bar{q}_0^2 C_{13}}. \tag{2.57}$$

Equation (2.57) should be contrasted with Eq.(2.50). In the case of an electret, the electric field created by the embedded charges influences the bending deformation of the block not only through the change of the thickness but also through a direct effect on the bending moment-curvature relation. In order to further clarify the effect of embedded charges on the bending deformation of thin films, we express the stretch and bending moment in terms of only the leading order terms of $\bar{\kappa}$

$$\lambda^4 = \lambda_0^4 + D_{11}\bar{\kappa} + o(\bar{\kappa}) \tag{2.58}$$

$$\text{and} \qquad \frac{M}{4\mu H^2} = M_0 + D_{12}\bar{\kappa} + o(\bar{\kappa}), \tag{2.59}$$

where

$$\lambda_0^4 = \frac{4}{(1-\alpha^2)\,\bar{q}_0^2 + 4}, \tag{2.60}$$

$$\text{and} \qquad M_0 = -\frac{\bar{q}_0^2\alpha(1-\alpha^2)}{2\bar{q}_0^2(1-\alpha^2)+8}. \tag{2.61}$$

Coefficients D_{ij} are recorded in the Appendix 2.7.1. Both Eq.(2.59) and (2.58) depend on $\bar{\kappa}$ and $\bar{q}_0$. The simple implication of this observation is that the coupling between the mechanical and electrical state of the dielectric block is significantly more intricate and

stronger in electret structures as compared to ordinary dielectrics. Notably, any change in the amount of charge or the position of charge layer will change the bending moment required to cause a specific value of curvature *even* if we were to ignore changes in the thickness. This is in contrast to what we observed in Eq.(2.53) for the small-deformation case of a thin homogeneous film under an external applied electric where the effect of the external voltage only emerges from a change in the thickness.

Equation (2.59) can be solved for $\bar{\kappa}$ to derive an approximate linear relation for the curvature in terms of the bending moment

$$\bar{\kappa} \approx \frac{M}{4\mu H^2 D_{12}} - \frac{M_0}{D_{12}}. \tag{2.62}$$

A rather interesting property of the electret may be realized from (2.62); unless the charge layer is *exactly* located in the middle of the block ($\alpha = 0$), a nonzero curvature will develop even in the *absence* of external mechanical loading. In other words, existence of Maxwell stress in non-symmetric block (block in which charge layer in not located in the mid-plane) leads to bending of the block. Setting $M = 0$, Eq.(2.62) may be used to ascertain that a nonzero curvature exists in the structure even in the absence of any mechanical loading.

In addition to embedded charges, we can also consider the effect of an external voltage to investigate actuator application of the electret structure. For this purpose, the Maxwell's equations are solved using the embedded charge given in (2.54) and boundary condition used in (2.40) to derive the electric field:

$$\mathbf{e} = \frac{1}{\epsilon r}\left(Aq\mathcal{H}(r - r_{ch}) - \frac{Aq\log\left(\frac{r_2}{r_{ch}}\right) + V\epsilon}{\log\left(\frac{r_2}{r_1}\right)}\right)\mathbf{e}_r. \tag{2.63}$$

Following a similar process as before, the mechanical boundary conditions are imposed to determine the stretch in terms of radius ratio and then all quantities are expressed in terms of the radius ratio. Since the process is straightforward but the resulting equations are rather long, we avoid listing them here and the details may be found in Appendix B. After deriving

the nonlinear bending moment radius ratio relation, we linearize this relation for $|\bar{\kappa}| \ll 1$ and derive an expression similar to (2.59) with modified values for D_{12} and M_0. Relation for D_{12} is given in Eq.(2.7.89). In order to provide insights into the bending behavior of electret under external voltage (in absence of any mechanical loading) we simply update the expression of M_0 presented in Eq.(2.61). The modified M_0 may be derived to have the following form:

$$M_0 = \left(1-\alpha^2\right)\bar{q}_0 \times \\ \frac{\widetilde{E}_0\sqrt{\left(\widetilde{E}_0^2-1\right)\left(\left(\alpha^2-1\right)\bar{q}_0^2-4\right)}+\alpha\left(\widetilde{E}_0^2-1\right)\bar{q}_0}{2\left(1-\alpha^2\right)\bar{q}_0^2+8}, \tag{2.64}$$

where $\widetilde{E}_0 = \frac{V}{2H}\sqrt{\frac{\epsilon}{\mu}}$. An intriguing implication from (2.64) is that in the presence of external electric field and absence of mechanical loading, a non-zero value for curvature is obtained—even for symmetric electrets ($\alpha = 0$). Moreover, this curvature depends on the value of external electric field and any change of the external field will also alter the curvature. As will be discussed in the next section, this behavior may be interpreted as converse bending piezoelectric behavior.

2.4.3 Identification of the apparent flexoelectric and d_{31} piezoelectric coefficients in electrets

As shown in the prior section, if a fixed bending moment is maintained, an electric field can change the curvature of the electret structure and conversely, a change in curvature can lead to a change in the electric field. This can be made more explicit by examining the electric displacement. For a short circuited electret strucuture, $\widetilde{\mathbf{D}}$ may be determined by using Eq.(2.55), (2.39) and(2.3)

$$\widetilde{\mathbf{D}} = q\left(\mathcal{H}(X-X_{ch}) - \frac{\log\left(C_{22}\right)}{\log\left(\Lambda\right)}\right)\mathbf{e}_X. \tag{2.65}$$

Electric displacement in Eq.(2.65) depends on Λ, signifying that electric displacement changes with the change of curvature. Using Taylor series for small values of $\bar{\kappa}$ we can

elucidate a linear relation between the change of electric displacement and curvature

$$\widetilde{\mathbf{D}} = D^f \mathbf{e}_X = \left(D^i + \frac{1}{4} q(1-\alpha^2)\bar{\kappa} + o(\bar{\kappa}) \right) \mathbf{e}_X. \tag{2.66}$$

In the present context, we may identify the initial state as the zero curvature (flat) state and the curved state as the final deformed state of the bending. Denoting D^f and D^i, respectively, to represent the electric displacement in the final and initial states, we can write D^i as

$$D^i = \begin{cases} \frac{1}{2} q(1+\alpha) & \text{for} \quad X > X_{ch}, \\ -\frac{1}{2} q(1-\alpha) & \text{for} \quad X < X_{ch}. \end{cases}$$

The linear relation between curvature and electric displacement, or polarization, is a tell-tale signature of flexoelectricity. In an experimental setting, flexoelectric coefficient of a material can be determined by measuring the electric current generated during bending deformation. We use such a *gedanken* on these lines to define an apparent (and emergent) flexoelectric coefficient for the electret structure [105].

Interchangeably, and somewhat ambiguously, the same basic logic may also be interpreted as an emergent d_{31} piezoelectric coefficient. However, this requires some further nuanced discussion. As already discussed briefly in the introductory section, because the average strain is zero in bending, a (net) electric polarization is not generated from the bending deformation of a single layer piezoelectric film unless a bimorph configuration is used. Bending of a piezoelectric bimorph with opposite poling directions (shown in Fig. 2.9) leads to the development of a non-zero (net) electric polarization inside the material. In addition, a uniform external electric field can cause bending in the bimorph with opposite poling directions. We remark that an electret with embedded charges is similar to a bimorph with opposite poling directions. So, in order to interpret the flexure of electrets in terms of emergent piezoelectric or interchangeably, flexoelectric response, we must compare it with either a piezoelectric bimorph or a homogeneous material with flexoelectric effect. Since it is not possible to analytically solve a non-linear three-dimensional bending problem of a flexoelectric or piezoelectric block, we use a simple linear piezoelectric or flexoelectric Euler-beam theory to find the correlation between mechanical loading and induced charge.

Then, this correlation is compared with the results of our nonlinear model for electrets to suggest expressions for the apparent flexoelectric and piezoelectric coefficients.

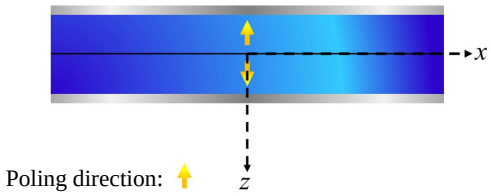

(a)

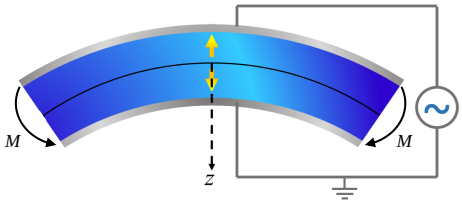

(b)

Figure 2.9: Piezoelectric bimorph made of two layers of piezoelectric materials with different poling directions. (a) Undeformed configuration (b) Deformed configuration.

Apparent piezoelectric coefficient. The definition of the apparent piezoelectric coefficient requires the solution to the bending problem of a bimorph. The derivation is recorded in Appendix 2.7.3 and specifically the central result used in this section appears in (2.7.130). In contrast to the piezoelectric *beam* model, our model for the flexure of an electret is nonlinear and three-dimensional. To relate them and derive apparent piezoelectricity as would be measured in experiments, we introduce the notion of average curvature $\langle\kappa\rangle$ as

$$\langle\kappa\rangle = \frac{1}{2H}\int_{r_1}^{r_2}\frac{1}{r}dr = \frac{\bar{\kappa}}{2H} + o(\bar{\kappa}). \tag{2.67}$$

Apparent bending stiffness κ_b^{app} and apparent piezoelectric coefficient d_{31}^{app} of the electret structure can therefore be defined as

$$\kappa_b^{app} = \left(\frac{\partial\langle\kappa\rangle}{\partial M}\right)^{-1}, \tag{2.68}$$

$$\text{and} \qquad d_{31}^{app} = -\frac{2\kappa_b^{app}}{3\mu H}\frac{\partial D^f}{\partial M}. \tag{2.69}$$

Equation (2.67) can be used to replace $\bar{\kappa}$ with $\langle\kappa\rangle$ in Eq.(2.62) and extract the average curvature of the block and the electric displacement (2.66) in terms of bending moment. Then, substituting Eq.(2.59) into Eq.(2.69) we have:

$$d_{31}^{app} = -\frac{q}{3\mu}(1-\alpha^2). \tag{2.70}$$

It is clear that the best position for the charge layer, which maximizes the emergent and apparent piezoelectric coefficient, is exactly in the middle of the block. Furthermore, there is an inverse relation between material stiffness and the apparent d_{31}^{app} piezoelectric coefficient of the electret block.

Apparent flexoelectric coefficient. To alternatively interpret the electret structure in terms of flexoelectricity, we must first define an apparent flexoelectric coefficient. This requires the solution for the bending problem of a homogeneous flexoelectric beam and the relevant derivation is recorded in Appendix 2.7.4. The key result we use in this section is Eq.(2.7.140) and based on this, we may define the apparent flexoelectric coefficient f^{app} of the electret structure as

$$f^{app} = \frac{1}{(\epsilon-\epsilon_0)}\frac{\partial D^f}{\partial M}\kappa_b^{app}. \tag{2.71}$$

Substituting Eq.(2.66) into (2.71), the apparent flexoelectric coefficient is derived as

$$f^{app} = \frac{Hq}{2(\epsilon-\epsilon_0)}\left(1-\alpha^2\right). \tag{2.72}$$

The apparent emergent flexoelectric coefficient in (2.72) is directly proportional to the thickness of the block and therefore an increase of the thickness would appear to be a way to increase the flexoelectric coefficient. This notion is somewhat deceptive however. We must recognize that increasing the thickness will also require substantially larger mechanical energy to bend the structure (which scales with H^3). In addition, it should be mentioned that the reason for negligible flexoelectric effect in conventional materials at large scales is that in this effect, polarization is proportional to strain gradient and there is an inverse relation

between magnitude of strain gradient and characteristic size-scale of the problem. However, for the electret structure under consideration, the apparent flexoelectric coefficient is not a structure-independent *constant* as in the case of a non-electret material. The apparent flexoelectric coefficient of the electret structure increases with increasing size scale which compensates for the decrease of strain gradient with increasing size scale and in this sense it leads to a size-independent effect. Finally, we remark that, in the present setting of a simple homogeneous electret structure, the maximum apparent flexoelectric coefficient corresponds to the electret in which the charge layer is located exactly in the middle of the block ($\alpha = 0$).

Energy conversion ratio. In addition to flexoelectric and piezoelectric coefficients, a physically meaningful measure to study is the effectiveness of the electret material to convert applied mechanical energy into electric energy as compared with conventional piezoelectric materials. For this purpose, we compare the amount of energy required to induce an identical amount of electric charge at the electrodes. Electric charge induced at electrodes for the electret structure is $D^f - D^i$ and can be computed from Eq.(2.66). For the appropriate interpretation, this value may be equated to the induced charge on the electrode surface of the comparison piezoelectric material—which is equal to d given in Eq.(2.7.129). For this comparison, the bending moment M_{piezo} which should be applied to piezoelectric material in order to induce $d = D^f - D^i$ can be determined from (2.66) and (2.7.129):

$$M_{piezo} = \frac{q(1-\alpha^2)\kappa_b}{2Hb_{31}(\epsilon_{33}-\epsilon_0)}\bar{\kappa} + o(\bar{\kappa}), \tag{2.73}$$

where b_{31} is the piezoelectric coefficient introduced in (2.7.114) and ϵ_{33} is the dielectric coefficient in the poling direction of material. The mechanical energy required to induce this amount of charge is obtained through the work done on the system by means of the applied bending moment. The work done by the applied bending moment on piezoelectric material with unit volume is equal to $W_{piezo} = \frac{M_{piezo}^2}{2H\kappa_b}$ where κ_b is given in (2.7.127). Substituting the value of the bending moment from (2.73), W_{piezo} can be determined as

$$W_{piezo} = \frac{12q^2(1-\alpha^2)^2\kappa_b}{b_{31}^2(\epsilon_{33}-\epsilon_0)^2 I}\bar{\kappa}^2 + o(\bar{\kappa}^2). \tag{2.74}$$

Also, using Eq.(2.59), the work done by the applied mechanical loading to deform a unit-volume electret from an initially flat configuration to deformed configuration is given as

$$W_{electret} = \frac{1}{2L \times 2H}(M - 4\mu H^2 M_0)\theta\Big|_{Y=-L}^{Y=L}. \tag{2.75}$$

Substituting Eq.(2.57) and (2.36) into Eq.(2.75), and using Eq.(2.56), (2.45) and (2.48), $W_{electret}$ can be written as

$$W_{electret} = \frac{\mu\left(1 + \bar{q}_0^2 D_{14}\right)}{3\left(1 + \frac{\bar{q}_0^2}{4}(1-\alpha^2)\right)^{\frac{3}{2}}}\bar{\kappa}^2 + o(\bar{\kappa}^2). \tag{2.76}$$

With these required energetic quantities at hand for both the piezoelectric and electret materials, we define Energy Conversion Ratio (ECR) as

$$\text{ECR} = \frac{W_{piezo}}{W_{electret}}. \tag{2.77}$$

If we consider a single crystal barium titanate piezoelectric film with $\epsilon_{33} = 109\epsilon_0$, $d_{31} = -34.5$ pC/N and $c_{11} \approx 124$ GPa [106] and a symmetric polypropylene (PP) electret with $q = 10^{-3}$ C/m^2, $\mu = 0.95$ MPa and $\epsilon = 2.35\epsilon_0$ [107], we will have ECR $= 0.23$. This implies that in barium titanate, the mechanical energy required to produce a given amount of electrical energy is almost four times less than that of PP electret. However, although in this example, the ECR value for electret is smaller than 1 and energetically it is more favorable to use barium titanate film, soft electrets can tolerate much larger deformation. Furtheremore, it is evident that ECR $\propto \frac{q^2(1-\alpha^2)}{\mu}$ and that increasing the amount of embedded charges or using softer materials can be used to increase ECR.

2.4.4 The effect of embedded dipoles on the apparent flexoelectric and d_{31} piezoelectric behavior

In addition to embedded charges, embedded dipoles are also used in electrets. The widely used soft cellular polymer foams may be considered to consist of embedded dipoles in voids of a soft matrix. As shown in Fig. 2.10, these polymer foams are soft porous

materials with huge number of entrapped air voids such that volume fraction of voids are often more than 50 percent. Trapped charges on the surfaces of voids create large dipoles inside the foam (Fig. 2.10(a)). In some sense, this is analogous to large dipoles created by the charge layer in the composite of the preceding section and the top and bottom electrodes. In this section, we use a layered structure to model voided film where there is a layer of air between two layers of polymer (Fig. 2.10(b)). Embedded charges with surface charge densities q and $-q$ exist at the interface of the air layer and polymer layer to mimic dipoles. Two parameters α_1 and α_2 have been introduced to identify position of charge layers. The solution to the bending problem of an electret made of two layers of different materials is given in Appendix 2.7.5. This can be extended for a soft dielectric block made of three different layers. We avoid giving details of the derivation for this case since the process is identical to what was presented before. Ignoring higher order terms and following the same notation introduced in Eq.(2.66), electric displacement for this structure is given as

$$D_f = D_i + \frac{q\epsilon_r(\alpha_2^2 - \alpha_1^2)}{(2 + \frac{H_a}{H}(\epsilon_r - 1))^2}\bar{\kappa} + o(\bar{\kappa}), \tag{2.78}$$

where $\epsilon_r = \epsilon/\epsilon_0$ and H_a is the thickness of air layer. Note that $D_f - D_i$ for all three layers is the same. In charged polymers, dipoles are almost uniformly distributed inside the material. It is clear that for a symmetric distribution of embedded dipoles ($\alpha_2 = -\alpha_1$), change in the electric displacement will be zero and bending will not induce any change in the charges induced at the electrodes. This explains the reason for the observation of small d_{31} in charged polymer foams. However, there is a simple way to obtain desirable values for α_1 and α_2 and a non-symmetric distribution of dipoles. The basic ideas are illustrated in Fig. 2.11(a). Essentially, electret structures can be combined with non-electret material (i.e. ordinary dielectric) to facilely create the asymmetry needed to obtain a non-trivial d_{31}. Although we do not present further details, a slight modification to the current models (developed so far) may be easily used to find the apparent properties of a film composed asymmetric electret structures shown in Fig. 2.11(b).

Upon substituting Eq.(2.78) into Eq.(2.71) and (2.69) the apparent flexoelectric coeffi-

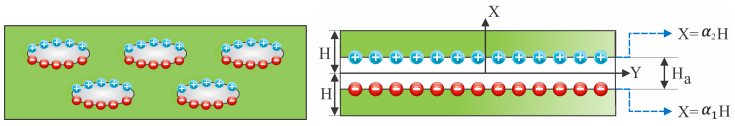

(a) (b)

Figure 2.10: (a) Existence of external dipoles in polymer foams. (b) A layered structure is used to model charged porous polymer. Constants α_1 and α_2 show the positions of charge layers.

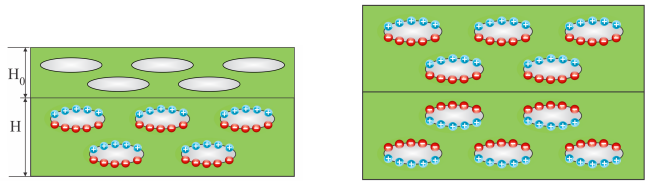

(a) (b)

Figure 2.11: Methods to break symmetry in distribution of dipoles. (a) Attachment of a non-electret material to an electret material. (b) Attachment of two asymmetric electrets.

cient and apparent piezoelectric coefficient can be derived:

$$f^{app} = \frac{2Hq\epsilon_r}{(\epsilon' - \epsilon_0)} \frac{\alpha_2^2 - \alpha_1^2}{(2 + \frac{H_a}{H}(\epsilon_r - 1))^2} \tag{2.79}$$

$$\text{and} \qquad d_{31}^{app} = -\frac{4q\epsilon_r(\alpha_2^2 - \alpha_1^2)}{3\mu(2 + \frac{H_a}{H}(\epsilon_r - 1))^2}, \tag{2.80}$$

where μ in (2.80) is an effective shear modulus which accounts for both polymer section and air voids. Qualitatively, the results do not differ in any significant manner from the previous section.

2.5 Results and discussion

The nonlinear models presented in the preceding sections can be used to obtain several interesting insights into the design of flexoelectricity and d_{31} piezoelectricity in soft electrets. However, first, in order to highlight the similarities and differences between conventional dielectrics and electret materials, we present the bending deformation behavior of an ordinary soft dielectric in Fig. 2.12. Relations (2.49) and (2.50) have been used to draw this

figure. In Fig.2.12(a) we illustrate the change in thickness of a soft dielectric block under the action of a combined bending moment and electric field. As expected, Fig. 2.12(a) shows that applying a constant external electric field leads to the thinning of the block. As it was discussed earlier in preceding sections, this change of thickness leads to emergence of a coupling between electric field and curvature of the block. Change of curvature in response to applied electric field is shown in Fig. 2.12(b) to investigate possibility of using ordinary dielectrics as bending actuator. We introduce the following dimensionless measure of the curvature $\bar{\kappa}_0 = \frac{\bar{\kappa}}{\lambda}$ and use this quantity throughout the section. Figure 2.12(b) shows that for fixed non-zero values of bending moment, increasing external field results in the increase of the curvature observed in the block. However it is evident, from this figure, that if the applied bending moment is zero, electric field alone will not induce a change in curvature. In the other words, some pre-existing curvature should be present to observe a coupling between the curvature and electric field for ordinary dielectrics. This is one of limitations of dielectric actuators. Another one is that the electromechanical coupling in the non-electret soft dielectric block is generated from Maxwell stress effect which, by nature, is quadratic with respect to electric field. Accordingly, a change in the direction of the applied electric field will not alter the direction of the induced curvature.

Flexure behavior of electret with a single layer of embedded charge. The formulation presented in section 2.4.2 is used to analyze the flexure behavior of the electrets with embedded charges. Equations (2.56) and (2.57) are used to plot the variation of the dimensionless bending moment with dimensionless curvature in Fig. 2.13 for a short circuited electret with asymmetric distribution of charges ($\alpha = 0.5$). As evident, the presence of the charge has a profound effect on the bending moment-curvature relation. In particular, the curvature does not vanish even when the applied bending moment is zero. This is due to the asymmetric distribution of charges and consequently a non-uniform state of Maxwell stress inside the material.

As discussed earlier, when two layers of piezoelectric materials with opposite poling directions are exposed to an external electric filed in the thickness direction; the d_{31} converse piezoelectric effect leads to bending. The same behavior is seen in electrets. Using (2.7.113),

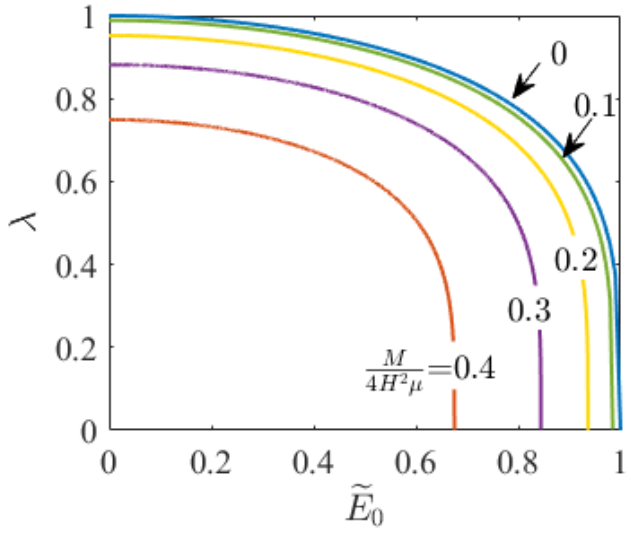

(a)

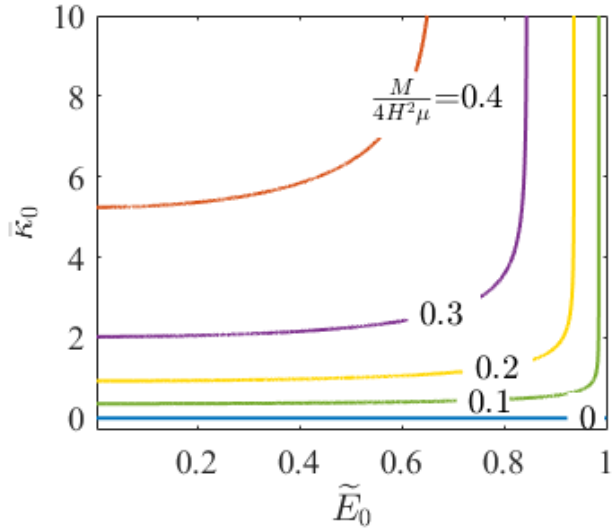

(b)

Figure 2.12: Behavior of soft dielectric block under the action of a combined bending moment and electric field. (a) Change of thickness in response to applied electric field and bending moment. (b) Coupling between electric field and curvature.

fig. 2.14 shows that an electret made of a dielectric with a layer of charge with $\bar{q}_0 = 0.225$ bends in response to external electric field and in *absence* of any external mechanical load. This value of electric charge will be attainable upon insertion of a layer of electric charge with $q = 10^{-3}$ C/m^2 into a PP film with $\mu = 0.95$ MPa and $\epsilon = 2.35\epsilon_0$ [107]. Furthermore, Fig. 2.14 shows that the direction of curvature depends on the direction of applied field.

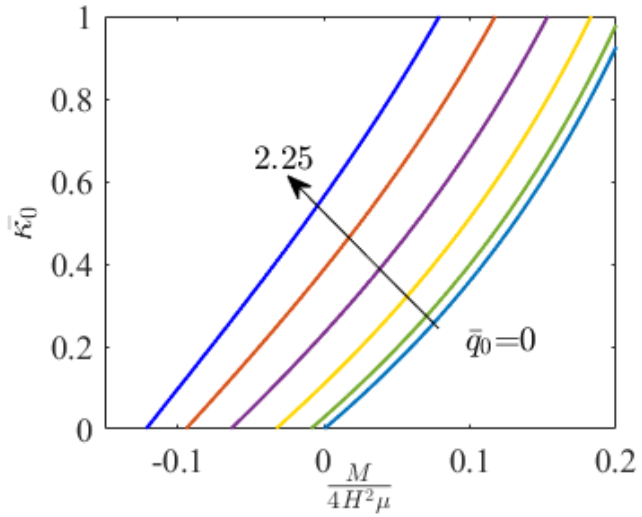

Figure 2.13: Effects of external charges on the curvature of the block for $\alpha = 0.5$.

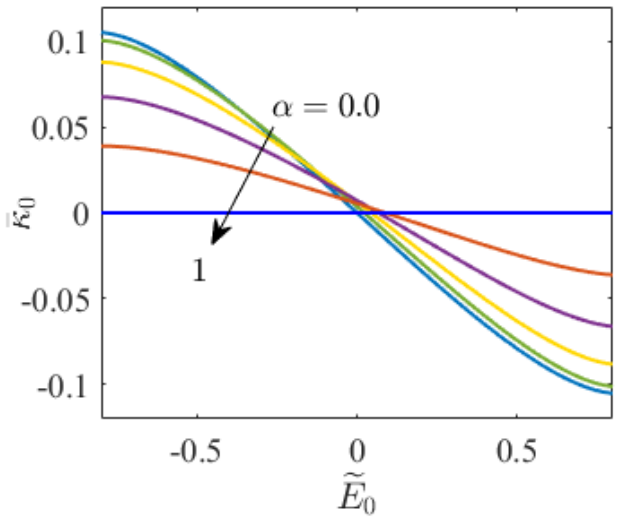

Figure 2.14: Converse piezoelectric behavior of electret with $\bar{q}_0 = 0.225$.

This linear relation is in contrast with the quadratic behavior of an ordinary dielectric under external voltage in the absence of external charges and proves the capability of soft electrets to be used as a bending actuator. The emergent d_{31} effect is stronger when the charge layer is in the middle of the block ($\alpha = 0$).

Energy harvesting application and emergent properties of electrets. The possibility of using electrets as sensors and their apparent and emergent piezoelectric/flex-

oelectric coefficients are studied in Figs. 2.15 to 2.18. Bending of a short circuited electret changes the electric field and electric polarization inside the material. In order to show this electro-mechanical coupling, we use Eq.(2.65) to plot the change of electric displacement versus the dimensionless curvature in Fig. 2.15 for a homogeneous dielectric with an embedded layer of electric charge.The change of the electric displacement, and hence the capability to generate current, in response to changes in curvature illustrates the potential application of the electret structure as an energy harvester and sensor. Also, for small curvatures a linear change is observed in the electric displacement. Since the flexoelectric behavior is the linear development of polarization in response to imposed curvature in vicinity of zero curvature (small deformation), this change of the electric displacement and consequently electric polarization seen in electret can be interpreted as an emergent flexoelectric-like behavior and this effect is stronger when charge layer is closer to the middle surface of the block. Plotting the apparent flexoelectric coefficient using the definition in (Eq.(2.72)) in Fig. 2.15(b), we see that a flexoelectric coefficient of the order of $f^{app}(\epsilon - \epsilon_0) \approx 10^{-8} C/m$ is possible for an electret with micro scale thickness and with a realistic surface charge density $q = 10^{-3}$ C/m^2.

Fig. 2.16 shows the apparent d_{31} piezoelectric coefficient for a PP film with $\mu = 0.95MPa$ with one layer of external charges using Eq.(2.70). The apparent piezoelectric coefficient is found to be roughly ten times more than the corresponding value of barium titanate where $d_{31}^{BaTiO_3} = -34.5\ pC/N$ [106] and $q = 1$ mC/m^2. While a high longitudinal piezoelectric coefficient for electrets has been already reported, this is the first prediction for such a large d_{31} value.

In order to present the piezoelectric coefficient for a polymer with embedded dipoles, we consider a polymer foam with $H = 30\mu m$ and assume an air volume fraction of 50% or $H_a = H$ (see Fig. 2.10). Initially dipoles have a symmetric distribution and the apparent piezoelectric coefficient is zero. Another piece of the identical polymer film of thickness H_0, free of dipoles, is attached to the electret material (Fig .2.11(a)). A shear modulus of $\mu = 1MPa$ is assumed. The apparent piezoelectric coefficient for this structure versus thickness of the attached film is shown in Fig.2.17 using Eq.(2.80). The apparent piezoelectric

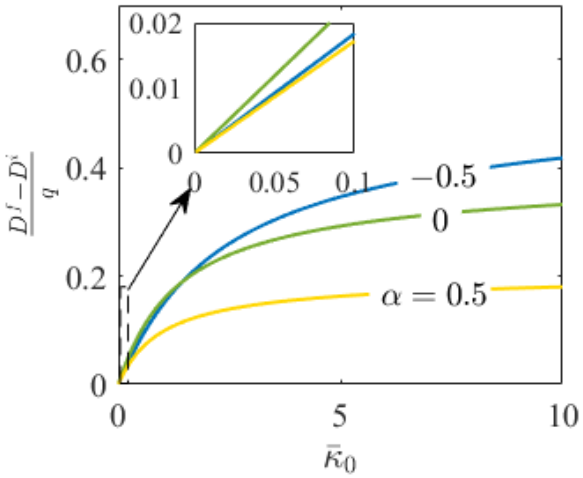

(a)

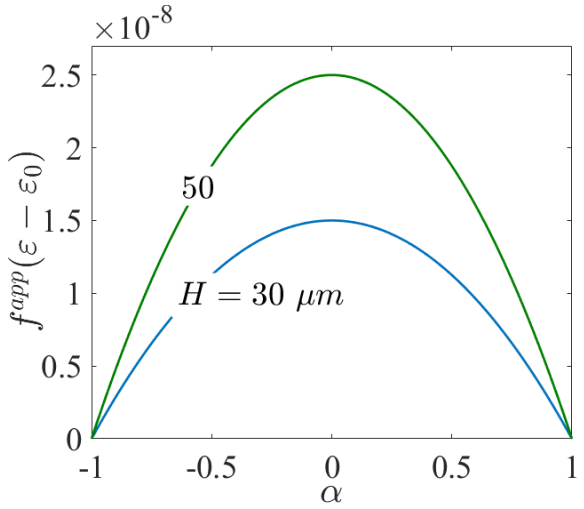

(b)

Figure 2.15: Flexoelectric behavior of the electret. (a) Charge harvested in the bending deformation of a short circuited electret. (b) Apparent flexoelectric coefficient of a homogeneous film with $\bar{q}_0 = 0.225$.

coefficient increases with H_0 until it obtains an optimum. The thickness which maximizes the apparent piezoelectric coefficient of the structure depends on the electric permittivity of the material and can be determined mathematically from: $H_0 = 2H + H_a(\epsilon_r - 1)$.

In what follows, we use Equations (2.74), (2.76) and (2.77) to plot the ECR coefficient to compare energy conversion efficiency of an electret with a single layer of embedded charge to a homogeneous barium titanate piezoelectric. Barium titanate properties are considered

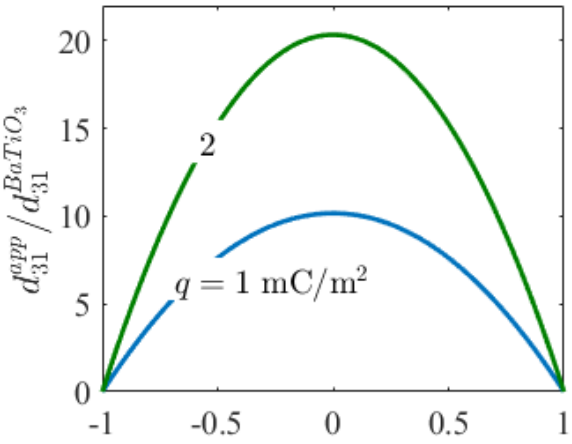

Figure 2.16: Apparent piezoelectric coefficient for a PP film with a layer of external charge inserted versus position of charge layer

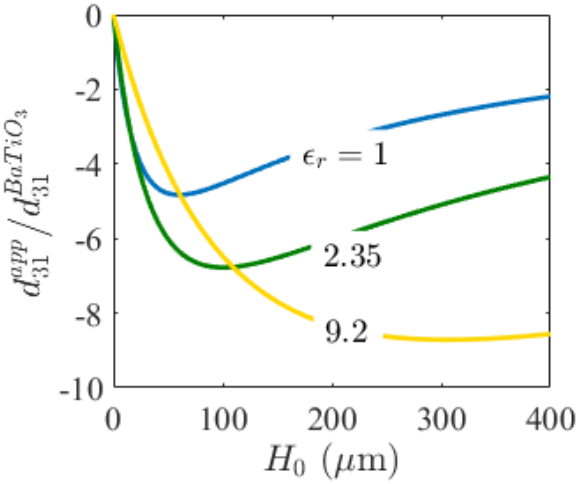

Figure 2.17: Apparent piezoelectric coefficient of a polymer film with embedded dipoles attached to another material free of dipoles with thickness H_0.

as $\epsilon_{33} = 109\epsilon_0$, $d_{31} = -34.5$ pC/N and $c_{11} \approx 124$ GPa [106]. As expected from prior results, Fig. 2.18(a) shows that ECR is maximized when the charge layer is located in the middle of the block. Furthermore, increasing the amount of surface charge density to 2 mC/m^2 in an electret with a shear modulus 0.95 MPa will perform almost as well as barium titanate. Given that the electret is capable of orders of magnitude larger deformation, this comparision is quite astounding. Another avenue to obtain an higher ECR is suggested in Fig. 2.18(b). The figure shows that softer electrets have higher ECR and an order of

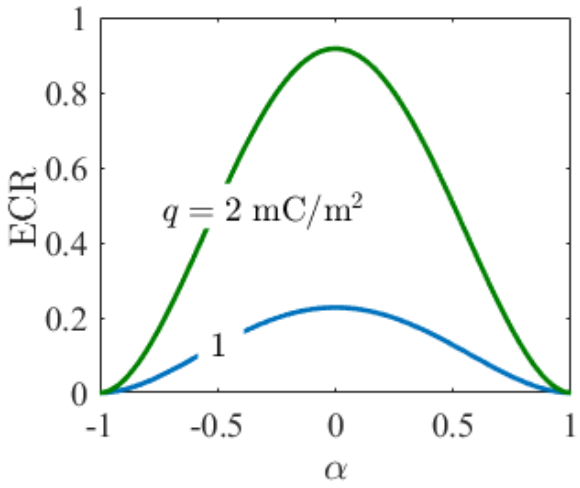

(a)

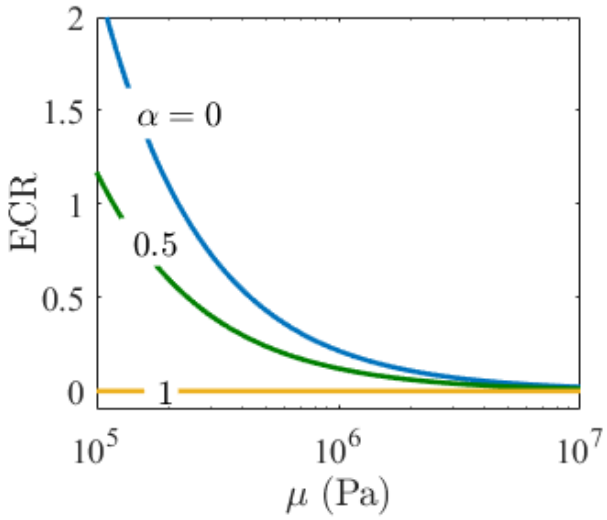

(b)

Figure 2.18: ECR coefficient to compare energy efficiency of electret with a barium titanate piezoelectric material. (a) ECR versus α for an electret with $\mu = 1$ MPa and $\epsilon = 2.35\epsilon_0$. (b) ECR versus shear modulus of electret for an electret $q = 10^{-3}$ C/m^2.

magnitude reduction in the shear modulus can dramatically increase the ECR.

2.6 Concluding remarks

Soft electret materials have been proposed as candidates for applications that require a strong electro-mechanical coupling as well as a capability for large deformation. Although

a large apparent d_{33} piezoelectric coefficient has been reported for some soft polymer foam electrets, their d_{31} piezoelectric coefficient is rather small and the electro-mechanical coupling in flexure motion is quite weak. In this work we provide a physical rationale for observed low value of d_{31} in typical electrets. We analyze the behavior of electrets under bending deformation and pathways to obtain substantive d_{31} piezoelectricity or alternatively a flexoelectric like behavior, are suggested. Our central formulation is quite general and may be used, beyond the simple examples studied in the present work, for future numerical design and optimization of flexoelectric and bending piezoelectric electrets. We obtain the following insights:

1. The microstructure of electrets must lead to non-trivial inhomogeneous deformation for the emergence of d_{31} piezoelectric effect.

2. Ordinary dielectrics may not fit applications that require a linear electro-mechanical coupling in bending deformation. The reason is that some pre-existing curvature is required to observe coupling between externally applied electric field and curvature in dielectrics. Also, even when pre-existing curvature is present, this coupling only depends on the magnitude of electric field and it is independent of the direction of the field.

3. A converse d_{31} piezoelectric behavior is obtained for an electret with one layer of embedded charges, implying that an externally applied electric field can bend this electret and a change in the direction of electric field will also alter the direction of the deformation. In addition, bending of such an electret will also alter the electric field and polarization inside the material and this change of polarization can be interpreted as either a d_{31} piezoelectric effect or alternatively, flexoelectricity.

4. We estimate the apparent flexoelectric and d_{31} piezoelectric coefficient for electrets and suggest approaches to improve the overall energy conversion ability of the material.

2.7 Appendices

2.7.1 Coefficients C_{ij}, D_{ij} and E_{ij} introduced in section 2.4

The coefficients C_{ij} are defined as:

$$C_{11} = (\frac{\log(C_{22})}{\log(\Lambda)})^2 - \frac{(1-\alpha)\log(C_{22}^2)}{C_{21}\log(\Lambda)}, \tag{2.7.81}$$

$$\begin{aligned} C_{12} = & \frac{(\Lambda^4-1)\log^2(C_{22})}{\log^2(\Lambda)} \\ & + \frac{\log(C_{22}^2)\left(C_{21}\Lambda^2\log\left(\frac{2}{C_{21}}\right)+C_{23}\right)}{C_{21}\log(\Lambda)} - \frac{C_{23}}{C_{21}}, \end{aligned} \tag{2.7.82}$$

$$C_{13} = \frac{(\Lambda^2-1)^2\left((\alpha-1)\log(\Lambda)\log\left(\frac{C_{22}^2}{\Lambda}\right)+C_{21}\log^2(C_{22})\right)}{C_{21}\log^2(\Lambda)}, \tag{2.7.83}$$

$$C_{21} = 1+\Lambda^2+\alpha(\Lambda^2-1), \tag{2.7.84}$$

$$C_{22} = \frac{\sqrt{2}\Lambda}{\sqrt{C_{21}}}, \tag{2.7.85}$$

$$C_{23} = (1-\alpha)\left(1-\Lambda^4\right), \tag{2.7.86}$$

$$\text{and} \qquad C_{24} = \frac{(\Lambda_b-1)}{\Lambda_b}\sqrt{\frac{\alpha+2\Lambda_b^2-1}{\alpha+1}}. \tag{2.7.87}$$

Coefficients D_{ij} are given as

$$D_{11} = \frac{8\bar{q}_0^2\alpha(1-\alpha^2)}{(4+\bar{q}_0^2(1-\alpha^2))^2}, \tag{2.7.88}$$

$$D_{12} = D_{13} + \frac{\alpha\left(1-\alpha^2\right)\widetilde{E}_0\bar{q}_0\left(\left(1-\alpha^2\right)\bar{q}_0^2-8\right)}{3\left(\left(1-\alpha^2\right)\bar{q}_0^2+4\right)^2}\times$$
$$(\sqrt{\left(1-\widetilde{E}_0^2\right)\left(\left(1-\alpha^2\right)\bar{q}_0^2+4\right)}+\alpha\widetilde{E}_0\bar{q}_0), \tag{2.7.89}$$

$$D_{13} = \frac{\bar{q}_0^4(1-\alpha^2)^3+\bar{q}_0^2(-44\alpha^4+24\alpha^2+20)+64}{12(\bar{q}_0^2(1-\alpha^2)+4)^2}, \tag{2.7.90}$$

$$\text{and} \qquad D_{14} = \frac{1}{16}\left(-11\alpha^4+6\alpha^2+5+\bar{q}_0^2\frac{(1-\alpha^2)^3}{4}\right). \tag{2.7.91}$$

In Eq.(2.7.89) for coefficient D_{12}, the contributions of both electric field and electric charges have been considered. So, the electric field $\widetilde{E}_0$ should be set to zero in the relation (2.7.89) to obtain coefficient D_{12} used in Eq.(2.59).

Coefficients E_{ij} are given as

$$E_{11} = \frac{(\alpha+1)\left(\Lambda_b+1\right)^4}{4\left(\epsilon_t\log\left(\Lambda_b\right)+\epsilon_b\log(C_{24})\right)^2}\times$$
$$\left((\alpha-1)\epsilon_t\log^2\left(\Lambda_b\right)-\epsilon_b\log^2(C_{24})\left(\alpha+2\Lambda_b^2-1\right)\right), \tag{2.7.92}$$

$$E_{12} = (\Lambda^2-1)^2, \tag{2.7.93}$$

$$E_{13} = (C_{21}-2)(3C_{21}+2), \tag{2.7.94}$$

$$E_{14} = (1-\alpha)(\Lambda^2-1)(3+5\Lambda^2+3\alpha(\Lambda^2-1)), \tag{2.7.95}$$

$$E_{15} = \frac{(2-\sqrt{2C_{21}})}{4}\times(2+\sqrt{2C_{21}})^5, \tag{2.7.96}$$

$$E_{16} = -\frac{2E_{21}(1-\alpha)(\Lambda^2-1)}{\Lambda^2}, \tag{2.7.97}$$

$$E_{17} = -(2+\sqrt{2C_{21}})^4, \tag{2.7.98}$$

$$\text{and} \qquad E_{18} = \frac{E_{22}(1+\sqrt{\frac{C_{21}}{2}})^4}{8\Lambda^2(\Lambda^2-1)^2\left(\epsilon_b \log(C_{22}) + \epsilon_t \log(\sqrt{\frac{C_{21}}{2}})\right)^2}, \tag{2.7.99}$$

where

$$\begin{aligned} E_{21} &= \alpha^2 + (\alpha+1)^2\Lambda^4 - 2(\alpha-7)(\alpha+1)\Lambda^2 - 14\alpha \\ &+ 4\sqrt{2}\sqrt{C_{21}}\left(\alpha\left(\Lambda^2-1\right) + \Lambda^2 + 3\right) + 17, \end{aligned} \tag{2.7.100}$$

$$\begin{aligned} \text{and} \qquad E_{22} &= (\alpha-1)\left(\Lambda^2-1\right)\epsilon_a \log^2\left(\frac{\sqrt{C_{21}}}{\sqrt{2}}\right) - 4\Lambda^2\epsilon_a \log\left(C_{22}\right)\log^2\left(\frac{\sqrt{C_{21}}}{\sqrt{2}}\right) \\ &+ \Lambda^2\epsilon_b \log^2\left(C_{22}\right)\left(-\alpha\Lambda^2 + \alpha - 2\log\left(C_{21}\right) - \Lambda^2 + 1 + \log(4)\right). \end{aligned} \tag{2.7.101}$$

2.7.2 Derivation of relation between bending moment and curvature for electret under external voltage introduced in section 4.2

In order to determine the relations for stretch and bending moment in terms of curvature for the electret shown in Fig. 2.8 which is also under an external electric voltage, Eq.(2.63) is substituted into Eq.(2.43) to determine the stresses. The boundary condition given in second equation of (2.46a) can be written as:

$$F_{11} + F_{12}\lambda^2 + F_{13}\lambda^4 = 0, \tag{2.7.102}$$

where

$$F_{11} = 4(\Lambda-1)\left(\frac{\widetilde{E}_0^2(1-\Lambda)^2(1+\Lambda)}{\Lambda^2(\log\Lambda)^2} - \frac{4}{1+\Lambda}\right), \tag{2.7.103}$$

$$F_{12} = \frac{4\widetilde{E}_0\bar{q}_0(-1+\Lambda^2)^2}{C_{21}\Lambda^2(\log\Lambda)^2} \times \left(C_{21}\log(C_{22}) + (-1+\alpha)\log(\Lambda)\right), \tag{2.7.104}$$

$$F_{13} = \frac{(-1+\Lambda)(1+\Lambda)^3}{C_{21}\Lambda^2(\log(\Lambda))^2} \times F_{21}, \tag{2.7.105}$$

$$\begin{aligned} \text{and} \qquad F_{21} = {} & C_{21}\bar{q}_0^2(\log(C_{22}))^2 + 2\bar{q}_0(-1+\alpha)\log(C_{22})\log(\Lambda) \\ & + (\log(\Lambda))^2\left(1+\bar{q}_0^2(1-\alpha)+\Lambda^2-\alpha(1-\Lambda^2)\right). \end{aligned} \tag{2.7.106}$$

Also, Eq.(2.63) is used to write the boundary condition (2.46b) as

$$\frac{8M}{H^2\mu} = F_{14} + F_{15}\lambda^2 + F_{16}\lambda^4, \tag{2.7.107}$$

where

$$F_{14} = -\frac{4\widetilde{E}_0^2\left(\Lambda^2-1\right)}{\log^2(\Lambda)} - \frac{8\widetilde{E}_0^2}{\log(\Lambda)} + \frac{8\left(3\Lambda^2+1\right)}{\Lambda^2-1}, \tag{2.7.108}$$

$$F_{15} = -\frac{4\widetilde{E}_0(\Lambda+1)\bar{q}_0\left(C_{21}\left(\Lambda^2-1\right)\log(C_{22}) + \left(C_{21}-2\Lambda^2\right)\log(\Lambda)\right)}{C_{21}(\Lambda-1)\log^2(\Lambda)}, \tag{2.7.109}$$

$$F_{16} = \frac{\lambda^4(\Lambda+1)^2}{C_{21}(\Lambda-1)^2\log^2(\Lambda)} \times F_{22}, \tag{2.7.110}$$

$$\begin{aligned} \text{and} \qquad F_{22} = {} & 2\bar{q}_0^2\log(C_{22})\log(\Lambda)\left((\alpha-1)\left(\Lambda^2-1\right)+C_{21}\log(\Lambda)\right) \\ & + C_{21}\bar{q}_0^2\log^2(C_{22})\left(\Lambda^2-2\log(\Lambda)-1\right) \\ & + \log^2(\Lambda)\left(2C_{21}\log(\Lambda) + C_{21}\left(\Lambda^2-\bar{q}_0^2-1\right)+2\Lambda^2\bar{q}_0^2\right). \end{aligned} \tag{2.7.111}$$

We now simply solve Eq.(2.7.102) for stretch λ and substitute the solution into (2.7.107). This will yield the relation between bending moment and curvature. Since the algebra is simple and the non-linear bending moment curvature relation is extremely tedious, we only present its Taylor series expansion for small $\bar{\kappa}$:

$$\frac{M}{4\mu H^2} = M_0 + D_{12}\bar{\kappa} + o(\bar{\kappa}), \tag{2.7.112}$$

where M_0 and D_{12} is given by (2.64) and (2.7.89), respectively. As a result, curvature induced in the block because of electrical loading and in absence of bending moment is

determined as

$$\bar{\kappa}_0 = \frac{\bar{\kappa}}{\lambda} = -\frac{M_0}{D_{12}\lambda}. \tag{2.7.113}$$

2.7.3 Solution for bending problem of piezoelectric bimorph beam introduced in section 4.3

In this section, we present the solution to the bending problem of a piezoelectric bimorph. The final result is necessary to define the apparent piezoelectric coefficient for the electret problem considered in Section 4.3. Using Euler beam kinematics, we find a relation for piezoelectric coefficient in terms of applied bending moment. Consider Fig. 2.9 which shows a material composed of two layers of the same piezoelectric material with opposite poling directions. Let x and z be, respectively, axial and thickness directions of the beam. Axial elastic modulus of the material is denoted by c_{11} and both layers have the same thickness H . We assume a unit width for the beam and the length of the beam is $2L$. This beam is deformed in response to bending moment M applied at the two ends. Short circuit boundary condition is imposed using two mechanically compliant electrodes which are attached to the surfaces $z = \pm H$. The energy density function can be expressed as [97]

$$\psi[\mathbf{x}; \mathbf{u}, \mathbf{p}] = \frac{1}{2}\mathbf{S}\cdot\mathbf{c}\mathbf{S} + \frac{1}{2}\mathbf{p}\cdot\mathbb{D}^{-1}\mathbf{p} + \mathbf{p}\cdot\mathbf{B}\mathbf{S}, \tag{2.7.114}$$

where $\mathbf{u}$ and $\mathbf{c}$, $\mathbf{S}$ are displacement, fourth order elasticity tensor and linear strain tensor, respectively. Also, $\mathbb{D} = \boldsymbol{\epsilon} - \epsilon_0\mathbf{I}$ where $\boldsymbol{\epsilon}$ is the dielectric tensor and $\mathbf{B}$ is third order piezoelectric tensor. In a one-dimensional setting, $\boldsymbol{\epsilon}$ and $\mathbf{B}$ can be replaced by ϵ_{33} and B_{31}, respectively. Since the beam is composed of two layers of the same piezoelectric materials with opposite poling directions, we introduce piezoelectric coefficient b_{31} such that for $B_{31} = b_{31}$ for $z > 0$ and $B_{31} = -b_{31}$ for $z \leq 0$. Also, We can relate B_{31} piezoelectric

coefficient to commonly used d_{31} coefficient as [13]

$$d_{31} = -\frac{B_{31}(\epsilon_{33} - \epsilon_0)}{c_{11}}. \tag{2.7.115}$$

Based on Euler beam kinematics, the deformation $\mathbf{u}$ for the beam is given as

$$\mathbf{u} = -z\frac{\partial u_z(x)}{\partial x}\mathbf{e}_x + u_z(x)\mathbf{e}_z. \tag{2.7.116}$$

Consequently, linear strain tensor is simply derived as $\mathbf{S} = -z\frac{\partial^2 u_z(x)}{\partial x^2}\mathbf{e}_x \otimes \mathbf{e}_x$. Due to the piezoelectric effect and in response to deformation, polarization is developed inside the bimorph. We assume that the polarization and electric field are only developed in the thickness direction ($\mathbf{p} = p\mathbf{e}_z$ and $\mathbf{e} = -\frac{d\xi}{dz}\mathbf{e}_z$). Accordingly the Maxwell equation (2.4) reduces to:

$$-\epsilon_0\frac{d^2\xi}{dz^2} + \frac{dp}{dz} = 0. \tag{2.7.117}$$

Also, free energy of the system can be written as

$$\begin{aligned}\mathcal{F}[u_z, p] = \int_\Omega \Big[\frac{1}{2}c_{11}z^2\left(\frac{\partial^2 u_z(x)}{\partial x^2}\right)^2 + \frac{|p|^2}{2(\epsilon_{33} - \epsilon_0)} - pB_{31}z\frac{\partial^2 u_z(x)}{\partial x^2} \\ + \frac{\epsilon_0}{2}\left(-\frac{d\xi}{dz}\right)^2\Big] - M\frac{\partial u_z(x)}{\partial x}\Big|_{x=-L}^{x=L},\end{aligned} \tag{2.7.118}$$

where all quantities are expressed in a one-dimensional setting. The equilibrium state of

[13] There are multiple ways to present constitutive equations for piezoelectricity. From (2.7.114), we can relate stress components σ_{ij} to electric field components E_k and strain component S_{kl} through the following relations

$$\sigma_{ij} = \left(c_{ijkl} - B_{mij}(\mathcal{D}^{-1})_{mn}B_{nkl}\right)S_{kl} + \mathcal{D}_{km}B_{mij}E_k,$$

where $\mathcal{D}_{km}$ are the components of tensor $\mathbb{D}$. Another alternative for the constitutive relation for piezoelectric materials may be expressed as

$$S_{ij} = s^E_{ijkl}\sigma_{kl} + d_{kij}E_k,$$

where s_{ijkl} and d_{kij} are, respectively, components of compliance tensor and piezoelectric tensor and superscript E indicates that the quantity has been measured in constant or zero electric field. Introducing ${s^E_{mnij}}^{-1}$ such that ${s^E_{mnij}}^{-1}s^E_{ijkl} = \delta_{mk}\delta_{nl}$ this constitutive relation can be rearranged as

$$\sigma_{ij} = {s^E_{ijkl}}^{-1}S_{kl} - {s^E_{ijkl}}^{-1}d_{mkl}E_m,$$

Comparing this constitutive relation with the stress-strain relation presented based on the energy formulation and assuming $c_{ijkl} - B_{mij}(\mathcal{D}^{-1})_{mn}B_{nkl} \approx c_{ijkl}$, we arrive at the relation in (2.7.115) for a one-dimensional model.

the system is obtained by minimizing the free energy of the system subjected to Maxwell's equations:

$$\min\{\mathcal{F}[u_z, p] : (u_z, p) \in \mathcal{S} \quad \text{and} \quad (u_z, p) \quad \text{satisfies (2.7.117)}\}, \tag{2.7.119}$$

where $\mathcal{S}$ is the admissible set of functions

$$\mathcal{S} = \{(u_z, p)| \quad u_z \in C^4([-H, H]; \mathbb{R}), \quad \int_\Omega |p|^2 < +\infty\}. \tag{2.7.120}$$

Using standard calculus of variation, equilibrium equations and boundary conditions for a beam with unit width are derived as

$$c_{11} I \frac{\partial^4 u_z}{\partial x^4} - \frac{\partial^2}{\partial x^2}\left(\int_{-H}^{H} B_{31} p z dz\right) = 0, \tag{2.7.121}$$

$$\frac{d\xi}{dz} + \frac{p}{\epsilon_{33} - \epsilon_0} - B_{31} z \frac{\partial^2 u_z}{\partial x^2} = 0, \tag{2.7.122}$$

$$\left[c_{11} I \frac{\partial^3 u_z}{\partial x^3} - \frac{\partial}{\partial x}\left(\int_{-H}^{H} B_{31} p z dz\right)\right]\Big|_{x=-L}^{x=L} = 0, \tag{2.7.123}$$

$$\text{and} \qquad \left[c_{11} I \frac{\partial^2 u_z}{\partial x^2} - \int_{-H}^{H} B_{31} p z dz - M\right]\Big|_{x=-L}^{x=L} = 0, \tag{2.7.124}$$

where $I = \int_{-H}^{H} z^2 dz$. Polarization can be determined in terms of displacement by substituting Eq.(2.7.122) into Eq.(2.7.117):

$$p = \frac{\epsilon_0(\epsilon_{33} - \epsilon_0)}{\epsilon_{33}} B_{31} \frac{\partial^2 u_z}{\partial x^2} z + \frac{(\epsilon_{33} - \epsilon_0)^2}{\epsilon_{33}} \frac{H}{2} b_{31} \frac{\partial^2 u_z}{\partial x^2}. \tag{2.7.125}$$

Substituting Eq.(2.7.125) into Eq.(2.7.121), we have

$$\kappa_b \frac{\partial^4 u_z}{\partial x^4} = 0, \tag{2.7.126}$$

where κ_b is an apparent bending stiffness:

$$\kappa_b = c_{11} I - \frac{(\epsilon_{33} - \epsilon_0)(3\epsilon_{33} + \epsilon_0)}{4\epsilon_{33}} b_{31}^2 I. \tag{2.7.127}$$

Solving Eq.(2.7.126) using boundary conditions Eq.(2.7.123) and (2.7.124), we find that the relation between bending moment and deformation is

$$\frac{M}{\kappa_b} = \frac{\partial^2 u_z}{\partial x^2}. \tag{2.7.128}$$

Equation (2.7.128) can be used to describe all quantities in terms of applied bending moment M. Electric displacement $\mathbf{d} = d\mathbf{e}_z$ can be determined using Eq.(2.7.128), (2.7.125), (2.7.122) and (2.1), namely

$$d = \frac{Mb_{31}(\epsilon_{33} - \epsilon_0)H}{2\kappa_b}. \tag{2.7.129}$$

Physically, $\frac{M}{\kappa_b}$ and d represent the curvature of the Euler beam and induced charge at the electrodes, respectively. The piezoelectric coefficient of this bimorph can be obtained by measuring the electric displacement due to bending and by using relation (2.7.129). From Eq.(2.7.129) and (2.7.115) we have

$$d_{31} = -\frac{2\kappa_b}{c_{11}H}\frac{\partial d}{\partial M}. \tag{2.7.130}$$

2.7.4 Solution for bending problem of flexoelectric beam introduced in section 4.3

The solution of bending of an Euler beam accounting for flexoelectricity is presented here and is needed to define the apparent flexoelectric coefficient for the electret considered in Section 4.3. The procedure is similar to what was documented in Appendix 2.7.3 for a piezoelectric bimorph. We assume that the beam has dimensions $2H \times 2L$ and with unit width. Coordinates are considered to be similar to Fig. 2.9 and following Euler beam kinematics, deformation is considered to be same as Eq.(2.7.116). We assume polarization only exists in thickness direction and introduce $p^S(x) = \int_{-H}^{H} p(x)dz$ where $\mathbf{p} = p(x)\mathbf{e}_z$. The energy density function is given as [108, 105]:

$$\psi[x; u_z, p^S] = \frac{1}{2}c_{11}I(\Delta u_z)^2 - fp^S\Delta u_z + \frac{1}{2}a|p^S|^2, \tag{2.7.131}$$

where f is flexoelectric coefficient[14]. Also, $\Delta(\cdot)$ is Laplace operator and $a = \frac{1}{2H(\epsilon-\epsilon_0)}$ where ϵ is electric permittivity for this homogeneous flexoelectric material. From Eq.(2.7.131), the free energy of the system can be written as

$$\begin{aligned}&\mathcal{F}[u_z, p] = \\ &\int_{-L}^{L}\left[\frac{1}{2}c_{11}I\left(\frac{\partial^2 u_z(x)}{\partial x^2}\right)^2 - fp^S\frac{\partial^2 u_z(x)}{\partial x^2} + \frac{1}{2}a|p^S|^2\right]dx - M\frac{\partial u_z(x)}{\partial x}\Big|_{x=-L}^{x=L}.\end{aligned} \tag{2.7.132}$$

Again, using standard calculus of variation, the equilibrium equations and boundary conditions are derived as

$$\frac{\partial^2}{\partial x^2}\left(c_{11}I\frac{\partial^2 u_z}{\partial x^2} - fp^S\right) = 0, \tag{2.7.133}$$

$$ap^S - f\frac{\partial^2 u_z}{\partial x^2} = 0, \tag{2.7.134}$$

$$\left[\frac{\partial}{\partial x}\left(c_{11}I\frac{\partial^2 u_z}{\partial x^2} - fp^S\right)\right]\Big|_{x=-L}^{x=L} = 0, \tag{2.7.135}$$

$$\text{and} \qquad \left[c_{11}I\frac{\partial^2 u_z}{\partial x^2} - fp^S - M\right]\Big|_{x=-L}^{x=L} = 0. \tag{2.7.136}$$

Substituting Eq.(2.7.134) into Eq.(2.7.133), we have

$$\kappa_b\frac{\partial^4 u_z}{\partial x^4} = 0, \tag{2.7.137}$$

where κ_b here is

$$\kappa_b = c_{11}I - 2Hf^2(\epsilon - \epsilon_0). \tag{2.7.138}$$

Using Eq.(2.7.137) and boundary conditions Eq.(2.7.135) and (2.7.136), relation between bending moment and deformation is derived exactly similar to Eq.(2.7.128). This relation

[14]In some of the literature, flexoelectric tensor $\boldsymbol{\mu}$ is defined such that constitutive relation between polarization P_i, strain gradient $\frac{\partial S_{jk}}{X_l}$ and electric field E_i is expressed as $P_i = \mathcal{D}_{ij}E_j + \mu_{ijkl}\frac{\partial S_{jk}}{\partial X_l}$,where $\mathcal{D}_{ij}$ is a component of $\mathbb{D}$. However, we can also define the flexoelectric tensor $\mathbf{f}$ such that the internal energy density function is given by $\psi = W^{elast} + \frac{1}{2}P_i(\mathcal{D}^{-1})_{ij}P_j + f_{ijkl}P_i\frac{\partial S_{jk}}{\partial X_l} + \frac{\partial S_{ij}}{\partial X_j}g_{ijklmn}\frac{\partial S_{lm}}{\partial X_n}$. This internal energy density function will lead to the following equation:$P_i = \mathcal{D}_{ij}E_i - \mathcal{D}_{ij}f_{jklm}\frac{\partial S_{jk}}{\partial X_l}$. So, we can conclude that $\mathcal{D}_{ij}f_{jklm} = -\mu_{ijkl}$ or in a one-dimensional setting, $f(\epsilon - \epsilon_0) = -\mu^{flexo}$.

may be used to write down the electric displacement $\mathbf{d} = d\mathbf{e}_z$ in terms of bending moment:

$$d = \frac{M}{\kappa_b} f(\epsilon - \epsilon_0). \tag{2.7.139}$$

We observe that the flexoelectric coefficient of the beam may be identified by measuring curvature and induced charge at the electrodes. Flexoelectric coefficient is determined from Eq.(2.7.139):

$$f = \frac{\kappa_b}{(\epsilon - \epsilon_0)} \frac{\partial d}{\partial M}. \tag{2.7.140}$$

2.7.5 Bending of soft composite dielectric block

In a prior work, Bigoni et al. [109] extended Rivlin's analysis of a purely mechanical flexure problem of a soft block to that of a composite consisting of multiple layers. In this section, we use their analysis as a starting point and extend their analysis for a dielectric electret structure made of two materials where a layer of electric charge with surface charge density q has been inserted at their interface of two materials (Fig. 2.19). Throughout this section, we will use subscripts t and b to describe properties of layers on top and bottom, respectively. Two different coordinate systems are used to specify material points in the reference configuration for the two different materials.

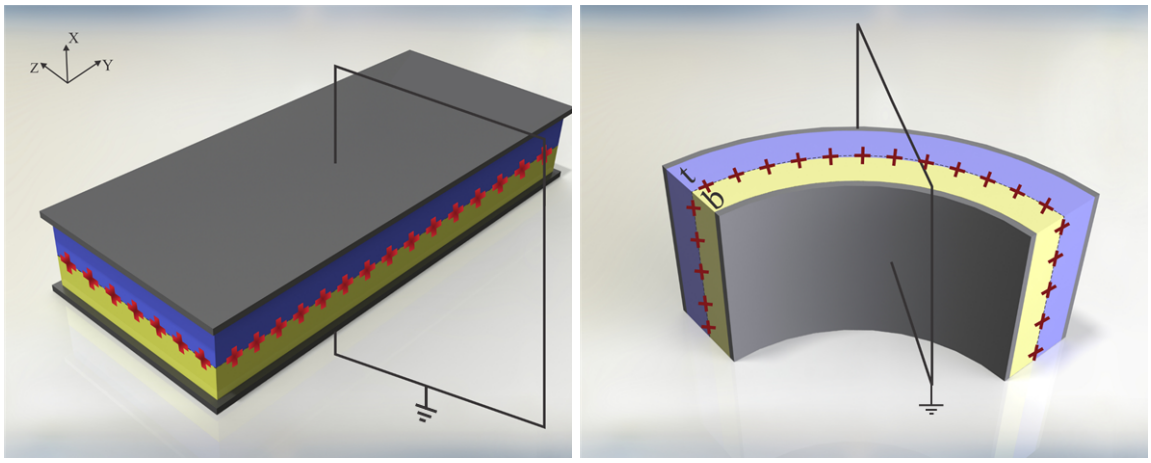

(a) (b)

Figure 2.19: A composite block made of two layers with two different dielectric materials and a layer of charge is inserted between two layers. (a) Undeformed configuration. (b) Deformed configuration.

$$\Omega_{Rb} = \{(X_b, Y, Z) \in \mathbb{R}^3 : |X_b| \leq H\frac{\alpha+1}{2}, |Y| \leq L, |Z| \leq W\} \quad \text{and} \tag{2.7.141a}$$

$$\Omega_{Rt} = \{(X_t, Y, Z) \in \mathbb{R}^3 : |X_t| \leq H\frac{1-\alpha}{2}, |Y| \leq L, |Z| \leq W\}. \tag{2.7.141b}$$

We consider the same class of deformation and kinematic constraints as we did in the preceding sections while analyzing homogeneous structures:

$$\begin{aligned} r_b &= \sqrt{2A_bX + B_b}, \quad \theta_b = \frac{Y}{A_b}, \quad z = Z \qquad \text{for layer b} \quad \text{and} \\ r_t &= \sqrt{2A_tX + B_t}, \quad \theta_t = \frac{Y}{A_t}, \quad z = Z \qquad \text{for layer t.} \end{aligned} \tag{2.7.142}$$

Electric boundary conditions are identified as

$$\xi(r_1) = 0, \tag{2.7.143a}$$

$$\xi(r_2) = 0, \tag{2.7.143b}$$

$$\text{and} \qquad \xi(r_{ch}) = V_i, \tag{2.7.143c}$$

where r_1, r_{ch} and r_2 are the inner radius, interface radius and outer radius of the deformed structure, respectively. The voltage V_i is the unknown electric potential at the interface of two materials and is created due to insertion of the charge layer. Charge distribution is exactly same as Eq.(2.54). So, using Maxwell's equations, voltage V_i can be determined from following equation

$$Aq = V_i \left(\frac{\epsilon_b}{\log \frac{r_{ch}}{r_1}} + \frac{\epsilon_t}{\log \frac{r_2}{r_{ch}}} \right). \tag{2.7.144}$$

Consequently, the electric field in the layers may be determined to be

$$\begin{aligned} \mathbf{e}_b &= -\frac{V_i}{r}\frac{1}{\log \frac{r_{ch}}{r_1}}\mathbf{e}_r, \\ \text{and} \qquad \mathbf{e}_t &= \frac{V_i}{r}\frac{1}{\log \frac{r_2}{r_{ch}}}\mathbf{e}_r. \end{aligned} \tag{2.7.145}$$

Since purely circular bending is considered, the mechanical boundary conditions for the

model are as follows

$$\theta_b(L) = \theta_t(L), \tag{2.7.146a}$$

$$r_b = r_t \qquad \text{at} \quad r = r_{ch}, \tag{2.7.146b}$$

$$\mathbf{t}_{rb} = (\boldsymbol{\sigma}_b^* - \mathcal{L}_{ab}\mathbf{I})\,\mathbf{e}_r = \mathbf{0} \qquad \text{at} \quad r = r_1, \tag{2.7.146c}$$

$$\mathbf{t}_{rt} = (\boldsymbol{\sigma}_t^* - \mathcal{L}_{at}\mathbf{I})\,\mathbf{e}_r = \mathbf{0} \qquad \text{at} \quad r = r_2, \tag{2.7.146d}$$

$$[\![\mathbf{t}_r]\!] = \mathbf{0} \qquad \text{at} \quad r = r_{ch}, \tag{2.7.146e}$$

$$\text{and} \qquad M = \int_{r_1}^{r_{ch}} r(\sigma^*_{\theta\theta b} - \mathcal{L}_{ab})dr + \int_{r_{ch}}^{r_2} r(\sigma^*_{\theta\theta t} - \mathcal{L}_{at})dr. \tag{2.7.146f}$$

Lagrange multipliers $\mathcal{L}_{ab}$ and $\mathcal{L}_{at}$ can be determined solving equilibrium equation for each layer and using boundary conditions (2.7.146c) and (2.7.146d)

$$\begin{aligned} &\mathcal{L}_{ab} = \sigma^*_{rrt} + \int_{r_1}^{r} \frac{1}{r'}\left(\sigma^*_{rrb}(r') - \sigma^*_{\theta\theta b}(r')\right) dr' \\ \text{and} \qquad &\mathcal{L}_{at} = \sigma^*_{rrt} + \int_{r_{ch}}^{r} \frac{1}{r'}\left(\sigma^*_{rrt}(r') - \sigma^*_{\theta\theta t}(r')\right) dr' \\ &\quad - \int_{r_{ch}}^{r_2} \frac{1}{r}\left(\sigma^*_{rrt}(r) - \sigma^*_{\theta\theta t}(r)\right) dr. \end{aligned} \tag{2.7.147}$$

From Eq.(2.7.146a), we conclude that $A_b = A_t = A$. Similar to Eq.(2.45), A, B_b and B_t can be expressed in terms of r_1, r_2 and r_{ch} and using continuity of deformation (Eq.(2.7.146b)) at the interface between two materials, $r = r_{ch}$, deformation can be expressed in terms of the two independent constants

$$\lambda_b = \left|\frac{r_{ch} - r_1}{(1+\alpha)H}\right| \qquad \text{and} \qquad \Lambda_b = \frac{r_{ch}}{r_1}, \tag{2.7.148}$$

where $\Lambda^2 = \frac{\Lambda_b^2 + \alpha - 1}{\alpha}$. Finally, Eq.(2.7.146e) can be used to determine stretch λ_b in terms of radius ratio Λ

$$\lambda_b^4 = \frac{32C_{11}\Lambda^2((1-\alpha^2)\mu_t + (\alpha+1)^2\mu_b)}{\left(\sqrt{C_{11}} + \sqrt{2}\right)^4((1-\alpha^2)\mu_t + (\alpha+1)^2\mu_b\Lambda^2) - 16q^2E_{11}}, \tag{2.7.149}$$

where coefficients E_{ij} are listed in the Appendix 2.7.1. Also, Eq.(2.7.146f) can be written

in terms of radius ratio and stretch

$$M = H^2 q^2 \lambda_b^4 E_{18} + \frac{H^2}{64 E_{12}} \Bigg\{ 32(E_{13}\mu_b + E_{14}\mu_t) + \lambda_b^4 \Big[E_{15}\mu_b + E_{16}\mu_t \\ - E_{17}(\mu_b - \mu_t) \log\left(\frac{2}{C_{21}}\right) + 2E_{17}\mu_a \log(\Lambda) \Big] \Bigg\}. \tag{2.7.150}$$

We can simply substitute Eq.(2.7.149) into (2.7.150) to obtain a relation between the radius ratio and bending moment. Also, in order to extract a linear relation similar to (2.59), the resulting relation can be linearized for small values of $\bar{\kappa}$ using Taylor series expansion and Eq.(2.51). Since the linearized relation is rather long, we avoid presenting it here and just present the following limiting case:

$$\lim_{\bar{\kappa}\to 0} \frac{M}{4H^2} = \frac{q^2(1-\alpha^2)((1-\alpha)^2\epsilon_b\mu_t - (\alpha+1)^2\mu_b\epsilon_t)}{4\left((1-\alpha)\epsilon_b + (\alpha+1)\epsilon_t\right)^2} \times \\ \left((\alpha+1)\mu_b + (1-\alpha)\mu_t + \frac{(1-\alpha^2)q^2}{(1-\alpha)\epsilon_b + (\alpha+1)\epsilon_t}\right)^{-1}. \tag{2.7.151}$$

Earlier we had emphasized that for an electret made of a single material, a non-zero curvature is observed in the block even in the absence of mechanical loading unless the charge layer is located exactly in the middle of the block. However, Eq.(2.7.151) shows that a non-zero bending moment is required to maintain a flat block even if the charge layer is located in the middle. In the other words, for a composite electret, and in absence of mechanical loading, a non-zero curvature can be observed in the block even if the charge layer is located in the middle of the block. The reason is that the material in-homogeneity intensifies non-uniformity of the Maxwell stress inside the material and this non-uniform distribution of stress bends the block.

As before for a single homogeneous electret material, the definitions (2.71) and (2.68) may be used to determine the apparent flexoelectric coefficient of the composite block

$$f^{app} = \frac{1}{(\epsilon' - \epsilon_0)} \frac{2Hq\left(1-\alpha^2\right)\epsilon_t\epsilon_b}{(\alpha\epsilon_t - \alpha\epsilon_b + \epsilon_t + \epsilon_b)^2}. \tag{2.7.152}$$

where ϵ in relation (2.71) has been replaced with ϵ' and is defined as

$$\frac{2}{\epsilon'} = \frac{(1+\alpha)}{\epsilon_b} + \frac{(1-\alpha)}{\epsilon_t}. \tag{2.7.153}$$

In contrast to a homogeneous electret, we now note that the optimal position for the charge layer is *not* in the center of the structure and there is an optimum thickness for each layer which maximizes the apparent flexoelectric coefficient.

Chapter 3

Homogenization of Electrets with Ellipsoidal Microstructure and Pathways for Designing Piezoelectricity in Soft Materials.

True piezoelectricity in soft materials is rare if not virtually non-existent. This impedes applications where both large deformation and a strong electromechanical coupling are desirable e.g. soft robotics, biomedical sensors and actuators, a class of energy harvesting devices among others. The widely used soft dielectric elastomers rely on the electrostatic Maxwell stress effect for electromechanical coupling which is a *one-way* quadratic effect, requires extremely large voltage for actuation and does not allow for the facile conversion of mechanical deformation into electricity. Prior research has shown that embedding (and stabilizing) immobile charges or dipoles in soft matter i.e. creating so-called *electrets*, can lead to an emergent piezoelectric effect. In this work, using a recently developed homogenization theory for soft electret materials, we derive closed-form expressions to design soft apparently piezoelectric materials with an ellipsoidal microstructure. Specifically, we determine both effective longitudinal (d_{33}) and transverse (d_{31}) piezoelectric coefficients of the material and study impact of the material properties on these two coefficients. Conventional electrets exhibit a rather weak d_{31}, which is quite disadvantageous for applications where flexure is important (e.g. energy harvesting). Either an elastic, or a dielectric contrast is essential to the emergence of piezoelectricity in electrets and, depending on the microstructural details, these two effects can either strengthen or diminish the other. Our results indicate that the microstructure and material properties which lead to an optimum d_{33} effect are different from the conditions underlying the optimal d_{31} response. The maximum d_{31} effect is observed in electrets where the inclusions are mechanically harder but dielectrically softer than the matrix material. Finally, we find that a significantly large d_{33} piezoelectric response is possible for spheroid inclusion microstructures with large aspect ratios.

3.1 Introduction

Soft materials are capable of large deformation and thus enable applications in the area of soft robotics[110], stretchable and wearable electronics[111], large deformation sensor and actuators [112, 40] and biocompatible devices [113]. A key imperative in the design of soft materials is to induce a mechanical response when subjected to a suitable stimuli e.g. electrical or magnetic fields fields, pH, temperature among others. Many applications of soft materials require a piezoelectric effect–a two way *linear* coupling between electric field and mechanical deformation. However, piezoelectricity only exists in noncentrosymmetric crystals [114]. These materials are hard and brittle materials and are ill-suited for some of the aforementioned applications. The electromechanical coupling in soft dielectrics is limited to the electrostatic Maxwell stress effect (or alternatively electrostriction). Due to electrostriction, all dielectric material deform in response to an applied electric field [95]. However, this effect is rather weak so hard dielectrics barely exhibit any discernible deformation. While soft materials like dielectric elastomers are well-able to exploit this form of electromechanical coupling, we note that electrostriction is a nonlinear (quadratic) coupling where the deformation scales as the square of the imposed electric field. This implies that deformation does not reverse if the imposed electric field is reversed [115]. In addition, electrostriction is a one-way coupling i.e. the material deforms in response to an electric field but the applied deformation does not generate an electric field [94]. Finally, significantly large electrical fields are necessary to induce actuation.

There appear to be two approaches to engineer a piezoelectric-like behavior in otherwise non-piezoelectric soft materials: (i) exploitation of the phenomenon of flexoelectricity [82, 83, 81], and (ii) embedding immobile charges and dipoles in materials thus creating so-called electrets. Discussion of flexoelectricity is beyond the scope of this work and we refer the reader to several original works [116, 117, 118, 119, 120, 121, 122, 123, 124, 124, 125, 126] and review articles [127, 81, 128, 85] for further information. The exploitation of electrets as materials that can mimic piezoelectrics began in earnest in the eighties when researchers created soft foamy polymers with charges and dipoles trapped on void surfaces [129, 130, 64, 129]. Piezoelectric coefficient as large as 1200 pC/N has been reported for

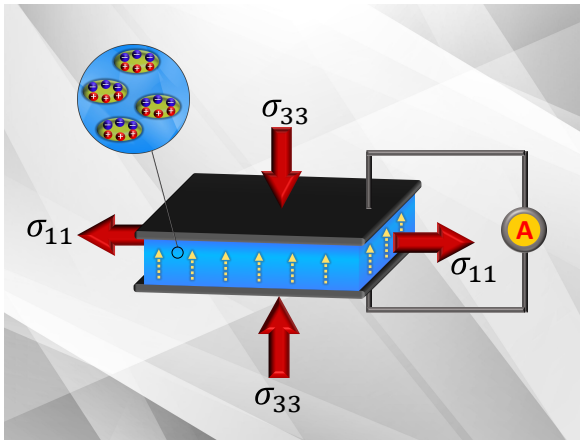

Figure 3.1: Longitudinal and transverse piezoelectric effects in electret materials which is composed of a matrix and embedded inclusions.

such materials[65, 131].

Electret materials have been subject of experimental research for several decades [132, 64, 133] including recent in the context of 2D materials. They have found applications in microphones [134], sensors[135], data storage[136]. Electret materials are specifically interesting for energy harvesting applications as they offer a higher power output compare to electromagnetic or intrinsic piezoelectric counterparts at low frequencies [137, 138]. Thus, electrets have been widely studied for energy harvesting applications [139, 140]. At this point of development, electret materials with large surface charge densities can be easily fabricated [141]. In addition, there has been several successful attempts for improving charge stability in electrets—a key issue impeding their practical application. For example, Luo et al. [142] developed a spray coating method for charge deposition to improve long term charge stability.

Recently, a few theoretical studies have also provided insights into the design of electromechanical coupling in electret materials. Deng et al. [98, 99] presented a continuum model to explain the emergence of piezoelectricity in simple 1-D layered electret structures. They were able to interpret existing experimental results in which a large longitudinal piezoelectric effect (so-called d_{33} effect) is frequently observed in electret materials(see Fig. 3.1 for explanation of longitudinal and transverse piezoelectric effect). We remark that the transverse piezoelectric coefficient is singularly important for applications (so-called d_{31} effect) such as energy harvesting and in general, for both sensing and actuation where flexure

(the most facile deformation mode) is important. However, conventional electrets exhibit a large d_{33} but not d_{31}. Rahmati et al. [143] created a model to explain the reason for small transverse piezoelectric effect in charged polymer foams and propose simple beam-based designs to improve this feature. Recently, Liu and Sharma [100] presented a comprehensive theory of homogenization of electret materials. Works prior to this reference focussed on simple boundary value problems to illustrate apparent piezoelectricity. In the work of Liu and Sharma, they were able to rigorously predict a true bulk piezoelectric effect and the conditions necessary to achieve this. Specifically, they also presented some explicit results for effective piezoelectric properties of some simple specific microstructures (e.g. laminates). In addition, they showed that either elastic mismatch or dielectric mismatch in electrets is essential for the emergence of an apparent piezoelectric effect. We remark that electrets have also been used to create other forms of multifunctional materials such as magneto-electrics [144, 144, 145], pyroelectric/electrocaloric materials [146] or understand biological phenomena.

Despite the work on electrets so far, there remain several unanswered questions about the emergent piezoelectric. effect:

- Elastic heterogeneity is essential for the emergence of piezoelectricity in electrets however it is unclear how the interplay of elastic properties impact the average piezoelectric response.

- Although a large d_{33} piezoelectric coefficient has been achieved in electrets, the d_{31} effect is usually quite small[3]. What design strategy may be employed to improve d_{31} coefficient in electrets?

- Liu and Sharma [100] argue that either elastic or dielectric mismatch must be present in electrets for apparent piezoelectricity. What is the interplay between dielectric and elastic mismatch in terms of tuning the effective response of electrets?

- Existing theoretical work have typically analyzed one-dimensional (or quasi-one-dimensional) electrets. While these studies have been insightful, little is known about how a 3D dimensional microstructure could impact the effective piezoelectric response of elec-

trets.

In this chapter, using the broad homogenization theoretical framework of Liu and Sharma [100], we analyze soft electret materials with ellipsoidal inclusions. The ellipsoidal microstructure is versatile enough for us to comment on issues such as the role of aspect ratio of heterogeneities and address the questions and observations highlighted in the preceding section.

3.2 A Summary of Homogenization Theory for Electrets

In this section, we present a very brief summary of the homogenization theory for electrets presented by Liu and Sharma [100]. The essential relations required to determine effective properties of electrets are listed in this section without presenting the details. See Liu and Sharma [100] for detailed derivation.

3.2.1 Energy formulation

We follow the the exact same notation as the notation used by Liu and Sharma [100]. The deformable elastic body of the electret in the reference configuration is denoted by $\mathcal{D}$. The deformation $\mathbf{y}$ and the nominal polarization $\mathbf{p}$ are two independent thermodynamic variables which describe the state of the system $(\mathbf{y}, \mathbf{p}) : \mathcal{D} \to \mathbb{R}^3 \times \mathbb{R}^3$. Material points in the reference configuration are denoted by $\mathbf{x}$. Also, deformation gradient tensor, Jacobian and the right Cauchy-Green deformation tensore are denoted by $\mathbf{F} = \nabla \mathbf{y}$, $J = \det\mathbf{F}$ and $\mathbf{C} = \mathbf{F}^T\mathbf{F}$, respectively. The electric potential is represented by $\xi : D \to \mathbb{R}$. Dirichlet boundary condition has been applied to the whole boundary of the body $\partial\mathcal{D}$:

$$\xi = \xi_b \qquad \text{on} \quad \partial\mathcal{D} \qquad \text{and} \qquad \mathbf{y} = \mathbf{x} + \mathbf{u}_b \qquad \text{on} \quad \partial\mathcal{D}, \tag{3.2.1}$$

where ξ_b and $\mathbf{u}_b$ are, respectively, prescribed electric potential and displacement on the boundary. Following convention is used fo inner products of tensors: for third order tensor $\mathbf{A}$ and second order tensor $\mathbf{B}$ we have $\mathbf{A} : \mathbf{B} = A_{ijk}B_{jk}\mathbf{e}_i$, for forth order tensors $\mathbf{A}$ and $\mathbf{B}$ we have $\mathbf{AB} = A_{ijkl}B_{klmn}(\mathbf{e}_i \otimes \mathbf{e}_j \otimes \mathbf{e}_m \otimes \mathbf{e}_n)$ and for second order tensor $\mathbf{A}$ and vector $\mathbf{a}$

we have $\mathbf{Aa} = A_{ij}a_j\mathbf{e}_i$.

The free energy of the system is expressed as

$$\begin{aligned} F[\mathbf{y},\mathbf{p}] &= \int_{\mathcal{D}} \left[\Psi(\nabla\mathbf{y},\mathbf{p}) + \frac{\epsilon_0}{2}\nabla\xi\cdot J\mathbf{C}^{-1}\nabla\xi\right]\mathrm{d}\mathbf{x} \\ &+ \int_{\partial\mathcal{D}} \xi_b\mathbf{n}\cdot(-\epsilon_0 J\mathbf{C}^{-1}\nabla\xi + \mathbf{F}^{-1}\mathbf{p}), \end{aligned} \tag{3.2.2}$$

where $\Psi : \mathbb{R}^{3\times3}\times\mathbb{R}^3 \to \mathbb{R}$ is the internal energy density function. Also, ϵ_0 and $\mathbf{n}$ are electric permittivity of the vacuum and unit normal to the boundary, respectively. The equilibrium state of the system is the state that minimizes free energy give in the Eq.(3.2.2) and also satisfies the Maxwell equation. The Maxwell equation in the reference configuration is expressed as

$$\nabla\cdot(-\epsilon_0 J\mathbf{C}^{-1}\nabla\xi + \mathbf{F}^{-1}\mathbf{p} + \mathbf{F}^{-1}\mathbf{p}^e) = \rho^e, \tag{3.2.3}$$

where $\mathbf{p}^e$ and ρ^e are external electric dipoles and charges, respectively. In order to obtain a linear theory, we restrict ourselves to the regime of small deformation and moderately small electric field

$$\nabla\mathbf{u} \sim \varepsilon \ll 1 \quad \text{and} \qquad \mathbf{p} \sim \varepsilon^{1/2}, \tag{3.2.4}$$

where $\mathbf{u}(\mathbf{x}) = \mathbf{y}(\mathbf{x}) - \mathbf{x}$ is the displacement. We Introduce tensors $\boldsymbol{\chi}$, $\mathbb{C}$ and $\mathbb{M}$ as

$$\boldsymbol{\chi} = \frac{\partial^2\Psi}{\partial\mathbf{p}\partial\mathbf{p}}, \qquad \mathbb{C} = \frac{\partial^2\Psi}{\partial\mathbf{F}\partial\mathbf{F}}, \quad \text{and} \quad \mathbb{M} = \frac{1}{2}\frac{\partial^3\Psi}{\partial\mathbf{F}\partial\mathbf{p}\partial\mathbf{p}}, \tag{3.2.5}$$

where all derivatives have been evaluated at $(\mathbf{F},\mathbf{p}) = (\mathbf{I},\mathbf{0})$. Using the Taylor series expansion and the scaling given in the Eq.(3.2.4), the free energy can be decomposed [147, 58, 97]:

$$F[\mathbf{y},\mathbf{p}] = F^{(0)} + F^{(1)} + F^{(2)} + o(\varepsilon^2), \tag{3.2.6}$$

where $F^{(0)} := F[\mathbf{y}=\mathbf{x},\mathbf{p}=\mathbf{0}]$,

$$F^{(1)}[\mathbf{p}] = \int_{\mathcal{D}}\left[\frac{1}{2}\mathbf{p}\cdot\boldsymbol{\chi}\mathbf{p} + \frac{\epsilon_0}{2}|\nabla\xi|^2\right]\mathrm{d}\mathbf{x} + \int_{\partial\mathcal{D}}\left[\xi_b\mathbf{n}\cdot(-\epsilon_0\nabla\xi + \mathbf{p} + \mathbf{p}^e)\right]\mathrm{d}\mathbf{x} \sim \varepsilon, \tag{3.2.7}$$

$$\text{and} \qquad F^{(2)}[\mathbf{u},\mathbf{p}] = \int_{\mathcal{D}}\left[\frac{1}{2}\nabla\mathbf{u}\cdot\mathbb{C}\nabla\mathbf{u} + \nabla\mathbf{u}\cdot\mathbb{M}(\mathbf{p}\otimes\mathbf{p}) + \nabla\mathbf{u}\cdot\boldsymbol{\sigma}_{\mathrm{MW}}\right]\mathrm{d}\mathbf{x} \sim \varepsilon^2, \tag{3.2.8}$$

where $\boldsymbol{\sigma}_{\mathrm{MW}}$ is given as

$$\boldsymbol{\sigma}_{\mathrm{MW}} = -\frac{\epsilon_0}{2}|\nabla\xi|^2\mathbf{I} + \epsilon_0\nabla\xi\otimes\nabla\xi - \nabla\xi\otimes\mathbf{p}. \tag{3.2.9}$$

We identify the forth order electrostrictive coupling tensor $\mathbb{A}$ as

$$\mathbb{A}_{ijkl} = (\mathbb{M})_{ijk'l'}(\boldsymbol{\chi}^{-1})_{kk'}(\boldsymbol{\chi}^{-1})_{ll'} + \frac{\epsilon_0}{2}\mathbb{T}_{ijkl} + \frac{1}{2}[\delta_{ik}(\boldsymbol{\chi}^{-1})_{jl} + \delta_{il}(\boldsymbol{\chi}^{-1})_{jk}], \tag{3.2.10}$$

where the fourth-order tensor $\mathbb{T} : \mathbb{R}^{3\times3} \to \mathbb{R}^{3\times3}$ is given as

$$\begin{aligned} &\mathbb{T}\mathbf{F} = \mathbf{F} + \mathbf{F}^T - (\mathrm{Tr}\mathbf{F})\mathbf{I} \qquad \forall\mathbf{F}\in\mathbb{R}^{3\times3}, \\ &\mathbb{T}_{ijkl} = \delta_{ik}\delta_{jl} + \delta_{il}\delta_{jk} - \delta_{ij}\delta_{kl}. \end{aligned} \tag{3.2.11}$$

We identify the dielectric tensor as $\boldsymbol{\epsilon} = \epsilon_0\mathbf{I} + \boldsymbol{\chi}^{-1}$. The dielectric tensor and the electrostrictive coupling tensor for isotropic materials are expressed as $\boldsymbol{\epsilon} = \epsilon\mathbf{I}$ and $\mathbb{A} = \frac{\epsilon}{2}\mathbb{T}$. We can use first of Eq.(3.2.7) to write equilibrium equations of the system in terms of electric potental and displacement

$$\nabla\cdot(-\boldsymbol{\epsilon}\nabla\xi + \mathbf{p}^e) = \rho^e \qquad \text{in} \quad \mathcal{D}, \tag{3.2.12}$$

$$\text{and} \qquad \nabla\cdot(\mathbb{C}\nabla\mathbf{u} + \mathbb{A}\,(\nabla\xi\otimes\nabla\xi)) = \mathbf{0} \qquad \text{in} \quad \mathcal{D}. \tag{3.2.13}$$

3.2.2 Effective propeties of the electrets

We assume electrostatic body of the electret $\mathcal{D}$ has a periodic microstructure (see Fig. 3.2). The rescaled unit cell (or RVE) of the composite is denoted by $Y = (0,1)^3 \subset \mathcal{D}$. We identify fast variables $\widetilde{\mathbf{x}} = \mathbf{x}/\delta$, where δ is the scaling parameter δ reflects the fine microstructure of the composite as compared with the macroscopic length-scale of the domain $\mathcal{D}$. For a domain $\mathcal{D}$, $\fint_{\mathcal{D}}$ denotes the average of the integrand on $\mathcal{D}$. Dielectric tensor, stiffness tensor and electrostrictive coupling tensor are assumed to be Y-periodic functions:

$$\left(\boldsymbol{\epsilon}^{(\delta)}(\mathbf{x}), \mathbb{C}^{(\delta)}(\mathbf{x}), \mathbb{A}^{(\delta)}(\mathbf{x})\right) = \left(\boldsymbol{\epsilon}_{\#}\left(\widetilde{\mathbf{x}}\right), \mathbb{C}_{\#}\left(\widetilde{\mathbf{x}}\right), \mathbb{A}_{\#}\left(\widetilde{\mathbf{x}}\right)\right), \tag{3.2.14}$$

where $\widetilde{\mathbf{x}} = \frac{\mathbf{x}}{\delta}$ is the fast variable.

Effective stiffness and effective electric permittivity tensor

We identify the effective electric permittivity tensor $\boldsymbol{\epsilon}^{\text{eff}}$, the effective stiffness tensor $\mathbb{C}^{\text{eff}}$ and the effective electrostrictive tensor $\mathbb{A}^{\text{eff}}$ as [58, 147]

$$\boldsymbol{\epsilon}^{\text{eff}}\bar{\mathbf{e}} = \fint_Y [\boldsymbol{\epsilon}_{\#}(\widetilde{\mathbf{x}})(-\nabla\xi_{\bar{\mathbf{e}}})] \qquad \text{for} \quad \bar{\mathbf{e}} \in \mathbb{R}^3, \tag{3.2.15}$$

$$\mathbb{C}^{\text{eff}}\bar{\mathbf{H}} = \fint_Y [\mathbb{C}_{\#}(\widetilde{\mathbf{x}})(\nabla \mathbf{u}_{\bar{\mathbf{H}}})] \qquad \text{for} \quad \bar{\mathbf{H}} \in \mathbb{R}^{3\times 3}, \tag{3.2.16}$$

$$\bar{\mathbf{H}} \cdot \mathbb{A}^{\text{eff}}(\bar{\mathbf{e}} \otimes \bar{\mathbf{e}}) =$$

$$\text{and} \qquad \fint_Y [\nabla \mathbf{u}_{\bar{\mathbf{H}}} \cdot \mathbb{A}_{\#}(\widetilde{\mathbf{x}})(\nabla\xi_{\bar{\mathbf{e}}} \otimes \nabla\xi_{\bar{\mathbf{e}}})] \qquad \text{for} \quad (\bar{\mathbf{e}}, \bar{\mathbf{H}}) \in \mathbb{R}^3 \times \mathbb{R}^{3\times 3}, \tag{3.2.17}$$

where the electric potential $\xi_{\bar{\mathbf{e}}} \in \mathcal{P}_{\bar{\mathbf{e}}}$ and $\mathbf{u}_{\bar{\mathbf{H}}} \in \mathcal{U}_{\bar{\mathbf{H}}}$ satisfy unit cell equilibrium equations

$$\text{div}[\boldsymbol{\epsilon}_{\#}(\widetilde{\mathbf{x}})(-\nabla\xi_{\bar{\mathbf{e}}})] = 0 \tag{3.2.18}$$

$$\text{and} \qquad \text{div}[\mathbb{C}_{\#}(\widetilde{\mathbf{x}})(\nabla \mathbf{u}_{\bar{\mathbf{H}}})] = \mathbf{0}. \tag{3.2.19}$$

Also, admissible spaces $\mathcal{P}_{\bar{\mathbf{e}}}$ and $\mathcal{U}_{\bar{\mathbf{H}}}$ are defined as

$$\mathcal{P}_{\bar{\mathbf{e}}} \equiv \left\{ \xi : -\fint_Y \nabla\xi = \bar{\mathbf{e}} \qquad \text{and} \quad \nabla\xi \quad \text{is Y-periodic} \right\} \tag{3.2.20}$$

$$\text{and} \qquad \mathcal{U}_{\bar{\mathbf{H}}} \equiv \left\{ \mathbf{u} : \fint_Y \nabla \mathbf{u} = \bar{\mathbf{H}} \qquad \text{and} \quad \nabla \mathbf{u} \quad \text{is Y-periodic} \right\}. \tag{3.2.21}$$

Multiscale analysis and effective piezoelectric tensor

We represent microstructural distribution of external dipoles and charges by $(\mathbf{p}^{(\delta)}, \rho^{\delta})$. We assume a periodic distribution for external charges and dipoles inside the material:

$$(\mathbf{p}^{(\delta)}, \rho^{\delta}) = \left(\bar{\mathbf{p}} + \mathbf{p}_{\#}(\frac{\mathbf{x}}{\delta}), \bar{\rho} + \frac{1}{\delta}\rho_{\#}(\frac{\mathbf{x}}{\delta}) \right), \tag{3.2.22}$$

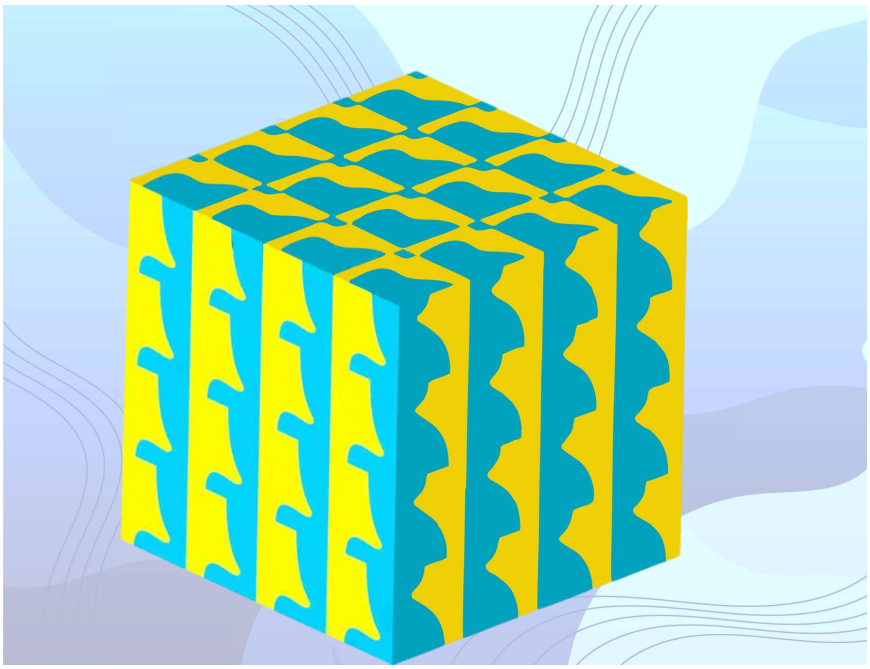

Figure 3.2: A schematic of a periodic microstructure. The color in each unit cell could be heterogeneities or external, immobile positive and negative charges.

where $\mathbf{p}_{\#}$ and $\rho_{\#}$ are Y-periodic functions

$$\fint_Y (\mathbf{p}_{\#}, \rho_{\#}) = 0. \tag{3.2.23}$$

Existence of external charges and/or dipoles will lead to a piezoelectric effect in electret materials. We use multiscale analysis based on the method of two-scale convergence [148, 149] in order to define effective piezoelectric tensor. Using scaling discussed earlier, electrostatic problem is decoupled from the elasticity. Thus, we perform multi-scale analysis on the electrostatic equilibrium equation first. The local electric field can be determined solving

$$\begin{cases} \operatorname{div}[-\epsilon^{(\delta)}\nabla\xi^{(\delta)} + \mathbf{p}^{(\delta)}] = \rho^{(\delta)} & \text{in} \quad \mathcal{D}, \\ \xi^{(\delta)} = \xi_b & \text{on} \quad \partial\mathcal{D}. \end{cases} \tag{3.2.24}$$

The goal of current theory is to analyze the behavior of the material in the limit $\delta \to 0$. Following the formal procedure of multiscale analysis, the solution to Eq.(3.2.24) is given

as

$$\xi^{(\delta)}(\mathbf{x}) = \xi^{(0)}(\mathbf{x}, \widetilde{\mathbf{x}}) + \delta\xi^{(1)}(\mathbf{x}, \widetilde{\mathbf{x}}) + \cdots \quad , \tag{3.2.25}$$

where $\widetilde{\mathbf{x}} \mapsto \xi^{(i)}(\mathbf{x}, \widetilde{\mathbf{x}})$ is Y-periodic for all i and $\fint_Y \xi^{(i)} = 0$ if $i \neq 0$. Using chain rule we can rewrite gradient and divergence operators as $\nabla \to \nabla_{\mathbf{x}} + \frac{1}{\delta}\nabla_{\widetilde{\mathbf{x}}}$ and div $\to$ div$_{\mathbf{x}} + \frac{1}{\delta}div_{\widetilde{\mathbf{x}}}$. It can be proved that the first order of the solution (3.2.25) is independent of the fast variable $\widetilde{\mathbf{x}} = \frac{\mathbf{x}}{\delta}$ and can be determined from following equation

$$\begin{cases} \text{div}_{\mathbf{x}} \left(-\boldsymbol{\epsilon}^{\text{eff}} \nabla_{\mathbf{x}} \xi^{(0)} + \chi_D(\bar{\mathbf{p}} + \bar{\mathbf{d}}') \right) = \bar{\rho} & \text{in} \quad \mathcal{D} \\ \text{and} \qquad \xi^{(0)} = \xi_b & \text{on} \quad \partial\mathcal{D}, \end{cases} \tag{3.2.26}$$

where $\chi_D = 1$ on D and $\chi_D = 0$ otherwise. Also, $\bar{\mathbf{d}}'$ is defined as

$$\bar{\mathbf{d}}' = \fint_Y \boldsymbol{\epsilon}_{\#}(-\nabla_{\widetilde{\mathbf{x}}}\xi'), \tag{3.2.27}$$

and $\xi' \in \mathcal{P}_0$ and is a solution to the following equation

$$\text{div}_{\widetilde{\mathbf{x}}}[\boldsymbol{\epsilon}_{\#}(\widetilde{\mathbf{x}})(-\nabla_{\widetilde{\mathbf{x}}}\xi') + \mathbf{p}_{\#}] = \rho_{\#} \qquad \text{in Y.} \tag{3.2.28}$$

The equation (3.2.28) is a key equation in the calculation of the effective piezoelectric tensor which we will use later. Also, ξ' can be related to $\xi^{(1)}$ defined in the Eq.(3.2.25). For more details, reader is referred to the [100].

Next, we can analyze the elasticity problem using a similar procedure as we used for the electrostatic problem. The mechanical equilibrium equation is expressed as

$$\begin{cases} \text{div}[\mathbb{C}^{(\delta)} \nabla \mathbf{u}^{(\delta)} + \mathbb{A}^{(\delta)} \nabla \xi^{(\delta)} \otimes \xi^{(\delta)}] = 0 & \text{in} \quad \mathcal{D} \\ \text{and} \qquad \mathbf{u}^{(\delta)} = \mathbf{u}_b & \text{on} \quad \partial\mathcal{D}. \end{cases} \tag{3.2.29}$$

The solution to above equation can be written as

$$\mathbf{u}^{(\delta)}(\mathbf{x}) = \mathbf{u}^{(0)}(\mathbf{x}, \widetilde{\mathbf{x}}) + \delta\mathbf{u}^{(1)}(\mathbf{x}, \widetilde{\mathbf{x}}) + \cdots \quad , \tag{3.2.30}$$

where $\mathbf{u}^{(i)}(\mathbf{x}, \widetilde{\mathbf{x}})$ is Y-periodic for all i and $\fint_Y \mathbf{u}^{(i)} = 0$ if $i \neq 0$. We identify $\mathbf{u}_1' \in \mathcal{U}_0$ which satisfies

$$\mathrm{div}_{\widetilde{\mathbf{x}}} \left[\mathbb{C}_{\#}(\widetilde{\mathbf{x}}) \nabla_{\widetilde{\mathbf{x}}} \mathbf{u}_1' + 2\mathbb{A}_{\#}(\widetilde{\mathbf{x}}) (\nabla_{\widetilde{\mathbf{x}}} \xi' \otimes \nabla_{\widetilde{\mathbf{x}}} \xi_{\bar{\mathbf{e}}}) \right] = 0. \tag{3.2.31}$$

It can be shown that the macroscopic displacement $\mathbf{u}^{(0)}$ is independent of the fast variable ($\mathbf{u}^{(0)} = \mathbf{u}^{(0)}(\mathbf{x})$). The boundary value problem for the macroscopic displacement $\mathbf{u}^{(0)}$ is given as

$$\begin{cases} \mathrm{div}_{\mathbf{x}} \boldsymbol{\sigma} = 0, & \text{in} \quad D \\ \text{and} \qquad \mathbf{u}^{(0)} = \mathbf{u}_b & \text{on} \quad \partial D, \end{cases} \tag{3.2.32}$$

where the total stress $\boldsymbol{\sigma}$ is defined as

$$\boldsymbol{\sigma} \equiv \mathbb{C}^{\mathrm{eff}} \nabla_{\mathbf{x}} \mathbf{u}^{(0)} - \mathbb{B}^{\mathrm{eff}} \nabla_{\mathbf{x}} \xi^{(0)} + \mathbb{A}^{\mathrm{eff}} (\nabla_{\mathbf{x}} \xi^{(0)} \otimes \nabla_{\mathbf{x}} \xi^{(0)}) + \boldsymbol{\sigma}^0. \tag{3.2.33}$$

The second order tensor $\boldsymbol{\sigma}^0$ is independent of the average electric field and strain. The definition of the tensor $\boldsymbol{\sigma}^0$ is available in [100]. Also, $\mathbb{B}^{\mathrm{eff}}$ is the effective piezoelectric tensor and is defined as

$$\mathbb{B}^{\mathrm{eff}} \bar{\mathbf{e}} = \fint_Y [\mathbb{C}_{\#}(\widetilde{\mathbf{x}}) \nabla_{\widetilde{\mathbf{x}}} \mathbf{u}_1' + 2\mathbb{A}_{\#}(\widetilde{\mathbf{x}}) (\nabla_{\widetilde{\mathbf{x}}} \xi' \otimes \nabla_{\widetilde{\mathbf{x}}} \xi_{\bar{\mathbf{e}}})]. \tag{3.2.34}$$

3.3 Effective piezoelectric properties of an electret with ellipsoidal inclusion

In this section, we use the theory presented earlier to obtain the effective piezoelectric properties of an electret with ellipsoidal inclusion. The unit cell of the material is shown in the Fig.3.3(a). We assume both matrix and inclusion are homogeneous isotropic materials. We identify unit cell by Y and the inclusion is represented by Ω. We denote the stiffness tensor for the matrix (resp. inclusion) by $\mathbb{C}^m$ (resp. $\mathbb{C}^p$). Also, we represent the electric permittivity the tensor of the matrix and inclusion with $\boldsymbol{\epsilon}_m = \epsilon_m \mathbf{I}$ and $\boldsymbol{\epsilon}_p = \epsilon_p \mathbf{I}$, respectively. We assume that there exist a nonzero uniform polarization $\mathbf{p}_s$ inside the inclusion. In order

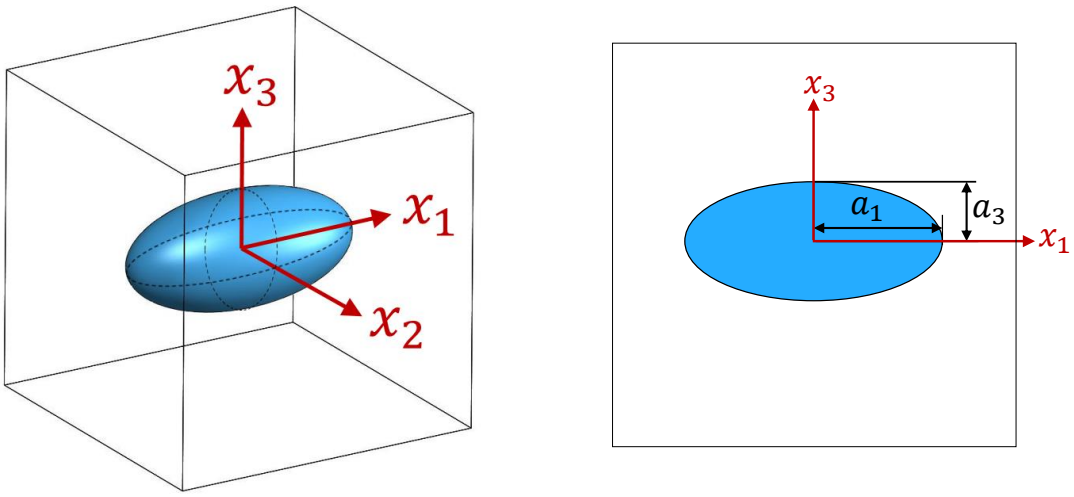

(a) Three dimensional view. (b) Front view.

Figure 3.3: The schematic of the electret material with ellipsoidal inclusion. (a) Three dimensional view. (b) Front view.

to determine the piezoelectric tensor for this material, first we need to solve electrostatic equations (3.2.28) and (3.2.18). Introducing the variable χ_p (resp. χ_m) such that $\chi_p = 1$ (resp. $\chi_m = 1$) for $x \in \Omega$ (resp. $x \in Y/\Omega$) and $\chi_p = 0$ (resp. $\chi_m = 0$) otherwise, we rewrite these two equations as

$$\operatorname{div}[-(\epsilon_m\chi_m + \epsilon_p\chi_p)\nabla\xi' + \mathbf{p}_s\chi_p] = 0 \qquad \text{in} \quad Y \tag{3.3.1}$$

$$\text{and} \qquad \operatorname{div}[-(\epsilon_m\chi_m + \epsilon_p\chi_p)\nabla\xi_{\bar{\mathbf{e}}}] = 0 \qquad \text{in} \quad Y, \tag{3.3.2}$$

where

$$\fint_Y \nabla\xi' = \mathbf{0} \quad \text{and} \qquad \fint_Y \nabla\xi_{\bar{\mathbf{e}}} = -\bar{\mathbf{e}}. \tag{3.3.3}$$

After we solve electrostatic equations (3.3.1) and (3.3.2), we need to solve elasticity equation (3.2.31) which can be rewritten as

$$\operatorname{div}\left((\mathbb{C}^p\chi_p + \mathbb{C}^m\chi_m)\nabla\mathbf{u}' + \boldsymbol{\sigma}^{(e)}\right) = \mathbf{0}, \tag{3.3.4}$$

where here we have dropped the subscript 1 from $\mathbf{u}'_1$ for brevity. Also, we identify $\boldsymbol{\sigma}^{(e)}$ as

$$\boldsymbol{\sigma}^{(e)} = \epsilon_{\#}\mathbb{T}(\nabla\xi' \otimes \nabla\xi_{\bar{\mathbf{e}}}). \tag{3.3.5}$$

Effective dielectric tensor is defined as

$$\boldsymbol{\epsilon}^{\text{eff}}\bar{\mathbf{e}} = -\fint_Y \epsilon_{\#}\nabla\xi_{\bar{\mathbf{e}}}. \tag{3.3.6}$$

Once we have determined ξ', $\xi_{\bar{\mathbf{e}}}$ and $\mathbf{u}'$ we can obtain the effective piezoelectric tensor using

$$\mathbb{B}^{\text{eff}}\mathbf{e} = \fint_Y \left[\mathbb{C}_{\#}\nabla\mathbf{u}' + \boldsymbol{\sigma}^{(\bar{\mathbf{e}})}\right]. \tag{3.3.7}$$

3.3.1 Solution to electrostatic problems

The solution for equations (3.3.1) and (3.3.2) is obtained solving following equation for the ellipsoidal inclusion

$$\text{div}(-\nabla\hat{\psi}_{\mathbf{m}} + \mathbf{m}\chi_p) = 0, \tag{3.3.8}$$

where $\mathbf{m} \in \mathbb{R}^3$ is a constant vector and $\nabla\hat{\psi}_{\mathbf{m}} \to \mathbf{0}$ at the infinity. In order to obtain solution for Eq.(3.3.8), we express $\hat{\psi}_{\mathbf{m}}$ and $\mathbf{m}$ in terms of their Fourier transforms $\bar{\psi}_{\mathbf{m}}$ and $\bar{\mathbf{m}}$, respectively:

$$\hat{\psi}_{\mathbf{m}} = \int_{\mathbb{R}^3} \bar{\psi}_{\mathbf{m}}(\mathbf{k})\text{exp}\left(i\mathbf{k}\cdot\mathbf{x}\right)\text{d}\mathbf{k}, \tag{3.3.9}$$

$$\text{and} \qquad \mathbf{m} = \int_{\mathbb{R}^3} \bar{\mathbf{m}}(\mathbf{k})\text{exp}\left(i\mathbf{k}\cdot\mathbf{x}\right)\text{d}\mathbf{k}. \tag{3.3.10}$$

Substituting Eq.(3.3.10) and (3.3.9) into (3.3.8), we have

$$\int_{\mathbb{R}^3} \left(\bar{\psi}_{\mathbf{m}}k_ik_i + i\bar{m}_jk_j\right)\text{exp}\left(i\mathbf{k}\cdot\mathbf{x}\right) = 0. \tag{3.3.11}$$

Thus, $\bar{\psi}_{\mathbf{m}}$ can be determined as

$$\bar{\psi}_{\mathbf{m}} = -\frac{ik_j\bar{m}_j}{k_ik_i}. \tag{3.3.12}$$

Now consider the Green's function $G(\mathbf{x}-\mathbf{x}')$ as

$$G(\mathbf{x}-\mathbf{x}') = \frac{1}{4\pi}\frac{1}{|\mathbf{x}-\mathbf{x}'|}. \tag{3.3.13}$$

The Green's function $G(\mathbf{x}-\mathbf{x}')$ is expressed in terms of its Fourier transform $\bar{G}(\mathbf{k})$ as [150, 151]

$$G(\mathbf{x}-\mathbf{x}') = \int_{\mathbb{R}^3} \bar{G}(\mathbf{k})\exp\left(i\mathbf{k}\cdot(\mathbf{x}-\mathbf{x}')\right)\mathrm{d}\mathbf{k}, \tag{3.3.14}$$

where

$$\bar{G}(\mathbf{k}) = \frac{1}{(2\pi)^3}\frac{1}{k_i k_i}. \tag{3.3.15}$$

Substituting Eq.(3.3.12) into Eq.(3.3.9) and using Eq.(3.3.15) we have:

$$\hat{\psi_{\mathbf{m}}} = -(2\pi)^3 \int_{\mathbb{R}^3} \overline{G_{,j}}\bar{m}_j \exp\left(i\mathbf{k}\cdot\mathbf{x}\right)\mathrm{d}\mathbf{k}, \tag{3.3.16}$$

where $\overline{G_{,j}}$ is the Fourier transform of $G_{,j}$ where throughout this chapter subscript "," means partial derivative. For example, $G_{,j} = \frac{\partial G}{\partial x_j}$. Using convolution theorem we can rewrite (3.3.16) as [151]

$$\hat{\psi_{\mathbf{m}}} = -\int_{\Omega} G_{,j}(\mathbf{x}-\mathbf{x}')m_j \mathrm{d}\mathbf{x}'. \tag{3.3.17}$$

We identify function $\Phi(\mathbf{x}) = \int_\Omega \frac{1}{|\mathbf{x}-\mathbf{x}'|}\mathrm{d}\mathbf{x}'$. For constant $\mathbf{m}$ and using Eq.(3.3.17) and (3.3.13), we express $\nabla\hat{\psi_{\mathbf{m}}}$ as

$$\nabla\hat{\psi_{\mathbf{m}}} = \mathbf{Q}\mathbf{m} \qquad \text{for} \quad x \in Y, \tag{3.3.18}$$

where $Q_{ij} = -\frac{1}{4\pi}\Phi_{,ij}$. We introduce following elliptic integrals

$$I(s) = 2\pi a_1 a_2 a_3 \int_s^\infty \frac{\mathrm{d}s}{\Delta(s)}, \tag{3.3.19}$$

$$I_i(s) = 2\pi a_1 a_2 a_3 \int_s^\infty \frac{\mathrm{d}s}{(a_i^2+s)\Delta(s)} \tag{3.3.20}$$

$$\text{and} \qquad I_{ij}(s) = 2\pi a_1 a_2 a_3 \int_s^\infty \frac{\mathrm{d}s}{(a_i^2+s)(a_j^2+s)\Delta(s)}, \tag{3.3.21}$$

where

$$\Delta(s) = \sqrt{(a_1^2 + s)(a_2^2 + s)(a_3^2 + s)}. \tag{3.3.22}$$

Components of Q_{ij} for elliptical inclusion with principal semi-axes a_1, a_2 and a_3 can be determined as [150, 152]

$$Q_{ij} = Q_{ij}^{-} = \frac{1}{4\pi}\left(\delta_{ij} I_I(0)\right) \qquad \text{for} \quad x \in \Omega, \tag{3.3.23}$$

$$\text{and} \qquad Q_{ij}(\mathbf{x}) = Q_{ij}^{+} = \frac{1}{4\pi}\left(\delta_{ij} I_I(s) - x_i I_{I,J}\right) \qquad \text{for} \quad x \in \mathbb{R}^3/\Omega, \tag{3.3.24}$$

where the following summation convention has been used: repeated lower case indices are summed up from 1 to 3; upper case indices take on the same numbers as the corresponding lower case ones but are not summed. Note that can be proved that for elliptical shapes the electric field inside the inclusion is constant [153, 154]. Also, the elliptical integrals (3.3.19), (3.3.20) and (3.3.21) can be explicitly determined for several kinds of ellipsoid. Here, in this chapter, we consider a prolate spheroid with radii a_1, a_2 and a_3 (see Fig. 3.3(b)). For prolate spheroid with $a_2 = a_3 < a_1$, the components of $\mathbf{Q}$ tensor for interior points ($\mathbf{Q}^{-}$) can be determined substituting Eq.(3.3.19) into Eq.(3.3.23)

$$\mathbf{Q}^{-} = Q_{11}^{-}\mathbf{e}_1 \otimes \mathbf{e}_1 + Q_{22}^{-}\mathbf{e}_2 \otimes \mathbf{e}_2 + Q_{33}^{-}\mathbf{e}_3 \otimes \mathbf{e}_3, \tag{3.3.25}$$

where $\{\mathbf{e}_1, \mathbf{e}_2, \mathbf{e}_3\}$ represents the coordinate system and

$$Q_{33}^{-} = Q_{22}^{-} = \frac{a_3^2 a_1}{2(a_1^2 - a_3^2)^{3/2}} \times \left[\frac{a_1}{a_3}\left(\frac{a_1^2}{a_3^2} - 1\right)^{1/2} - \cosh^{-1}\frac{a_1}{a_3}\right] \tag{3.3.26}$$

$$\text{and} \qquad Q_{11}^{-} = 1 - 2Q_{22}^{-}. \tag{3.3.27}$$

Also, using jump conditions, the solution on the outer surface of the inclusion can be determined in terms of the solution inside the inclusion as

$$\nabla\hat{\psi}_{\mathbf{m}}|_{\partial\Omega^+} = \mathbf{Q}^{-}\mathbf{m} - (\mathbf{n}\cdot\mathbf{m})\mathbf{n}. \tag{3.3.28}$$

Having the solution (3.3.18) for the equation (3.3.8), we can determine $\nabla\xi'$ and $\nabla\xi_{\bar{\mathbf{e}}}$. We introduce $\mathbf{m}_1$ and $\mathbf{m}_2$ as

$$\mathbf{m}_1 = [\epsilon_m \mathbf{I} + (\epsilon_p - \epsilon_m)\mathbf{Q}^-]^{-1}\mathbf{p}_s \tag{3.3.29}$$

$$\text{and} \qquad \mathbf{m}_2 = (\epsilon_p - \epsilon_m)[\epsilon_m \mathbf{I} + (\epsilon_p - \epsilon_m)\mathbf{Q}^-]^{-1}\bar{\mathbf{e}}. \tag{3.3.30}$$

By setting $\mathbf{m} = \mathbf{m}_1$ and $\mathbf{m} = \mathbf{m_2}$ in Eq.(3.3.8), the electric fields $\nabla\xi'$ and $\nabla\xi_{\bar{\mathbf{e}}}$ can be determined respectively. The solution to Eq.(3.3.1) and (3.3.2) is given as

$$\nabla\xi' = \nabla\hat{\psi}_{\mathbf{m}_1} \tag{3.3.31}$$

$$\text{and} \qquad \nabla\xi_{\bar{\mathbf{e}}} = -\bar{\mathbf{e}} + \nabla\hat{\psi}_{\mathbf{m}_2}. \tag{3.3.32}$$

In order to determine piezoelectric coefficient defined in the Eq.(3.3.7), we need to calculate $\fint_Y \boldsymbol{\sigma}^{(\bar{\mathbf{e}})}$. We have

$$\fint_Y \boldsymbol{\sigma}^{(\bar{\mathbf{e}})} = (1-\theta)\fint_{Y/\Omega} \boldsymbol{\sigma}^{(\bar{\mathbf{e}})} + \theta \fint_\Omega \boldsymbol{\sigma}^{(\bar{\mathbf{e}})}. \tag{3.3.33}$$

The second term on the right hand side of the Eq.(3.3.33) can be simply determined substituting Eq.(3.3.18), Eq.(3.3.31) and Eq.(3.3.32) into Eq.(3.3.33)

$$\theta \fint_\Omega \boldsymbol{\sigma}^{(\bar{\mathbf{e}})} = -\theta\epsilon_p \mathbb{T}\left(\mathbf{Q}^-\mathbf{m}_1 \otimes \bar{\mathbf{e}}\right) + \theta\mathbb{T}\epsilon_p\left(\mathbf{Q}^-\mathbf{m}_1 \otimes \mathbf{Q}^-\mathbf{m}_2\right). \tag{3.3.34}$$

As the values of the components of the tensor $\mathbf{Q}$ are not constant for the points located outside the inclusion, it is difficult to determine the first integral on the right hand side of the Eq.(3.3.33). Obtaining explicit relations for the effective piezoelectric tensor will not be possible unless we express all volume integrals in terms of the solutions obtained for electric fields inside the inclusion. Therefore, from Eq.(3.3.3), we write

$$\fint_{Y/\Omega} \nabla\xi' = \frac{-\theta}{1-\theta}\fint_\Omega \nabla\xi' = \frac{-\theta}{1-\theta}\mathbf{Q}^-\mathbf{m}_1 \tag{3.3.35}$$

$$\text{and} \qquad \fint_{Y/\Omega} \nabla\xi_{\bar{\mathbf{e}}} = \frac{1}{1-\theta}\left(-\bar{\mathbf{e}} - \theta\fint_\Omega \nabla\xi_{\bar{\mathbf{e}}}\right) = -\bar{\mathbf{e}} - \frac{\theta}{1-\theta}\mathbf{Q}^-\mathbf{m}_2. \tag{3.3.36}$$

We introduce $\nabla\xi^{(1)}_{\bar{\mathbf{e}}}$ and $\nabla\xi'^{(1)}$ such that

$$\nabla\xi_{\bar{\mathbf{e}}} = \left(\fint_{Y/\Omega}\nabla\xi_{\bar{\mathbf{e}}}\right) + \nabla\xi^{(1)}_{\bar{\mathbf{e}}} \qquad \text{for} \quad \mathbf{x}\in Y/\Omega \tag{3.3.37}$$

$$\text{and} \qquad \nabla\xi' = \left(\fint_{Y/\Omega}\nabla\xi'\right) + \nabla\xi'^{(1)} \qquad \text{for} \quad \mathbf{x}\in Y/\Omega, \tag{3.3.38}$$

where

$$\fint_{Y/\Omega}\nabla\xi'^{(1)} = \mathbf{0} \quad \text{and} \qquad \fint_{Y/\Omega}\nabla\xi^{(1)}_{\bar{\mathbf{e}}} = \mathbf{0}. \tag{3.3.39}$$

Substituting Eqs.(3.3.37) and (3.3.38) into Eq.(3.3.33), we have

$$\begin{aligned}(1-\theta)\fint_{Y/\Omega}\boldsymbol{\sigma}^{(\bar{\mathbf{e}})} = (1-\theta)\epsilon_m\fint_{Y/\Omega}\mathbb{T}\left(\nabla\xi'^{(1)}\otimes\nabla\xi^{(1)}_{\bar{\mathbf{e}}}\right) + \\ (1-\theta)\epsilon_m\mathbb{T}\left(\left[\fint_{Y/\Omega}\nabla\xi'\right]\otimes\left[\fint_{Y/\Omega}\nabla\xi_{\bar{\mathbf{e}}}\right]\right).\end{aligned} \tag{3.3.40}$$

We can ignore the first term on the right hand side of the Eq. 3.3.40 and rewrite this equation as

$$(1-\theta)\fint_{Y/\Omega}\boldsymbol{\sigma}^{(\bar{\mathbf{e}})} \approx (1-\theta)\epsilon_m\mathbb{T}\left(\left[\fint_{Y/\Omega}\nabla\xi'\right]\otimes\left[\fint_{Y/\Omega}\nabla\xi_{\bar{\mathbf{e}}}\right]\right). \tag{3.3.41}$$

Substituting (3.3.41), (3.3.34), (3.3.36) and (3.3.35) into (3.3.33), we have

$$\fint_{Y}\boldsymbol{\sigma}^{(\bar{\mathbf{e}})} = \theta(\epsilon_m-\epsilon_p)\mathbb{T}\left(\mathbf{Q}^{-}\mathbf{m}_1\otimes\bar{\mathbf{e}}\right) + \theta\left(\frac{\theta}{1-\theta}\epsilon_m+\epsilon_p\right)\mathbb{T}\left(\mathbf{Q}^{-}\mathbf{m}_1\otimes\mathbf{Q}^{-}\mathbf{m}_2\right). \tag{3.3.42}$$

Equation (3.3.42) can be expressed in terms of $\boldsymbol{\epsilon}^{\text{eff}}$, ϵ_m, ϵ_p and θ. In order to do so, we rewrite Eq.(3.3.6) as

$$-\fint_{Y}\epsilon_{\#}\nabla\xi_{\bar{\mathbf{e}}} = -\fint_{Y}\left(\epsilon_m-\chi_p(\epsilon_m-\epsilon_p)\right)\nabla\xi_{\bar{\mathbf{e}}} = \boldsymbol{\epsilon}^{\text{eff}}\bar{\mathbf{e}}. \tag{3.3.43}$$

Therefore, from (3.3.18),(3.3.31) and (3.3.32) we have

$$\mathbf{Q}^{-}\mathbf{m}_2 = \frac{1}{\theta(\epsilon_m-\epsilon_p)}\left(\boldsymbol{\epsilon}^{\text{eff}}-\epsilon_m\mathbf{I}+\theta(\epsilon_m-\epsilon_p)\mathbf{I}\right)\bar{\mathbf{e}} \tag{3.3.44}$$

$$\text{and} \qquad \mathbf{Q}^{-}\mathbf{m}_1 = -\frac{1}{\theta(\epsilon_m-\epsilon_p)^2}\left(\boldsymbol{\epsilon}^{\text{eff}} - \epsilon_m\mathbf{I} + \theta(\epsilon_m-\epsilon_p)\mathbf{I}\right)\mathbf{p}_s. \tag{3.3.45}$$

Substituting Eq.(3.3.44) and (3.3.45) into (3.3.42), the average stress $\fint_Y \boldsymbol{\sigma}^{(\bar{\mathbf{e}})}$ is expressed in terms of $\boldsymbol{\epsilon}^{\text{eff}}$, ϵ_m, ϵ_p and θ:

$$\fint_Y \boldsymbol{\sigma}^{(\bar{\mathbf{e}})} = -\frac{1}{\epsilon_m-\epsilon_p}\mathbb{T}\left[(\boldsymbol{\epsilon}^*\mathbf{p}_s)\otimes\bar{\mathbf{e}}\right] - \left(\frac{\theta}{1-\theta}\epsilon_m+\epsilon_p\right)\frac{1}{\theta(\epsilon_m-\epsilon_p)^3}\mathbb{T}\left\{(\boldsymbol{\epsilon}^*\mathbf{p}_s)\otimes(\boldsymbol{\epsilon}^*\bar{\mathbf{e}})\right\}, \tag{3.3.46}$$

where

$$\boldsymbol{\epsilon}^* = \left(\boldsymbol{\epsilon}^{\text{eff}} - \epsilon_m\mathbf{I} + \theta(\epsilon_m-\epsilon_p)\mathbf{I}\right). \tag{3.3.47}$$

3.3.2 Elasticity problem

Next, we consider the elastic unit-cell problem (3.3.4). The source term $\boldsymbol{\sigma}^{(\bar{\mathbf{e}})}$ physically can be interpreted as an eigenstress induced by electric fields. It clear that the eigenstress $\boldsymbol{\sigma}^{(\bar{\mathbf{e}})}$ is uniform inside Ω since $\nabla\xi'$ and $\nabla\xi_{\bar{\mathbf{e}}}$ are both uniform on Ω. Further, since $\xi'_{,jj}=0$ and $\xi_{\bar{\mathbf{e}},jj}=0$ in $\mathbb{R}^3\setminus\Omega$, we find that

$$\sigma^{(\bar{\mathbf{e}})}_{ij,j} = \epsilon\xi'_{,ij}(\xi_{\bar{\mathbf{e}}})_{,j}\epsilon\xi'_{,j}(\xi_{\bar{\mathbf{e}}})_{,ij} - \epsilon\xi'_{,jij}(\xi_{\bar{\mathbf{e}}})_{,j} - \epsilon\xi'_{,j}(\xi_{\bar{\mathbf{e}}})_{,ji} = 0 \qquad \text{in} \quad \mathbb{R}^3\setminus\Omega. \tag{3.3.48}$$

Therefore, Maxwell stress is divergence free if restricted to interior or exterior of Ω. Jump on the Maxwell stress over the surface of ellipsoid can be determined substituting Eq.(3.3.28), (3.3.31), (3.3.32) to (3.3.5)

$$\mathbf{t}^{(\bar{\mathbf{e}})} := [\![\boldsymbol{\sigma}^{(\bar{\mathbf{e}})}]\!]\mathbf{n} = \boldsymbol{\sigma}^*\mathbf{n} + p^*\mathbf{n}, \tag{3.3.49}$$

where

$$\boldsymbol{\sigma}^* = (\epsilon_m-\epsilon_p)\mathbb{T}\left[(\mathbf{Q}^{-}\mathbf{m}_1)\otimes(-\bar{\mathbf{e}}+\mathbf{Q}^{-}\mathbf{m}_2)\right] - \epsilon_m\left[(-\bar{\mathbf{e}}+\mathbf{Q}^{-}\mathbf{m}_2)\otimes\mathbf{m}_1 + (\mathbf{Q}^{-}\mathbf{m}_1\otimes\mathbf{m}_2)\right], \tag{3.3.50}$$

and

$$p^* = \epsilon_m(\mathbf{m}_1\cdot\mathbf{n})(\mathbf{m}_2\cdot\mathbf{n}). \tag{3.3.51}$$

If there exist both elastic and dielectric contrast, we need to solve Eq.(3.3.4). We rewrite this equilibrium equation as

$$\operatorname{div}\left(\mathbb{C}^m\nabla\mathbf{u}' - \chi_p(\mathbb{C}^m - \mathbb{C}^p)\nabla\mathbf{u}' + \boldsymbol{\sigma}^{(\bar{\mathbf{e}})}\right) = \mathbf{0}. \tag{3.3.52}$$

Using Eq.(3.3.49), the solution to equilibrium equation (3.3.52) is given as [155]

$$\begin{aligned}\mathbf{u}'(\mathbf{x}) = &-\int_\Omega \left[\nabla_{\mathbf{x}}\mathbf{G}^{\text{elast}}(\mathbf{x}-\mathbf{x}') : \left(\boldsymbol{\sigma}^* + (\mathbb{C}^m - \mathbb{C}^p)\left(\nabla_{\mathbf{x}}\mathbf{u}'(\mathbf{x})\right)\right)\right]\mathrm{d}\mathbf{x}' \\ &+ \int_{\partial\Omega}[\mathbf{G}^{\text{elast}}(\mathbf{x}-\mathbf{x}')\mathbf{n}^*(\mathbf{x}')p^*]\mathrm{d}\mathbf{x}',\end{aligned} \tag{3.3.53}$$

where $\mathbf{G}^{\text{elast}}(\mathbf{x}-\mathbf{x}')$ is the elasticity greens function for isotropic materials and is given as

$$\begin{aligned}\mathbf{G}^{\text{elast}}(\mathbf{x}-\mathbf{x}') = &\frac{1}{16\pi\mu_m(1-\nu_m)|\mathbf{x}-\mathbf{x}'|}\times \\ &\left((3-4\nu_m)\delta_{ij} + \frac{(x_i-x_i')(x_j-x_j')}{|\mathbf{x}-\mathbf{x}'|^2}\right)(\mathbf{e}_i\otimes\mathbf{e}_j),\end{aligned} \tag{3.3.54}$$

where μ_m and ν_m are shear modulus and poisson's ratio of the matrix material. It is not easily possible to solve Eq.(3.3.53) for $\mathbf{u}'$ analytically. This is because existence of the term containing surface integral. This problem is equivalent of the conventional inclusion problem with nonuniform eigenstrain. In order to simplify this equation, we replace p^* with $< p^* >= \frac{1}{S}\int_{\partial\Omega} p^*\mathrm{d}S$, where S is the surface area of the inclusion. Therefore, we identify $\boldsymbol{\Sigma}^* = (\boldsymbol{\sigma}^* + < p^* > \mathbf{I})$ and write Eq.(3.3.49) as

$$\mathbf{t}^{(\bar{\mathbf{e}})} \approx \boldsymbol{\Sigma}^*\mathbf{n} = \left[\boldsymbol{\sigma}^* + \epsilon_m\left((\mathbf{m}_1\otimes\mathbf{m}_2) : (\mathbb{N})\right)\right]\mathbf{n}, \tag{3.3.55}$$

where the tensor $\mathbb{N}$ is defined as

$$\mathbb{N} = \frac{1}{S}\int_{\partial\Omega}[n_i n_j \mathbf{e}_i\otimes\mathbf{e}_j]\mathrm{d}S. \tag{3.3.56}$$

For the ellipsoidal inclusion with principal semi-axes a_1, a_2 and a_3 aligned along $\mathbf{e}_1$, $\mathbf{e}_2$ and $\mathbf{e}_3$ directions, the components of $\mathbb{N}$ are determined as [156]

$$\mathbb{N} = \frac{1}{S} 2\pi (a_1 a_2 a_3)^2 \int_0^\infty \frac{\delta_{ij}(\mathbf{e}_i \otimes \mathbf{e}_j)}{(a_I^2 + t^2)\Delta} \mathrm{d}t, \tag{3.3.57}$$

where summation convention is suppressed for upper case indices and

$$\Delta = \sqrt{(a_1^2 + t^2)(a_2^2 + t^2)(a_3^2 + t^2)}. \tag{3.3.58}$$

For a prolate spheroid with $a_1 = a_2$ and $a_3 > a_1$, we have

$$\mathbb{N} = N_{11}\mathbf{e}_1 \otimes \mathbf{e}_1 + N_{22}\mathbf{e}_2 \otimes \mathbf{e}_2 + N_{33}\mathbf{e}_3 \otimes \mathbf{e}_3, \tag{3.3.59}$$

where

$$N_{33} = N_{22} = \frac{2}{S}\pi (a_1 a_2 a_3)^2 \times \frac{\sqrt{1-k^2}}{2a_3^4 k^2} \times \left[\sqrt{1-k^2} - (1-2k^2)\frac{\sin^{-1} k}{k} \right] \tag{3.3.60}$$

and $$N_{11} = \frac{2}{S}\pi (a_1 a_2 a_3)^2 \times \frac{\sqrt{1-k^2}}{a_1^4 k^2} \left[\frac{\sin^{-1} k}{k} - \sqrt{1-k^2} \right], \tag{3.3.61}$$

and $k^2 = 1 - (\frac{a_3}{a_1})^2$. Therefore, substituting Eq.(3.3.55) into Eq.(3.3.52) we have

$$\mathrm{div}\left(\mathbb{C}^m \nabla \mathbf{u}' - \chi_p (\mathbb{C}^m - \mathbb{C}^p) \nabla \mathbf{u}' - \boldsymbol{\Sigma}^* \right) = \mathbf{0}. \tag{3.3.62}$$

The solution for (3.3.62) is given as

$$\mathbf{u}'(\mathbf{x}) = -\int_\Omega \left[\nabla_{\mathbf{x}} \mathbf{G}^{\mathrm{elast}}(\mathbf{x} - \mathbf{x}') : \left(\boldsymbol{\Sigma}^* + (\mathbb{C}^m - \mathbb{C}^p)\left(\nabla_{\mathbf{x}} \mathbf{u}'(\mathbf{x})\right) \right) \right] \mathrm{d}\mathbf{x}'. \tag{3.3.63}$$

In order to obtain the solution of the Eq.(3.3.63), we define the fourth order auxiliary tensor $\mathbb{S}$ as

$$\mathbb{S} = -\frac{1}{2}(\mathbf{e}_i \otimes \mathbf{e}_n \otimes \mathbf{e}_j \otimes \mathbf{e}_p) \Big(\int_\Omega \left[\frac{\partial^2 G_{ij}^{\mathrm{elast}}(\mathbf{x} - \mathbf{x}')}{\partial x_p \partial x_n} + \frac{\partial^2 G_{nj}^{\mathrm{elast}}(\mathbf{x} - \mathbf{x}')}{\partial x_p \partial x_i} \right] \mathrm{d}\mathbf{x}' \Big). \tag{3.3.64}$$

The tensor $\mathbb{S}$ can be related to so-called Eshelby tensor $\mathbb{S}^{\mathrm{E}}$ by $\mathbb{S}^{\mathrm{E}} = \mathbb{S}\mathbb{C}$ or

$$(\mathbb{C}^{-1})_{qrmn}(\mathbb{S}^{\mathrm{E}})_{ijmn} = \frac{1}{2}\left((\mathbb{S})_{ijqr} + (\mathbb{S})_{ijrq}\right). \tag{3.3.65}$$

It is obvious that tensor $\mathbb{S}$ does not satisfy one of the minor symmetries. Similar to the Eshelby tensor $\mathbb{S}^{\mathrm{E}}$, the components of the auxiliary tensor $\mathbb{S}$ can be determined for ellipsoidal inclusion by substituting Eq.(3.3.54) into Eq.(3.3.64). Reader is referred to the textbooks [152] and [151] for details of the integration of the relation (3.3.64) for elliptical inclusions. We have calculated the tensor $\mathbb{S}$ and listed its components in the *Appendix*. It should be mentioned that, throughout this chapter, we define we define $\mathbb{F}^{-1}$ as the inverse of an arbitrary fourth order tensor $\mathbb{F}$ if $(\mathbb{F}^{-1})_{ijkl} = (\mathbb{F}^{-1})_{jikl} = (\mathbb{F}^{-1})_{ijlk}$ and $(\mathbb{F}^{-1})_{ijkl}(\mathbb{F})_{klmn}\mathcal{A}_{mn} = \mathcal{A}_{ij}$ for any symmetric $\mathcal{A}_{ij}$.

Substituting Eq.(3.3.64) in to Eq.(3.3.63), the linear strain $\boldsymbol{\varepsilon}' = \frac{1}{2}(\nabla\mathbf{u}' + (\nabla\mathbf{u}')^T)$ can be written as

$$\boldsymbol{\varepsilon}' = \mathbb{S}\left(\boldsymbol{\Sigma}^* + (\mathbb{C}^m - \mathbb{C}^p)\boldsymbol{\varepsilon}'\right). \tag{3.3.66}$$

Using the definition given for the inverse of fourth order tensors, the strain $\boldsymbol{\varepsilon}'$ is determined as

$$\boldsymbol{\varepsilon}' = (\mathbb{C}^p - \mathbb{C}^m + \mathbb{S}^{-1})^{-1}\boldsymbol{\Sigma}^{\mathrm{SYM}}, \tag{3.3.67}$$

where

$$\boldsymbol{\Sigma}^{\mathrm{SYM}} = \frac{1}{2}\left(\boldsymbol{\Sigma}^* + (\boldsymbol{\Sigma}^*)^T\right) + \frac{1}{2}\mathbb{S}\,\mathbb{S}^{-1}\left(\boldsymbol{\Sigma}^* - (\boldsymbol{\Sigma}^*)^T\right). \tag{3.3.68}$$

3.3.3 Effective elastic and piezoelectric properties

In this section, we determine the effective stiffness tensor $\mathbb{C}^{\mathrm{eff}}$ and the effective piezoelectric tensor $\mathbb{B}^{\mathrm{eff}}$ for the material shown in the Fig. 3.3. In order to determine effective stiffness tensor defined in the Eq.(3.2.16), we need to solve Eq.(3.2.19). The equation (3.2.19) can be written in following fashion

$$\mathrm{div}\left(\mathbb{C}^m\nabla\mathbf{u}_{\bar{\mathbf{H}}} - \chi_p(\mathbb{C}^m - \mathbb{C}^p)\nabla\mathbf{u}_{\bar{\mathbf{H}}}\right) = \mathbf{0}, \tag{3.3.69}$$

where $\fint_Y \nabla \mathbf{u}_{\bar{\mathbf{H}}} = \bar{\mathbf{H}}$. We define $\mathbf{u}'_{\bar{\mathbf{H}}}$ such that $\nabla \mathbf{u}'_{\bar{\mathbf{H}}} = \nabla \mathbf{u}_{\bar{\mathbf{H}}} - \bar{\mathbf{H}}$. Thus, from Eq.(3.3.69), $\nabla \mathbf{u}'_{\bar{\mathbf{H}}}$ can be determined solving following equation

$$\operatorname{div}\left(\mathbb{C}_{\#}\nabla \mathbf{u}'_{\bar{\mathbf{H}}} - \chi_p(\mathbb{C}^m - \mathbb{C}^p)\bar{\mathbf{H}}\right) = \mathbf{0}. \tag{3.3.70}$$

As $\bar{\mathbf{H}}$ is arbitrary, we set $(\mathbb{C}^m - \mathbb{C}^p)\bar{\mathbf{H}} = \boldsymbol{\Sigma}^{\mathrm{SYM}}$. Substituting this relation into Eq.(3.3.70) yields

$$\operatorname{div}\left(\mathbb{C}_{\#}\nabla \mathbf{u}'_{\bar{\mathbf{H}}} - \chi_p \boldsymbol{\Sigma}^{\mathrm{SYM}}\right) = \mathbf{0}. \tag{3.3.71}$$

The solution to (3.3.71) is given as

$$\frac{1}{2}\left(\nabla \mathbf{u}'_{\bar{\mathbf{H}}} + \nabla \mathbf{u}'^{T}_{\bar{\mathbf{H}}}\right) = \left(\mathbb{C}^p - \mathbb{C}^m + \mathbb{S}^{-1}\right)^{-1} \boldsymbol{\Sigma}^{\mathrm{SYM}}. \tag{3.3.72}$$

Substituting the solution (3.3.72) in to the definition (3.2.16), a linear equation for effective stiffness tensor is derived as

$$\begin{aligned} &\mathbb{C}^{\mathrm{eff}}\bar{\mathbf{H}} = \fint_Y \mathbb{C}_{\#}\nabla \mathbf{u}_{\bar{\mathbf{H}}} = \fint_Y [\mathbb{C}_{\#}(\nabla \mathbf{u}'_{\bar{\mathbf{H}}} + \bar{\mathbf{H}})] = \\ &\bar{\mathbb{C}}\bar{\mathbf{H}} + \theta(\mathbb{C}^p - \mathbb{C}^m)\left(\mathbb{C}^p - \mathbb{C}^m + \mathbb{S}^{-1}\right)^{-1} \boldsymbol{\Sigma}^{\mathrm{SYM}}, \end{aligned} \tag{3.3.73}$$

where $\bar{\mathbb{C}} = \fint_Y \mathbb{C}$. From Eq.(3.3.73), the effective stiffness tensor is determined as

$$\mathbb{C}^{\mathrm{eff}} = \bar{\mathbb{C}} + \theta(\mathbb{C}^p - \mathbb{C}^m)\left(\mathbb{C}^p - \mathbb{C}^m + \mathbb{S}^{-1}\right)^{-1}(\mathbb{C}^m - \mathbb{C}^p). \tag{3.3.74}$$

Substituting Eq.(3.3.67) into Eq.(3.3.7), the effective piezoelectric tensor can be written as

$$\begin{aligned} &\mathbb{B}^{\mathrm{eff}}\mathbf{e} = \fint_Y \left[\boldsymbol{\sigma}^{(\bar{\mathbf{e}})}\right] + \theta \fint_\Omega [(\mathbb{C}^p - \mathbb{C}^m)\nabla \mathbf{u}'] = \\ &\fint_Y \left[\boldsymbol{\sigma}^{(\bar{\mathbf{e}})}\right] + \theta(\mathbb{C}^p - \mathbb{C}^m)\left(\mathbb{C}^p - \mathbb{C}^m + \mathbb{S}^{-1}\right)^{-1} \boldsymbol{\Sigma}^{\mathrm{SYM}}. \end{aligned} \tag{3.3.75}$$

From Eq.(3.3.74) we have

$$\begin{aligned} &\mathbb{B}^{\mathrm{eff}}\mathbf{e} = \\ &= \fint_Y \left[\boldsymbol{\sigma}^{(\bar{\mathbf{e}})}\right] + (\mathbb{C}^{\mathrm{eff}} - \bar{\mathbb{C}})(\mathbb{C}^m - \mathbb{C}^p)^{-1}\boldsymbol{\Sigma}^{\mathrm{SYM}}. \end{aligned} \tag{3.3.76}$$

Substituting Eq.(3.3.46) into (3.3.76), we obtain a linear set of equations which can simply be solved to determine each component of the piezoelectric tensor $\mathbb{B}^{\text{eff}}$

$$\begin{aligned}\mathbb{B}^{\text{eff}}\mathbf{e} &= (\mathbb{C}^{\text{eff}} - \bar{\mathbb{C}})(\mathbb{C}^m - \mathbb{C}^p)^{-1}\boldsymbol{\Sigma}^{\text{SYM}} - \frac{1}{\epsilon_m - \epsilon_p}\mathbb{T}\left[(\boldsymbol{\epsilon}^*\mathbf{p}_s)\otimes\bar{\mathbf{e}}\right] \\ &- \left(\frac{\theta}{1-\theta}\epsilon_m + \epsilon_p\right)\frac{1}{\theta(\epsilon_m-\epsilon_p)^3}\mathbb{T}\left\{(\boldsymbol{\epsilon}^*\mathbf{p}_s)\otimes(\boldsymbol{\epsilon}^*\bar{\mathbf{e}})\right\}.\end{aligned} \tag{3.3.77}$$

The equation (3.3.77) gives us a linear set of equations which can simply be solved to determine each component of the piezoelectric tensor $\mathbb{B}^{\text{eff}}$. The effective piezoelectric tensor depends on the effective electric permittivity tensor $\boldsymbol{\epsilon}^{\text{eff}}$ and effective stiffness tensor $\mathbb{C}^{\text{eff}}$ which can be determined using Eqs.(3.3.44) and (3.3.74), respectively. It is clear from Eq.(3.3.77) that the effective piezoelectric tensor linearly depends on the residual polarization $\mathbf{p}_s$. Also, from Eq.(3.3.42) and (3.3.75), it is obvious that existence of elastic mismatch or dielectric mismatch is necessary condition to have a non-zero piezoelectric coefficient. The effective piezoelectric tensor $\mathbb{B}^{\text{eff}}$ relates electric field to stress and vice versa (see the relation (3.2.33)). We can define third order piezoelectric tensor $^{\text{eff}}$ which can be used to relate electric field to strain and vice versa. The piezoelectric tensor $\mathbf{d}^{\text{eff}}$ is defined as

$$-(\mathbb{C})^{\text{eff}}_{ijkl}(\mathbf{d}^{\text{eff}})_{mkl} = (\mathbb{B}^{\text{eff}})_{ijm} \tag{3.3.78}$$

or

$$(\mathbf{d}^{\text{eff}})_{mij} = -((\mathbb{C}^{\text{eff}})^{-1})_{ijkl}(\mathbb{B}^{\text{eff}})_{klm}. \tag{3.3.79}$$

In what follows, we will use contracted notation and denote d_{333}, d_{311}, d_{111} and d_{133} by d_{33}, d_{31}, d_{11} and d_{13}, respectively.

3.4 Results and discussion

In this section, we use the formulation presented earlier and calculate effective piezoelectric coefficients for the material shown in the Fig. 3.3 in which a prolate spheroid with radii a_1, a_2 and a_3 has been embedded in a matrix material ($a_2 = a_3 < a_1$). Unless otherwise stated we set $\epsilon_m = 2.35\epsilon_0$, $\mu_m = 2.35\epsilon_0$ and $\mu_m = 1$ MPa, $\theta = 0.05$ and $a_1 = 5a_3$. Also,

we assume inclusion is softer than matrix with $\mu_m = 10^3\mu_p$ and $\nu_m = \nu_p$. In addition, we assume the inclusion has the polarization $\mathbf{p}_s = p_s\mathbf{e}_3$. We will change all these material properties and investigate effects of each one of them on the effective piezoelectric coefficients of the material.

We investigate the effect of direction of polarization inside the material on the effective piezoelectric coefficients in the Fig. 3.4. We have set

$$\mathbf{p}_s = p_s\left(\cos(\alpha)\mathbf{e}_3 + \sin(\alpha)\mathbf{e}_1\right), \tag{3.4.1}$$

and plotted different piezoelectric coefficients with respect to the angle α. This figure shows that the d_{31} and d_{33} coefficients are maximum if the polarization is along the $\mathbf{e}_3$ direction. The d_{31} and d_{33} decreases as the polarization direction rotates from $\mathbf{e}_3$ direction toward $\mathbf{e}_1$ direction and these coefficients become zero when residual polarization is perpendicular to the $\mathbf{e}_3$ direction. This result implies that if polarization is along $\mathbf{e}_3$ direction and we apply an external electric field along $\mathbf{e}_1$ direction, we will not observe any piezoelectric effect and the material will behave similar to a conventional dielectric material. A similar results is reported for d_{11} and d_{13} piezoelectric coefficients where these two coefficients are zero at $\mathbf{p}_s = \pm p_s\mathbf{e}_3$ and they peak at $\mathbf{p}_s = \pm p_s\mathbf{e}_1$.

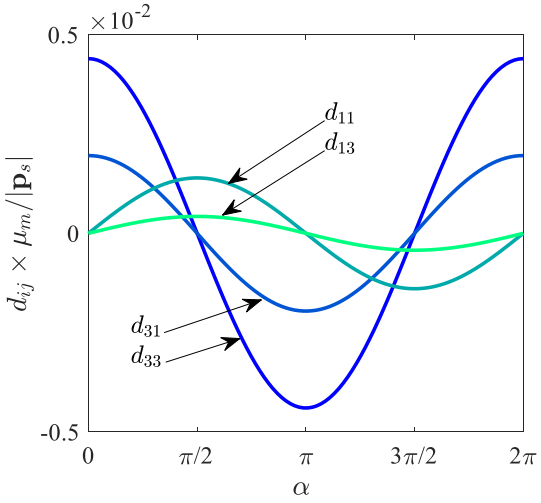

Figure 3.4: Rotation of preexisting dipole and its effect on effective dimensionless piezoelectric coefficients of a composite material with ellipsoidal inclusion.

In addition, Fig. 3.4 shows that d_{33} (resp. d_{11}) piezoelectric coefficient is always greater

than d_{31} (resp. d_{13}) piezoelectric coefficient for all values of α. This implies that the when an electric field is applied along the polarization direction of the material, the first order deformation observed along the polarization direction is always greater than the first order deformation observed along the direction perpendicular to polarization direction of the material. For the rest of this chapter we set $\mathbf{p}_s = p_s\mathbf{e}_3$ and focus on d_{33} and d_{31} coefficients.

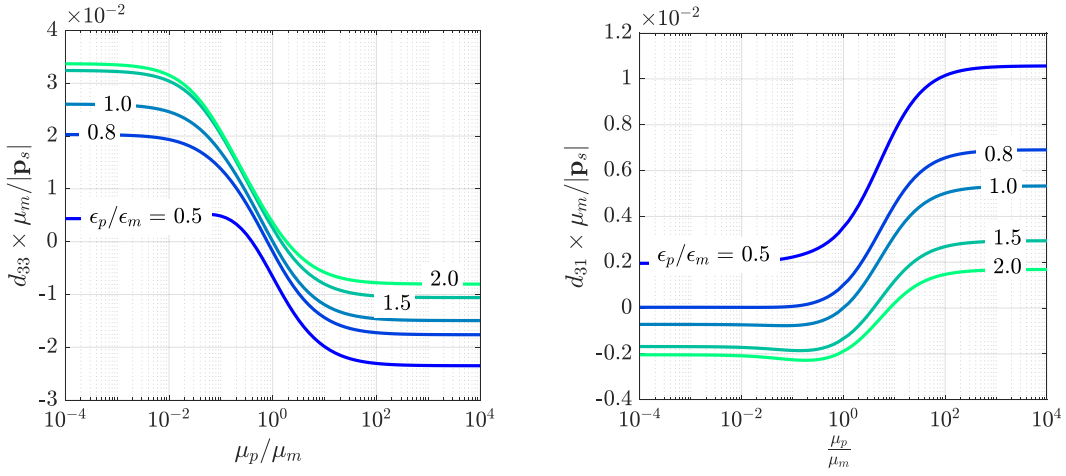

(a) Dimensionless effective d_{33} coefficient.

(b) Dimensionless effective d_{31} coefficient.

Figure 3.5: The effect of elastic contrast on the effective (a) d_{33} and (b) d_{31} piezoelectric coefficients.

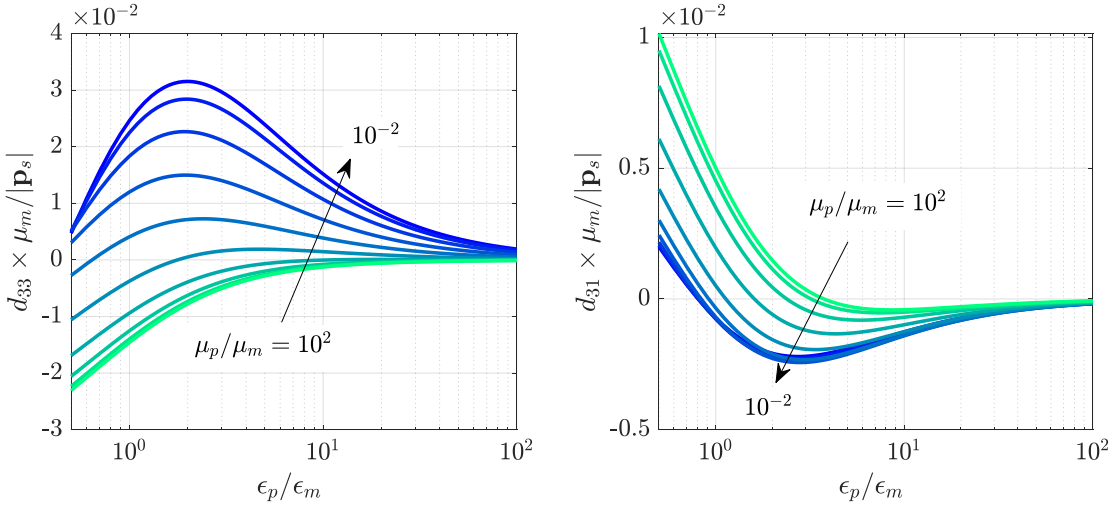

(a) Dimensionless effective d_{33} coefficient.

(b) Dimensionless effective d_{31} coefficient.

Figure 3.6: The effect of elastic contrast on the effective (a) d_{33} and (b) d_{31} piezoelectric coefficients.

Figure 3.5 show the effective piezoelectric coefficients versus ratio of inclusion shear modulus over matrix hear modulus ($\frac{\mu_p}{\mu_m}$) for different ratios of materials electric permittivity $\frac{\epsilon_p}{\epsilon_m}$. We have set the matrix electric permittivity to $\epsilon = 2.35\epsilon_0$ which is equivalent to polypropylene (PP) electric permittivity [107] and plotted piezoelectric coefficients. Note that the electric permittivity of the inclusion cannot be less than vacuum electric permittivity and minimum possible value for electric permittivity ratio is $\frac{\epsilon_p}{\epsilon_m} = 1/2.35 \approx 0.5$. Thus, we have plotted piezoelectric coefficients for $0.5 \leq \frac{\epsilon_p}{\epsilon_m} \leq 2$. We will further study effect of electric permittivity ratio later. Figs. 3.5(a) and 3.5(b) show that in absence of dielectric mismatch ($\frac{\epsilon_p}{\epsilon_m} = 1$) and elastic mismatch ($\frac{\epsilon_p}{\epsilon_m} = 1$) both piezoelectric coefficients d_{31} and d_{33} are zero and as the ratio $\frac{\epsilon_p}{\epsilon_m}$ increases to the values greater than one or decreases to the vale less than one the magnitude of the piezoelectric effect increases. Figure 3.5(a) shows that as the ratio $\frac{\mu_p}{\mu_m}$ increases d_{33} decreases toward negative values while Fig. 3.5(b) shows as the ratio $\frac{\mu_p}{\mu_m}$ increases d_{31} increases toward positive values. Also, Fig.3.5 shows that increasing $\frac{\mu_p}{\mu_m}$ to the values greater than 100 or decreasing it to the values less than 0.01 will not have a considerable impact on the value of the effective piezoelectric coefficients. In addition, Fig. 3.5(a) shows that increasing the ratio $\frac{\epsilon_p}{\epsilon_m}$ from 0.5 to 2 shift d_{33} graph upward and Fig. 3.5(b) shows that increasing the ratio $\frac{\epsilon_p}{\epsilon_m}$ from 0.5 to 2 shift d_{31} graph downward. This means that coexistence of elastic mismatch and dielectric mismatch may intensify or weaken piezoelectric effect. For example, for a composite material composed of a soft inclusion embedded in a hard matrix ($\frac{\mu_p}{\mu_m} \ll 1$), increasing $\frac{\epsilon_p}{\epsilon_m}$ from 0.5 to 0.8 increases d_{33} coefficient and decreases d_{31} coefficient to almost zero. However, if the inclusion is harder than the matrix material ($\frac{\mu_p}{\mu_m} \gg 1$), increasing $\frac{\epsilon_p}{\epsilon_m}$ from 0.5 to 0.8 increases d_{31} coefficient but decreases d_{33} coefficient.

Figures 3.6(a) and 3.6(b) show the effect of dielectric mismatch on the effective d_{31} and d_{33} piezoelectric coefficients, respectively. These figures show that sharp dielectric contrast with a very large value of $\frac{\epsilon_p}{\epsilon_m}$ leads to insignificant piezoelectric effect. Also, these figures show the maximum d_{33} achieved is for a material with $\frac{\epsilon_p}{\epsilon_m} \approx 11$ and soft inclusion in a hard matrix ($\frac{\mu_p}{\mu_m} \leq 10^{-2}$) while the maximum d_{31} piezoelectric coefficient is for hard inclusions embedded in soft matrices where inclusion has small $\frac{\epsilon_p}{\epsilon_m}$ ratio. Based on Fig. 3.5 and 3.6, we can conclude that the material composition that will lead to maximum d_{33} effect is not the

same as the material composition that will lead to maximum d_{31} effects. The formulation we presented here can be used to design materials with optimum desirable piezoelectric effect.

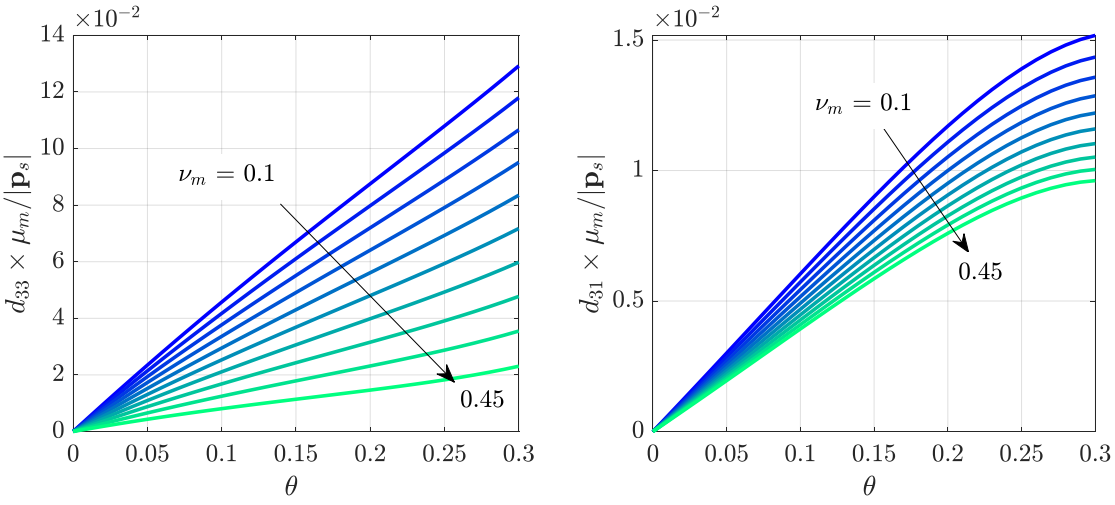

(a) Dimensionless effective d_{33} coefficient.

(b) Dimensionless effective d_{31} coefficient.

Figure 3.7: The effect of inclusion volume fraction and the compressibility of the material on the effective (a) d_{33} and (b) d_{31} piezoelectric coefficients($\frac{\mu_p}{\mu_m} = 10^{-3}$, $\frac{\epsilon_p}{\epsilon_m} = 0.5$, $\nu_p = 0.1$).

The effect of material compressibility on the effective piezoelectric coefficient is studied in the Fig.3.7. We have set the inclusion poisson's ratio to $\nu_p = 0.1$ and plotted d_{31} and d_{33} versus volume fraction for different values of matrix poisson's ratio ν_m in Fig.3.7(a) and Fig. 3.7(b), respectively. It is clear that as volume fraction of inclusion increases piezoelectric coefficients also increase. Also, these figures show that as ν_m increases both d_{31} and d_{33} piezoelectric coefficients. This means that compressibility improves the piezoelectric effect.

Figure 3.8 shows the impact of the spheroid aspect ratio $\frac{a_1}{a_3}$ on the piezoelectric behavior of composite material. We have assumed that the material is composed of a soft inclusion embedded in a hard matrix ($\mu_p/\mu_m = 10^{-3}$). Figure 3.8(a) shows that the magnitude of d_{33} piezoelectric coefficient increases as the aspect ratio increases unless there is no dielectric mismatch in which case the change in the aspect ratio will not have a significant impact on the piezoelectric coefficient. On the other hand, Fig. 3.8(b) shows that the d_{31} piezoelectric coefficient remains almost unchanged as the aspect ratio increases. Fig.3.8 shows that the d_{33} coefficient can be two to three orders of magnitude larger than d_{31} piezoelectric

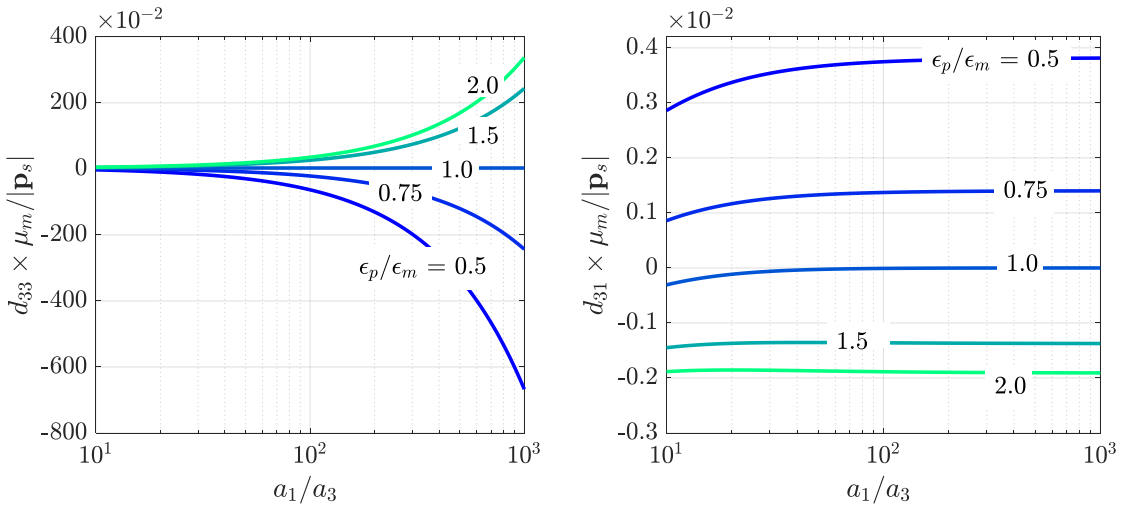

(a) Dimensionless effective d_{33} coefficient.

(b) Dimensionless effective d_{31} coefficient.

Figure 3.8: The effect of inclusion aspect ratio on the effective (a) d_{33} and (b) d_{31} piezoelectric coefficients.

coefficient. This behavior is consistent with experimental measurement of piezoelectric coefficients of charged polymer foams in which d_{33} coefficient has been reported to be two orders of magnitude greater than the d_{31} coefficient [3]. Based on this figure, we can conclude that one simple way to design composite material with large d_{33} piezoelectric coefficient is to use composite material is composed of spheroid inclusions with large aspect ratios.

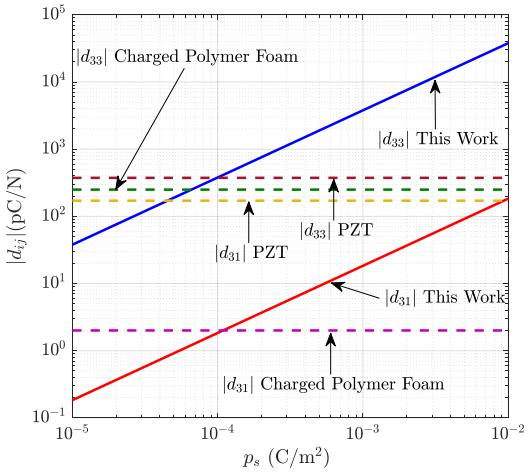

Figure 3.9: Comparison of the effective piezoelectric coefficients of electrets with spheroid inclusions with piezoelectric coefficients of PZT [2] and charged PP polymer foam [3].

The effective piezoelectric coefficient of a composite electret material with spheroid inclusion with $a_1/a_3 = 100$ and $\theta = 0.3$ versus residual polarization $\mathbf{p}_s = p_s\mathbf{e}_3$ has been plotted on Fig.3.9. In addition, we have plotted the piezoelectric coefficients of PZT [2] and a charged polymer foam electret material [3]. This figure shows that for $p_s \approx 10^{-4}$ C/m^2, both d_{31} and d_{33} coefficients of electret material considered in this work are almost equal to piezoelectric coefficient of charged the PP polymer foam. As the residual polarization increases to $p_s \approx 10^{-2}$, d_{31} piezoelectric coefficient of the electret with spheroid inclusion becomes close to that of a PZT material while d_{33} coefficient of the material considered in this work is two orders of magnitude greater than the piezoelectric coefficient of the PZT. This figure shows that electret material with large residual polarization can exhibit giant piezoelectric effect.

3.5 Conclusion

In summary, we used the theory of homogenization for presented by Liu and Sharma [100] in order to find the effective properties of a composite material in which an elliptical inclusion with nonzero electric polarization embedded in a matrix material. We analytically calculated effective electric permittivity tensor and stiffness tensor for this material. In addition, we presented close form solution for the effective piezoelectric tensor of the material in presence of both elastic mismatch and dielectric mismatch. We thoroughly investigated effect of all material properties on piezoelectric coefficients of the material. We showed that both elastic mismatch and dielectric mismatch can lead to a piezoelectric effect but these two may act against each other and weaken piezoelectric effect of the material. In addition we showed that effects of different material properties of constituent on different piezoelectric coefficients are not the same.

3.6 Appendix

3.6.1 The components of auxiliary Eshelby tensor $\mathbb{S}$ for a unit cell with ellipsoidal inclusion.

The integration of Eshelby tensor has been explained in the Eshelby's original paper [154] and the textbooks [151] and [152]. We have followed the same approach as explained in the [151] and calculated component of auxiliary Eshelby tensor $\mathbb{S}$ defined in Eq.(3.3.64). The components of $\mathbb{S}$ for an ellipsoidal inclusion is given as

$$\mathbb{S}_{1111} = C_A \left(\frac{C_B}{C_A} - 2\right) I_1 - 3C_A a_1^2 I_{11}, \tag{3.6.1}$$

$$\mathbb{S}_{1122} = C_A \left(I_1 - a_2^2 I_{12}\right), \tag{3.6.2}$$

$$\mathbb{S}_{1212} = C_A \left(-\frac{C_B}{2C_A} I_2 - \frac{1}{2} a_1^2 I_{12} - \frac{1}{2} a_2^2 I_{12} + \frac{1}{2} I_1\right) \tag{3.6.3}$$

and

$$\mathbb{S}_{1221} = \frac{C_A}{2} \left(I_2 - a_1^2 I_{12} - \frac{C_B}{C_A} I_1 - a_2^2 I_{12}\right), \tag{3.6.4}$$

where C_A and C_B are constants related to material properties of the matrix material and are defined as

$$C_A = -\frac{1}{a 6\pi \mu_m (1 - \nu_m)} \tag{3.6.5}$$

and

$$C_B = -\frac{1}{4\pi\mu_m} + \frac{1}{16\pi\mu_m(1-\nu_m)}, \tag{3.6.6}$$

and $I_{i,j}$ are elliptical integrals defined in Eq.(3.3.20) and (3.3.21). All other components of the tensor $\mathbb{S}$ can be obtained by permutation of $(1, 2, 3)$ indices.

Chapter 4

Giant Magnetoelectricity in Soft Materials Using Hard Magnetic Soft Material

Imagine a material that will produce electricity via a contactless, wireless signal. Further, we hope that this material is capable of large deformation reminiscent of soft robots and is soft enough to conform to irregular or curved geometries. This would all be possible if soft magnetoelectric materials were available; paving the way for applications such as remote drug delivery, energy harvesting, soft robots, multiple state memories among others. Here, for the first time, using the concept of hard magnetic soft matter in combination with electrets, we design and create a soft magnetoelectric material that exhibits an extremely strong, self-biased magnetoelectric effect. Further, using programmable pattern of deposition of magnetic dipoles and charges, we report a giant magnetoelectric coefficient in an ultra-soft deformable material that retains its strength even under infinitesimal external fields and at low frequencies.

4.1 Introduction

The magnetoelectric (ME) property is rare in single phase (natural) materials and restricted to certain hard exotic crystals that satisfy a stringent set of material symmetry constraints [157, 158, 159]. An alternative approach is to create artificial ME materials using composites of piezoelectric and magnetostrictive materials [160, 161, 162, 163, 164]. While such composites may exhibit significant magnetoelectricity [165, 166, 167], they are typically *hard* brittle materials and often painstakingly fabricated and frequently contain environmentally toxic materials such as lead. Even polymer based ME composites (in particular PVDF and its copolymers) which are regarded as lead-free, flexible and light weight class of ME composites, are not suitable candidate for applications in soft robotics, biology

and medicine due to several reasons: First, truly *s*oft ME composite do not exist! Even flexible PVDF based ME composites have elastic modulus on the order of several GPa and, therefore, are not really soft. Second, an *external* DC bias-field is often necessary to achieve an appreciable ME coupling in composites and this renders the resulting devices quite bulky and hinges on the integration of electronics [168]. We emphasize that the magnetoelectric coefficient α of such materials (which embodies the strength of the interconversion between electrical and magnetic fields) is directly proportional to the externally applied magnetic field h^e, and thus becomes negligible for small fields unless a pre-existing DC bias magnetic field is present. Finally, ME composites exhibit strong coupling only at high frequencies rendering them unsuited for wireless energy transfer for implantable medical devices where high frequency magnetic field may cause safety issues [169]. Examples of low frequency application includes targeted drug delivery [170], brain stimulation [171], and tissue regeneration [172].

Recently, we have made some progress in creating soft ME materials based on silicone rubber by exploiting the so-called Maxwell stress effect and electrets [145, 144]. While the fabricated materials were indeed mechanically soft, the magnetoelectric coefficient was modest especially under weak magnetic fields (and thus shares the same disadvantage as ME composites in that the magnetoelectric coefficient depends linearly on the external applied field ($\alpha \propto h^e$)).

In this work, however, we make a significant breakthrough. We use the concept of hard magnetic soft matter [173, 25, 174] and electrets (–referred in the following as hard magnetic soft electrets–HMSE). HMSEs are soft materials in which magnetically hard micro particles and electric charges and dipoles are embedded in a way to exhibit non-uniform magnetic field strain (See Fig. 4.1). The electrets provide the basis for an apparent piezoelectric-like behavior. As our theoretical work shows (see *Methods* and *Supplementary Information (SI) Section*), in this concept, the mechanical strain ε is linearly proportional to magnetic field $\varepsilon \propto B^r h^e$ and the magnetoelectric coefficient of these materials becomes independent of the externally applied magnetic field($\alpha \propto q_0 B^r$). Here, B^r is the residual magnetic flux density due to hard-magnetic particles and q_0 is the electret charge density. Therefore, HMSEs can enable extremely large ME coupling coefficient even under extremely small magnetic fields

and there is no need for a DC bias field.

We show that guided by a rigorous theoretical and computational framework, HMSEs with giant ME voltage coupling coefficient $\alpha_{\mathrm{ME}}^{\mathrm{eff}} \geq 1$ can be designed and fabricated in a rather facile manner. Indeed, the fabrication scheme for the HSMEs is accomplished at low temperatures and amenable for small scale and miniaturized applications. We remark that any soft dielectric material can be used to as the basis for the HSMEs e.g. rubber. As we demonstrate, the ME effect can be designed (even optimized) by modifying the arrangement of electric charges/dipoles or altering the alignment of magnetic particles inside the material. Specifically, for a system made of an electret polytetrafluoroethylene (PTFE) thin film layered with micro-hard-magnetic particle embedded silicone rubber, we demonstrate a room temperature ME voltage coupling coefficient of 332.7 $\mathrm{mVcm^{-1}Oe^{-1}}$ at low frequency (1Hz) and zero bias field. Finally, upon programmed patterned magnetic dipoles (guided by theory), under flexure deformation mode, we are able to report a giant ME voltage coupling coefficient of 15.36 $\mathrm{Vcm^{-1}Oe^{-1}}$ at resonance frequency of 6 Hz in an elastically uniform material with elastic modulus of 55 KPa. To the best of our knowledge, this is the only soft material fabricated so far which exhibits a "giant" ME effect. In fact, the ME coupling coefficient of our fabricated material is even comparable to the highest values reported in the literature for polymer based ME composite but with the caveat that our material is extremely soft (capable of large deformation), operable at low frequencies and no bias field is required(see Table-1 and Figure S1 in the *SI* for a comparison to other material systems.)

4.2 Results: Emergent magnetoelectricity in tension-compression deformation mode

The materials preparation is described in *Methods*. In the simplest design, HMSE is composed of two disc shape layers. One layer consists of a neodymium-iron-boron microparticles(NdFeB) in the soft rubber (Ecofelx-0010) which we refer to as NMISR and the second one is polytetrafluoroethylene(PTFE) thin film sandwiched between two mechanically compliant electrodes(see inset of Fig. 4.2a and Fig. S2). A layer of surface charge

was deposited onto one surface of the PTFE thin film by the corona charging technique to create the electret. PTFE is known to be better for electret charge stability [175] . In addition, since PTFE is no ferromagnetic, it hardly deforms under a magnetic field, while a nonzero strain is developed in NMISR layer in response to an applied magnetic field. This non-uniform deformation is vital to the appearance of a electromechanical response in the material(see Eq. S8 in the SI). In order to compare the behavior of HMSEs with previously developed Soft Magnetic Soft Electrets (SMSEs) [176], we also fabricated and examined a SMSE sample by attaching a soft magnetoactive rubber to a charged PTFE layer. The soft magnetoactive rubber which is denoted by IMISR is a mixture of iron microparticles and soft rubber (see *Methods* for details on fabrication of SMSE samples).

Our theoretical results show that an application of external magnetic field to HMSE will lead to expansion (resp. contraction) of NMISR along the thickness direction if applied field is in the same (resp. opposite) direction of the residual magnetic field, while PTFE layer remains almost undeformed. This non-uniform deformation alters the electric field inside the material which, under short circuit boundary condition, leads to the transfer of electric charges from one electrode to the another. This magnetic field induced transfer of charges can be interpreted as the ME effect. We have experimentally measured electric output charges generated as result of an AC magnetic field with frequency of 1 Hz applied to both HMSE and SMSE samples. The output charge versus time is plotted in the Fig. S3. Measured output charges are used to calculate the ME voltage coupling coefficient of material using the relation $\alpha_{\mathrm{ME}}^{\mathrm{eff}} = \frac{\partial(\Delta Q)}{C^{\mathrm{eff}} H \partial h^e}$, where ΔQ, H and C^{eff}, respectively, are the total output charges, total thickness and the effective capacitance of the material. The values of $C^{\mathrm{eff}} = 44.4$ pF and $C^{\mathrm{eff}} = 34.5$ pF have been experimentally measured for both HMSE and SMSE samples. Figure 4.2a shows the voltage coupling coefficient of two samples for different magnetic fields. This figure also illustrates that the voltage coupling coefficient of the SMSE is linearly proportional to the magnetic field and more importantly it vanishes at zero magnetic field (as expected). Therefore, SMSEs are similar to conventional ME composites, and show an exceedingly weak response for modest magnetic fields. This necessarily implies that a DC bias magnetic field has to be used to increase the sensitivity of SMSEs. On the contrary, $\alpha_{\mathrm{ME}}^{\mathrm{eff}}$ of HMSE is constant with respect to external magnetic

field, and is experimentally measured to be around 204 mV $cm^{-1}Oe^{-1}$, which is significant for practical applications [177]. As evident from the figure, our theoretical prediction of ME voltage coupling coefficient is consistent with experimental results (details of the theoretical approach is in the *Methods* section and *SI*). The mechanistic underpinnings for the distinct behavior of HMSEs compare to SMSEs and ME composites is further highlighted in the Fig. S4 where we illustrate strain versus applied magnetic field for NMISR, IMISR and magnetostrictive samples. We note a linear relationship between strain and external magnetic field for NMISR which is consistent with theoretical predictions (see *SI*). However, magnetic field induced strain in ME composites and SMSE vary quadratically with the external magnetic field. As a result, output charge in SMSEs and ME composites depends quadratically on the external field. This behavior is also obvious from Fig. S3 where frequency of output charge in HMSE is the same as the frequency of external field while in SMSEs, the frequency of output charge is twice as large as the applied field. The linear relationship between external magnetic field and output charges for HMSE is shown in the Fig. S5. As a result, the ME voltage coupling coefficient, which is the derivative of output charge with respect to magnetic field, is independent of external field in HMSEs.

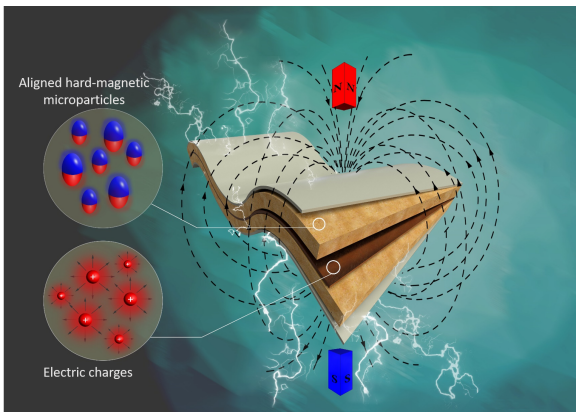

Figure 4.1: A schematic illustration of HMSE composed of two layers of dielectric material(s) with a layer of embedded charges at the interface (charge layer shown with dark brown color).

According to our theoretical predictions (see *SI*), $\alpha_{\mathrm{ME}}^{\mathrm{eff}}$ can be improved by either increasing surface charge density or increasing residual magnetic flux density in the materials. Experimental results for these two strategies, respectively, are shown in Fig. 4.2b and Fig.

S6. As we can observe from Fig. 4.2b, $\alpha_{\mathrm{ME}}^{\mathrm{eff}}$ monotonically increases as the interface charge density of two layers increases. The linear dependence of $\alpha_{\mathrm{ME}}^{\mathrm{eff}}$ on the interface charge density is in agreement with theoretical prediction (S8). The maximum surface charge density we are able to achieve experimentally is $\approx$2 mC/m^2 and the maximum ME voltage coupling coefficient we have achieved with this design of HMSE is 332.7 mV cm^{-1}Oe^{-1}. This value was measured at a very small frequency of 1 Hz. This result proves that HMSE materials can can exhibit very strong ME effect in weak magnetic fields and under very small frequencies without the need for a DC bias magnetic field. To the best of our knowledge, this is the first known soft material with such a compelling magnetoelectric effect without a DC bias magnetic field. Finally, in Table-1 and Fig. S1 (*SI*), we may note that the ME effect of our fabricated material at such small frequency is comparable to the highest self biased ME voltage coupling coefficient achieved with polymer based ME composites.

4.3 Flexure deformation mode and "giant" magnetoelectricity

In the design of HMSE presented in the preceding section, the ME effect is mediated by tension and compression deformation of the material. Since non-uniform deformation is necessary to generate a piezoelectric like effect in electret materials, having a hard layer in the structure of HMSE (which hardly deforms with respect to the magnetoactive layer) is essential to achieve ME effect in the previous design for compression/tension. This stiffens the overall material somewhat (although the material is still *relatively* soft compared to other contenders like composites). However, the manifestation of electromechanical coupling in electret materials is not just restricted to compression/tension [178, 179]. In a flexure mode, electrets can exhibit a large electromechanical effect regardless of whether they are elastically uniform (or not). The flexure deformation mode is also important because resonance frequency in bending deformation is much smaller than compression. Finally, we can theoretically show that in HMSEs designed in the tension and compression mode, we have $\alpha_{\mathrm{ME}}^{eff} \propto B^r q_0$ and for HMSEs designed for the flexure mode, we have $\alpha_{\mathrm{ME}}^{eff} \propto ARB^r q_0$ (see *SI*), where AR is the structural aspect ratio (typically greater than 10). Therefore, bend-

ing induced ME effect is at least one order of magnitude larger than tension/compression induced effect.

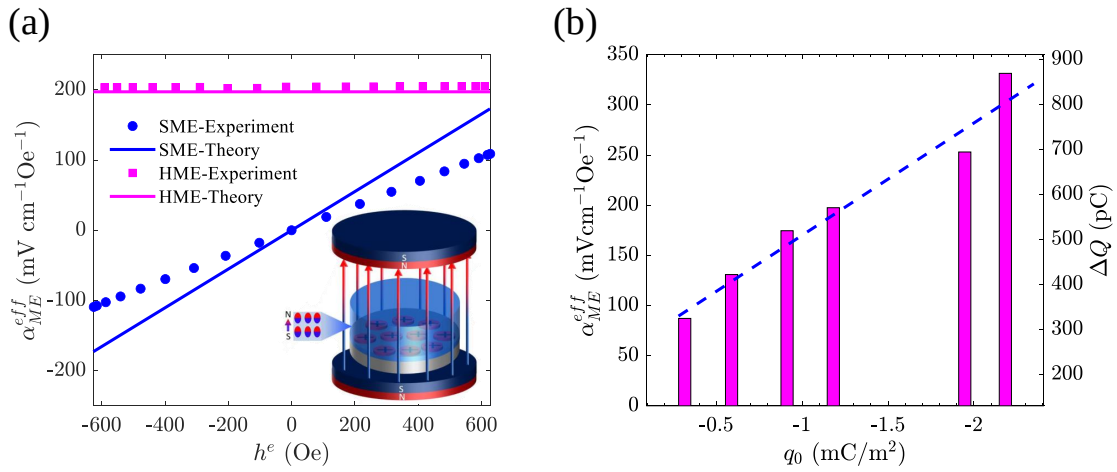

Figure 4.2: (a) The ME voltage coupling coefficient of HMSE and SMSE measured at different magnetic fields. (b) The ME voltage coupling coefficient of different HMSEs with different interfacial charge densities measured at $h^e = 627$ Oe.

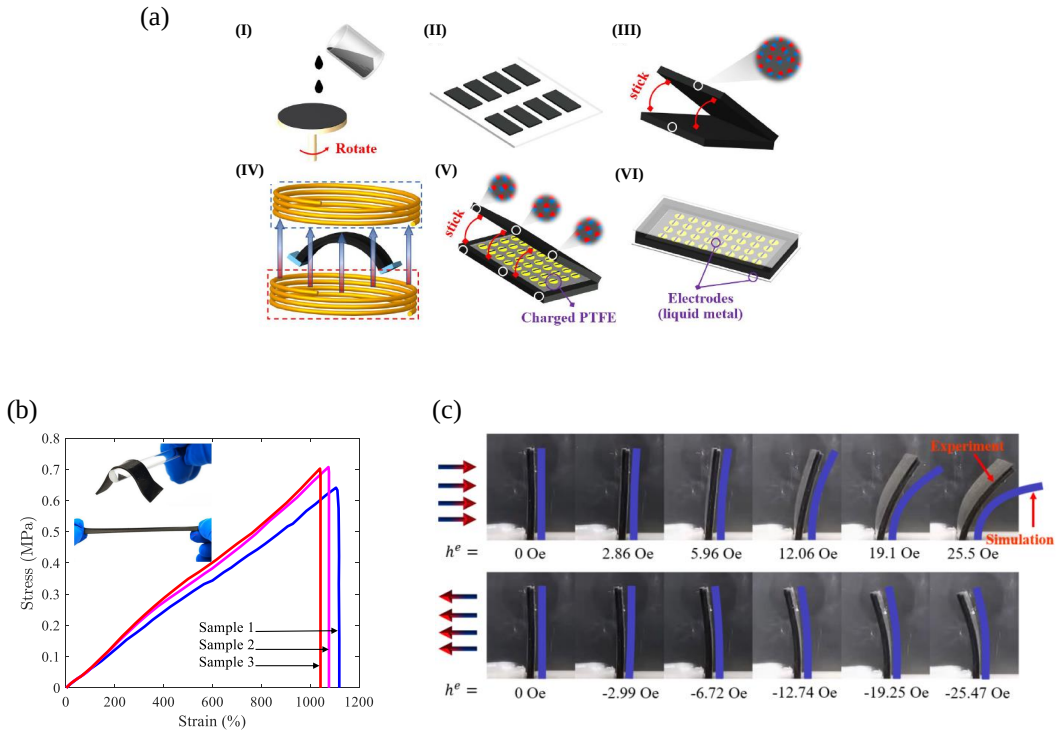

Figure 4.3: (a) Steps of creating PHMSE. (b) Stress-strain graph of three PHMSE samples. (c) Comparison of experimental and numerical simulation results for deformation of PHMSE under different static magnetic fields.

While it is difficult to achieve magnetic field induced bending deformation in SMSE materials, hard magnetic materials can be programmed to undergo any form of deformation in response to applied magnetic field [180]. This provides an extensive design space for designing HMSEs with desirable deformation and enhanced ME property. To demonstrate this, we create a programmed HMSE (–abbreviated as PHMSE) which is designed to exhibit bending deformation in response to an applied magnetic field.

Fig. 4.3a represents the steps for creating PHMSE (with further details in *Methods*). The shape programmability in PHMSEs is achieved by deforming the material in the magnetization step (4.3a step IV). Thus, we bend and fix the double-layer magnetoelastomer and apply a magnetic filed as high as 1.2T to the material which leads to alignment of microparticles along the applied field. Due to the high coercivity and high residual magnetic flux density of NdFeB micro particles, after alignment, the magnetization profile remains stable even after the magnetic field has been turned off. Once the magnetization magnetic field is removed and the deformation is reversed, the magnetic micro particles which are anchored to matrix material rotate as the material element rotates. The residual flux density achieved is $B^r = 0.0767$. The profile of the residual flux density has been theoretically calculated in Eq.(4.4.2). The material has dimensions $22 \times 12 \times 1.85$ mm, C^{eff} =6.40 pF and $q_0 = 0.0488$ mC/m^2 unless otherwise stated. We remark that since the thickness of PTFE is negligible compare to thickness of the overall material, overall the material is essentially uniform elastically. The softness of the fabricated material may be readily (and visually) appreciated from Fig. 4.3b. In addition, Fig. 4.3b shows the stress-strain response of the material indicating that the material can be stretched more than 10 times its size (– its elastic modulus is roughly 55 KPa).

We show the deformation behavior of PHME under a uniform DC magnetic field in Fig. 4.3c. As a uniform vertical field is applied to material, the magnetic particles tend to align themselves along the applied external field. The alignment of the particle occurs by deformation of the material as these hard-magnetic particles are anchored to the material points. Therefore, the whole material bends in response to applied magnetic field. The curvature of the material increases as the magnetic field increases (Fig. 4.3c). The deformation is asymmetric with respect to the magnetic field since the residual field is not symmetric with

respect to neutral axis of the beam. In addition to experimental results, we have also used numerical computation of our nonlinear fully coupled electro-magneto-mechanical theory to study the behavior of PHMSEs (see *Methods* and *SI* for details on the computational approach). As evident from Figure 4.3c, our numerical results are in good agreement with experimental results.

We measure frequency response of the PHMSE by applying an AC external magnetic field to the PHMSE. Figure 4.4a shows the ME voltage coupling coefficient and the output charge of the PHMSE in response to an external magnetic fields with amplitude of 12 Oe and the frequency of 1-10Hz. As fully anticipated by our theory, no ME effect is in evidence if the sample is not charged. The resonance frequency of PHMSE is near 6 Hz where the output charge reaches its peak value. At the peak point, we obtain a giant ME voltage coupling of $\alpha_{\mathrm{ME}}^{\mathrm{eff}} \approx 11.2$ V cm^{-1}Oe^{-1}. We emphasize that we obtain this extraordinarily large ME effect at low frequency and without any external DC bias field. The effect of the magnitude of the applied AC magnetic field on the ME coupling of the material is shown in Fig. 4.4b which illustrates that the output charge increases linearly with increase of amplitude of external field and ME voltage coupling coefficient of the material remains almost unchanged. This implies that our fabricated PHMSEs can exhibit giant ME coupling at extremely weak magnetic fields.

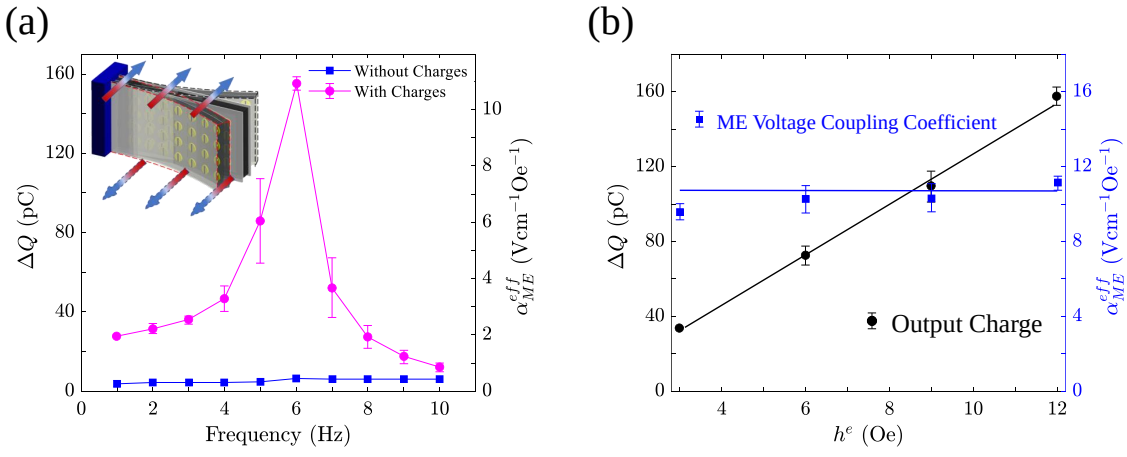

Figure 4.4: (a) ME voltage coupling coefficient and output charge for charged PHMSE and non-charged sample under different frequencies ($h^e = 12$). (b) The ME voltage coupling coefficient and output charge of PHMSE at resonance.

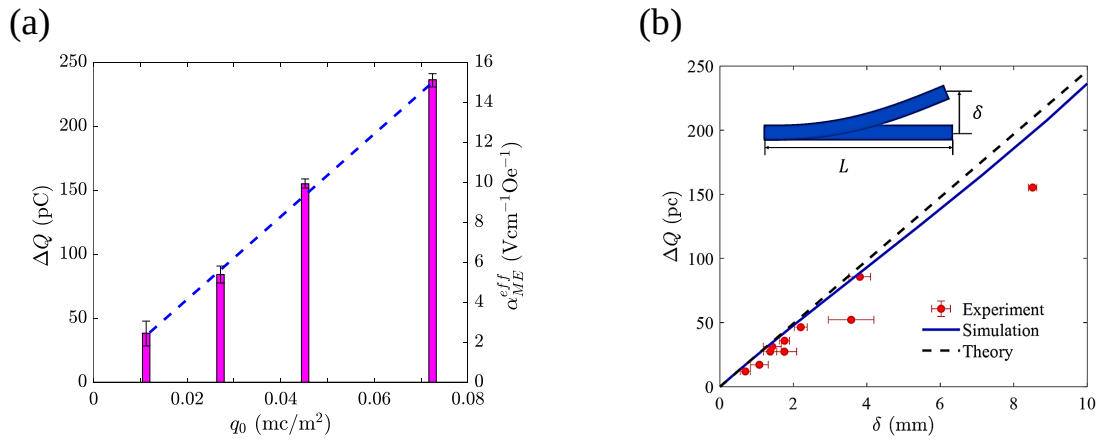

Figure 4.5: (a) Effect of interfacial surface charge density on the ME voltage coupling coefficient and output charge of PHMSE under AC magnetic field with the frequency of 6 Hz and amplitude of 12 Oe. (b) the deflection versus output charge.

Similar to HMSEs, the $\alpha_{\mathrm{ME}}^{\mathrm{eff}}$ of PHMSEs can be further increased by increasing charge density. Fig. 4.5a reveals there is a linear relationship between interface surface charge density and the voltage coupling coefficient of the material. As charge density increases, ΔQ and $\alpha_{\mathrm{ME}}^{\mathrm{eff}}$ increase. We have been able to achieve a value of $\alpha_{\mathrm{ME}}^{\mathrm{eff}} = 15.36$ Vcm $^{-1}$Oe^{-1} when the static charge density is equal to 0.078 mC/m^2. To the best of our knowledge, this is the first soft material created with giant ME voltage coupling. This is one of the largest self biased ME voltage coupling coefficients even when compared with polymer based ME composites (see Table-1 and Fig. S1).

The PHMSEs are not mechanistically different from HMSEs in this sense that their ME effect is strain mediated. The trends seen in the output charge behavior of PHMSE follows exact the trends as seen for deflection (see Fig. S7 and 4.4a). Any two external stimuli which result in the same deformation will lead to same electric signal. To better show this insight, the deflection versus output charges obtained from experimental observation is shown in Fig. 4.5b. The experimental results have been obtained by applying magnetic fields with different frequencies but the same amplitude. In addition, we also plot the deflection versus output charge obtained from our numerical simulations conducted for the static condition in which different deflections obtained by applying magnetic field with different magnitudes. We remark that we have previously shown that, for an electret under pure symmetric

bending, the output charges can be determined as $\Delta Q = A\frac{1}{4}q_0 H\kappa$, where A, H and κ are, respectively, surface area of the electrode, thickness of the material and curvature of the material. We can use this relation for cantilever beam to obtain a rough analytical relation between curvature and output charge. Curvature of a cantilever under pure bending can be roughly approximated as $\kappa = \frac{2\delta}{L^2}$, where δ is the tip deflection and L is the length. Therefore, the output charge may be roughly approximated as $\Delta Q = Aq_0 H\frac{\delta}{2L^2}$. This relation has been used in Fig. 4.5b to make a closed-form analytical prediction. Interestingly, despite the obvious approximations, we obtain a very good agreement between experimental, analytical and numerical results in Fig. 4.5b. From this, we arrive at two conclusions: First, the ME effect in PHMSEs is strain mediated. Second, the relation $\Delta Q = A\frac{1}{4}q_0 H\kappa$ can be used to obtain a reasonably good approximation for charge curvature relationship and electret materials can be used as a soft curvature sensor (for instance, in the context of biomedical applications).

4.4 Methods

4.4.1 Fabrication of disk shape HMSEs and SMSEs

The NMISR is prepared by mixing NdFeB microparticles with silicone elastomer(Ecoflex 00-10) at prescribed weight fraction (NdFeB particles: Ecoflex00-10=1:1). The mixture is poured into a mold to obtain desired geometry and the cured at 80°C for 10 min. The final disk shape NMISR has the diameter of 40 mm and thickness of 1 mm (Fig. S2). A nonzero residual flux density is achieved in the material by applying a magnetization field with magnitude of 1 T. The magnitude of residual flux density of NMISR layer is $B^r = 0.058$T and its direction is align with the thickness direction of the material. The NMISR layer is attached to a disk shape PTFE layer with the thickness of 30 μm and the same thickness as NMISR layer. Before bonding two layers together, a layer of electric charges is deposited onto one surface of the PTFE thin film by the corona charging technique (Fig. S8). During the corona charging, a voltage difference of 5.7 kv is applied between the conductive needle and the grid (see (Fig. S8) which leads to ionization of air and movement of charges toward PTFE layer. The surface charge density of PTFE layer q_0 is measured by measuring the

electric potential on the surface of the PTFE layer V_s using an electrostatic voltmeter (TRek MODEL P0865). The V_s and q_0 are related through

$$q_0 = \frac{\epsilon^{\text{eff}} V_s}{H}, \tag{4.4.1}$$

where ϵ^{eff} is the effective electric permittivity of the material. Unless otherwise stated, the surface charge density achieved for all samples was $q_0 = -1.95$ mC/m^2.

4.4.2 Fabrication of PHMSE

The steps for fabrication of PHMSE is illustrated in the Fig. 4.3. In the first step, we mix the NdFeB particles with silica gel (Ecoflex 0020) in equal proportion to obtain the turbid solution. Thin magnetoactive elastomers is prepared by centrifugal suspension coating. Then, by cutting, and stick the two layers of magnetic elastomers together, we obtain double layer magnetoactive elastomers with size of the $22 \times 12 \times 1.85$ mm. At this stage, the magnetic particles inside the material are randomly oriented and overall residual magnetic field of the material is zero. In order to program the material in a way that it bends in response to external magnetic field, we bend the material and place it in a magnetic field with magnetic flux density of 1.2 T. The radius of curvature is 11.14 mm. After removal of the magnetic field, the bending deformation is reversed. Using the model presented by Rivlin [103] for the flexure of rectangular incompressible block, the profile for residual magnetic flux density in the material is determined as [178, 180]

$$\widetilde{\mathbf{B}}^r = \mathbf{F}_{\text{b}}^{-1} \left[-B^r \cos\left(\frac{(2Y - L)\alpha}{L} \right) \mathbf{e}_r + B^r \sin\left(\frac{(2Y - L)\alpha}{L} \right) \mathbf{e}_\theta \right], \tag{4.4.2}$$

where $\mathbf{F}_{\text{b}}$ is the deformation gradient for the bending deformation of the rectangular block. Also, L represents length of the block(beam) and $0 \leq Y \leq L$. In addition, B^r is the magnitude of the residual magnetic flux density α is the bending angle applied in the magnetization step. Unless otherwise stated, $B^r = 0.0767$ and $\alpha = 52^\circ$. Next, we debond two layers of the material from each other and a charged PTFE layer between two layers of magnetoactive elastomer and bond three layers together. The charge density of the interface

is $q_0 = -0.048$ mC/m^2 unless otherwise stated. Finally, we coat the sample surface with liquid metal as electrode.

Measurement of material properties

Electroforce 3230 - TA testing machine is used to perform uniaxial testing and determine Young's modulus of the material. The effective capacitance of the material C^{eff} is determined using an impedance analyzer(Keysight E4990A, America). The relation $C^{\text{eff}} = \epsilon^{\text{eff}} A/H$ is used to determine the effective dielectric properties ϵ^{eff} of the material, where H is the thickness of the material and A is the surface area. Also, the reidual magnetic flux density B^r is related to magnetization M^r with the relation $B^r = \mu_0 M^r$. The magnetic hysteresis loop($h^e - M^r$) was plotted by Vibrating Sample Magnetometer MPMS-squid VSM-094. Figure S9 shows the magnetic hysteresis loop for hard magnetic particle and soft magnetic particle.

Measurement of the magnetic field induced deformation and the output charges

A customized solenoid is used to generate AC magnetic field. Unless otherwise stated, magnetic field with amplitude of 627 Oe and frequency of 1 Hz is used for disk shaped HMSEs and magnetic field with amplitude of 12 Oe and frequency of 6 Hz is used to study PHMSEs. The magnetic field induced deformation is measured using a Laser Scanning Vibrometer (Polytec OFV-5000, Germany). The output charge of the material is measured using a charge amplifier(Bruel & Kjaer 2692, Denmark). The measurement equipment and diagram are shown in the Figs. S10 and S11, respectively.

4.4.3 Theoretical modeling of the HMSEs

We use energy formulation to derive governing equations for magneto-electro-elastic behavior of a HMSEs. The distinction between reference configuration Ω_R and current configuration Ω is essential for capturing electro-mechanical coupling in the electret materials theoretically. Therefore, conventional linear elasticity models are unable to capture ME effect in the HMSEs and we have to use a nonlinear coupled formulation. Based on

the principle of minimum free energy, the equilibrium state of the system is the state that minimizes free energy of the system. Using the deformation $\boldsymbol{\chi}$ and the polarization $\mathbf{p}$ as two independent thermodynamic variables, We express free energy of the system as

$$\mathcal{F}[\boldsymbol{\chi}, \mathbf{p}] = \int_{\Omega_R} W^{\text{elast}} + \int_{\Omega} \frac{|\mathbf{p}|^2}{2(\epsilon - \epsilon_0)} + \int_{\Omega} \frac{\epsilon_0}{2} |\mathbf{e}|^2 - \int_{\Omega_R} \mathbf{F}\widetilde{\mathbf{B}}^r \cdot \mathbf{h}^{\text{e}}, \tag{4.4.3}$$

where ϵ, ϵ_0 and $\mathbf{h}^{\text{e}}$ are, respectively, electric permittivity of the material, electric permittivity of the vacuum and external magnetic field. Also, W^{elast} denotes elastic energy density of the material and $\mathbf{F}$ is the deformation gradient tensor. Our theory is based on the premise that the equilibrium state of the system must satisfy the Maxwell equation. The Maxwell equation for a material with charge density ρ_e in the current configuration is expressed as

$$\text{div}\,(\epsilon_0 \mathbf{e} + \mathbf{p}) = \rho_e \qquad \text{in} \quad \Omega. \tag{4.4.4}$$

We use standard calculus of variation to derive Euler-Lagrange equations and boundary conditions for the equilibrium state of the system. More details on the theoretical modeling of the HSMEs can be found in the *SI Section*.

4.4.4 Computational modeling of PHSMEs

Based on the nonlinear coupled formulation discussed earlier, we develop a finite element model in order to study ME effect in PHMSEs. We use open source finite element software FEniCS [181] to implement finite element formulation. We derive weak form of the governing equations of the system and encode weak formulation in Python using mathematical operators available in FEniCS. The FEniCS meshing component mshr which allows capability of defining subdomains is used to create mesh for this problem. We assume the material is incompressible and use neo-Hookean constitutive equation for elastic behavior of the material. The numerical values for material properties is consistent with the values obtained using our experimental measurement. More details on the finite element implementation, meshing and validation of the numerical solution is available in the *SI Section*.

4.5 Supplementary Information

4.5.1 Comparison of ME voltage coupling coefficient of PHMSEs and polymer based composites

Table 4.1: Comparison of properties of PHME with existing polymer based ME composites

Constitution	ME Voltage Coefficient (Vcm-1Oe-1)	Frequency (Hz)	DC Bias Field (Oe)	Soft and Stretchable	Ref
CFO-CNT-PVDF/P(VDF-TrFE) /CFO-CNT-PVDF	0.0167	1000	0	No	[4]
P(VDF-TrFE)/ Fe_3O_4	0.0008	6000	1500	No	[182]
P(VDF-TrFE)/ $CoFe_2O_4$	0.0065	6000	2600	No	[182]
P(VDF–TrFE)/$CoFe_2O_4$	0.164	16200	2600	No	[5]
P(VDF-TrFE)/$BiFeO_3$-$BaTiO_3$	0.357	150000	600	No	[6]
Cellulose/Metglas	1.41	56100	4.2	No	[7]
PVDF/$Gd5Si_{2.4}Ge_{1.6}$	2.2	(50000, 70000)	5000	No	[8]
P(VDF-TrFE)/$[C_4mim][FeCl_4]$	10	10000	0	No	[9]
PVDF-HFP/Metglas	20	20	4	No	[10]
PVDF/Metglas	22	20	1.6	No	[11]
PVDF/Metglas	30	25400	2	No	[12]
PVDF/epoxy/$Fe_{39}Ni_{39}Mo_4Si_6B_{12}$	53	(30000, 45000)	5.3	No	[13]
PVDF/Fe64Co17Si7B12	145.6	46800	4.7	No	[14]
PVDF-HFP/Metglas	320	68000	4	No	[10]
P(VDF-TrFE)/Metglas	850	27.8	6	No	[15]
PHMSE	**15**	**6**	**0**	**Yes**	

Figure 4.6 compares the ME voltage coupling coefficient of PHMSEs with the highest values reported in the literature for ME voltage coupling coefficient of polymer based ME composites [4, 5, 6, 7, 8, 9, 10, 11, 12, 13, 14, 15, 16, 17, 18, 19, 20, 21, 22, 23]. The dash horizontal line shows $\alpha_{\mathrm{ME}}^{\mathrm{eff}} = 1$. The solid red circles show the self bias ME materials. It is clear that the PHMSEs is the only self bias ME material with frequency under 100 Hz and $\alpha_{\mathrm{ME}}^{\mathrm{eff}} \geq 1$. Also, Table-1 shows that PHMSEs are the only soft and stretchable ME material with giant ME effect.

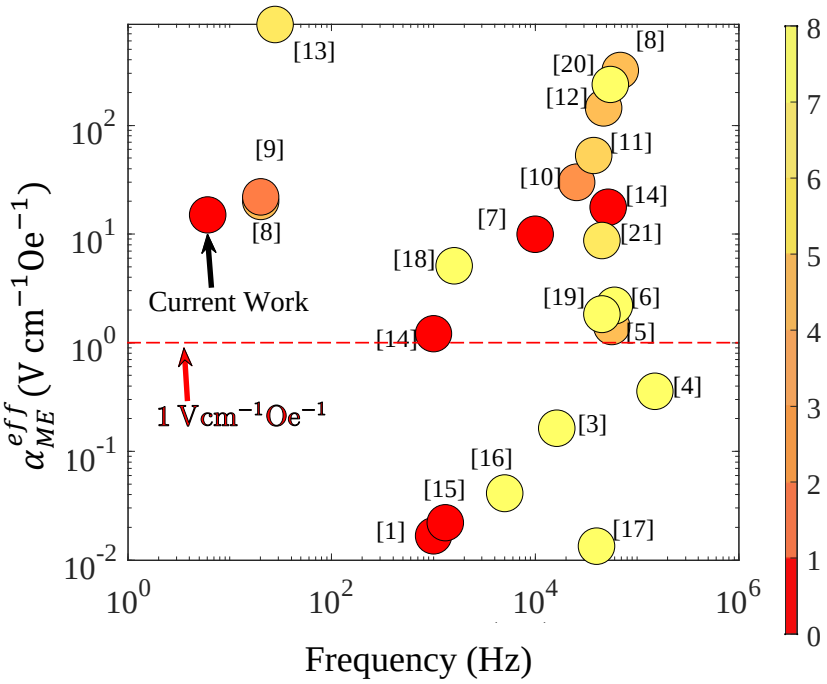

Figure 4.6: Comparison of ME voltage coefficient of PHME with ME voltage coefficient of polymer based ME composites [4, 5, 6, 7, 8, 9, 10, 11, 12, 13, 14, 15, 16, 17, 18, 19, 20, 21, 22, 23]. Color bar shows DC bias magnetic field.

4.5.2 The photographs of a PTFE film and a NMISR film

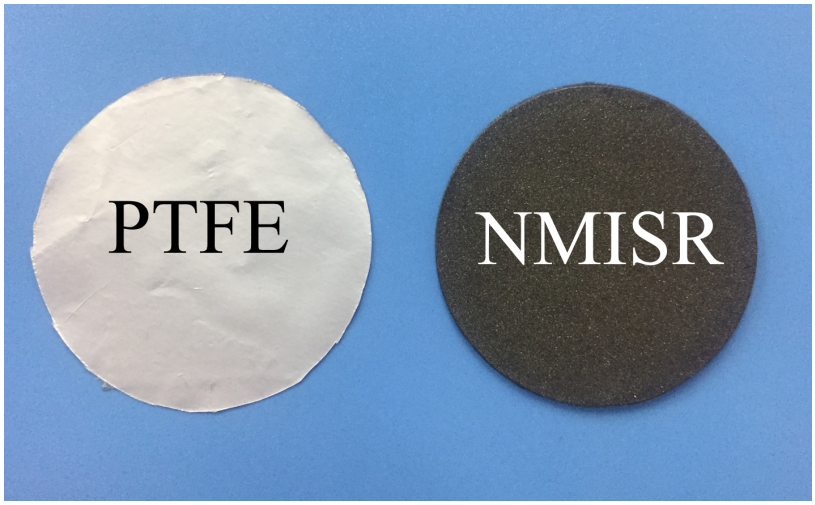

Figure 4.7: The photographs of a PTFE film and a NMISR film.

4.5.3 Comparison of output charges of the HMSE and SMSE.

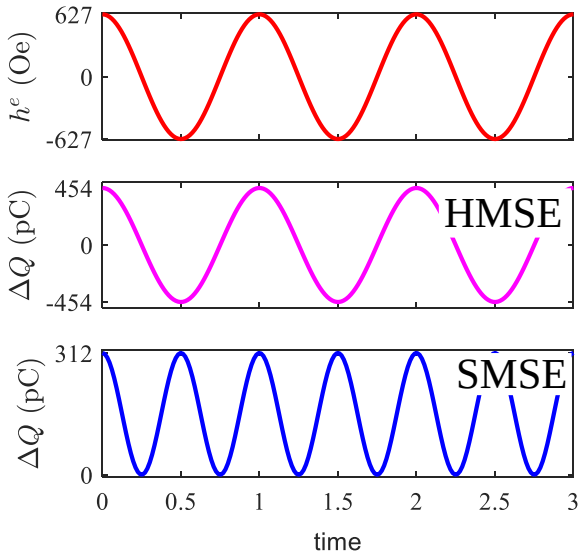

Figure 4.8: Experimental measurement for output charges of HMSE and SMSE under AC magnetic field.

4.5.4 Comparison of the deformation between IMISR, NMISR and Terfenol-D

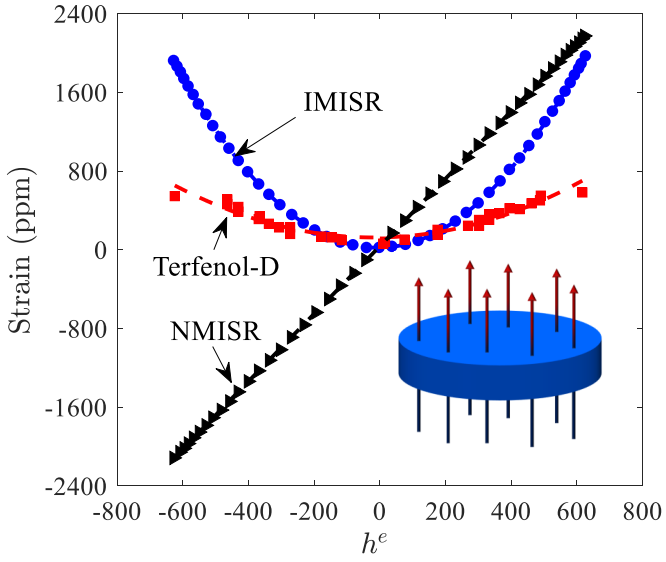

Figure 4.9: Experimental results for the magnetic field induced strain of NMISR, IMISR, and Terfenol-D. The deformation of Terfenol-D has been collected from Yang et al. [24].

4.5.5 Linear relationship between magnetic field and output charge in HMSE

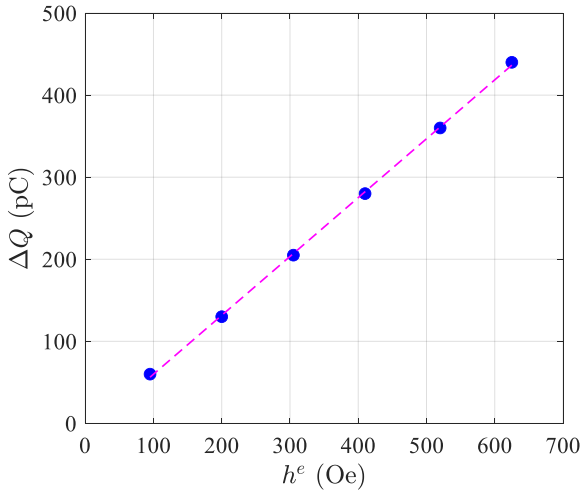

Figure 4.10: Magnetic field dependence of the output charge,where h_0^e is the amplitude of the external magnetic field .

4.5.6 Effect of residual magnetic flux density on ME effect of the HMSE

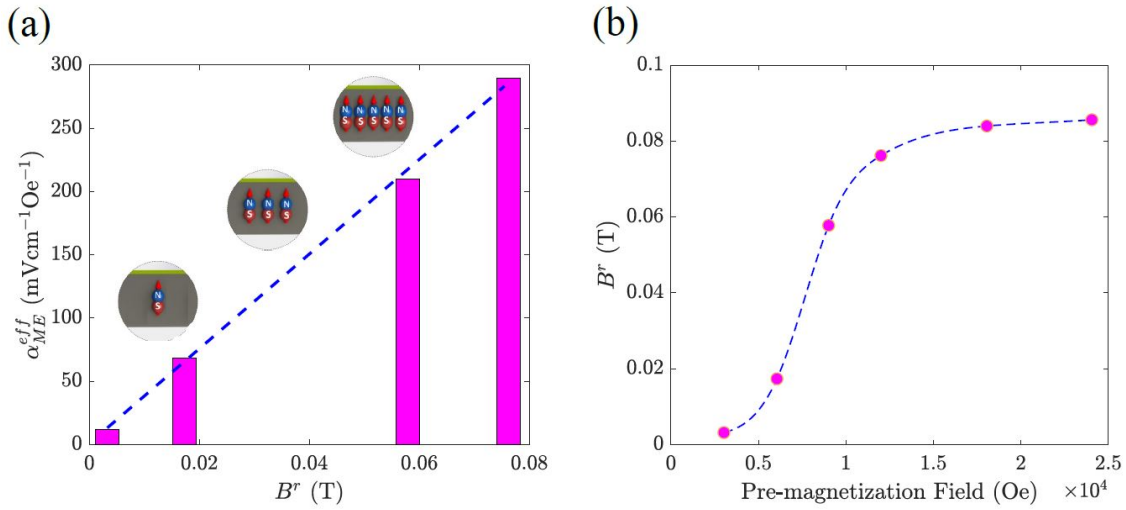

Figure 4.11: Effects of residual magnetic flux density of HMSEs on the ME behavior. (a) The effect of residual magnetic flux density on ME voltage coupling coefficient of the material. (b) Residual magnetization versus magnetic field used to align hard magnetic microparticles.

4.5.7 Magnetic field induced deflection in the PHMSE for different frequencies

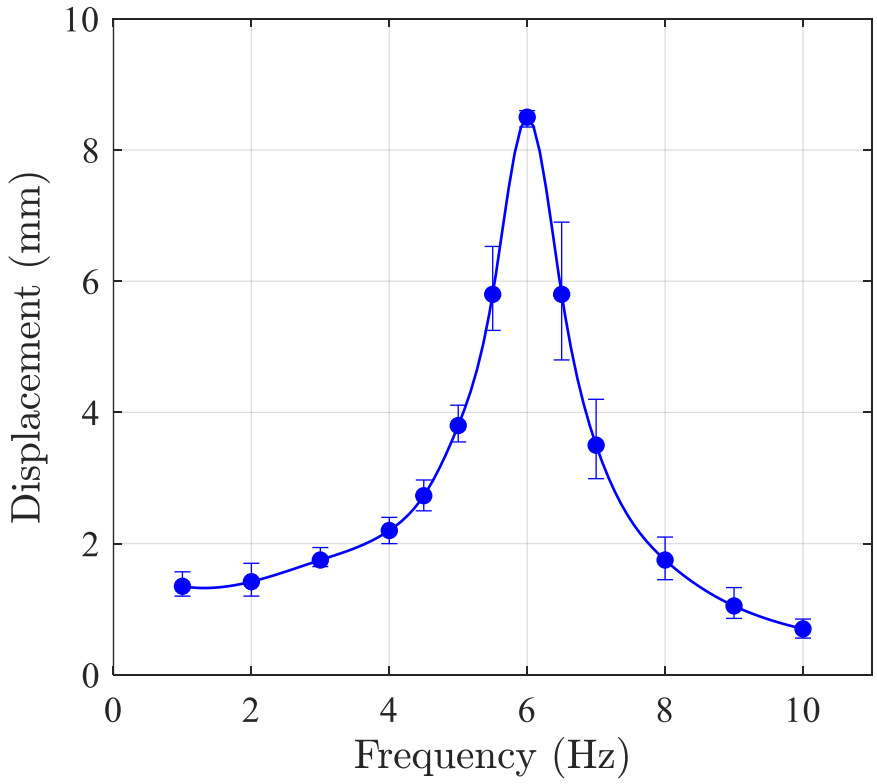

Figure 4.12: Deflection versus frequency for PHME under AC field with amplitude 12 Oe.

4.5.8 Corona charging

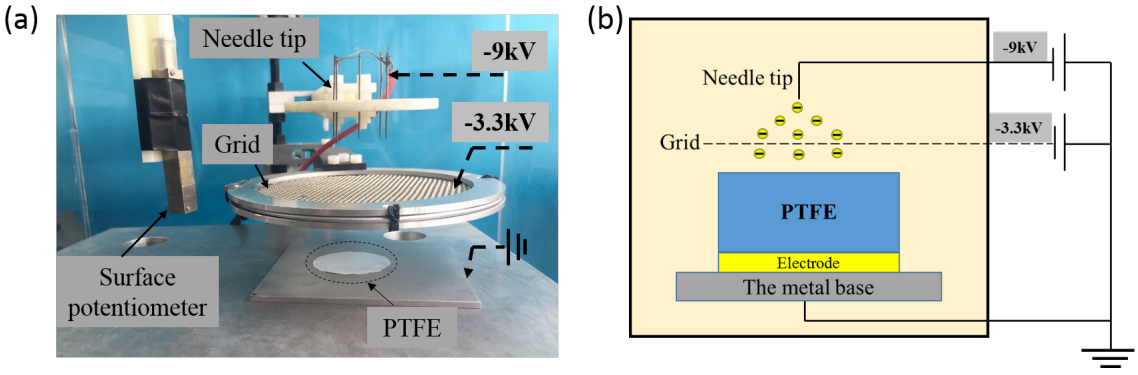

Figure 4.13: The photograph and the schematic diagram of the corona charging.

4.5.9 The hysteresis behavior of IMISR and NMISR

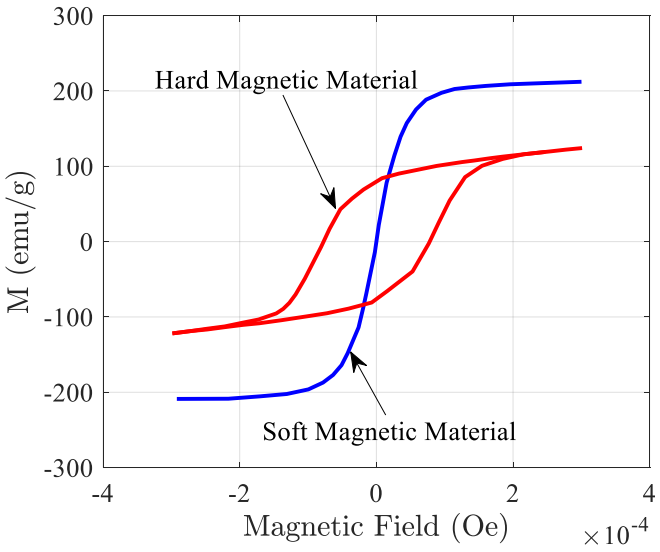

Figure 4.14: The hysteresis loop of iron particles and NdFeB particles. NdFeB particles exhibit high magnetic energy density and coercivity.

4.5.10 The measuring equipment for ME effect in HMSEs

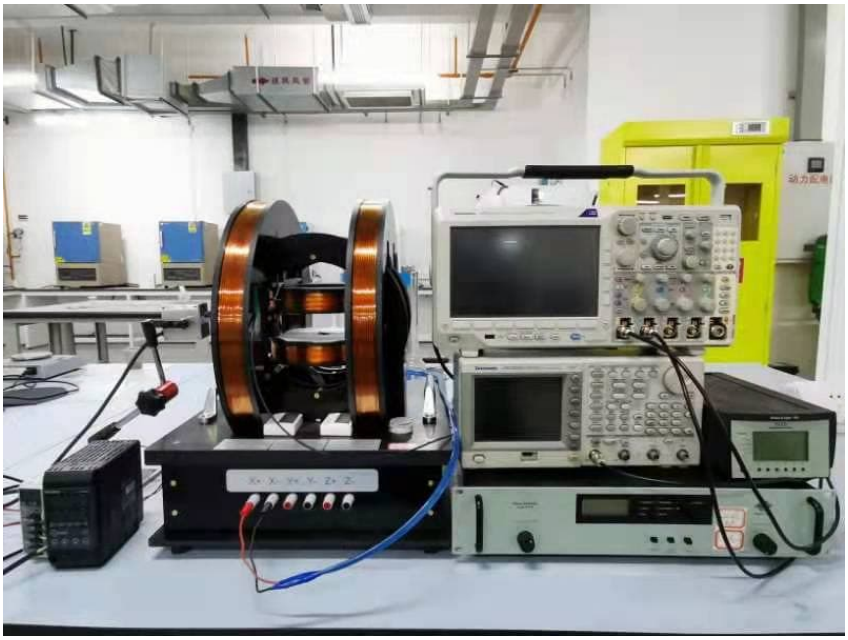

Figure 4.15: The measuring equipment used for soft magnetoelectric materials.

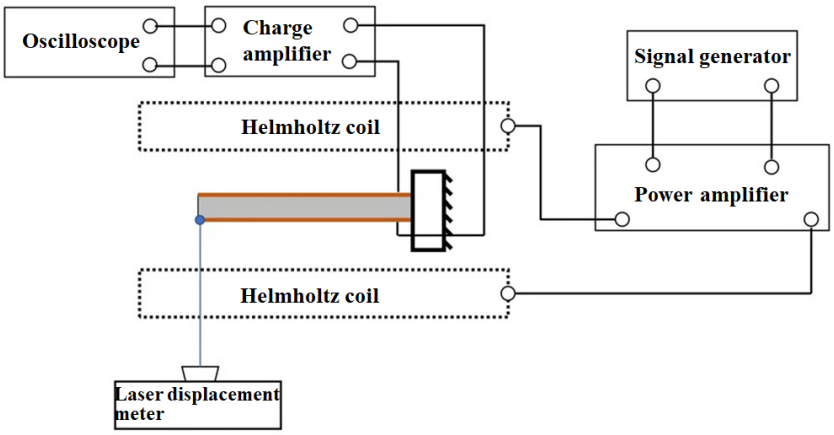

Figure 4.16: Measurement schematic diagram of soft magnetoelectric materials.

4.5.11 Theory of hard magnetic soft electret

A nonlinear magneto-electro-mechanically coupled theory for large deformation of hard magnetic soft electrets is presented here. We avoid presenting all the details of derivation as there are several similar derivations available in the literature [97, 25, 178]. We must distinguish between continuum deformable body of the material in the reference configuration $\Omega_R \subset \mathbb{R}^3$ and current configuration $\Omega \subset \mathbb{R}^3$ as the magnetoelectric coupling in these materials is non-linear in nature. To avoid confusion between gradients in the reference and deformed configurations, we reserve the symbol ∇ for the gradient in the reference configuration and the gradient and divergence in the current configuration is denoted by "grad" and "div", respectively. Identifying the deformation $\boldsymbol{\chi}$ and the polarization $\mathbf{p}$ as two independent thermodynamic variables, we express the total free energy of the system as

$$\mathcal{F}[\boldsymbol{\chi}, \mathbf{p}] = \int_{\Omega_R} W^{\text{elast}} + \int_{\Omega} \frac{|\mathbf{p}|^2}{2(\epsilon - \epsilon_0)} + \int_{\Omega} \frac{\epsilon_0}{2} |\mathbf{e}|^2 - \int_{\Omega_R} \mathbf{F}\widetilde{\mathbf{B}}^r \cdot \mathbf{h}^{\text{e}}, \tag{4.5.1}$$

where $\mathbf{F} = \nabla\boldsymbol{\chi}$ is the deformation gradient tensor, $\widetilde{\mathbf{B}}^r$ is the magnetic flux density represented in the reference configuration. In addition, ϵ, ϵ_0 and $\mathbf{h}^{\text{e}}$ are, respectively, electric permittivity of the material, electric permittivity of the vacuum and external magnetic field. Also, W^{elast} denotes elastic energy density of the material and using incompressible

neo-Hookean constitutive equation is expressed as

$$W^{elast}[\mathbf{F}] = \frac{G}{2}(\text{tr}(\mathbf{F}^T\mathbf{F}) - 3), \tag{4.5.2}$$

where G denotes the shear modulus of the material. Our theoretical formulation is based on this premise that the Maxwell equation must to be satisfied. The Maxwell equation in the current configuration is expressed as

$$\text{div}\,(\epsilon_0\mathbf{e} + \mathbf{p}) = \rho_e \qquad \text{in} \quad \Omega, \tag{4.5.3}$$

where ρ_e is the charge density of the material.

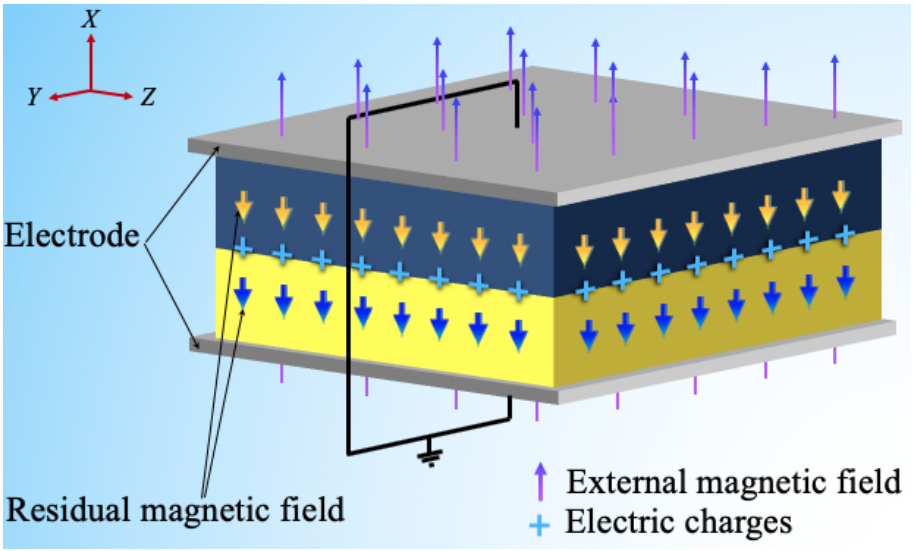

Figure 4.17: Hard magnetic soft electret made of two layers of materials with different material properties.

Double layer HMSE

Now consider hard magnetic soft electret shown in Fig. 4.17. This electret consists of two different materials on top and bottom which are referenced with subscripts "t" and "b", respectively. The top layer has thickness H_t and thickness of bottom layer is denoted by H_b. There is a layer of charge between two layers with surface charge density q_0. Material is sandwiched with two mechanically compliant electrodes on top and bottom

and a short circuit boundary condition has been applied. There is uniform residual magnetic flux density $\widetilde{\mathbf{B}}^r = B_t^r \mathbf{e}_X$ (resp. $\widetilde{\mathbf{B}}^r = B_t^r \mathbf{e}_X$) in top (resp. bottom) layer. Material will deform in response to externally applied magnetic field $\mathbf{h}^{\mathrm{e}} = h^{\mathrm{e}} \mathbf{e}_x$. Since two layers have different material properties, deformation in two layers will not be equivalent. Assuming uniform deformation, the deformation gradient tensor for each layer be expressed as

$$\mathbf{F} = \lambda_t \mathbf{e}_x \otimes \mathbf{e}_X + \lambda_t^{-1/2} \mathbf{e}_y \otimes \mathbf{e}_Y + \lambda_t^{-1/2} \mathbf{e}_z \otimes \mathbf{e}_Z \qquad \text{for} \quad H_b < X < H_b + H_t \tag{4.5.4}$$

$$\text{and} \qquad \mathbf{F} = \lambda_b \mathbf{e}_x \otimes \mathbf{e}_X + \lambda_b^{-1/2} \mathbf{e}_y \otimes \mathbf{e}_Y + \lambda_b^{-1/2} \mathbf{e}_z \otimes \mathbf{e}_Z \qquad \text{for} \quad 0 < X < H_b, \tag{4.5.5}$$

where λ represents the magnetic field induced stretch in any of the layers. Substituting Eq. 4.5.4 and Eq.(4.5.5) into Eq.(4.5.1) and using standard variational calculus of variation, the stretch in each layer is determined as

$$\lambda_t - 1 \approx \frac{B_t^r h^{\mathrm{e}}}{3G_t} \tag{4.5.6}$$

$$\text{and} \qquad \lambda_b - 1 \approx \frac{B_b^r h^{\mathrm{e}}}{3G_b}, \tag{4.5.7}$$

where we have linearized final equations assuming $|\lambda - 1| \ll 1$ and ignored effect of the Maxwell stress.

Having stretches in each layer, we can determine electric field and electric displacement in each layer. Substituting Eq. 4.5.4 and Eq.(4.5.5) into the Maxwell equation, electric displacement in top layer is determined as

$$D_t \approx D^i + \frac{q H_t H_b \epsilon_b \epsilon_t (\lambda_b - \lambda_t)}{(H_t \epsilon_b + H_b \epsilon_t)^2}, \tag{4.5.8}$$

where D^i is the deformation independent part of the electric displacement.

For conventional magnetostrictive/piezoelectric composites, magnetoelectric coupling coefficient is defined as [183, 184]

$$\alpha_{ij} = \frac{\partial P_i}{\partial h_j^e}, \tag{4.5.9}$$

where h_i^e and P_j, respectively, are components of magnetic field and electric polarization defined in a linear framework where there is no difference between reference and current configurations. Also, magnetoelectric voltage coefficient $\boldsymbol{\alpha}_{\mathrm{ME}}$ is defined as $\boldsymbol{\alpha} = \boldsymbol{\epsilon}\boldsymbol{\alpha}_{\mathrm{ME}}$, where $\boldsymbol{\epsilon}$ is the electric permittivity tensor of the material [185, 186]. In experimental settings and under short circuit boundary condition, polarization is often determined measuring electric charges. This is due to the reason that when electric field is zero, electric displacement and electric polarization are equivalent. Similarly, here, we perform a thought experiment and define the effective magneto electric voltage coefficient for hard magnetic soft electrets $\alpha_{\mathrm{ME}}^{\mathrm{eff}}$ as

$$\alpha_{\mathrm{ME}}^{\mathrm{eff}} = \frac{1}{\epsilon^{\mathrm{eff}}} \frac{\partial D_t}{\partial h^{\mathrm{e}}}, \tag{4.5.10}$$

where ϵ^{eff} is determined from following equation

$$\frac{H_t + H_b}{\epsilon^{\mathrm{eff}}} = \frac{H_t}{\epsilon_t} + \frac{H_b}{\epsilon_b}. \tag{4.5.11}$$

The effective magnetoelectric voltage coefficient of the material can also be written in terms of the output charges $\Delta Q = D_t A$ and the effective capacitance of the material $C^{\mathrm{eff}} = \frac{\epsilon^{\mathrm{eff}} A}{H}$:

$$\alpha_{\mathrm{ME}}^{\mathrm{eff}} = \frac{1}{C^{\mathrm{eff}} H} \frac{\partial (\Delta Q)}{\partial h^e}, \tag{4.5.12}$$

where h^e is the external magnetic field ($\mathbf{h}^{\mathrm{e}} = h^e \mathbf{e}_X$), A is the surface area of the electrodes and $H = H_t + H_b$ is the total thickness of the material. Effective voltage coefficient for the hard magnetic soft electret (shown in Fig. 4.17) is derived substituting Eq.(4.5.8) into eqn (4.5.12)

$$\alpha_{\mathrm{ME}}^{\mathrm{eff}} = \frac{1}{\epsilon^{\mathrm{eff}}} \frac{q_0 H_t H_b \epsilon_b \epsilon_t}{(H_t \epsilon_b + H_b \epsilon_t)^2} \times \frac{1}{3} \left(\frac{B_b^r}{G_b} - \frac{B_t^r}{G_t} \right). \tag{4.5.13}$$

Hard magnetic Euler beam

In this section, we aim to derive an approximate relation for the ME voltage coupling of the HMSEs mediated by bending deformation. As the analytical solution is not possible for this problem, we will make several simplifying assumptions.

Consider HMSE shown in the Fig. 4.18. The residual magnetic flux density of the

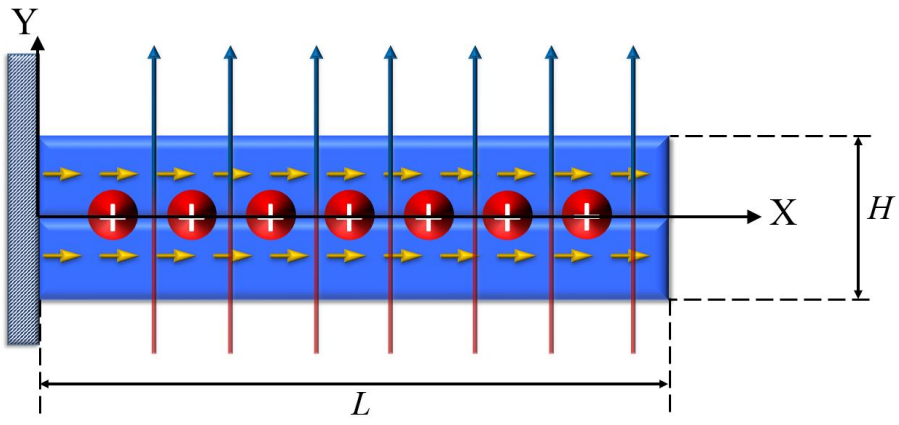

Figure 4.18: Euler beam made of Hard magnetic soft electret materials.

material is uniformly aligned along the axis of the beam $\widetilde{\mathbf{B}}^r = B^r \mathbf{e}_X$. This material bends in response to applied magnetic field $\mathbf{h}^{\mathrm{e}} = h^e \mathbf{e}_Y$ and the bending will lead to an ME effect. We assume the deformation is small ($|\nabla \mathbf{u}| \ll 1$) and use Euler beam theory. Ignoring contribution of electric terms in the Eq.(4.5.1) and minimizing free energy with respect to deformation, the relationship between applied magnetic field and induced curvature $\kappa = \frac{\partial^2 u}{\partial x^2}$ in the material is obtained as

$$\frac{\partial^2 u}{\partial x^2} = \frac{h^{\mathrm{e}} B^r}{G} \frac{4L}{H^2} \left(1 - \frac{x}{L}\right). \tag{4.5.14}$$

We cannot use the solution provided in this section to determine output charge of a hard magnetic soft electret under bending deformation because it was a linear decoupled problem. The relation between magnetic field and curvature is illustrated in Eq.(4.5.14). To obtain analytical relation between output charge and magnetic field, the fully coupled problem has to be solved which is rather difficult nonlinear problem. However, Rahmati et al. [178] presented a simple relationship between curvature and output charge for an electret under pure bending. According to their model, the output charge is related to curvature κ through $D^t = \frac{1}{4} q_0 H \kappa$ where q_0 is the surface charge density at the interface of two materials. Therefore, for illustrative purposes, the scale of the output charge for a hard magnetic sof electret with uniform distribution of residual magnetic flux density under

bending deformation can be roughly approximated as

$$D^t \propto \frac{h^{\mathrm{e}} B^r}{G} AR q_0, \tag{4.5.15}$$

and, as a result, we have

$$\alpha_{\mathrm{ME}}^{\mathrm{eff}} \propto (AR) \frac{B^r}{G} \frac{q_0}{\epsilon^{\mathrm{eff}}}. \tag{4.5.16}$$

Finite element implementation

In addition to experimental efforts, we use finite element simulation to show ME effect in PHMEs under bending deformation. Consider a PHMSE material with the thickness H and length L. The material is composed of two identical layers with layer of electric charges with surface charge density q_0 at their interface. The scematics of this material is similar to Fig.4.18 but any desirable profile can be used for the residual magnetic flux density $\widetilde{\mathbf{B}}^r$. The bending is induced in the material in response to the external magnetic field $\mathbf{h}^{\mathrm{e}} = h^e \mathbf{e}_Y$. Assuming a plane strain deformation, the weak form of the governing equation for this problem is given as

$$\int_0^L \int_{-H/2}^{H/2} \left(\nabla w_1 \cdot (-\epsilon \mathbf{F}^{-1} \mathbf{F}^{-T} \nabla \xi) \right) \mathrm{d}Y \mathrm{d}X + \int_{-H/2}^{H/2} w_1 \Big|_{Y=0} q_0 \mathrm{d}X = 0, \tag{4.5.17}$$

$$\int_0^L \int_{-H/2}^{H/2} \left[\nabla \mathbf{w}_2 : \left(\frac{\partial W^{\mathrm{elast}}}{\partial \mathbf{F}} - \mathcal{L}_a \mathbf{F}^{-T} + \widetilde{\mathbf{\Sigma}}_{\mathrm{elec}}^{MW} - \mathbf{h}^{\mathrm{e}} \otimes \widetilde{\mathbf{B}}^r \right) \right] \mathrm{d}Y \mathrm{d}X = 0, \tag{4.5.18}$$

and

$$\int_0^L \int_{-H/2}^{H/2} \left[w_3 \left(\det \mathbf{F} - 1 \right) \right] \mathrm{d}Y \mathrm{d}X = 0, \tag{4.5.19}$$

where the hydrostatic pressure $\mathcal{L}_a$ is a Lagrange multiplier which has been introduced to enforce incompressibility constraint. Also, w_1, $\mathbf{w}_2$ and w_3 are test functions corresponding to electric potential ξ, displacement $\mathbf{u}$ and the the hydrostatic pressure $\mathcal{L}_a$, respectively. Also, $\widetilde{\mathbf{\Sigma}}_{\mathrm{elec}}^{MW}$ is the Maxwell stress and is given as

$$\widetilde{\mathbf{\Sigma}}_{\mathrm{elec}}^{MW} = -\frac{\epsilon}{2} J |\mathbf{F}^{-T} \nabla \xi|^2 \mathbf{F}^{-T} - \mathbf{F}^{-T} \mathrm{Grad} \xi \otimes (-\epsilon \mathbf{F}^{-1} \mathbf{F}^{-T} \nabla \xi). \tag{4.5.20}$$

As the Taylor-Hood elements have been successfully used in various coupled problems [187, 188], we implement Taylor-Hood element in which the deformation is interpolated quadratically and linear shape functions are used for electric potential and hydrostatic pressure. This variational problem is solved using FEniCS [181], a collection of free and open-source software components created to solve PDEs. The short circuit electrical boundary condition $\xi = 0$ has been applied to surfaces $Y = \pm H/2$. The deformation is fully constrained on the cantilever side of the beam ($X = 0$). The FEniCS meshing component mshr which allows capability of defining subdomains is used to create mesh for this problem. The mesh size parameter has set to be 500 for all the results on this paper. Mesh convergence study shown in Fig. 4.19 shows by changeing mesh resolution from 500 to 900, less than 1% difference in results observed.

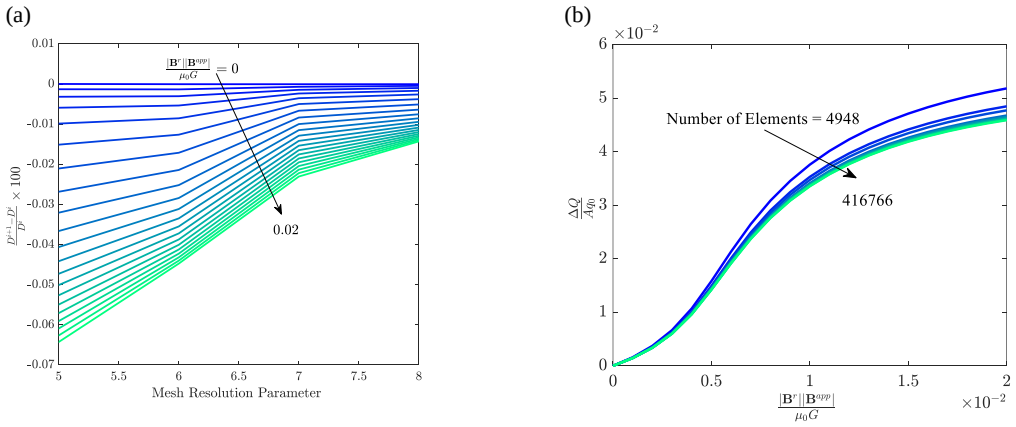

Figure 4.19: Mesh convergence study.

The material is assumed to be incompressible neo-Hookean (Eq.(4.5.2)) with shear modulus $G = 18.33KPa$. The electric permittivity of the material is set to $\epsilon = 5.0676\epsilon_0$, where ϵ_0 is the electric permittivity of vacuum. Unless otherwise stated, the charge density of the interface is $q_0 = -0.048$ mC/m^2. The output charge ΔQ over surface area of the electrode A can be determined as

$$\frac{\Delta Q}{A} = \frac{1}{L}\int_0^L \left(D^f(X) - D^i(X)\right) \mathrm{d}X, \tag{4.5.21}$$

where D^f and D^t are the electric displacements in presence and absence of external magnetic field, respectively.

We have checked accuracy of our finite element model by comparing the results obtained using our model and the experimental and simulation results given by Zhao et al. [25] for a hard magnetic soft material with uniform residual magnetic flux density under magnetic field induced bending deformation. The deflection of the material versus dimensionless magnetic field is plotted in the Fig. 4.20 where a good agreement is observed between our results given by Zhao et al. [25].

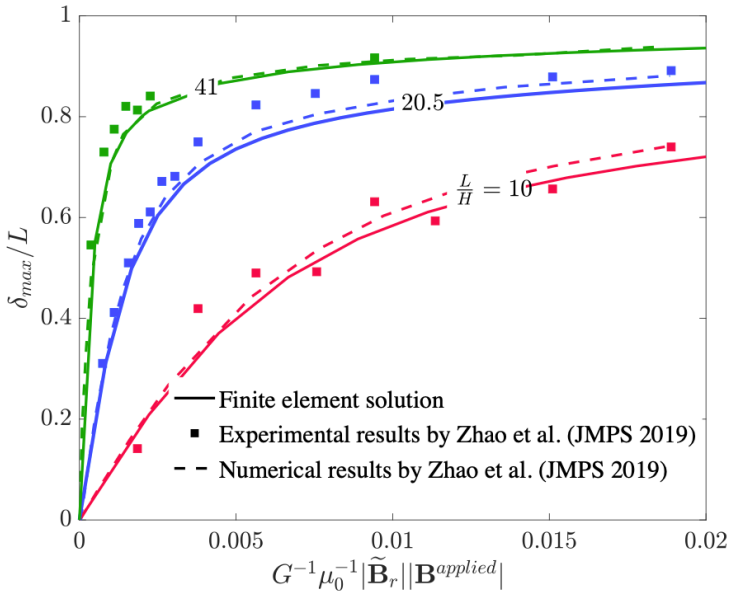

Figure 4.20: Comparison of the current numerical solution with experimental and simulation results given by Zhao et al. [25]. The pre-existing magnetic flux density is uniformly oriented along the horizontal axis of the material in the undeformed configuration. A uniform external magnetic field ($\mathbf{B}^{\text{applied}} = \mu_0 h^{\text{e}}$) is applied to material in the vertical direction to cause bending deformation. Comparison of simulation and experimental results for vertical displacement of the tip of the beam under different external magnetic fields.

Chapter 5

Theory of Hard Magnetic Soft Materials to Create Magnetoelectricity

Materials that generate electrical signals upon exposure to a well-controlled stimuli are high desirable. In that context, magnetoelectrics are unusual in the sense that the stimulus may be applied remotely (and wirelessly) without recourse to any physical contact. Wireless energy harvesting, remotely triggered biomedical agents, soft robots among others are some of the applications of such materials. The magnetoelectric property however is somewhat elusive in natural materials and artificial composites designed to exhibit this effect are invariably hard materials, require a pre-existing magnetic field and only exhibit a non-trivial coupling at high frequencies. Our recent experiments (presented elsewhere) demonstrated a facile route to create highly deformable soft magnetoeletric materials predicated on the concept of programmable hard magnetic soft materials with embedded immobile electric charges (electrets). In this work, we offer a nonlinear theoretical framework to both understand the emergent magnetoelectric effect in this class of soft materials as well as to design novel structures and devices with tailored functionality. Specifically, we are able to show that mechanical strain convects residual electrical and magnetic field states to mediate an unprecedented strong magnetoelectric coupling that is independent of the applied external magnetic field and retains its potency at low frequencies. We analytically solve simple illustrative examples to establish insights and present a finite element approach to handle complexities that may be otherwise intractable. The predictions of our theory agree very well with published experiments.

5.1 Introduction

There are several compelling reasons to develop magnetoelectric materials. Such materials enable extremely low power memories where data is written electrically but read magnetically [189]. Electrical energy may be harvested simply by the remote application of a magnetic field, which may be used for wireless charging of small-scale devices or sensing [190]. In a rather fascinating recent study, hollow magnetoelectric capsules were used drug delivery. Upon suitable application of a magnetic field, nano-electroporation mediated release of drugs at cancer sites was achieved [191]. We remark that biological media is transparent to magnetic fields thus is of special relevance for biomedical application[1].

Naturally occurring single-phase magnetoelectric materials are scarce and the reason is simple. Such materials must couple magnetic order parameter (typically found in a class of metals) with electrical polarization order (found in certain types of dielectrics). This contradictory requirement and other associated details (see [157, 158] for further information) imply that the discovered single phase natural magnetoelectrics, aside from being rare, have an exceedingly low magnetoelectric coupling; especially at temperature range typically associated with engineering applications [159]. A survey of research activities in the field of multiferroics (which are magntoelectric) can be found in several review articles [192, 193, 194, 195, 196, 197, 198, 199, 200].

An expedient route to design magnetoelectrics has been by creating composites composed of magnetostrictive (ferromagnetic) and piezoelectric (ferroelectric) constituents. The emergent magnetoelectric effect in such composites is due to the cross coupling between magnetostrictive and piezoelectric phases and is (usually) mediated through mechanical deformation. The strain generated in the magnetostrictive phase of the composite, in response to applied magnetic field, is transferred to piezoelectric phase through interface of two phases and the developed strain in the piezoelectric phase generates electrical polarization. Such

[1] A fact we rely on in medical equipment like MRI-magnetic resonance imaging where human bodies can be subjected to enormous magnetic fields. An analogous exposure to electrical fields, of course, would be fatal.

composites, like single phase magnetoelectrics are rather *hard* materials and earlier studies reported magnetoelectric voltage coupling coefficients that did not surpass 0.1 $\mathrm{Vcm^{-1}Oe^{-1}}$ [201, 183][2]. In early 2000s, theoretical [160, 161] and experimental [162, 163, 164] research confirmed the existence of giant ME effect (with the voltage coupling coefficient greater than 1 $\mathrm{Vcm^{-1}Oe^{-1}}$), in composites containing magnetostrictive rare-earth-iron alloy Tb1–xDyxFe2 (Terfenol-D). This observation made these composites desirable for technological applications. Further research into development of ME composite have enabled giant ME effect in different composite materials which contain polymer or ceramic as piezoelectric phase and a variety of magnetostrictive materials, including ferrites [165], Fe-Ga alloy [166] and Metglas [167]. We refer the reader to several reviews for a survey of the research in the topic [202, 203, 204, 205, 206, 207, 208, 177, 209].

Notwithstanding the progress made on the subject of magnetoelectrics, especially in the context of composites, we reiterate that soft magnetoelectrics are rather elusive. Soft materials capable of large elastic deformation offer new functionalities would not have been possible with their hard counterparts—e.g soft robotics, health care [113], stretchable, flexible and wearable electronics [51] among others. We remark that although there have been successful attempts in creating materials for power harvesting from different sources of energy including mechanical [210], thermal [211], chemical [212] or optical [213], surprisingly limited progress has been made in the development of soft materials suitable for magnetoelectric conversion despite all the advantages it could potentially offer.

There are several other disadvantages that plague the current state-of-the-art in composite magnetoeletrics:

- The design and fabrication of magnetoelectric composite is a complex process as there are a large number of factors including connectivity, microstructure, volume fraction of individual phases, the composite structures among others [203] that must be carefully tailored to achieve large magnetoelectric effect and avoid problems such as current

[2]The magnetoelectric voltage coupling coefficient $\boldsymbol{\alpha}_{\mathrm{ME}}$ is defined as $\boldsymbol{\alpha} = \boldsymbol{\epsilon}\boldsymbol{\alpha}_{\mathrm{ME}}$, where $\boldsymbol{\epsilon}$ is the electric permittivity tensor of the material and the magnetoelectric coupling coefficient $\boldsymbol{\alpha} = \frac{\partial \mathbf{P}}{\partial \mathbf{h}^{\mathrm{e}}}$ quantifies change in the polarization of the material $\mathbf{P}$ in response to applied magnetic field $\mathbf{h}^{\mathrm{e}}$.

leakage and substrate clamping [202]. The magnetoelectric coupling in these materials strongly depends on the strain transfer between the different phases and this aspect is not simple to control [208].

- A key disadvantage of the current high quality magnetoelectric composites are that they are not mechanically soft. Polymer based composites which, compare to ceramic and magnetic alloy based composites, offer some recourse however the ones created so far (see [209] and references therein) are thin materials that can accommodate deformations similar to bending in which deflection may be quite large but strain is small. This is partially because truly soft piezoelectric materials do not exist. Appreciable intrinsic piezoelectricity only exists in hard brittle materials with non-centrosymmetric crystals [203, 98, 178, 99]. Although some polymers such as PVDF and its co-polymers exhibit piezoelectricity in their semi-crystalline phase, the magnitude of their stiffness is in the range of GPa which is not considered soft enough [214, 215, 216, 217].

- Another significant disadvantage of magnetoelectric composites is that a static bias magnetic field is required for the composites to exhibit a significant coupling. As mentioned earlier, the magnetoelectric coupling in a composites is realized through the so-called "product property" of the two piezoelectric and magnetoelastic phases. The magnetic field induced strain generated in the magnetoactive phase is transferred to the piezoelectric which leads generation of an electric signal. The strain or stretch developed in a magnetostrictive material depends quadratically on the external magnetic field. Thus, the magnetoelectric coupling coefficient of the material (which is related to the rate of change of strain with respect to external magnetic field) depends *linearly* on the external magnetic field. Therefore, the magnetoelectric coefficient of the composites depends on the applied external field and is asymptotically zero as the applied field diminishes. Accordingly, an additional external applied static bias magnetic field is necessary to achieve a non-trivial magnetoelectric coupling in composites. This places requirements of additional weight and space [168] rendering any sort of miniaturization difficult. We remark that, in the past decade, notions of introducing internal/self- bias field in composite to replace the external bias field have

been proposed [218, 219, 175, 220, 221]. However, most self-biased composites are bulky in size and their fabrication requires special synthesis process which leads to additional steps in developing functional devices [201].

- Typical magnetoelectric composites exhibit strong a strong coupling only at high frequencies and their coupling coefficient significantly diminishes at small frequencies. This is unfortunate since many applications such as targeted drug delivery [170], brain stimulation [171], tissue regeneration and wireless energy transfer for implantable medical devices require lower frequency (since high frequency magnetic field may cause safety concenrs) [169].

Recently, we have proposed a new mechanism to create magnetoelectric coupling using soft materials like rubber and without the need for piezoelectric and magnetostrictive materials [222, 176]. The central idea is to embed immobile charges or dipoles in a soft material (–such materials are called electrets) and ensure that the magnetic permeability of the material is higher than that of vacuum (by introducing a modest fraction of magnetic particles that do not appreciably alter the mechanical stiffness). We showed both theoretically [222] and experimentally [223] that these soft magnetic electret(SMSE) materials exhibit a magnetoelectric effect. The mechanism underpinning such materials is predicated on the fact that electrets exhibit a significant artificial piezoelectric-like behavior [178, 98, 99, 100, 224, 62]. Based on the Maxwell stress effect, any material with relative permeability greater than one will deform in response to an external magnetic field. A non-uniform deformation in the electret materials can lead to a piezoelectric effect. Therefore, a magnetoelectric effect can be seen in SMSEs made of two different layers with different material properties. To the best of our knowledge, soft SMSEs are the only soft ME "*materials*" developed so far, even though there is precedent of ME coupling in soft "*structures*" through embedding multiferroic nanoparticles in soft materials [170, 225, 226, 227] or through electromagnetic induction [228, 229].

Despite the progress made recently in the context of soft magnetoelectric materials (summarized in the preceding paragraph), the magnetoelectric coupling itself is rather small

unless extraordinarily large magnetic fields are applied. This is because the relationship between magnetic field and strain induced as a result of the Maxwell stress is quadratic in SMSE materials. In this sense, SMSEs behave similar to magnetoelectric composite materials where a bias magnetic field required to achieve strong magnetoelectric coupling. Furthermore, since there is a quadratic relationship between strain developed in the material and applied magnetic field, the SMSEs are not sensible to the direction of applied magnetic field and the magnetoelectric response only depends on the magnitude of the applied field. This restricts application of SMSEs as magnetoelectric sensors. Moreover, non-uniform strain is required to achieve a large magnetic effect under uniform magnetic field in SMSEs and it is not straightforward to induce non-uniform strain without an elastic mismatch.

A recent development pertaining to a novel class of magnetosensitive materials present an alternative solutions to create soft materials that exhiit a giant magnetoelectric effect. Zhao et. al. used soft elastomers with embedded high-coercivity hard-magnetic microparticles [25]. A high remnant residual flux density allows them to exhibit a linear relationship between strain and magnetic field. Using the notion of programming the pattern of magnetic dipoles, tailored magnetic actuation can be achieved and remarkable experimental and theoretical results have been reported in a rather short time.

In this work, we present a mathematical theory that combines the concept of hard magnetic soft materials with electrets (HMSE). Like in prior works, the magnetic dipoles can be programmed—which we will refer to as programmable hard magnetic soft electrets(PHMSEs). Thus HMSEs are dielectric materials with immobile residual electric charges/dipoles and residual magnetic flux density(Fig. 5.1). The magnetoelectric effect will emerge in HMSEs if the magnetic field generates a non-uniform strain in the material. We present a nonlinear coupled theory for the behavior of HMSEs. We also present a finite element (FE) implementation of the theory. Similar to SMSEs, the simplest possible geometry for HMSEs is composed of a bi-layer with different elastic or/and different magnetic flux density with a layer of external charges at the interface. Moreover, as it is quite simple to

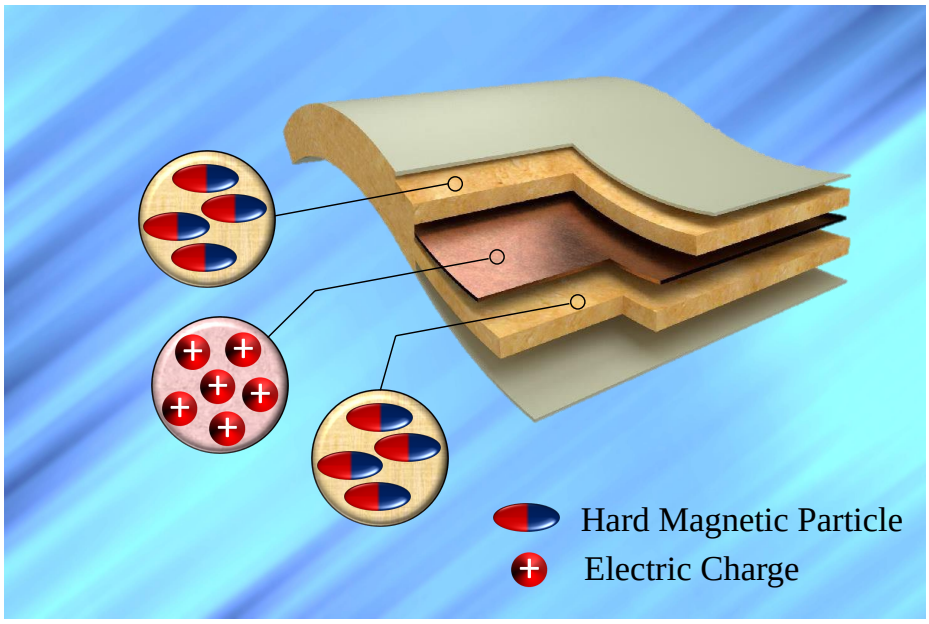

Figure 5.1: Schematics of the hard magnetic soft electret materials.

program residual flux density of hard magnetic soft materials to exhibit desired form of deformation [180], we propose PHMSEs in which non-uniform strain is generated in response to a uniform external magnetic field due to presence of gradient in the residual magnetic flux density in the elastically homogeneous soft material. Since bending deformation yields lower resonance frequency and large strain gradient, we design a PHMSE with the residual magnetic flux density tailored to obtain bending deformation in response to uniform magnetic field. We show that the the bending deformation mediated coupling in HMSEs can lead to a remarkably strong magnetoelectric effect. We find excellent agreement between our theoretical predictions and experimental realization of both HMSEs and PHMSEs.

This chapter is organized as follows. Theoretical study of the HMSEs is presented in the section 5.2. The governing equation and bounday conditions require to analyze behavior of the HMSEs is presented in the section 5.2.1 using a variational approach. Moreover, we prove the symmetry of the Cauchy stress in these material in this section 5.2.2. A simple FE implementation for incompressible HMSEs is presented in the section 5.3. The voltage coupling coefficient for a bi-layer HMSE is determined in the section 5.4.1. A rough estimate the voltage coupling coefficient enabled through magnetic field induced bending deformation of a HMSE is obtained in the section 5.4.2. We elaborate shape programmable

feature of HMSE materials in the section 5.4.3. The results obtained using FEA is available in the section 5.5. In the section 5.5.1, we compare our FE results with the results given by Zhao et al. [25]. The ME energy harvesting using a parallel plate capacitor made of hard magnetic soft material is studied in the section 5.5.2. The behavior of a PHMSE under magnetic field induced bending is studied in the section 5.5.3.

5.2 Theory of hard magnetic soft electrets

In this section, we present a variational approach to derive the governing equations and boundary conditions for hard magnetic soft electret materials. We also comment on the symmetry of the stress tensor–a notion that appears occasionally to be misinterpreted in the literature.

5.2.1 Formulation

As will become evident, the emergent magnetoelectric effect (ME) requires accounting for nonlinear deformation and accordingly we must distinguish the continuum deformable body in the reference configuration $\Omega_R \subset \mathbb{R}^3$ and current configuration $\Omega \subset \mathbb{R}^3$. The deformation $\boldsymbol{\chi}$ transforms material points $\mathbf{X}$ in the reference configuration to the spatial points $\mathbf{x}$ in the current configuration. We reserve the symbol ∇ for the gradient in the reference configuration and the differential operators in the current configuration are denoted by "grad" and "div". Hard magnetic soft electret materials contain both pre-existing immobile charges or dipoles as well as residual magnetic fields. We denote the residual magnetic flux density of the material by $\mathbf{b}^r : \Omega \to \mathbb{R}^3$ and the external charge density by $\rho_e : \Omega \to \mathbb{R}$. Since the magnetic particles are magnetically hard, the magnetic permeability of the material may be taken to be the same as that of the vacuum. The Maxwell equations may then be written as:

$$\mathbf{e} = -\text{grad}\xi, \qquad \text{div}(\mathbf{d}) = \rho_e, \qquad \mathbf{d} = \epsilon_0\mathbf{e} + \mathbf{p}, \qquad \text{in} \quad \mathcal{D}, \tag{5.2.1}$$

$$\mathbf{h} = -\text{grad}\phi^s - \text{grad}\phi^e \qquad \text{div}(\mathbf{b}) = 0, \qquad \mathbf{b} = \mu_0\mathbf{h} + \mathbf{b}^r \qquad \text{in} \quad \mathbb{R}^3, \tag{5.2.2}$$

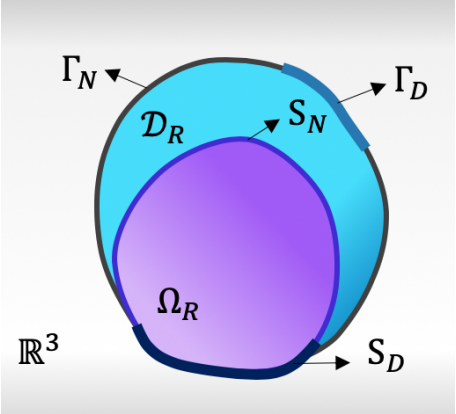

Figure 5.2: Continuum deformable body and surrounding medium in the reference configuration.

where $\mathcal{D}$ is the medium in which the body is located (see Fig. 5.2). $\xi : \mathcal{D} \to \mathbb{R}$ is the electric potential and $\mathbf{p} : \Omega \to \mathbb{R}^3$ is the polarization in the current configuration. The field $\mathbf{d}$ represents the electric displacement. True total magnetic field and magnetic flux density are denoted by $\mathbf{h}$ and $\mathbf{b}$, respectively. The electric permittivity of the vacuum is denoted by ϵ_0. Externally applied magnetic field and self-magnetic field due to existence of residual field both contribute to the total magnetic field. The external magnetic potential, which exists even if there in no material, is denoted by $\phi^e : \mathbb{R}^3 \to \mathbb{R}$ and the self magnetic potential, which vanishes if residual field is zero, is represented by $\phi^s : \mathbb{R}^3 \to \mathbb{R}$. We identify applied magnetic flux $\mathbf{b}^{\text{app}} = -\mu_0 \text{grad}\phi^e = \mu_0 \mathbf{h}^{\text{e}}$, where $\mathbf{h}^{\text{e}}$ is the external magnetic field. Since $\mathbf{b}^{\text{app}}$ is divergence free in $\mathbb{R}^3$, we can rewrite Eq.(5.2.2) as

$$\text{div}\mathbf{b}^s = \text{div}\left(-\mu_0 \text{ grad}\phi^s + \mathbf{b}^r\right) = 0 \qquad \text{in} \quad \mathbb{R}^3. \tag{5.2.3}$$

As conventional, the deformation gradient is $\mathbf{F} = \nabla\boldsymbol{\chi}$, the right Cauchy-Green strain tensor $\mathbf{C} = \mathbf{F}^T\mathbf{F}$ and the Jacobian $J = \det\mathbf{F}$. The Maxwell equations in the reference configuration can be written as

$$\nabla \cdot \widetilde{\mathbf{D}} = \widetilde{\rho}_e, \qquad \widetilde{\mathbf{D}} = -\epsilon_0 J\mathbf{C}^{-1}\nabla\xi + \mathbf{F}^{-1}\widetilde{\mathbf{P}}, \qquad \text{in} \quad \mathcal{D}_R \tag{5.2.4}$$

$$\text{and} \qquad \nabla \cdot \widetilde{\mathbf{B}}^s = 0, \qquad \widetilde{\mathbf{B}}^s = -\mu_0 J\mathbf{C}^{-1}\nabla\phi^s + \widetilde{\mathbf{B}}^r, \qquad \text{in} \quad \mathbb{R}^3, \tag{5.2.5}$$

where

$$\widetilde{\mathbf{P}} = J\mathbf{p}, \qquad \widetilde{\rho}_e = J\rho_e \qquad \text{and} \quad \widetilde{\mathbf{B}}^r = J\mathbf{F}^{-1}\mathbf{b}^r. \tag{5.2.6}$$

Dirichlet boundary condition $\boldsymbol{\chi} = \boldsymbol{\chi}_b$ are imposed on S_D and tractions $\widetilde{\mathbf{t}}^e$ are applied on S_N ($S_D \cup S_N = \partial\Omega_R$) (Figure 5.2). An external voltage $\xi = \xi_b$ may be imposed on Γ_D and $\widetilde{\mathbf{D}} \cdot \mathbf{N} = D_b$ on Γ_N where $\Gamma_D \cup \Gamma_N = \partial\mathcal{D}_R$ and $\mathbf{N}$ denotes unit normal to the boundary in the reference configuration. Also, $\text{grad}\phi^s \to \mathbf{0}$ as $|\mathbf{X}| \to \infty$.

The free energy of the system is postulated as [97, 230]

$$\mathcal{F}[\boldsymbol{\chi}, \widetilde{\mathbf{P}}] = U[\boldsymbol{\chi}, \widetilde{\mathbf{P}}] + \mathcal{E}^{\text{elec}}[\boldsymbol{\chi}, \widetilde{\mathbf{P}}] + \mathcal{E}^{\text{magnet}}[\boldsymbol{\chi}] - \int_{S_N} \widetilde{\mathbf{t}}^e \cdot \boldsymbol{\chi}, \tag{5.2.7}$$

where $U[\boldsymbol{\chi}, \widetilde{\mathbf{P}}]$ is the internal energy, $\mathcal{E}^{\text{elec}}[\boldsymbol{\chi}, \widetilde{\mathbf{P}}]$ and $\mathcal{E}^{\text{magnet}}[\boldsymbol{\chi}]$ are the total electric and magnetic field energy, respectively. The internal energy $U[\boldsymbol{\chi}, \widetilde{\mathbf{P}}]$ may be further sub-divided as [97, 230]

$$U[\boldsymbol{\chi}, \widetilde{\mathbf{P}}] = \int_{\Omega_R} \Psi[\mathbf{F}, \widetilde{\boldsymbol{P}}] = \int_{\Omega_R} W^{\text{elast}}[\mathbf{F}] + \int_{\Omega_R} \frac{|\widetilde{\mathbf{P}}|^2}{2J(\epsilon - \epsilon_0)}, \tag{5.2.8}$$

where ϵ is the electric permittivity of the material and the internal energy density function $\Psi : \mathbb{R}^{3\times3} \times \mathbb{R}^3 \to \mathbb{R}$ prescribes the electro-elastic constitutive laws of the material. Contribution of electric field energy $\mathcal{E}^{\text{elec}}$ to the total internal energy is expressed as

$$\mathcal{E}^{\text{elec}} = \int_{\mathcal{D}_R} \frac{\epsilon_0}{2} J\mathbf{C}^{-1}\nabla\,\xi \cdot \nabla\,\xi + \int_{\Gamma_D} \xi_b \mathbf{N} \cdot \widetilde{\mathbf{D}}. \tag{5.2.9}$$

Finally, $\mathcal{E}^{\text{magnet}}$ by

$$\mathcal{E}^{\text{magnet}} = \int_{\mathbb{R}^3} \frac{\mu_0}{2}|\mathbf{h}|^2 = \int_{\mathbb{R}^3} \frac{\mu_0}{2}|\text{grad}\phi^e|^2 + \int_{\mathbb{R}^3} \frac{\mu_0}{2}|\text{grad}\phi^s|^2 + \int_{\mathbb{R}^3} \mu_0 \text{grad}\phi^s \cdot \text{grad}\phi^e. \tag{5.2.10}$$

The first term on the right hand of Eq.(5.2.10) is independent of deformation and polarization and can be dropped. Multiplying both sides of Eq.(5.2.3) by the external magnetic

potential ϕ^e and integrating over $\mathbb{R}^3$, we can show that (5.2.10) can be written as

$$\mathcal{E}^{\text{magnet}} = \int_{\mathbb{R}^3} \frac{\mu_0}{2} |\text{grad}\phi^s|^2 - \int_\Omega \frac{1}{\mu_0} \mathbf{b}^r \cdot \mathbf{b}^{\text{app}} = \int_{\mathbb{R}^3} \frac{\mu_0}{2} J\mathbf{C}^{-1} \nabla\phi^s \cdot \nabla\phi^s - \int_{\Omega_R} \frac{1}{\mu_0} \mathbf{F}\widetilde{\mathbf{B}}^r \cdot \mathbf{b}^{\text{app}}. \tag{5.2.11}$$

The equilibrium state minimizes free energy of the system

$$\min_{(\boldsymbol{\chi}, \widetilde{\mathbf{P}}) \in \mathcal{S}} \mathcal{F}[\boldsymbol{\chi}, \widetilde{\mathbf{P}}], \tag{5.2.12}$$

where admissible space $\mathcal{S}$ is defined as

$$\mathcal{S} \equiv \{(\boldsymbol{\chi}, \widetilde{\mathbf{P}}) \in H^1(\Omega_R; \mathbb{R}^3) \times L^2(\Omega_R; \mathbb{R}^3) \quad | \quad \boldsymbol{\chi} = \boldsymbol{\chi}_b \qquad \text{on} \quad S_D\}. \tag{5.2.13}$$

Imposing Maxwell's equations as constraint, we use the standard variational process to derive the governing Euler-Lagrange equations associated with Eq.(5.2.12). We avoid presenting details of derivation here since the procedure is standard and key elements may be found in many references including (as example) Liu [97]. The system of equations for the equilibrium state are

$$\mathbf{F}^{-T} \nabla\xi + \frac{\widetilde{\mathbf{P}}}{J(\epsilon - \epsilon_0)} = \mathbf{0} \qquad \text{in} \quad \Omega_R, \tag{5.2.14}$$

$$\nabla \cdot \widetilde{\mathbf{D}} = \widetilde{\rho}_e \qquad \text{in} \quad \mathcal{D}_R, \tag{5.2.15}$$

$$\nabla \cdot \widetilde{\mathbf{B}}^s = 0 \qquad \text{in} \quad \mathbb{R}^3, \tag{5.2.16}$$

$$\nabla \cdot \left(\boldsymbol{\Sigma} + \widetilde{\boldsymbol{\Sigma}}^{MW}_{\text{elec}} + \widetilde{\boldsymbol{\Sigma}}^{MW}_{\text{magnet}} \right) = \nabla \cdot \left(\frac{1}{\mu_0} \mathbf{b}^{\text{app}} \otimes \widetilde{\mathbf{B}}^r \right) \qquad \text{in} \quad \Omega_R, \tag{5.2.17}$$

$$\nabla \cdot \left(\widetilde{\boldsymbol{\Sigma}}^{MW}_{\text{elec}} + \widetilde{\boldsymbol{\Sigma}}^{MW}_{\text{magnet}} \right) = \mathbf{0} \qquad \text{in} \quad \mathcal{D}_R \setminus \Omega_R, \tag{5.2.18}$$

$$\nabla \cdot \left(\widetilde{\boldsymbol{\Sigma}}^{MW}_{\text{magnet}} \right) = \mathbf{0} \qquad \text{in} \quad \mathbb{R}^3 \setminus \mathcal{D}_R, \tag{5.2.19}$$

$$[\![\boldsymbol{\Sigma} + \widetilde{\boldsymbol{\Sigma}}^{MW}_{\text{elec}} + \widetilde{\boldsymbol{\Sigma}}^{MW}_{\text{magnet}} - \frac{1}{\mu_0} \mathbf{b}^{\text{app}} \otimes \widetilde{\mathbf{B}}^r]\!] \cdot \mathbf{N} + \widetilde{\mathbf{t}}^e = \mathbf{0} \qquad \text{in} \quad \partial\Omega_R, \tag{5.2.20}$$

and $$[\![\widetilde{\boldsymbol{\Sigma}}^{MW}_{\text{elec}} + \widetilde{\boldsymbol{\Sigma}}^{MW}_{\text{magnet}}]\!] \cdot \mathbf{N} = \mathbf{0} \qquad \text{in} \quad \partial\mathcal{D}_R. \tag{5.2.21}$$

where

$$\boldsymbol{\Sigma} = \frac{\partial W^{\text{elast}}}{\partial \mathbf{F}}, \tag{5.2.22}$$

$$\widetilde{\boldsymbol{\Sigma}}^{MW}_{\text{elec}} = -\frac{\epsilon}{2} J|\mathbf{F}^{-T}\nabla\xi|^2\mathbf{F}^{-T} - \mathbf{F}^{-T}\text{Grad}\xi \otimes (-\epsilon_0 J\mathbf{C}^{-1}\nabla\xi + \mathbf{F}^{-1}\widetilde{\mathbf{P}}), \tag{5.2.23}$$

and $$\widetilde{\boldsymbol{\Sigma}}^{MW}_{\text{magnet}} = -\frac{\mu_0}{2} J|\mathbf{F}^{-T}\nabla\phi^s|^2\mathbf{F}^{-T} + \mu_0 J\mathbf{F}^{-T}\nabla\phi^s \otimes \mathbf{C}^{-1}\nabla\phi^s. \tag{5.2.24}$$

Identifying $\boldsymbol{\sigma} = \frac{1}{J}\boldsymbol{\Sigma}\mathbf{F}^T$, $\boldsymbol{\sigma}^{MW}_{\text{elec}} = \frac{1}{J}\boldsymbol{\Sigma}^{MW}_{\text{elec}}\mathbf{F}^T$ and $\boldsymbol{\sigma}^{MW}_{\text{magnet}} = \frac{1}{J}\boldsymbol{\Sigma}^{MW}_{\text{magnet}}\mathbf{F}^T$, we may also write equilibrium equations in the current configuration as

$$\text{div}\,(-\epsilon\text{grad}\xi) = \rho_e \qquad \text{in} \quad \mathcal{D}, \tag{5.2.25}$$

$$\text{div}\,(-\mu_0\ \text{grad}\phi^s + \mathbf{b}^r) = 0 \qquad \text{in} \quad \mathbb{R}^3, \tag{5.2.26}$$

$$\text{div}\left(\boldsymbol{\sigma} + \boldsymbol{\sigma}^{MW}_{\text{elec}} + \boldsymbol{\sigma}^{MW}_{\text{magnet}}\right) = \text{div}(\frac{1}{\mu_0}\mathbf{b}^{\text{app}} \otimes \mathbf{b}^r) \qquad \text{in} \quad \Omega, \tag{5.2.27}$$

$$\text{div}\left(\boldsymbol{\sigma}^{MW}_{\text{elec}} + \boldsymbol{\sigma}^{MW}_{\text{magnet}}\right) = \mathbf{0} \qquad \text{in} \quad \mathcal{D}\setminus\Omega, \tag{5.2.28}$$

$$\text{div}\left(\boldsymbol{\sigma}^{MW}_{\text{magnet}}\right) = \mathbf{0} \qquad \text{in} \quad \mathbb{R}^3\setminus\mathcal{D}, \tag{5.2.29}$$

$$[\![\boldsymbol{\sigma} + \boldsymbol{\sigma}^{MW}_{\text{elec}} + \boldsymbol{\sigma}^{MW}_{\text{magnet}} - \frac{1}{\mu_0}\mathbf{b}^{\text{app}} \otimes \mathbf{b}^r]\!] \cdot \mathbf{n} + \mathbf{t}^e = \mathbf{0} \qquad \text{on} \quad \partial\Omega \tag{5.2.30}$$

and $$[\![\boldsymbol{\sigma}^{MW}_{\text{elec}} + \boldsymbol{\sigma}^{MW}_{\text{magnet}}]\!] = \mathbf{0}, \qquad \text{on} \quad \partial\mathcal{D}, \tag{5.2.31}$$

where we have used Eq.(5.2.14) to eliminate polarization from the equations.

5.2.2 Symmetry of the Cauchy stress

A frequent contention is that in the context of magnetism "stress" is asymmetric. Usually, such statements emerge due to the difference in how the so-called "stress" is identified. Here in this section, we use the method of virtual power to prove symmetry of the *true* Cauchy stress that consists of several sub-parts. Each of the sub-part can certainly be asymmetric but the to the total Cauchy stress as identified by us below is symmetric. We write the rate of change of internal energy as

$$\mathcal{W} = \int_{\Omega_R} (\boldsymbol{\Sigma} + \widetilde{\boldsymbol{\Sigma}}^{MW}_{\text{elec}} + \widetilde{\boldsymbol{\Sigma}}^{MW}_{\text{magnet}}) \cdot \dot{\mathbf{F}}. \tag{5.2.32}$$

The power expended by any rigid transformation is zero. Therefore, for any skew symmetric tensor $\mathbf{Q}$ we have

$$\mathcal{W} = \int_P (\boldsymbol{\Sigma} + \widetilde{\boldsymbol{\Sigma}}^{MW}_{\text{elec}} + \widetilde{\boldsymbol{\Sigma}}^{MW}_{\text{magnet}}) \cdot \mathbf{QF} = \int_P (\boldsymbol{\Sigma} + \widetilde{\boldsymbol{\Sigma}}^{MW}_{\text{elec}} + \widetilde{\boldsymbol{\Sigma}}^{MW}_{\text{magnet}}) \mathbf{F}^T \cdot \mathbf{Q} = 0. \tag{5.2.33}$$

where P is any arbitrary closed smooth subset of Ω_R. Consequently, $(\boldsymbol{\Sigma}+\widetilde{\boldsymbol{\Sigma}}^{MW}_{\text{elec}}+\widetilde{\boldsymbol{\Sigma}}^{MW}_{\text{magnet}})\mathbf{F}^T \cdot \mathbf{Q} = 0$ and since $\mathbf{Q}$ is a skew tensor we can conclude that

$$(\boldsymbol{\Sigma} + \widetilde{\boldsymbol{\Sigma}}^{MW}_{\text{elec}} + \widetilde{\boldsymbol{\Sigma}}^{MW}_{\text{magnet}})\mathbf{F}^T = \mathbf{F}(\boldsymbol{\Sigma} + \widetilde{\boldsymbol{\Sigma}}^{MW}_{\text{elec}} + \widetilde{\boldsymbol{\Sigma}}^{MW}_{\text{magnet}})^T, \tag{5.2.34}$$

or equivalently

$$\boldsymbol{\sigma} + \boldsymbol{\sigma}^{MW}_{\text{elec}} + \boldsymbol{\sigma}^{MW}_{\text{magnet}} = (\boldsymbol{\sigma} + \boldsymbol{\sigma}^{MW}_{\text{elec}} + \boldsymbol{\sigma}^{MW}_{\text{magnet}})^T. \tag{5.2.35}$$

5.3 Numerical solution procedure for incompressible materials

The equations in the preceding section can only be solved analytically for simple geometries. To handle non-trivial boundary value problems we have developed a finite element solution for the our framework. There are several implementations for similar coupled problems available in the literature [231, 232, 25]. We use an approach which enables numerical solutions without using any commercial packages. Our computational procedure for incompressible materials, with minor modifications, can be used for compressible materials as well. The weak form of the governing equations of the system is given as

$$\int_{\mathcal{D}_R} \nabla w_1 \cdot \widetilde{\mathbf{D}} + \int_{\mathcal{D}_R} w_1 \widetilde{\rho}_e = 0, \tag{5.3.1}$$

$$\int_{\mathbb{R}^3} \nabla w_2 \cdot \widetilde{\mathbf{B}}^s = 0, \tag{5.3.2}$$

$$\int_{\mathbb{R}^3} \left[\nabla \mathbf{w}_3 : \left(\theta_1 \boldsymbol{\Sigma} - \theta_1 \mathcal{L}_a \mathbf{F}^{-T} + \theta_2 \widetilde{\boldsymbol{\Sigma}}^{MW}_{\text{elec}} + \widetilde{\boldsymbol{\Sigma}}^{MW}_{\text{magnet}} - \theta_1 \frac{1}{\mu_0} \mathbf{b}^{\text{app}} \otimes \widetilde{\mathbf{B}}^r \right) \right] = \mathbf{0} \tag{5.3.3}$$

and $$\int_{\Omega_R} [w_4 \, (\det \mathbf{F} - 1)] = 0, \tag{5.3.4}$$

where $(w_1, w_2, \mathbf{w}_3, w_4) \in \mathcal{W}$ and

$$\begin{aligned}\mathcal{W} \equiv &\{(w_1, w_2, \mathbf{w}_3, w_4) \in H^1(\mathcal{D}_R;\mathbb{R}) \times H^1(\mathbb{R}^3;\mathbb{R}) \times H^1(\mathbb{R}^3;\mathbb{R}^3) \times L_2(\Omega_R;\mathbb{R})\big| \\ &w_1 = 0 \quad \text{on} \quad \Gamma_D, \quad \mathbf{w}_3 = 0 \quad \text{on} \quad S_D\}.\end{aligned} \tag{5.3.5}$$

Also, θ_1 (resp. θ_2) is equal to 1 inside Ω_R (resp. $\mathcal{D}_R$) and zero otherwise. The hydrostatic pressure $\mathcal{L}_a$ is a Lagrange multiplier which has been introduced to enforce the incompressibility constraint to avoid numerical oscillations and volumetric locking. We make use of Taylor-Hood elements which implies that the order of shape functions used for the discretization of displacement is one order higher than the that for the pressure. The Taylor-Hood elements have been successfully used in various problems [187, 188]. It can be proved that Taylor-Hood elements satisfy the Ladyzhenskaya–Babuska–Brezzi (LBB) condition which is required for the stability of mixed method in incompressible elasticity and Stokes flow [233, 234, 235, 236]. Therefore, we use quadratic interpolation for displacement and linear shape function for electric potential, magnetic potential and hydrostatic pressure. The actual solution of the equations is through the open-source solver FEniCS [181][3].

5.4 Illustrative analytical examples

5.4.1 Magnetoelectricity under tension or compression

Consider the hard magnetic soft electret configuration shown in Fig. 5.3. This electret consists of two different materials on top and bottom which are referenced with subscripts "t" and "b", respectively. Let $\mathbf{X} = X\mathbf{e}_X + Y\mathbf{e}_Y + Z\mathbf{e}_Z$ be the representation of the points in the Lagrange coordinates while points in the Euler coordinates are denoted by $\mathbf{x} = x\mathbf{e}_x + y\mathbf{e}_y + z\mathbf{e}_z$. The top layer has thickness H_t and thickness of bottom layer is denoted by H_b. There is a layer of charge between two layers with surface charge density q_0. The material is sandwiched between two mechanically compliant electrodes on top and bottom and short circuit boundary condition is imposed. There is uniform residual magnetic flux density $\widetilde{\mathbf{B}}^r = B_t^r \mathbf{e}_X$ (resp. $\widetilde{\mathbf{B}}^r = B_t^r \mathbf{e}_X$) in top (resp. bottom) layer. The material will

[3]The FEniCS files to computationally solve the equations are available on....

deform in response to an externally applied magnetic flux density $\mathbf{b}^{\text{app}} = b^{\text{app}}\mathbf{e}_x$. Since the two layers have different material properties, deformation in two layers will not be the same[4].

Let the deformation gradient tensor for each layer be expressed as

$$\mathbf{F} = \lambda_t \mathbf{e}_x \otimes \mathbf{e}_X + \lambda_t^{-1/2}\mathbf{e}_y \otimes \mathbf{e}_Y + \lambda_t^{-1/2}\mathbf{e}_z \otimes \mathbf{e}_Z \qquad \text{for} \quad H_b < X < H_b + H_t, \tag{5.4.1}$$

and

$$\mathbf{F} = \lambda_b \mathbf{e}_x \otimes \mathbf{e}_X + \lambda_b^{-1/2}\mathbf{e}_y \otimes \mathbf{e}_Y + \lambda_b^{-1/2}\mathbf{e}_z \otimes \mathbf{e}_Z \qquad \text{for} \quad 0 < X < H_b. \tag{5.4.2}$$

Considering uniform deformation, thickness of each layer in the deformed configuration

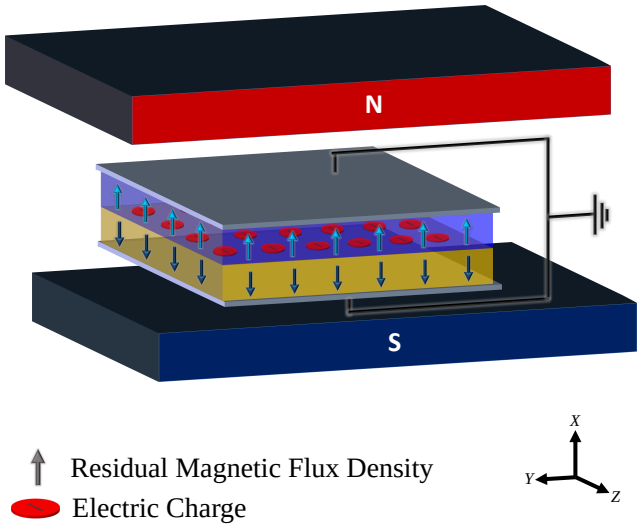

Figure 5.3: The schematic of bilayer HMSE made of two layers with different material properties.

may be determined to be:

$$h_t = \lambda_t H_t, \tag{5.4.3}$$

and

$$h_b = \lambda_b H_b. \tag{5.4.4}$$

[4]It is important to note that unequal deformation in the two layers may lead to the bending. However, for this simplified example, we ignore this contribution

Moreover, considering short circuit boundary condition and assuming uniform electric field in both top and bottom layers, electric fields can be derived to be

$$\mathbf{e} = -\frac{\mathrm{d}\xi}{\mathrm{d}x} = \begin{cases} \frac{V}{h_t} & \text{for} \quad h_b < X < h_b + h_t \\ -\frac{V}{h_b} & \text{for} \quad 0 < X < h_b, \end{cases} \tag{5.4.5}$$

where, using Maxwell's equations, V is determined from the following equation

$$\epsilon_t \frac{V}{h_t} + \epsilon_b \frac{V}{h_b} = q_0. \tag{5.4.6}$$

We use the incompressible neo-Hookean constitutive relation:

$$W^{elast}[\mathbf{F}] = \frac{G_i}{2}(\mathrm{tr}(\mathbf{F}^T\mathbf{F}) - 3) \qquad \text{for} \quad i = t, b \tag{5.4.7}$$

where G denotes the shear modulus of the material. Ignoring the self-magnetic field ($\mathrm{Grad}\phi^s \approx 0$), the equilibrium equations for each layer reduces to

$$(\lambda_t^2 - \frac{1}{\lambda_t}) - \lambda_t \bar{B}_t + \frac{\epsilon_t}{G_t}\left(\frac{V}{h_t}\right)^2 = 0, \tag{5.4.8}$$

$$\text{and} \qquad (\lambda_b^2 - \frac{1}{\lambda_b}) - \lambda_b \bar{B}_b + \frac{\epsilon_b}{G_b}\left(\frac{V}{h_b}\right)^2 = 0. \tag{5.4.9}$$

where $\bar{B} = \mu_0^{-1} G^{-1} \widetilde{\mathbf{B}}^r \cdot \mathbf{b}^{\mathrm{app}}$ and $\bar{B}_t$ and $\bar{B}_b$ are the corrseponding values of $\bar{B}$ in top and bottom layers, respectively. We can then analytically determine the linearized solution for the above equations assuming $|\lambda_b - 1| \ll 1$ and $|\lambda_t - 1| \ll 1$:

$$\lambda_t \approx \frac{1}{1 - \bar{B}_t/3} - \frac{\epsilon_t/3G_t}{1 - \bar{B}_t/3}\left(\frac{H_b q_0}{H_t\epsilon_b + H_b\epsilon_t}\right)^2, \tag{5.4.10}$$

$$\text{and} \qquad \lambda_b \approx \frac{1}{1 - \bar{B}_b/3} - \frac{\epsilon_b/3G_b}{1 - \bar{B}_b/3}\left(\frac{H_t q_0}{H_b\epsilon_t + H_t\epsilon_b}\right)^2. \tag{5.4.11}$$

Unless an external electric field is applied to the material, the magnitude of electric Maxwell stress is often negligible. Ignoring the effect of electric Maxwell stress in Eqs.(5.4.10) and

(5.4.11), we can rewrite the last two equations as

$$\lambda_t - 1 \approx \frac{B_t^r b_t^{\text{app}}}{3\mu_0 G_t} \tag{5.4.12}$$

$$\text{and} \qquad \lambda_b - 1 \approx \frac{B_b^r b_b^{\text{app}}}{3\mu_0 G_b}. \tag{5.4.13}$$

With the stretches in each layer at hand, we can determine both the electric field and electric displacement. Electric displacement in top layer is expressed as $\widetilde{\mathbf{D}} = D_t \mathbf{e}_X$ where D_t is determined by substituting Eq.(5.4.6) into Eq.(5.4.5):

$$D_t \approx D^i + \frac{qH_t H_b \epsilon_b \epsilon_t (\lambda_b - \lambda_t)}{(H_t \epsilon_b + H_b \epsilon_t)^2}, \tag{5.4.14}$$

where D^i is the deformation independent part of the electric displacement. For brevity and ease in presentation of equation, we have assumed $\mathbf{d} \approx \widetilde{\mathbf{D}}$ in derivation of Eq.(5.4.14).

For conventional magnetostrictive/piezoelectric composites, magnetoelectric coupling coefficient is defined as [183, 184]

$$\alpha_{ij} = \frac{\partial P_i}{\partial h_j^e}, \tag{5.4.15}$$

where h_i^e and P_j, respectively, are the components of the magnetic field and electric polarization defined in a linear framework where there is no difference between reference and current configurations. Also, magnetoelectric voltage coefficient $\boldsymbol{\alpha}_{\text{ME}}$ is defined as $\boldsymbol{\alpha} = \boldsymbol{\epsilon}\boldsymbol{\alpha}_{\text{ME}}$, where $\boldsymbol{\epsilon}$ is the electric permittivity tensor of the material [185, 186]. In experimental settings and under closed circuit boundary condition, polarization is often determined by measuring electric charges. This is due to the reason that when the electric field is zero, electric displacement and electric polarization are equivalent. Similarly, here, we perform a thought experiment and define the effective ME voltage coupling coefficient for HMSE $\alpha_{\text{ME}}^{\text{eff}}$ as

$$\alpha_{\text{ME}}^{\text{eff}} = \frac{\mu_0}{\epsilon^{\text{eff}}} \frac{\partial D_t}{\partial b^{\text{app}}}, \tag{5.4.16}$$

where ϵ^{eff} is determined from following equation

$$\frac{H_t + H_b}{\epsilon^{\text{eff}}} = \frac{H_t}{\epsilon_t} + \frac{H_b}{\epsilon_b}. \tag{5.4.17}$$

The effective magnetoelectric voltage coefficient of the material can also be written in terms of the output charges $\Delta Q = D_t A$ and the effective capacitance of the material $C^{\text{eff}} = \frac{\epsilon^{\text{eff}} A}{H}$

$$\alpha_{\text{ME}}^{\text{eff}} = \frac{1}{C^{\text{eff}} H} \frac{\partial(\Delta Q)}{\partial h^e}, \tag{5.4.18}$$

where h^e is the external magnetic field ($\mathbf{h}^{\text{e}} = h^e \mathbf{e}_X$), A is the surface area of the electrodes and $H = H_t + H_b$ is the total thickness of the material. Effective voltage coefficient for the hard magnetic soft electret (shown in Fig. 5.3) is derived by substituting Eq.(5.4.10), (5.4.11) and (5.4.14) into Eq.(5.4.16)

$$\alpha_{\text{ME}}^{\text{eff}} = \frac{1}{\epsilon^{\text{eff}}} \frac{q_0 H_t H_b \epsilon_b \epsilon_t}{(H_t \epsilon_b + H_b \epsilon_t)^2} \times \frac{1}{3} \left(\frac{B_b^r}{G_b} - \frac{B_t^r}{G_t} \right). \tag{5.4.19}$$

If the bottom layer does not deform in response to the magnetic field, $\alpha_{\text{ME}}^{\text{eff}}$ can be be further simplified as

$$\alpha_{\text{ME}}^{\text{eff}} = -\frac{1}{\epsilon^{\text{eff}}} \frac{q_0 H_t H_b \epsilon_b \epsilon_t}{(H_t \epsilon_b + H_b \epsilon_t)^2} \times \frac{B_t^r}{3 G_t}. \tag{5.4.20}$$

Several interesting aspects may be noted in Eq.(5.4.20). First, the ME voltage coupling coefficient of the HMSE is *independent* of external magnetic field. Therefore, as external field approaches to zero, $\alpha_{\text{ME}}^{\text{eff}}$ remains unchanged. This behavior is in contrast with the behavior of ME composites and SMSEs where their ME voltage coupling coefficient vanishes at zero external magnetic field. Also, Eq.(5.4.20) shows $\alpha_{\text{ME}}^{\text{eff}} \propto B^r$ for HMSEs while we have shown that for SMSEs $\alpha_{\text{ME}}^{\text{eff}} \propto \mu_0 h^e$. This implies that the voltage coupling coefficient of a HMSE with $B^r \sim 1\text{T}$ under external field $B^r \sim 1\text{mT}$ is three orders of magnitude larger than a SMSE material under same external magnetic field.

5.4.2 Flexure deformation and magnetoelectricity

Flexure is arguably the most suitable deformation mode for energy harvesting and therefore it is of interest to explore the ME effect under bending. We also remark that the resonance frequency of the bending model is smaller than for tension and compression. Finally, since bending is inherently a non-uniform deformation process, a strong electromechanical coupling can be generated in electret materials [178] which may then amplify the magnetoelectric response. Pertaining to this, we note that it is not easily possible to create bending deformation with SMSE materials however quite simple in the context of hard magnetic soft materials as already demonstrated in past work [25]. The flexure problem for HMSE materials is rather difficult to solve analytically however we attempt an approximate solution using Euler-Bernoulli beam theory assumptions (Fig. 5.4). We will comment on the accuracy of the results in the next section where we will present numerical solutions.

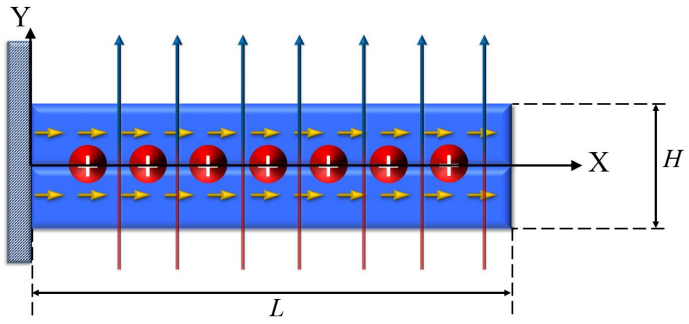

Figure 5.4: Schematic of HMSE material that undergoes bending deformation in response to applied magnetic field. The gold arrows show the direction of residual flux density and red circles are electric charges.

Consider the hard magnetic material shown in the Fig. 5.4. The residual magnetic flux density of the material is uniformly aligned along the axis of the beam $\widetilde{\mathbf{B}}^r = B^r \mathbf{e}_X$. Due to the pattern of residual magnetic dipoles, this particular configuration undergoes bending deformation in response to applied magnetic field across the thickness of the material. We assume the deformation is small ($|\nabla \mathbf{u}| \ll 1$) and the effect of the Maxwell stress is negligible. The applied magnetic flux density is denoted by $\mathbf{b}^{\text{app}} = b^{app} \mathbf{e}_Y$. Using Euler-Bernoulli beam

theory, the displacement $\mathbf{u}$ can be expressed as

$$\mathbf{u} = -Y\frac{\partial u_Y}{\partial X}\mathbf{e}_X + u_Y\mathbf{e}_Y. \tag{5.4.21}$$

We assume a unit width for the beam and use Euler-Bernoulli theory to express the internal energy of the material as

$$U[u_Y] = \int_0^L \left(\frac{3}{2}GI\left(\frac{\partial^2 u_Y}{\partial X^2}\right)^2 - \frac{H}{\mu_0}\frac{\partial u_Y}{\partial X}b^{app}B^r\right)\mathrm{d}X. \tag{5.4.22}$$

The moment of inertia for beam with unit width is $I = \frac{1}{12}H^3$. The equilibrium equations of the beam is derived using standard calculus of variation as

$$\begin{aligned}
&\frac{\mathrm{d}U[u_Y+\varepsilon\eta]}{\mathrm{d}\varepsilon}\bigg|_{\varepsilon=0} = \int_0^L \left(3GI\frac{\partial^2 u_Y}{\partial X^2}\frac{\partial^2\eta}{\partial X^2} - \frac{H}{\mu_0}\frac{\partial\eta}{\partial X}b^{app}B^r\right)\mathrm{d}X = \\
&\left(3GI\frac{\partial^2 u_Y}{\partial X^2}\frac{\partial\eta}{\partial X}\right)\Big]_0^L - \left(3GI\frac{\partial^3 u_Y}{\partial X^3}\eta + \frac{H}{\mu_0}b^{app}B^r\eta\right)\Big]_0^L \\
&+ \int_0^L \left[\eta\frac{\partial}{\partial X}\left(3GI\frac{\partial^3 u_Y}{\partial X^3} + \frac{1}{\mu_0}b^{app}B^r\right)\right]\mathrm{d}X = 0.
\end{aligned} \tag{5.4.23}$$

Thus, the deflection of cantilever beam may be obtained by solving the following system of equations

$$\begin{aligned}
&\frac{\partial}{\partial X}\left(3GI\frac{\partial^3 u_Y}{\partial X^3} + \frac{1}{\mu_0}b^{app}B^r\right) = 0, \\
&u_Y(X=0) = \frac{\partial u_Y}{\partial X}\bigg|_{X=0} = \frac{\partial^2 u_Y}{\partial X^2}\bigg|_{X=L} = 0, \\
\text{and}\qquad &\left(3GI\frac{\partial^3 u_Y}{\partial X^3} + \frac{H}{\mu_0}b^{app}B^r\right)\bigg|_{X=L} = 0.
\end{aligned} \tag{5.4.24}$$

Considering a uniform magnetic field and uniform residual magnetic field, the magnetic field induced deflection of the beam can simply be obtained by solving system of equations (5.4.24)

$$\frac{u_Y}{L} = 2(AR)^2\frac{b^{app}B^r}{G\mu_0}\left((\frac{x}{L})^2 - \frac{1}{3}(\frac{x}{L})^3\right), \tag{5.4.25}$$

where $AR = L/H$ is the aspect ratio of the material. Thus, the local curvature of the beam

$\kappa = \frac{\partial^2 u}{\partial x^2}$ is determined as

$$\frac{\partial^2 u}{\partial x^2} = \frac{b^{app} B^r}{G\mu_0} \frac{4L}{H^2} \left(1 - \frac{x}{L}\right). \tag{5.4.26}$$

We cannot use the solution provided in this section to determine output charge of a hard magnetic soft electret under bending deformation because it was a linear decoupled problem. The relation between magnetic field and curvature is illustrated in Eq.(5.4.26). To obtain an analytical relation between the output charge and magnetic field, the fully coupled problem has to be solved which is a rather difficult nonlinear problem. However, Rahmati et al. [178] presented a simple relationship between curvature and output charge for an electret under pure bending. According to their model, the output charge is related to curvature κ through $D^t = \frac{1}{4} q_0 H \kappa$ where q_0 is the surface charge density at the interface of two materials. Therefore, for illustrative purposes, the scale of the output charge for a hard magnetic soft electret with uniform distribution of residual magnetic flux density under bending deformation can be roughly approximated as

$$D^t \propto \frac{b^{app} B^r}{G\mu_0} AR q_0, \tag{5.4.27}$$

and, as a result, we have

$$\alpha_{\mathrm{ME}} \propto (AR) \frac{B^r}{G} \frac{q_0}{\epsilon^{\mathrm{eff}}}. \tag{5.4.28}$$

Eq.(5.4.28) shows that the ME voltage coupling coefficient of the material shown in the Fig. 5.4 linearly depends on the aspect ratio of the material.

5.4.3 Shape programmable property of HMSEs

Hard magnetic soft elastomers can be quite easily programmed to develop any desirable deformation in response to external magnetic field by designing the residual flux density profile of the material [180]. As the ME response of the material directly depends on the actuation strain in these materials, the ME response too can be designed by suitably programming the residual flux density. The profile of the residual flux density in these materials depends on the deformation imposed to the material during magnetization step. In this section, we will show that if the material is helt in a bent configuration during

the magnetization step, the residual magnetic profile of the material will reflect this bent shape. This behavior can be generalized to any desired pattern of deformation. We have chosen flexure deformation mode for illustrative purpose because our theoretical calculations showed that the ME effect mediated with bending deformation can lead to a significantly strong ME effect (Eq.(5.4.28)). We calculate the profile for residual magnetic flux density of the material in this section and subsequently use a numerical approach (next section) to evaluate the ME response.

Figure 5.5 illustrates the three steps for creation of a PHMSE which bends in response to magnetic field. Initially, the magnetic micro-particles inside the material are randomly oriented and the residual magnetic flux density of the material is zero(Fig. 5.5a). In the second step, a pure bending deformation is imposed to the material and a large magnetic field is imposed on the structure(Fig. 5.5b). The deformation gradient tensor for this deformation is denoted by $\mathbf{F}_{\mathrm{b}}$. In this step, magnetic micro particles rotate and align themselves with the external field and, as a result, a net magnetic flux density is created inside the material. The re-alignment of the magnetic micro particles itself does not create any substantive deformation in the material. Due the high coercivity and high residual magnetic flux density of NdFeB micro particles, subsequent to the alignment, the magnetization profile remains stable even after we the magnetization magnetic field of step two is turned off. Thus, in the last step, we remove the magnetic field used to magnetize the material and reverse the deformation. The magnetic micro particles are anchored to the matrix material and they rotate as the material element rotates. Therefore, the reversed deformation developed from step two to step three leads to creation of the residual magnetic flux density profile shown in the Fig. 5.5c.

We denote the magnetic flux density in step three by $\widetilde{\mathbf{B}}^r$. The residual magnetic flux density in the configuration shown in the step two is denoted by $\mathbf{b}^{\mathrm{mag}}$ and is expressed as

$$\mathbf{b}^{\mathrm{mag}} = -B^r \cos(\theta)\mathbf{e}_r + B^r \sin(\theta)\mathbf{e}_\theta. \tag{5.4.29}$$

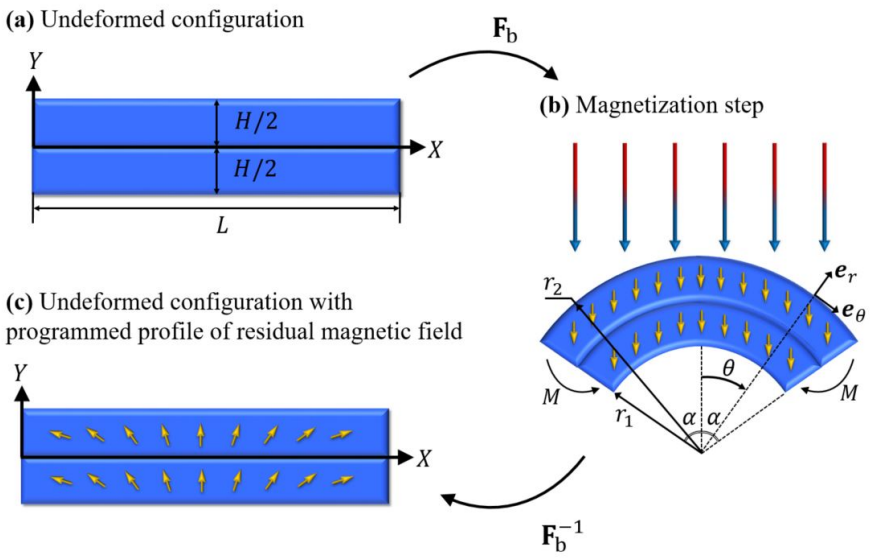

Figure 5.5: The steps for creating PHMSE. (a) Undeformed configuration. (b) The desired deformation is induced and the pre-magnetization magnetic field is applied. (c)The imposed deformation and applied magnetic field is removed.

The magnetic flux densities $\mathbf{b}^{\text{mag}}$ and $\widetilde{\mathbf{B}}^r$ are related to each other through the third of Eq.(5.2.6) $\widetilde{\mathbf{B}}^r = \det(\mathbf{F}_\text{b})\mathbf{F}_\text{b}^{-1}\mathbf{b}^{\text{mag}}$. Therefore, we need to determine the deformation $\mathbf{F}_\text{b}$ in order to determine the profile for magnetization flux density. The analytical solution for large elastic deformation of material under pure bending was first presented by Rivlin [103]. Motivated by Rivlin's solution, recently we have derived the solution for bending deformation of electret materials [178]. We simply present the final expression for $\mathbf{F}_\text{b}$. The reader is referred to Rivlin [103] and Rahmati et al. [178] for further details.

The material point in the undeformed configuration (step one and three) are denoted by $\mathbf{X} = X\mathbf{e}_X + Y\mathbf{e}_Y$. The spatial points in step two are denoed by $\mathbf{r} = r\mathbf{e}_r$. For a deformation that is a pure symmetric plane strain bending such that material point each plane originally located in plane with normal $\mathbf{e}_Y$ (resp. $\mathbf{e}_X$) will transfer to a plane with normal $\mathbf{e}_r$ (resp. $\mathbf{e}_\theta$) as a result of this deformation. The desired bending angle α (see Fig. 5.5b) is achieved by controlling the bending moment applied to the material. Stipulating incompressibility,

the deformation gradient $\mathbf{F}_b$ is determined as

$$\mathbf{F}_{\mathrm{b}} = \frac{L}{2\alpha \times r(Y)} \mathbf{e}_r \otimes \mathbf{e}_Y + \frac{2\alpha \times r(Y)}{L} \mathbf{e}_\theta \otimes \mathbf{e}_X, \tag{5.4.30}$$

where

$$r(Y) = \sqrt{(r_2^2 - r_1^2)\frac{Y}{H} + \frac{r_2^2 + r_1^2}{2}} \quad \text{and} \qquad \theta(X) = \frac{(2Y - L)\alpha}{L}. \tag{5.4.31}$$

and r_1 and r_2, respectively, are radii of curved surfaces initially located at $Y = 0$ and $Y = H$ (Fig. 5.5b). For a neo-Hookean constitutive response and traction-free boundary surfaces normal to $\mathbf{e}_r$, r_1 and r_2 may be determined by solving the following nonlinear system of algebraic equation

$$\frac{L}{\alpha} = \frac{r_2^2 - r_1^2}{H} \quad \text{and} \quad \left(\frac{r_2 - r_1}{H}\right)^4 = \frac{16\frac{r_2^2}{r_1^2}}{\left(\frac{r_2}{r_1} + 1\right)^4}. \tag{5.4.32}$$

Finally, the magnetic flux density at each point of PHMSE is determined substituting Eqs.(5.4.30) and (5.4.29) into third of Eq.(5.2.6)

$$\widetilde{\mathbf{B}}^r = \frac{B^r L}{2\alpha r(Y)} \sin\left[\theta(X)\right] \mathbf{e}_X - \frac{2B^r \alpha r(Y)}{L} \cos\left[\theta(X)\right] \mathbf{e}_Y. \tag{5.4.33}$$

Clearly, the obtained profile for the residual flux density restores information about the deformed configuration in the magnetization step. We will use this profile in the subsequent section in our numerical simulations. Unless otherwise stated, we set value of $B^r = 0.0767$ T and use the profile given in Eq.(5.4.33) in all simulation results.

5.5 Numerical results, comparison with experiments and discussion

In this section, we use the formulation presented in the section 5.3 to simulate the ME behavior of HMSE and PHMSEs using the open source finite element code, FEniCS. In order to check accuracy of our computational model, first we compare our results with the

available theoretical, experimental and numerical results. Then, we present solutions for the bending deformation of HMSEs and PHMSEs. Throughout this section, we have assumed that the self magnetic field is negligible($\nabla\phi^s \sim 0$). We use the incompressible neo-Hookean constitutive law given in the Eq.(5.4.7) and plane strain conditions. Unless otherwise stated, Ythe oung's elastic modulus of the material is set to 55 KPa, the magnitude of the residual flux density is $B^r = 0.0767$, the electric permittivity of the material is equal to $\epsilon = 5.0676\epsilon_0$ and the interface charge density is q_0 =0.0488 mC/m^2. Also, the length and the thickness of the sample, respectively, are set to be $L = 22$ mm, $H = 1.85$ mm. These numerical values are consistent with the material fabricated and examined by the Qian Deng Research Group.

5.5.1 The bending deformation of hard magnetic soft elastomer without electrets

As the first step of our analysis, we simulate the material shown in the Fig. 5.4 without considering effects of external charges ($\widetilde{\rho}_e = 0$). The residual flux density is uniformly aligned with the axis direction of the material and an external magnetic field is applied across the thickness of the material. This problem has been solved by Zhao et al. [25] both numerically (using an ABAQUS UMAT) and experimentally. Figure 5.6 shows that there is an excellent agreement between our finite element results and the experimental and simulation results given by Zhao et al. [25]. Figure 5.6(a) compared the deformed configuration from our simulation with the experimental observations for two materials with two different aspect ratios under the same magnetic field. Also, Fig. 5.6(b) shows that the deflection versus dimensionless magnetic field for materials with different aspect ratios and we see excellent agreement with Zhao et al. [25].

5.5.2 Magnetoelectric energy harvesting using parallel plate capacitor made of hard magnetic soft elastomer

In the next step, we illustrate the ability of electric energy harvesting by applying an external magnetic field to a parallel plate capacitor made of hard magnetic soft elastomer and compare the numerical results with analytical results. Consider the material shown in

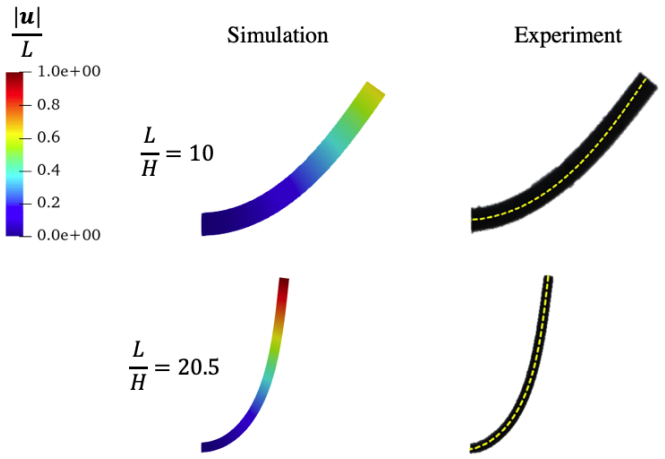

(a)

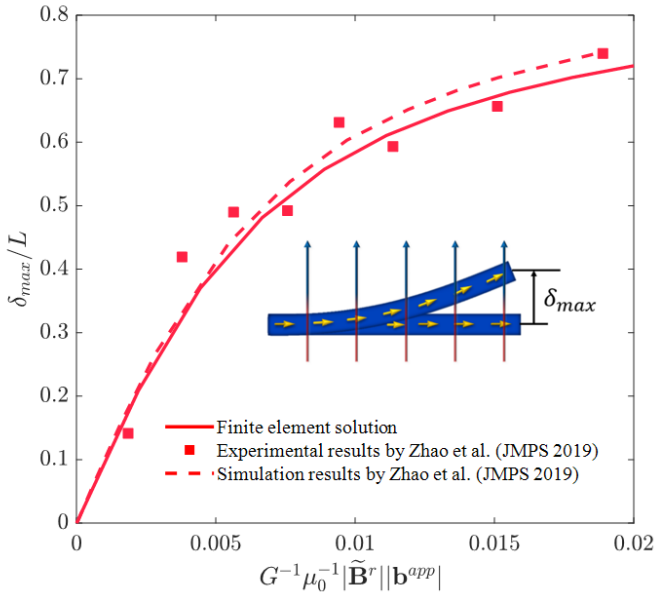

(b)

Figure 5.6: Comparison of the current numerical solution with experimental and simulation results given by Zhao et al. [25]. (a)The deformed configuration for $\frac{|\mathbf{b}^r||\mathbf{B}^{\text{app}}|}{G\mu_0} = 0.0094$ and $AR = \frac{L}{H} = 10$. (b) The vertical displacement of the tip of the beam.

the Fig. 5.7(a) where residual magnetic field is aligned parallel with the thickness direction of the material. A voltage difference V has been applied across the thickness of the material. Once a magnetic field is applied to the material along the thickness direction and in the opposite direction with respect to residual field, the material tends to compress. This compression increases the electric field inside the material and enables material to do work

on the boundary electric device. This work can be determined as

$$W = -\int_{\Gamma_D} \left[\xi_b \left(\widetilde{\mathbf{D}} - \widetilde{\mathbf{D}}^i\right) \cdot \mathbf{N}\right], \tag{5.5.1}$$

where $\widetilde{\mathbf{D}}^i = \lim_{\mathbf{B}^{app}\to\mathbf{0}} \widetilde{\mathbf{D}}$. The value of W can be determined analytically. The procedure for analytical solution is very similar to what was mentioned in section 5.4.1. The only difference is that, here, we enforce a plane strain condition to be consistent with numerical calculations. Under plane strain condition, equilibrium equation is written as

$$(\lambda^4 - 1) - \lambda^3 \frac{\widetilde{\mathbf{B}}^r \cdot \mathbf{b}^{app}}{G\mu_0} + \frac{\epsilon}{G}\left(\frac{V}{H}\right)^2 = 0, \tag{5.5.2}$$

where λ is the stretch along the thickness direction. Assuming $|\lambda - 1| \ll 1$, above equation can be linearized and solved for λ. The calculated value of the stretch can be substituted in Eq.(5.5.1) to determine energy harvested at the boundary. Therefore, the electric work done on the boundary electric device for $G^{-1}\mu_0^{-1}|\mathbf{b}^r||\mathbf{b}^{app}| \ll 1$ is determined as

$$\bar{W} = \frac{W}{A} \times \left(\epsilon \frac{V}{H} \times \frac{|\mathbf{b}^r||\mathbf{b}^{app}|}{G^{-1}\mu_0^{-1}}\right)^{-1} \approx \frac{8 - 4\bar{E}^2}{\left(4 - 3\bar{E}^2\right)^2}, \tag{5.5.3}$$

where A is the top surface area of the material. Also, dimensionless electric energy $\bar{E}$ is defined as

$$\bar{E} = \frac{V}{H}\sqrt{\frac{\epsilon}{G}}. \tag{5.5.4}$$

The relation (5.5.3) has been used to generate Fig. 5.7(b). Good agreement is seen between our analytical results and simulations. Also, it is clear in the relation (5.5.3) that $\bar{W}$ is independent of the magnetic field and only depends on dimensionless electric field. Our numerical solution for compression problem also shows that $\bar{W}$ is independent of magnetic field. Therefore, we can conclude that magnetic field will not change $\bar{W}$ in the compression problem under small strain assumption. In the other words, according to Eq.(5.5.3), the amount of electric energy can be harvested at the boundary W *linearly* increases as dimensionless magnetic field $G^{-1}\mu_0^{-1}|\mathbf{b}^r||\mathbf{b}^{app}|$ increases.

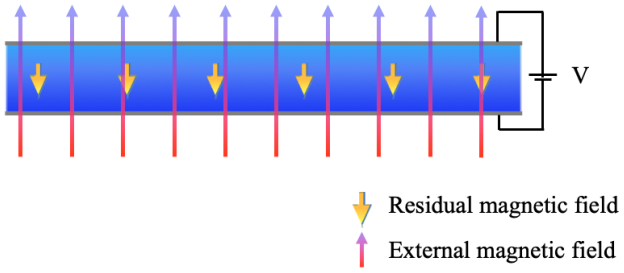

(a)

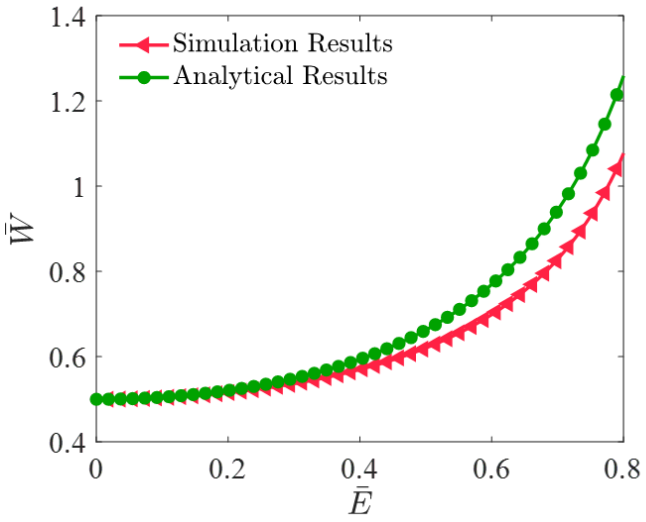

(b)

Figure 5.7: The electric energy harvesting by applying magnetic filed to a parallel plate HMSE capacitor. (a) Schematics of the material. (b) The electric energy harvested by applying a magnetic field to a parallel plate capacitor made of HMSE.

5.5.3 The magnetoelectric effect in PHMSEs

In the next step, we simulate the behavior of the PHMSE shown in the Fig. 5.8. The profile of the residual magnetic flux density is given in the Eq.(5.4.33). We assume the material is cantilevered from the left end and a magnetic field across its thickness is applied ($\mathbf{h}^e = h^e \mathbf{e}_Y$). The short circuit electrical boundary condition $\xi = 0$ has been applied to surfaces $Y = \pm H/2$. The deformation is fully constrained on the cantilever side of the

beam ($X = 0$). Unless otherwise stated, a layer of external charges with the surface charge density $q_0 = -0.048$ mC/m^2 has been inserted to the material at $Y = 0$. Due to existence of interface charges, the electric potential inside the material is not zero even in absence of the external loading. Therefore, we have to compare the solution in two states, in presence and absence of the externally applied magnetic field, in order to determine generated voltage inside the material. We identify the generated electric potential $\xi - \xi^0$, where ξ^0 is the electric potential of the system determined at $\mathbf{h}^{\mathrm{e}} = \mathbf{0}$. Similarly, the output charge ΔQ over surface area of the electrode A can be determined as

$$\frac{\Delta Q}{A} = \frac{1}{L}\int_0^L \Big(D^f(X) - D^i(X)\Big)\,\mathrm{d}X, \tag{5.5.5}$$

where D^f is defined as $D^f = (\widetilde{\mathbf{D}}\cdot\mathbf{e}_Y)|_{Y=H}$ determined at $\mathbf{h}^{\mathrm{e}} = h^e\mathbf{e}_Y$. Also, D^t is defined as $D^t = (\widetilde{\mathbf{D}}\cdot\mathbf{e}_Y)|_{Y=H}$ determined at $\mathbf{h}^{\mathrm{e}} = \mathbf{0}$. The ME voltage coupling coefficient is calculated substituting Eq.(5.5.5) into Eq.(5.4.18)

$$\alpha_{\mathrm{ME}}^{\mathrm{eff}} = \frac{1}{\epsilon^{eff}}\frac{\partial}{\partial h^e}\left(\frac{1}{L}\int_0^L D^f(X)\mathrm{d}X\right). \tag{5.5.6}$$

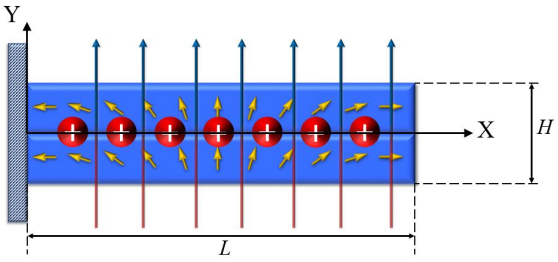

Figure 5.8: Schematic of the PHMSE. The gold arrows show the direction of residual magnetic field.

We have ensured mesh convergence for our FENICS calculations (see Fig. 5.9). Figure 5.10 compares our simulation results with experimental observations for this problem and good agreement is found. The shape programmable ability of the PHMSE is illustrated in this figure where a uniform magnetic field leads to a non-uniform deformation. Also, it is clear that the deformation is not symmetric with respect to the magnetic field. This is because the direction of residual magnetic field is not symmetric. Therefore, as the direction

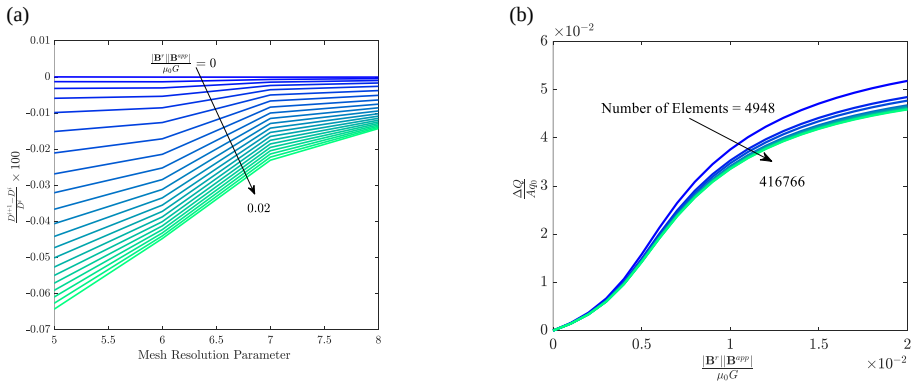

Figure 5.9: Mesh convergence study.

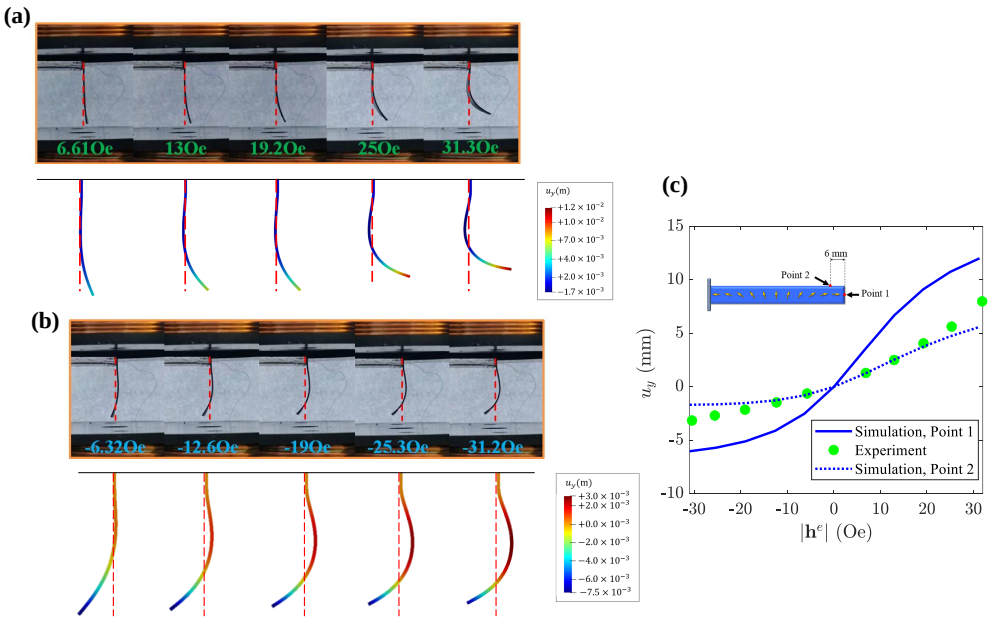

Figure 5.10: The deformed configuration observed in the experiment versus the deformed configuration obtained using FE model for the PHMSE under different (a) positive and (b) negative magnetic fields. (c) The deflection of the material.

of the applied magnetic field is reversed, the direction of the deformation does not reverse completely.

Figure 5.11a shows the deformed configuration and contours of generated dimensionless electric potential for different values of magnetic fields. The dimensionless electric potential is defined as $\epsilon(\xi - \xi^0)/(q_0 H)$, where ξ, ϵ, q_0 and H, respectively, are electric potential,

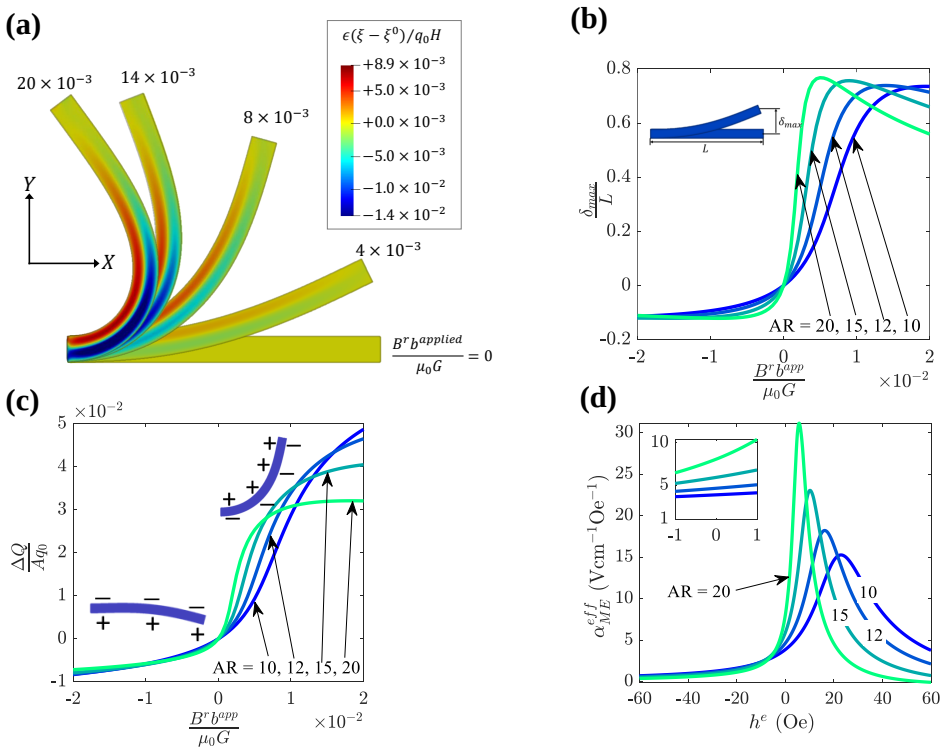

Figure 5.11: The numerical results showing ME effect in PHMSE. (a) Contour plots showing changes observed in the distribution of electric potential. (b) Dimensionless deflection, (c) dimensionless output charges and (d) the ME voltage coefficient.

electric permittivity, surface charge density at the interface and the thickness of the material. The potential ξ^0 is the electric potential at each point in absence of external magnetic field. This figure shows that the applied magnetic field changes the distribution of electric potential and the electric field is generated within the material in response to applied magnetic. The generated electric field increases as external magnetic field increases. The contours of generated electric potential are compared with strain components in the Fig. 5.12. Evidently, inhomogeneous strain leads to the presence of electric potential difference and this implies that emergence of electric potential difference and ME effect is mediated by strain gradients. It is convenient to achieve magnetoelectric coupling through bending deformation since bending is one of the simplest way to induce strain gradient in the material without using a composite structure (last section).

The dimensionless vertical displacement of the tip point of the beam is shown in Fig.

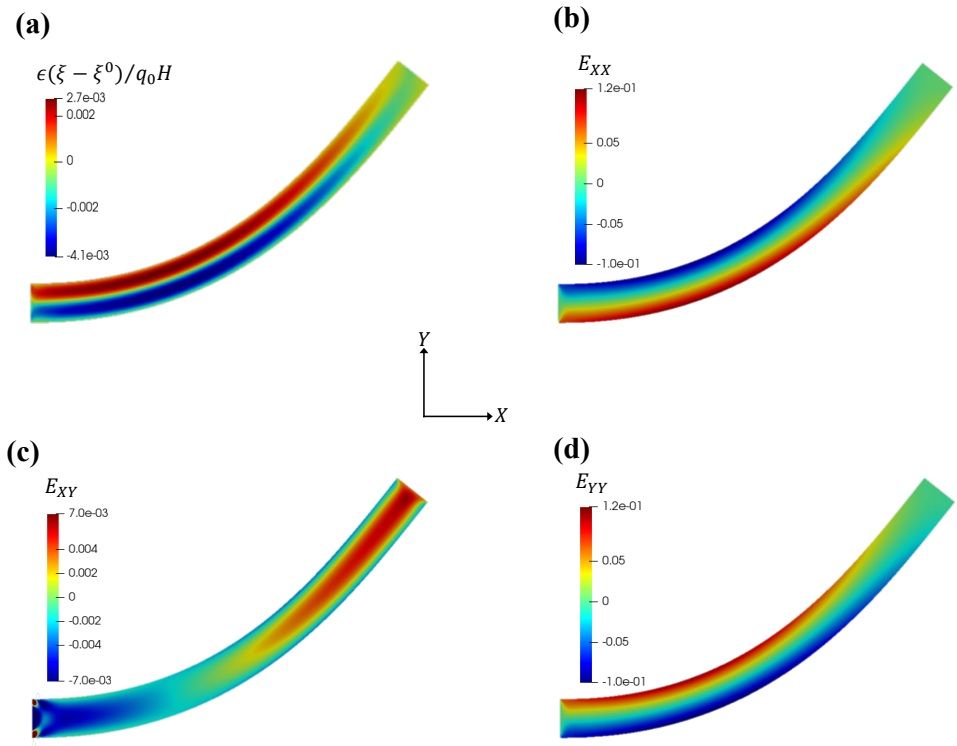

Figure 5.12: The contours of (a) dimensionless generated electric potential (b-d) and strain components for PHMSE where $\mathbf{E} = \mathbf{F}^T\mathbf{F} - \mathbf{I}$.

5.11b for beams with different aspect ratios (AR $= L/H$). Also, the dimensionless output charges $\frac{\Delta Q}{Aq_0}$ (calculated using (5.5.5)) versus applied dimensionless magnetic field $\frac{B^r b^{app}}{\mu_0 G}$ is plotted in Fig. 5.11c. A larger deflection and output charge is observed for the materials with larger aspect ratios under small magnetic fields. However, as the magnetic field increases, the deflection and output charges increase until they reach a plateau where maximum deflection and output charges have been reached. For beams with greater ARs, the maximum deflection is reached at smaller magnetic fields. In addition, we observe that the deformation (and consequently output charges) is not symmetric with respect to the applied magnetic field. This is because the residual field is not symmetric. Figure 5.13 shows a symmetric behavior in HMSEs with residual field uniformly aligned along the axis of the beam ($\widetilde{\mathbf{B}}^r = B^r\mathbf{e}_X$). Figure 5.13 shows that for the material with a symmetric alignment of the residual field, imposing external magnetic fields with opposite signs will lead to deflections (Fig. 5.13b), output charges (Fig. 5.13b) and magnetoelectric voltage coupling coefficients (Fig. 5.13c) with the opposite sign.

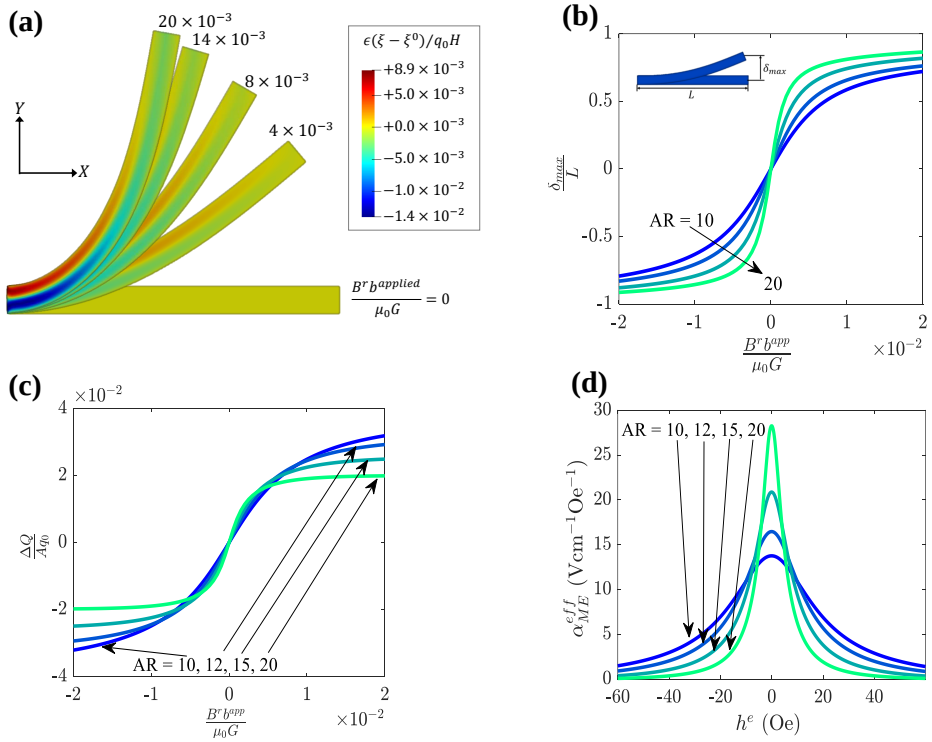

Figure 5.13: The numerical results showing ME effect in HMSE with uniform residual magnetic field. (a) Contour plots showing changes observed in the distribution of electric potential. (b) Dimensionless deflection, (c) dimensionless output charges and (d) the ME voltage coefficient.

We show, using Fig. 5.11, that external magnetic field induces bending and electric charges can be harvested at the electrodes attached to the surface of material in response to the bending. This resulting magnetoelectric effect can be quantified using the magnetoelectric voltage coupling coefficient. The ME voltage coupling coefficient of the PHMSE is numerically calculated using relation (5.5.6). The voltage coupling coefficients versus magnetic field for PHMSEs with different aspect ratios are plotted in Fig. 5.11d. A giant value (greater than 1 Vcm^{-1}Oe^{-1}) for voltage coupling coefficient of the material is reported at zero external magnetic field. The ME voltage coupling at zero magnetic field increases as AR increases. This shows that PHMSEs not only enable substantially large ME coupling but they make it unnecessary to have a bias magnetic field. Thus hard magnetic soft electret form a unique class of materials which provide soft and biocompatible

magnetielectric property which is significantly sensitive to weak magnetic fields. This value is even comparable with highest values of the ME voltage coupling coefficients of polymer based magnetoelectric composites.

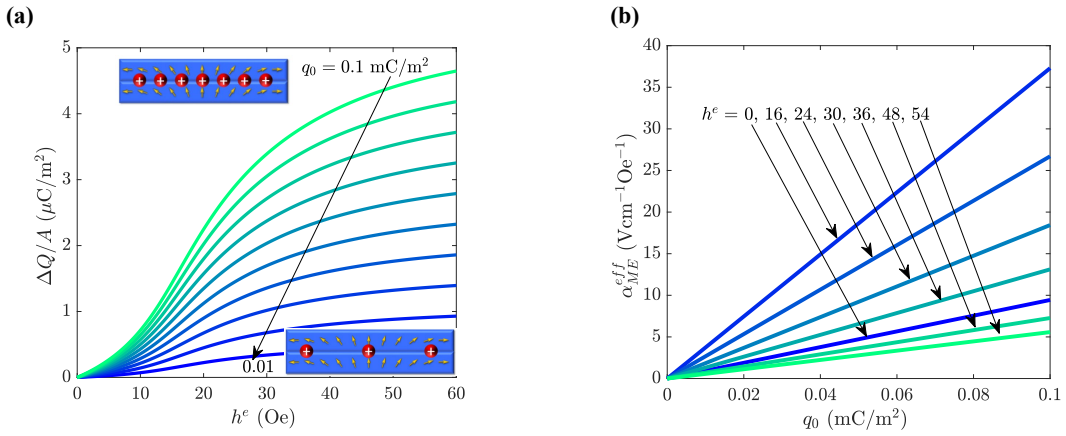

Figure 5.14: The effect of surface charge density in ME effect in PHMSEs under bending deformation. (a) FE results for $\Delta Q/A$ versus h^e for different values of interface charge density. (b) FE results for the $\alpha_{\text{ME}}^{\text{eff}}$ versus q_0.

Effect of interfacial charge density. There is a direct relationship between interface charge density and the amount of charge tjat can be harvested from the PHMSEs under magnetic field induced bending deformation. Results obtained from our finite element model shows that the larger the interface surface charge density is, more electrical energy can be harvested (5.14a). The voltage coupling coefficient versus interface surface charge density for PHMSEs under different external magnetic field is plotted in Fig. 5.14b. A linear relation between ME voltage coupling coefficient of the material and interface charge density is reported.

Effect of deformation resulting from the magnetization step. The magnetoelectric effect in PHMSEs may be impacted by the initial curvature induced in the material in the magnetization stage. The initial curvature is controlled by bending angle α (see the inset of Fig. 5.15) which has a direct impact on the profile of residual magnetic flux density given in Eq.(5.4.33). The effect of bending angle in magnetization stage on the ME effect of the PHMSE is studied in the Fig. 5.15. Evidently, the output charge can be modified by changing the bending angle in the pre-magnetization stage. This is a proof of concept that

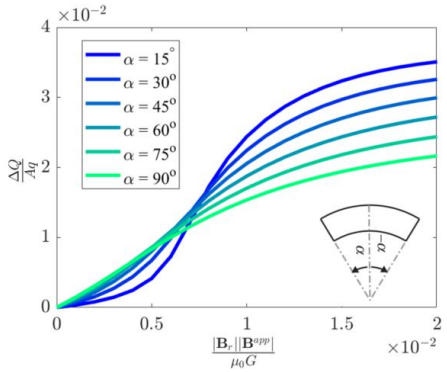

Figure 5.15: The effect of bending angle in the pre-magnitization stage on the harvested electric charges of PHMSE. The length of the beam is 35 mm and its thickness is 0.8 mm. Also, $q_0 = 0.1$ mC/m^2.

shows PHMSE materials can be customized to show desired actuation and magnetoelectric effect that may be tailored for a particular application. We remark that past work has shown that hard magnetic soft materials can be easily programmed to actuate into very complex configurations in response to uniform external magnetic field. Thus, very complex electric signals can be produced in response to applied magnetic field [180] paving the way for remote transfer of information.

5.6 Concluding remarks

In summary, as a replacement for ME composite materials, we introduced hard magnetic soft electret materials as a new class of materials which enable large deformation and strong ME coupling in one single material. In sharp contrast to ME composite materials and recently developed soft magnetic electret materials, we showed that ME effect in hard magnetic electrets can be independent of magnetic field. Therefore, HMSEs show a significant ME coupling at infinitesimal magnetic fields without any bias magnetic field. We showed the ME effect in soft HMSEs are strain mediated. The magnetic field independent ME effect of HMSEs is attributed to their linear magnetic filed-deformation relation. Our investigation indicated that the room-temperature magnetoelectric voltage coefficient in a simple bi-layer HMSE is as high as 332.7 mVcm^{-1} Oe^{-1}. Also, we showed that HMSEs can simply be programmed to exhibit a ME effect mediated by desired deformation. We showed

giant voltage coupling coefficient of greater than 15.36 Vcm^{-1} Oe^{-1} is simply possible in elastically homogeneous PHMSE at resonance frequency of 6 Hz in which ME effect is mediated by bending deformation. Therefore, HMSEs are the first known soft materials with giant ME coupling which eliminate the bias magnetic field requirement.

Chapter 6

Theory of Photo-Flexoelectricity in Nematic Liquid Crystal Elastomers and the Coupling of Light, Deformation and Electricity

Photoactive nematic liquid crystal elastomers permit generation of large mechanical deformation through impingement by suitably polarized light. The light-induced deformation in this class of soft matter allows for devices such as transducers and robots that may be triggered wirelessly. While there is no ostensible direct coupling between light and electricity in nematic liquid crystal elastomers, in this work, we take cognizance of the fact that the phenomenon of flexoelectricity is universal and present in all dielectrics. Flexoelectricity involves generation of electrical fields due to strain gradients or conversely, the production of mechanical deformation through gradients of electrical fields. Barring some specific contexts, the flexoelectric effect is in general rather weak in *hard* materials. However, due to the facile realization of strain gradients (e.g. flexure) in soft materials, we expect flexoelectricity to be highly relevant for liquid crystal elastomers thus, *prima facie*, furnishing a deformation-mediated mechanism to couple light and electricity. In this chapter, we develop a nonlinear theory of photo-flexoelectricity for nematic liquid crystal elastomers and analyze the precise conditions underpinning an appreciable coupling between light and electricity. A careful scaling analysis reveals that there is an optimal size-scale at which the flexoelectricity-mediated photo-electric effect is maximized. We find that with conservative estimates of the flexoelectric coefficients of these materials, the electrical power generation is rather modest for typical optical load. However, our proposed coupling is an appropriate modality for optical sensing. Furthermore, design of next-generation liquid crystal elastomers with high flexoelectricity as well as exploitation of size-effects could ameliorate extraction of electrical power from light illumination.

6.1 Introduction

The prospects of producing electricity through radiation and specifically, light, needs little motivation. The mechanism is wireless and thus can be remotely administered and proceeds at maximal speed allowed by the known physical laws (Fig. 6.1). The intense and storied research in the broadly defined field of photovoltaics is a testament to this. In this work, we attempt to understand the mechanics underpinning of coupling between light and electricity in an entirely different class of materials: photoactive nematic liquid crystal elastomers.

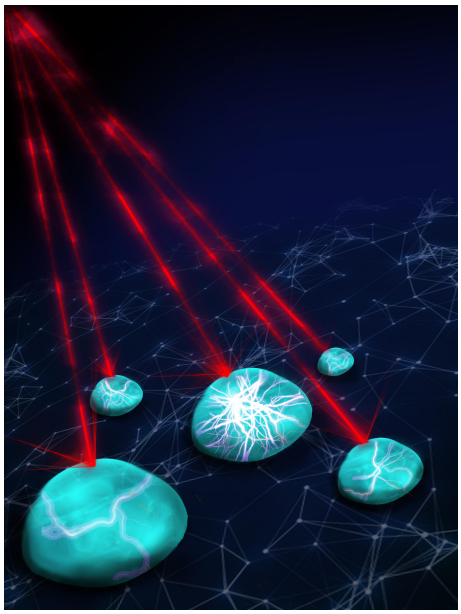

Figure 6.1: Optimum size scale for manifestation of photo-flexoelectric effect.

Crudely, a liquid crystal elastomers (LCE) is a marriage between conventional rubbery polymers and liquid. The result is a rubber-like very soft solid but one that appears to inherit several idiosyncracies of the liquid crystal structure [237]. They can exhibit large deformation (up to 400%)[238] in response to wide range of stimuli including heat[239], electric field[240], magnetic field[241] and light[242]. The explored applications for these materials include soft robotics [243], optics[244], biomedicine[245, 246] and consumer devices[247]. In addition, recent developments in synthesis methods for LCEs have simplified the fabrication processes which has focused considerably increased attention on these materials [248].

The LCE materials are cross linked polymer network containing mesogens[249]—rigid rod like molecules that have a strong tendency toward self-organization [238]. The mesogens are covalently linked to a polymer chain backbone where flexibility of polymer network permits rotation and motion of mesogens retaining liquid crystalline property of the material[248, 250]. The LCEs can exhibit different phases and their phase transition can lead to large macroscopic strains. Fig. 6.2 shows an LCE initially in the the so-called nematic phase (where mesogens are aligned in one direction). Application of an external stimulus such as heat can trigger phase transition from this nematic to isotropic state in which nematic mesogens are randomly oriented. This causes a contraction along the direction of nematic mesogens. The LCEs can be found in different phases distinguished by the positional and orientation order of the mesogens: e.g. nematic, smectic and cholestric. Further discussion on the molecular structure of LCE's is avoided and we simply refer the reader to several overviews on this topic. The focus of our work is on the more common embodiment of LCEs based on the nematic phase.

Central to this chapter is the very unique property of the LCEs pertaining to photo-induced actuation [309, 310, 311, 312, 313]. Essentially, light can induced rapid, large and reversible strain in these materials. The strain generated in the LCEs in response to light irradiation can be due to either photothermal or photochemical reasons[316]. The photothermal effect is due to conversion of light to heat inside the material which can raise the temperature and trigger phase transition (thus leading to a large deformation). Photothermal effect is not th subject of current work and we refer the reader to other works for further information (see reviews [317, 318, 319]). On the other hand, the photochemical effect may be observed in the LCEs if liquid crystal molecule contain photoisomerizable groups such as azobenzene[320]. The irradiation of light to azobenzene molecules can lead to trans→cis and cis→trans isomerizations generating a macroscopic deformation. The trans→cis isomerization occurs when azobenzene molecules are exposed to UV light. This isomerization changes the shape of the molecules from rod-like to strongly kinked rods which act as impurities and dilute the nematic ordering and lead to nematic to isotropic phase transition [320]. This phase transition can be reversed by exposing the material to

visible light[321]. In addition to this effect, the exposure of NLCE to a polarized light can induce reorientation of the nematic mesogens[316]. The light induced reorientation effect, also known as the Weigert Effect [322], is a result of repeated trans–cis–trans isomerization cycles in response to polarized light irradiation[323]. Several experimental studies have highlighted photo-induced reorientation in nematic liquid crystal polymers [324, 325, 326].

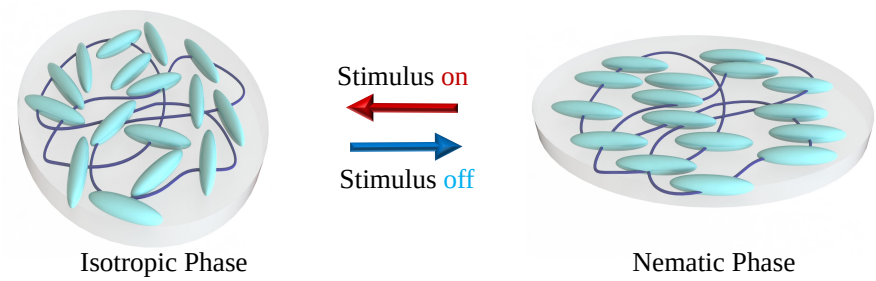

Figure 6.2: Schematic illustration of strain induced as a result of phase transition in LCE in response to stimulus.

From the viewpoint of the development of mathematical theories to describe LCE's, three broad topics are relevant to the present study)[1]: mechanical behavior, electromechanical coupling, photoactivity. We briefly summarize the some representative literature on each of these in the following paragraphs.

In an early work, a phenomenological strain energy function for ideal nematic solids was proposed by Bladon et al. [257]—the so-called BTW model. This neo-classical strain-energy function, which is a simple extension of the classical theory of rubber based on Gaussian polymer chains, emerged from statistical mechanics considerations of LCE microstructure [258]. Several other followed. For instance, a continuum theory for nematic elastomers was presented by Anderson et al.[259] where they considered directional effect of nematic mesogens by introducing orientational forces –which were distinct from conventional deformational forces– that expend power over the time-rate of the orientation field and required that these forces comply with an orientational momentum balance. This approach was motivated by Ericksen [260] and Leslie [261] works originally developed to study liquid crystals. Chen and Fried [262] emphasized the need to correctly incorporate kinematic constraints

[1]Of course, we focus only on aspects germane to the topic of our paper and there are many aspects pertaining theory for LCE's that are beyond the scope of our paper e.g. statistical mechanics of LCE's at the microscale, atomistics considerations

while DeSimone and Teresi[263] refined anisotropic part of BTW model and presented two new nonlinear models. In contrast to the BTW model, the approach of DeSimone and Teresi was able to capture the semi-soft behavior of LCEs. Agostiniani and Antonio DeSimone [264] presented an Ogden type extension of free energy of nematic elastomer. In addition to monodomain LCEs, extension of theoretical approach to polydomain LCEs is also available in the literature[265, 258].

The behavior of LCE's under the action of electrical fields has also received attention in the literature [266, 267, 240]. LCE's are not piezoelectric so the key electromechanical coupling mechanism (at least the one explored in the literature) is that due to electrostatic Maxwell stress. A conventional dielectric elastomer film, when subjected to a potential difference across its thickness, tends to due to the contract along the direction of an applied electric field [178, 48, 268, 269, 270]. However, LCEs may contract[240, 271, 272] or expand [273, 274] along the direction of applied electric field. This distinction is due to the markedly different microstructure of LCEs compared to conventional elastomers. The LCEs have an anisotropic dielectric tensor [237] and the material properties along the direction of the nematic mesogens are different from the perpendicular direction. The electrical Maxwell stress generates a compressive force in an LCE thin film sandwiched between two electrodes and under electric potential difference but this effect is anisotropic and this force depends on the alignment direction of the nematic mesogens [272]. Also, the electric field may trigger reorientation of nematic mesogens which tend to align themselves with electric field[275]. This behavior that leads to an expansion along the direction of the electric field is also due to anisotropic nature of the LCEs[276]. Therefore, there is a competition between the Maxwell stress and reorientation effects in these materials[277] and the response is significantly more nuanced as compared to conventional elastomers and highly variable based on the boundary condition of the problem and material properties including viscoelastic behavior[277]. Modeling the complex electro-mechanical response of LCEs has motivated several theoretical studies [278, 276, 279, 280, 281, 282, 283, 284, 285, 286, 287, 275, 277]. Although it has been shown that the effect of the Maxwell stress could be considerable [240, 271, 272], the effect the Maxwell stress is rarely considered [287, 275, 277, 288]. In addition, these theoretical works often have focused on one specific boundary value problem

and they are not extendable to other problems. Among some recent works, Pampolini and Triantafyllidis[289] proposed a variational formulation for nematic continua with a potential energy depending on four independent variables (the displacement, director, specific polarization and electric displacement perturbation) and used their developed theory to study bifurcation of an infinite layer of a nematic liquid crystal confined between two parallel plates and subjected to a uniform electric field perpendicular to these plates under full anchored boundary conditions (so-called Fréedericksz transition phenomena). Also, Xu and Huo [287] used the continuum model given by Zhang et al.[290], which was originally based on dissipation principle for viscoelastic solids with micro order, and extended it to dielectric LCEs to study Fréedericksz transition.

Light-induced actuation in photoactive LCE's has been modeled by several groups [327, 328, 329, 330, 331, 332, 333]. Many studies have primarily focused on one specific class of deformation such as bending [328, 332] or they do not consider effect of the light polarization [334, 335, 331]. Recently, Bai and Bhattacharya [336] used a free-energy developed by [337] to study photomechanical coupling in a photoactive LCE under both light illumination and mechanical stress. They explored the effect of light polarization direction on the reorientation of nematic directors and showed that nematic mesogens tend to align themselves in the direction perpendicular to light polarization direction.

We find it somewhat ironic that although the phenomenon of flexoelectricity was first noted in liquid crystals [291], a theory for flexoelectricity in LCE's is conspicuously absent. While flexoelectricity in conventional elastomers (to various degrees of sophistication) has been addressed, there is little literature on this effect in LCEs (with just a few exceptions which we will highlight below). In liquid crystals, flexoelectricity refers to electrical polarization caused by a gradient of the mesogens orientation pattern [291, 292, 293]. The mechanism of flexoelectricity in liquid crystals depends on the molecule shape of the mesogens(see Fig. 6.3)[85]. As shown, for wedge (pear) shaped molecule (Fig. 6.3a) a splay arrangement of the molecules leads to generation of a non-zero polarization and for banana shaped molecules(Fig. 6.3b) polarization is produced in response to bending arrangement of the molecules[298]. For rod shaped molecules shown in Fig. 6.3c, both bending and splay rotation of molecules can break the anti-parallel polarization symmetry of the polarization

and create a net polarization [299, 300]. The formation of a quadrupoles can also contribute to exhibition of flexoelectric effect (Fig. 6.3c) [300]. It has been observed experimentally that liquid crystals with rod shaped molecule have flexoelectric coefficient in the order of 1 pC/m while the flexoelectric coefficient of the banana shaped molecules is three orders of magnitude larger [301, 296, 297, 302]. As already hinted earlier, we are aware of just a few works on LCE's. Harden et al. [304] experimentally showed side bent bent core LCEs can exhibit a "giant" flexoelectric coefficient($\sim$ 30 nC/m). Chambers et al. [305] reported a large flexoelectric coupling in a calamitic LCE swollen with bent-core liquid crystal ($\sim$ 20 nC/m). Recently, Rajapaksha et al. [306] also observed a flexoelectric-like response in ionic LCE.

In this chapter, to explore the interplay between light, mechanics and electricity, we develop a nonlinear theory for flexoelectricity for nematic liquid crystal elastomers that also incorporates, photoactivity, Frank elasticity, and anisotropy. Also, we present linearized form of the equation and asymptotic theories which have been proposed to facilitate the analytic solution of future boundary value problems. Moreover, we develop a dissipative dynamic model for LCEs including effects of electro-mechanical coupling. Furthermore, we present finite element implementation of theory and investigate flexoelectric behavior of LCEs under stretch and bending deformations. We study size effect in flexoelectric behavior of LCEs and show that LCEs may enable a photo-flexoelectric effect.

6.2 Formulation

*Notation:*Let V_R be the body of the nematic elastomer in the reference undeformed configuration. The deformation $\boldsymbol{\chi}$ maps reference configuration V_R to the current configuration V. The material points in the reference configuration are denoted by $\mathbf{x}$ and the material points in the current configuration are denoted by $\mathbf{y}$. The boundary of the body in the current (rep. reference) configuration is denoted by ∂V (resp. ∂V_R). The unit normal to the surface in the current (rep. reference) configuration is denoted by $\boldsymbol{\nu}$ (resp. $\boldsymbol{\nu}_R$). The gradient operator in the Lagranian (resp. Eulerian) coordinates are represented by ∇ (resp. ∇_y). The thermodynamic state of the NLCE is described by order parameter Q,

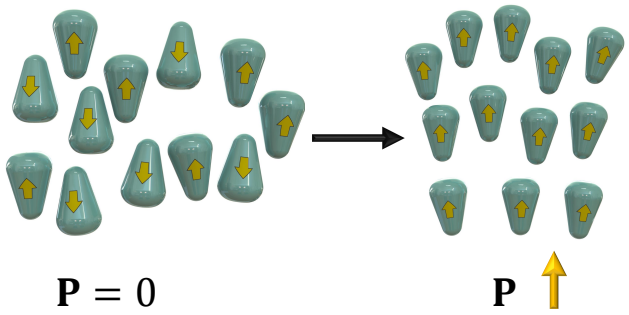

(a)

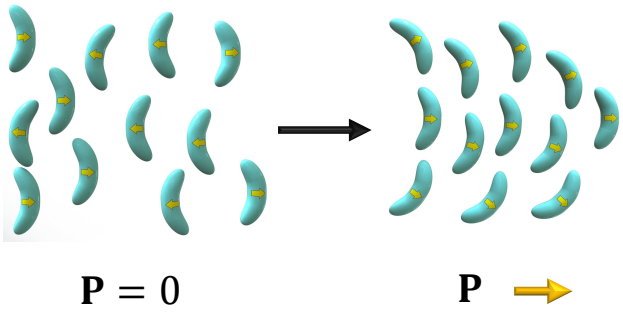

(b)

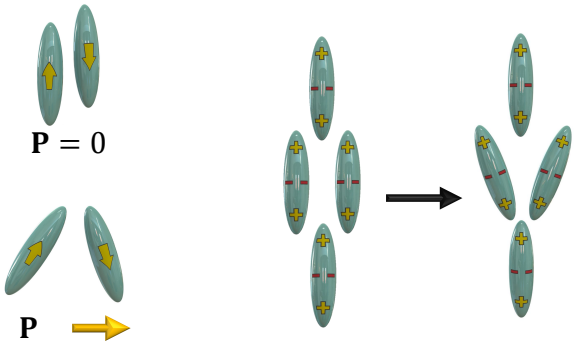

(c)

Figure 6.3: The mechanism of the flexoelectricity for LCs with (a) wedge (pear) shaped molecules, (b) banana shaped molecules and (c) rod shaped molecules.

director field $\mathbf{n}$, polarization $\mathbf{p}$ and deformation $\mathbf{y}$, $(Q, \mathbf{n}, \mathbf{p}, \mathbf{y}) : V \to \mathbb{R} \times \mathbb{R}^3 \times \mathbb{R}^3 \times \mathbb{R}^3$. It is important to note that we ignore variations of the order parameter and assume it remains constant unless material is exposed to light. Therefore, we will present general theory assuming it is variable but later on we simplify the theory assuming this variable is constant. Also, it is worthwhile to note that the reference configuration is an isotropic

phase with randomly distributed director field before the nematic transition. The reference configuration is undeformed but it is not stress free.

We identify deformation gradient tensor$\mathbf{F}$, Jacobian J, the right Cauchy-Green strain tensor $\mathbf{C}$, the left Cauchy-Green strain tensor $\mathbf{B}$ and the polarization in the reference configuration $\widetilde{\mathbf{P}}$ as

$$\mathbf{F}=\nabla\mathbf{y},\qquad J=\det\mathbf{F},\qquad \mathbf{C}=\mathbf{F}^T\mathbf{F},\qquad \mathbf{B}=\mathbf{F}\mathbf{F}^T\quad\text{and}\quad \widetilde{\mathbf{P}}=J\mathbf{p}. \tag{6.2.1}$$

We identify electric potential $\xi : V \to \mathbb{R}$ and electric field $\mathbf{e} = -\nabla_y\xi$. Our theory is established based on this premise that the electrostatic Maxwell equation has to be satisfied. The Maxwell equation in the current and reference configurations are expressed as

$$\mathbf{d}=-\epsilon_0\nabla_y\xi+\mathbf{p}\qquad\qquad \operatorname{div}(\mathbf{d})=0\qquad\text{in}\quad V, \tag{6.2.2}$$

$$\text{and}\qquad \widetilde{\mathbf{D}}=-\epsilon_0 J\mathbf{C}^{-1}\nabla\xi+\mathbf{F}^{-1}\widetilde{\mathbf{P}}\qquad\qquad \operatorname{Div}(\widetilde{\mathbf{D}})=0\qquad\text{in}\quad V_R. \tag{6.2.3}$$

Moreover, we identify the material properties $\mathbb{A}_{\mathbf{n}}$ and $\mathbb{D}_{\mathbf{n}}$ as

$$\mathbb{D}_{\mathbf{n}}=\epsilon_0\left[(\epsilon_c-\epsilon_a)\,\mathbf{n}\otimes\mathbf{n}+\epsilon_a\mathbf{I}\right], \tag{6.2.4}$$

$$\mathbb{A}_{\mathbf{n}}=\left(\mathbb{D}_{\mathbf{n}}-\epsilon_0\mathbf{I}\right)^{-1}=A_1\mathbf{n}\otimes\mathbf{n}+A_2\mathbf{I}, \tag{6.2.5}$$

$$\text{and}\qquad A_1=-\frac{\epsilon_c-\epsilon_a}{\epsilon_0(\epsilon_c-1)(\epsilon_a-1)},\qquad A_2=\frac{1}{\epsilon_0(\epsilon_a-1)}, \tag{6.2.6}$$

where ϵ_a (resp. ϵ_c) is the relative permittivity along the a-axis (resp. c-axis) of the mesogen. Also, ϵ_0 is the electric permittivity of the vacuum.

The total free energy $\mathcal{F}^{\text{tot}}$ of the system for a flexoelectric NLCE under electro-thermo-opto-mechanical loading is expressed as

$$\begin{aligned}\mathcal{F}^{\text{tot}}[Q,\mathbf{n},\mathbf{p},\mathbf{y}]&=U^{\text{ee}}[Q,\mathbf{n},\mathbf{p},\mathbf{y}]+\mathcal{F}^{\text{Frank}}[\nabla\mathbf{n},\mathbf{y}]+\mathcal{F}^{\text{flexo}}[\mathbf{n},\mathbf{p}]\\&+\mathcal{F}^{\text{opt}}[Q,\mathbf{n}]+\mathcal{E}^{\text{elect}}[\mathbf{y},\mathbf{p}]+U^{\text{BC}}[\xi,\mathbf{y}],\end{aligned} \tag{6.2.7}$$

where $\mathcal{F}^{\text{Frank}}$, $\mathcal{F}^{\text{flexo}}$, $\mathcal{F}^{\text{opt}}$, $\mathcal{E}^{\text{elect}}$ and U^{BC}, respectively, are the contribution of the Frank elasticity, flexoelectricity, optical effects, electric energy and boundary conditions to the

free energy of the system. Also, U^{ee} is the internal electro-elastic internal energy which is defined as

$$U^{\text{ee}}[Q, \mathbf{n}, \mathbf{p}, \mathbf{y}] = \int_{V_R} W^{\text{elast}} + W^{\text{anis}} + \frac{1}{2J}\mathbb{A}_{\mathbf{n}}\widetilde{\mathbf{P}} \cdot \widetilde{\mathbf{P}}, \tag{6.2.8}$$

where W^{elast} is the internal elastic energy density of the LCE and W^{anis} is the energy contribution due to anisotropy of the nematic mesogens in the load free state. As it was discussed in the introductory section, we use the internal energy density given by DeSimone and Teresi [263]

$$W^{\text{elast}} = \frac{\mu}{2}J^{-2/3}(\mathbf{F}\mathbf{F}^T) \cdot (\mathbf{F}_{\mathbf{n}}\mathbf{F}_{\mathbf{n}}^T)^{-1} + \frac{1}{2}\kappa(J-1)^2, \tag{6.2.9}$$

where μ and κ are shear modulus and bulk modulus of the material. Also, $\mathbf{F}_{\mathbf{n}}$ is defined as

$$\mathbf{F}_{\mathbf{n}} = a^{1/3}\mathbf{n} \otimes \mathbf{n} + a^{-1/6}\left(\mathbf{I} - \mathbf{n} \otimes \mathbf{n}\right), \tag{6.2.10}$$

where a is a material parameter characterizing the amount of spontaneous strain is generated along the nematic director direction as a result of the isotropic-to-nematic phase transformation [338]. It is a combined measure of the degree of order and of the strength of the nematic elastic coupling [338]. Here, we assume the NLCE is prolate ($a > 1$) which means isotropic-to-nematic phase transformation leads to expansion along the nematic direction. Also, we will ignore effect of temperature on all material properties including a assuming constant temperature, well below the isotropic-to-nematic transition temperature.

The existence of the energy term W^{anis} is due to the fact that the fabrication process of the LCEs is often lead to an anisotropic isotropic to nematic phase transition which means that, in the symmetry breaking phase transformation leading to a nematic phase, the parent phase is not really isotropic [263]. Also, it has been shown experimentally that the LCEs with localized alignment of the nematic directors can be fabricated [339]. Therefore, it is important to consider effect of this anisotropic behavior in the formulation. Using a simple model given by by DeSimone and Teresi [263], the energy term W^{anis} is expressed as

$$W^{\text{anis}} = \frac{\mu_\beta}{2}J^{-2/3}(\mathbf{F}^T\mathbf{F}) : (\mathbf{F}_{\mathbf{N}_a}^T\mathbf{F}_{\mathbf{N}_a})^{-1}, \tag{6.2.11}$$

where $\mathbf{N}_a$ is the prescribed direction of the anisotropy and $\mathbf{F}_{\mathbf{N}_a}$ is defined as

$$\mathbf{F}_{\mathbf{N}_a} = a^{1/3}\mathbf{N_a} \otimes \mathbf{N_a} + a^{-1/6}\left(\mathbf{I} - \mathbf{N_a} \otimes \mathbf{N_a}\right). \tag{6.2.12}$$

Also, μ_β is a material constant that characterizes how large the anisotropic contribution may be. We also consider opto-mechanical coupling effects in this paper. The energy densities (6.2.9) and (6.2.11) needs to be updated in order to consider optical effects. In this case, the energy densities are function of variable order parameter Q. We will use following energy densities for this purpose [336]

$$W^{\text{elast}} = \frac{\mu}{2}\left[(\mathbf{F}\mathbf{F}^T) : \mathbf{L}_\mathbf{n}^{-1} + \log\left(\det\mathbf{L_n}\right)\right], \tag{6.2.13}$$

where $\mathbf{L_n}$ is given as

$$\mathbf{L_n} = 3Q\mathbf{n} \otimes \mathbf{n} + (1-Q)\mathbf{I}. \tag{6.2.14}$$

Similarly, we can update anisotropic part of the energy to be function of the order parameter. In order to avoid confusion between light dependent (6.2.13) and light independent energy densities(6.2.9), we introduce two parameters a_1 and a_2 and express energy elastic and anisotropic energies as

$$W^{\text{elast}} = \frac{1}{2}\mu a_1|\mathbf{F}|^2 + \frac{1}{2}\mu a_2|\mathbf{F}^T\mathbf{n}|^2 \tag{6.2.15}$$

$$\text{and} \qquad W^{\text{anis}} = \frac{1}{2}\mu_\beta a_1|\mathbf{F}|^2 + \frac{1}{2}\mu_\beta a_2|\mathbf{F}\mathbf{N}_a|^2. \tag{6.2.16}$$

If the optical effects are included in the analysis

$$a_1 = \frac{1}{1-Q}, \qquad a_2 = \frac{1}{1+2Q} - \frac{1}{1-Q}, \tag{6.2.17}$$

and if the optical effects are exclude from the analysis

$$a_1 = a^{1/3} \qquad \text{and} \qquad a_2 = a^{-2/3}(1-a). \tag{6.2.18}$$

It should be mentioned that by setting $a_1 = 1$ and $a_2 = a - 1$, the elastic energy density (6.2.15) is reduced to BTW energy density [257, 340].

We have included the effect of the Frank elasticity term in Eq.(6.2.7). This is against common formulation of LCEs where the effect of the Frank elasticity is neglected as the Frank elasticity coefficient K_F is often very small and the effect of the Frank elasticity is negligible [252]. As it will be shown here, the Frank elasticity effect is a size dependent effect and this effect becomes stronger at smaller size scale where the flexoelectric effect becomes important. Also, it will be shown that the formulation becomes thermodynamically unstable if we include flexoelectric effect and neglect the Frank elasticity effect. The energetic contribution of the Frank elasticity to the free energy of the system is given as

$$\mathcal{F}^{\text{Frank}}[\nabla \mathbf{n}, \mathbf{y}] = \int_V \frac{1}{2} K_F |\nabla_y \mathbf{n}|^2 = \int_{V_R} \frac{1}{2} K_F J |\nabla \mathbf{n} \mathbf{F}^{-1}|^2. \tag{6.2.19}$$

Also, electric energy term is given as

$$\mathcal{E}^{\text{elect}}[\mathbf{y}, \mathbf{p}] = \int_V \frac{\epsilon_0}{2} |\mathbf{e}|^2 + \int_{\Gamma_D^c} \xi_b \mathbf{d} \cdot \boldsymbol{\nu} = \int_{V_R} \frac{\epsilon_0}{2} J |\mathbf{F}^{-T} \nabla \xi|^2 + \int_{\Gamma_D} \xi_b \widetilde{\mathbf{D}} \cdot \boldsymbol{\nu}_R, \tag{6.2.20}$$

where $\Gamma_D \subset \partial V$ is the part of the surface of the material on which electrical Dirichlet boundary condition has been applied and Γ_D^c is the same surface in the current configuration. Also, $\xi_b : \Gamma_D \to \mathbb{R}$ is the prescribed electric potential applied on the surface of the LCE. The coupling between elasticity and light is included in the formulation through $\mathcal{F}^{\text{opt}}[Q, \mathbf{n}]$

which is given as [336]

$$\mathcal{F}^{\text{opt}}[Q,\mathbf{n}] = \int_{V_R} W^{\text{opt}} = \int_{V_R} \mu_n(1-c(Q,\mathbf{n}))\left[g^{-1}(Q)Q - \log Z(Q) - \frac{1}{2}(1-c(Q,\mathbf{n}))\bar{J}_n Q^2\right], \tag{6.2.21}$$

$$g(x) = -\frac{1}{2} - \frac{1}{2x} + \frac{1}{2x}\sqrt{\frac{3x}{2}}\frac{\exp(\frac{3}{2}x)}{\int_0^{\sqrt{\frac{3x}{2}}}\exp(y^2)\mathrm{d}y}, \tag{6.2.22}$$

$$Z(Q) = \frac{\exp\left[g^{-1}(Q)\right]}{1+g^{-1}(Q)(1+2Q)} \tag{6.2.23}$$

and $$c(Q,\mathbf{n}) = f\frac{I\left[1+Q(3(\mathbf{n}\cdot\mathbf{m})^2-1)\right]}{3+I\left[1+Q(3(\mathbf{n}\cdot\mathbf{m})^2-1)\right]}, \tag{6.2.24}$$

where $\mathbf{m}$ is a unit normal representing direction of applied light to the material. Also, I, f, $\bar{J}_n$ and μ_n respectively, represent light intensity, fraction of photoactive mesogens, interaction between mesogens and photoactivation modulus. We introduce splay f_s and bending f_b flexoelectric coefficients and express $\mathcal{F}_{\text{flexo}}$ as

$$\begin{aligned}\mathcal{F}^{\text{flexo}}[\mathbf{n},\nabla\mathbf{n},\mathbf{F},\mathbf{p}] &= \int_V -f_s(\nabla_y\cdot\mathbf{n})(\mathbf{p}\cdot\mathbf{n}) + f_b(\mathbf{n}\times(\nabla_y\times\mathbf{n}))\cdot\mathbf{p} \\ &= \int_V -f_s(\nabla_y\cdot\mathbf{n})(\mathbf{p}\cdot\mathbf{n}) + f_b(\nabla_y\mathbf{n})\mathbf{p}\cdot\mathbf{n} - f_b(\nabla_y\mathbf{n})^T\mathbf{p}\cdot\mathbf{n} \\ &= \int_{V_R} -f_s(\nabla\mathbf{n}:\mathbf{F}^{-T})(\widetilde{\mathbf{P}}\cdot\mathbf{n}) + f_b\nabla\mathbf{n}\mathbf{F}^{-1}\widetilde{\mathbf{P}}\cdot\mathbf{n} - f_b\mathbf{F}^{-T}(\nabla\mathbf{n})^T\widetilde{\mathbf{P}}\cdot\mathbf{n}.\end{aligned} \tag{6.2.25}$$

It should be mentioned that following symmetry arguments, it has been proven that f_b and f_s are only nonzero components of flexoelectric tensor [291, 341]. Also, we should note that the common practice in formulation of flexoelectric effect for the liquid crystals is to use electric field as independent thermodynamic variable and describe the flexoelectric energy as [295]

$$\mathcal{F}^{\text{flexo}} = \int_V e_s(\nabla_y\cdot\mathbf{n})(\nabla_y\xi\cdot\mathbf{n}) - e_b(\mathbf{n}\times\nabla_y\times\mathbf{n})\cdot\nabla_y\xi, \tag{6.2.26}$$

where e_b and e_s are flexoelectric coefficients. However, we use polarization as independent variable and, therefore, prefer the energy (6.2.25) over the energy (6.2.26). Also, the sign convention for two different terms given in (6.2.26) are different in different literature and communities [295, 342, 252, 291].

As it was mentioned, we assume that an electric potential ξ_b has been applied on the surface Γ_D. Also, $\widetilde{\mathbf{D}} \cdot \boldsymbol{\nu}_R = 0$ on Γ_N ($\Gamma_D \cup \Gamma_N = \partial V_R$). In addition to that, $\mathbf{y} = \mathbf{y}_b$ on S_D and the LCE is under dead load $\widetilde{\mathbf{t}}_a : S_N \to \mathbb{R}^3$ such that $S_D \cup S_N = \partial V_R$. Also, the direction of the nematic director may be prescribed on the parts of the boundary. For brevity in the illustration of the equations, we have not considered Dirichlet boundary condition for the nematic director in this section. The U^{BC} is expressed as

$$U^{\mathrm{BC}}[\xi, \mathbf{y}] = -\int_{S_N} \widetilde{\mathbf{t}}_a \cdot \mathbf{y}. \tag{6.2.27}$$

As presentation of the equations in a dimensionless manner simplifies interpretation of the problem and ease numerical solution, we identify following dimensionless variables

$$\begin{aligned} &\bar{\widetilde{\mathbf{P}}} := \frac{\widetilde{\mathbf{P}}}{\sqrt{\epsilon_0 \mu}}, \qquad \bar{\xi} := \frac{\xi}{H}\sqrt{\frac{\epsilon_0}{\mu}}, \qquad \bar{\mathbb{A}}_{\mathbf{n}} := \epsilon_0 \mathbb{A}_{\mathbf{n}}, \qquad \bar{A}_1 := \epsilon_0 A_1, \qquad \bar{A}_2 := \epsilon_0 A_2, \\ &\bar{f}_b := \frac{f_b}{H}\sqrt{\frac{\epsilon_0}{\mu}}, \qquad \bar{f}_s := \frac{f_s}{H}\sqrt{\frac{\epsilon_0}{\mu}}, \qquad \bar{K}_F := \frac{K_F}{\mu H^2}, \qquad \bar{\mu}_\beta := \frac{\mu_\beta}{\mu} \quad \text{and} \quad \bar{\kappa} := \frac{\kappa}{\mu}, \end{aligned} \tag{6.2.28}$$

where H is the characteristic length of the LCE. We identify dimensionless gradient operators as

$$\bar{\nabla} := H\nabla \quad \text{and} \quad \bar{\nabla}_y := H\nabla_y. \tag{6.2.29}$$

From this point forward, we will only deal with dimensionless equations. For the brevity of the presentation, we will drop over bar but all the equations are dimensionless.

The equilibrium state of the system is the state that satisfies these boundary condition and minimizes free energy of the system. We use standard calculus of variation to derive governing equilibrium equation of system. For a given state $(Q, \mathbf{n}, \widetilde{\mathbf{P}}, \mathbf{y})$ the infinitesimal admissible variation is given as $(Q, \mathbf{n}, \widetilde{\mathbf{P}}, \mathbf{y}) \to (Q_\delta, \mathbf{n}_\delta, \widetilde{\mathbf{P}}_\delta, \mathbf{y}_\delta) = (Q + \delta Q_1, \mathbf{n} + \delta \mathbf{n}_1, \widetilde{\mathbf{P}} + \delta \widetilde{\mathbf{P}}_1, \mathbf{y} + \delta \mathbf{y}_1)$ such that $\delta \in \mathbb{R}$ and $|\delta| \ll 1$. Therefore, $\mathbf{F} \to \mathbf{F}_\delta = \mathbf{F} + \delta \mathbf{F}_1$ and $\nabla \mathbf{n} \to \nabla \mathbf{n}_\delta = \nabla \mathbf{n} + \delta \nabla \mathbf{n}_1$.

The variation of internal energy U^{ee} is given as

$$U^{\text{ee}}[Q_\delta, \mathbf{n}_\delta, \widetilde{\mathbf{P}}_\delta, \mathbf{y}_\delta] = U^{\text{ee}}[Q, \mathbf{n}, \widetilde{\mathbf{P}}, \mathbf{y}] + \delta \int_{V_R} \Bigg[\left(\frac{\partial W^{\text{elast}}}{\partial Q} + \frac{\partial W^{\text{anis}}}{\partial Q} \right) Q_1 + \frac{1}{J} \mathbb{A}_{\mathbf{n}} \widetilde{\mathbf{P}} \cdot \widetilde{\mathbf{P}}_1 + \left(\frac{\partial W^{\text{elast}}}{\partial \mathbf{n}} + A_1 (\mathbf{n} \cdot \widetilde{\mathbf{P}}) \frac{\widetilde{\mathbf{P}}}{J} \right) \cdot \mathbf{n}_1 + \left(\frac{\partial W^{\text{elast}}}{\partial \mathbf{F}} + \frac{\partial W^{\text{anis}}}{\partial \mathbf{F}} - \frac{1}{2J} (\mathbb{A}_{\mathbf{n}} \widetilde{\mathbf{P}} \cdot \widetilde{\mathbf{P}}) \mathbf{F}^{-T} \right) : \mathbf{F}_1 \Bigg]. \tag{6.2.30}$$

The variation of the Frank elasticity energy term is given as

$$\mathcal{F}^{\text{Frank}}[\nabla \mathbf{n}_\delta, \mathbf{y}_\delta] = \mathcal{F}^{\text{Frank}}[\nabla \mathbf{n}, \mathbf{y}] + \delta \int_{V_R} \boldsymbol{\Sigma}^{\text{EL}} : \mathbf{F}_1 + K_F J \nabla \mathbf{n} \mathbf{F}^{-1} \mathbf{F}^{-T} : \nabla \mathbf{n}_1, \tag{6.2.31}$$

where

$$\boldsymbol{\Sigma}^{\text{EL}} = \frac{1}{2} J K_F \mathbf{F}^{-T} |\nabla \mathbf{n} \mathbf{F}^{-1}|^2 - J K_F \mathbf{F}^{-T} (\nabla \mathbf{n})^T (\nabla \mathbf{n}) \mathbf{F}^{-1} \mathbf{F}^{-T}. \tag{6.2.32}$$

We refer the reader to the reference [97] for the details of the derivation for variation of the electric energy (6.2.20) and here only present the final expression as

$$\mathcal{E}^{\text{elect}}[\mathbf{y}_\delta, \widetilde{\mathbf{P}}_\delta] = \mathcal{E}^{\text{elect}}[\mathbf{y}, \widetilde{\mathbf{P}}] + \delta \int_{V_R} \left[\mathbf{F}^{-T} \nabla \xi \cdot \widetilde{\mathbf{P}}_1 + \left(-\frac{1}{2} J \mathbf{F}^{-T} |\mathbf{F}^{-T} \nabla \xi|^2 + (-\mathbf{F}^{-T} \nabla \xi) \otimes (-J \mathbf{C}^{-1} \nabla \xi + \mathbf{F}^{-1} \widetilde{\mathbf{P}}) \right) : \mathbf{F}_1 \right]. \tag{6.2.33}$$

Also, the variation of the optical energy term is given as

$$\mathcal{F}^{\text{opt}}[Q_\delta, \mathbf{n}_\delta] = \mathcal{F}^{\text{opt}}[Q, \mathbf{n}] + \delta \int_{V_R} \left[\frac{\partial W^{\text{opt}}}{\partial Q} Q_1 + \frac{\partial W^{\text{opt}}}{\partial \mathbf{n}} \cdot \mathbf{n}_1 \right]. \tag{6.2.34}$$

Finally, the variation of the flexoelectric energy term is given as

$$\begin{aligned} &\mathcal{F}^{\text{flexo}}[\mathbf{n}_\delta, \nabla \mathbf{n}_\delta, \mathbf{F}_\delta, \widetilde{\mathbf{P}}_\delta] = \mathcal{F}^{\text{flexo}}[\mathbf{n}, \nabla \mathbf{n}, \mathbf{F}, \widetilde{\mathbf{P}}] \\ &+ \delta \int_{V_R} \left[\boldsymbol{\Sigma}^{\text{flexo}} : \mathbf{F}_1 + \widetilde{\mathbf{P}}^{\text{flexo}} \cdot \widetilde{\mathbf{P}}_1 + \mathbf{n}^{\text{flexo}} \cdot \mathbf{n}_1 + \mathbf{m}^{\text{flexo}} : \nabla \mathbf{n}_1 \right], \end{aligned} \tag{6.2.35}$$

where

$$\boldsymbol{\Sigma}^{\text{flexo}} = f_s\mathbf{F}^{-T}(\nabla\mathbf{n})^T\mathbf{F}^{-T}(\widetilde{\mathbf{P}}\cdot\mathbf{n}) - f_b\mathbf{F}^{-T}(\nabla\mathbf{n})^T\mathbf{n}\otimes\mathbf{F}^{-1}\widetilde{\mathbf{P}} + f_b\mathbf{F}^{-T}(\nabla\mathbf{n})^T\widetilde{\mathbf{P}}\otimes\mathbf{F}^{-1}\mathbf{n}, \tag{6.2.36}$$

$$\widetilde{\mathbf{P}}^{\text{flexo}} = -f_s(\nabla\mathbf{n} : \mathbf{F}^{-T})\mathbf{n} + f_b\mathbf{F}^{-T}(\nabla\mathbf{n})^T\mathbf{n} - f_b\nabla\mathbf{n}\mathbf{F}^{-1}\mathbf{n}, \tag{6.2.37}$$

$$\mathbf{n}^{\text{flexo}} = f_b\nabla\mathbf{n}\mathbf{F}^{-1}\widetilde{\mathbf{P}} - f_b\mathbf{F}^{-T}(\nabla\mathbf{n})^T\widetilde{\mathbf{P}} - f_s(\nabla\mathbf{n} : \mathbf{F}^{-T})\widetilde{\mathbf{P}}, \tag{6.2.38}$$

and $$\mathbf{m}^{\text{flexo}} = -f_s\mathbf{F}^{-T}(\widetilde{\mathbf{P}}\cdot\mathbf{n}) + f_b\mathbf{n}\otimes\mathbf{F}^{-1}\widetilde{\mathbf{P}} - f_b\widetilde{\mathbf{P}}\otimes\mathbf{F}^{-1}\mathbf{n}. \tag{6.2.39}$$

We introduce the Lagrnage multiplier λ_p in order to enforce incompressibility constraint $\det\mathbf{F} = 1$. In addition, we include the Lagrnage multiplier $\lambda_{\mathbf{n}}$ in order to enforce constraint $|\mathbf{n}| = 1$. Moreover, from Eqs.(6.2.15), (6.2.16) and (6.2.30), we identify $\boldsymbol{\Sigma}$ and $\boldsymbol{\Sigma}^{\text{anis}}$ as

$$\boldsymbol{\Sigma} = a_1\mathbf{F} + a_2\mathbf{n}\otimes\mathbf{F}^T\mathbf{n} \tag{6.2.40}$$

$$\text{and} \qquad \boldsymbol{\Sigma}^{\text{anis}} = \mu_\beta\left[a_1\mathbf{F} + a_2\mathbf{F}\mathbf{N}_a\otimes\mathbf{N}_a\right]. \tag{6.2.41}$$

Also, we introduce the Maxwell stress$\boldsymbol{\Sigma}^{\text{MW}}$ as

$$\boldsymbol{\Sigma}^{\text{MW}} = -\frac{1}{2}J\mathbf{F}^{-T}|\mathbf{F}^{-T}\nabla\xi|^2 + (-\mathbf{F}^{-T}\nabla\xi)\otimes(-J\mathbf{C}^{-1}\nabla\xi + \mathbf{F}^{-1}\widetilde{\mathbf{P}}) - \frac{1}{2J}(\mathbb{A}_{\mathbf{n}}\widetilde{\mathbf{P}}\cdot\widetilde{\mathbf{P}})\mathbf{F}^{-T}. \tag{6.2.42}$$

Substituting (6.2.30), (6.2.31), (6.2.33), (6.2.34),(6.2.35), (6.2.15) and (6.2.16) into (6.2.7), The weak form of the equations can be written as

$$\begin{aligned}
&\frac{d}{d\delta}\mathcal{F}^{\text{tot}}\left[Q+\delta Q_1, \mathbf{n}+\delta\mathbf{n}_1, \mathbf{F}+\delta\mathbf{F}_1, \widetilde{\mathbf{P}}+\delta\widetilde{\mathbf{P}}_1\right]\Big|_{\delta=0} = \\
&\int_{V_R}\Big\{Q_1\frac{\partial}{\partial Q}(W^{\text{opt}} + W^{\text{elast}} + W^{\text{anis}}) + \\
&\mathbf{F}_1 : \left[\boldsymbol{\Sigma} + \boldsymbol{\Sigma}^{\text{anis}} + \boldsymbol{\Sigma}^{\text{EL}} + \boldsymbol{\Sigma}^{\text{MW}} + \boldsymbol{\Sigma}^{\text{flexo}} - \lambda_p J\mathbf{F}^{-T}\right] + \widetilde{\mathbf{P}}_1\cdot\left[\mathbf{F}^{-T}\nabla\xi + \frac{1}{J}\mathbb{A}_{\mathbf{n}}\widetilde{\mathbf{P}} + \widetilde{\mathbf{P}}^{\text{flexo}}\right] + \\
&\mathbf{n}_1\cdot\left[a_2\mathbf{F}\mathbf{F}^T\mathbf{n} + A_1(\mathbf{n}\cdot\widetilde{\mathbf{P}})\frac{\widetilde{\mathbf{P}}}{J} + \mathbf{n}^{\text{flexo}} + \frac{\partial W^{\text{opt}}}{\partial\mathbf{n}} - 2\lambda_{\mathbf{n}}\mathbf{n}\right] + \\
&\nabla\mathbf{n}_1 : \left[K_F J\nabla\mathbf{n}\mathbf{F}^{-1}\mathbf{F}^{-T} + \mathbf{m}^{\text{flexo}}\right]\Big\} - \int_{S_N}\widetilde{\mathbf{t}}_a\cdot\mathbf{y}_1 = 0.
\end{aligned} \tag{6.2.43}$$

Finally, the equilibrium equations for a flexoelectric NLCE under opto-electro-mechanical

of the system are derived as

$$\frac{\partial}{\partial Q}(W^{\text{opt}} + W^{\text{elast}} + W^{\text{anis}}) = 0, \tag{6.2.44}$$

$$\nabla \cdot \left(\boldsymbol{\Sigma} + \boldsymbol{\Sigma}^{\text{anis}} + \boldsymbol{\Sigma}^{\text{EL}} + \boldsymbol{\Sigma}^{\text{MW}} + \boldsymbol{\Sigma}^{\text{flexo}} - \lambda_p J\mathbf{F}^{-T}\right) = \mathbf{0}, \tag{6.2.45}$$

$$\mathbf{F}^{-T}\nabla\xi + \frac{1}{J}\mathbb{A}_{\mathbf{n}}\widetilde{\mathbf{P}} + \widetilde{\mathbf{P}}^{\text{flexo}} = \mathbf{0}, \tag{6.2.46}$$

$$\begin{aligned} &- \nabla \cdot \left(K_F J\nabla\mathbf{n}\mathbf{F}^{-1}\mathbf{F}^{-T} + \mathbf{m}^{\text{flexo}}\right) \\ &+ a_2\mathbf{F}\mathbf{F}^T\mathbf{n} + A_1(\mathbf{n}\cdot\widetilde{\mathbf{P}})\frac{\widetilde{\mathbf{P}}}{J} + \mathbf{n}^{\text{flexo}} + \frac{\partial W^{\text{opt}}}{\partial \mathbf{n}} - 2\lambda_{\mathbf{n}}\mathbf{n} = \mathbf{0}, \end{aligned} \tag{6.2.47}$$

$$\nabla \cdot \left(-J\mathbf{C}^{-1}\nabla\xi + \mathbf{F}^{-1}\widetilde{\mathbf{P}}\right) = 0, \tag{6.2.48}$$

$$\mathbf{n}\cdot\mathbf{n} = 1, \tag{6.2.49}$$

$$\text{and} \qquad \det\mathbf{F} = 1. \tag{6.2.50}$$

The boundary conditions are given as

$$\mathbf{y} = \mathbf{y}_b \qquad \text{on} \quad S_D, \tag{6.2.51}$$

$$\boldsymbol{\nu}_R \cdot \left(\boldsymbol{\Sigma} + \boldsymbol{\Sigma}^{\text{anis}} + \boldsymbol{\Sigma}^{\text{EL}} + \boldsymbol{\Sigma}^{\text{MW}} + \boldsymbol{\Sigma}^{\text{flexo}} - \lambda_p J\mathbf{F}^{-T}\right) = \widetilde{\mathbf{t}}_a \qquad \text{on} \quad S_N, \tag{6.2.52}$$

$$- \boldsymbol{\nu}_R \cdot \left(K_F J\nabla\mathbf{n}\mathbf{F}^{-1}\mathbf{F}^{-T} + \mathbf{m}^{\text{flexo}}\right) = 0 \qquad \text{on} \quad \partial V_R, \tag{6.2.53}$$

$$\xi = \xi_b \qquad \text{on} \quad \Gamma_D \tag{6.2.54}$$

$$\text{and} \qquad \boldsymbol{\nu}_R \cdot \widetilde{\mathbf{D}} = 0 \qquad \text{on} \quad \Gamma_N. \tag{6.2.55}$$

6.3 Upper bounds for flexoelectric coefficients

In this section, we will find the upper bound for flexoelectric coefficients which satisfy thermodynamics stability condition. The energy will not be bounded unless the following condition is satisfied

$$E = \frac{1}{2}K_F|\nabla_y\mathbf{n}|^2 + \frac{1}{2}\mathbf{p}\cdot\mathbb{A}_{\mathbf{n}}\mathbf{p} - f_s(\nabla_y\cdot\mathbf{n})(\mathbf{p}\cdot\mathbf{n}) + f_b(\nabla_y\mathbf{n})\mathbf{p}\cdot\mathbf{n} - f_b(\nabla_y\mathbf{n})^T\mathbf{p}\cdot\mathbf{n} \geq 0. \tag{6.3.1}$$

Using Eq.(6.2.5), Eq.(6.3.1) can be written as

$$E = \frac{1}{2}K_F|\nabla_y \mathbf{n}|^2 + A_1\frac{1}{2}(\mathbf{p}\cdot\mathbf{n})^2 + A_2\frac{1}{2}(\mathbf{p}\cdot\mathbf{p}) - f_s(\nabla_y\cdot\mathbf{n})(\mathbf{p}\cdot\mathbf{n}) + f_b(\nabla_y\mathbf{n})\mathbf{p}\cdot\mathbf{n} - f_b(\nabla_y\mathbf{n})^T\mathbf{p}\cdot\mathbf{n} \geq 0. \tag{6.3.2}$$

We introduce $\mathbf{p}_n$ and $\mathbf{p}_t$ such that $\mathbf{p} = \mathbf{p}_t + \mathbf{p}_n$ where $\mathbf{p}_n = (\mathbf{p}\cdot\mathbf{n})\mathbf{n}$. Therefore, we can write eq (6.3.2) as

$$\begin{aligned} E = &\frac{1}{2}K_F|\nabla_y\mathbf{n}|^2 + (A_1+A_2)\frac{1}{2}|\mathbf{p}_n|^2 + A_2\frac{1}{2}|\mathbf{p}_t|^2 \\ &- f_s(\nabla_y\cdot\mathbf{n})(\mathbf{p}_n\cdot\mathbf{n}) - f_b(\mathbf{p}_t+\mathbf{p}_n)\cdot\left(\frac{\nabla_y n - (\nabla_y n)^T}{2}\mathbf{n}\right) \geq 0. \end{aligned} \tag{6.3.3}$$

From eqn (6.3.3), we can conclude that following conditions have to be satisfied in order to obtain thermodynamic stability

$$A_1 + A_2 \geq 0 \qquad \text{and} \qquad A_2 \geq 0. \tag{6.3.4}$$

We introduce $\nabla_y^{\text{dev}}\mathbf{n}$ as

$$\nabla_y^{\text{dev}}\mathbf{n} = \frac{\nabla_y\mathbf{n} + (\nabla_y\mathbf{n})^T}{2} - \frac{1}{3}(\nabla_y\cdot\mathbf{n})\mathbf{I}. \tag{6.3.5}$$

Therefore, we have

$$\frac{1}{2}K_F|\nabla_y\mathbf{n}|^2 = \frac{1}{2}K_F|\nabla_y^{\text{dev}}\mathbf{n}|^2 + \frac{1}{6}K_F(\nabla_y\cdot\mathbf{n})^2 + \frac{1}{4}K_F|\nabla_y\times\mathbf{n}|^2. \tag{6.3.6}$$

Using equaion above, we can write eqn (6.3.3) as

$$\begin{aligned} E = &\frac{1}{2}K_F|\nabla_y^{\text{dev}}\mathbf{n}|^2 + \left(\frac{1}{6}K_F - \frac{3}{2}\frac{f_s^2}{A_1+A_2}\right)(\nabla_y\cdot\mathbf{n})^2 \\ &+ \frac{1}{2}\left(\frac{1}{2}K_F - \frac{2f_b^2}{A_1+A_2} - \frac{2f_b^2}{A_2}\right)|\nabla_y\times\mathbf{n}|^2 \\ &+ \frac{A_1+A_2}{2}\left[(\mathbf{p}_n\otimes\mathbf{n}) - \frac{f_s}{A_1+A_2}(\nabla_y\cdot\mathbf{n})\mathbf{I} - \frac{2f_b}{A_1+A_2}\frac{\nabla_y\mathbf{n} - (\nabla_y\mathbf{n})^T}{2}\right]^2 \\ &+ \frac{A_2}{2}\left[(\mathbf{p}_t\otimes\mathbf{n}) - \frac{2f_b}{A_2}\frac{\nabla_y\mathbf{n} - (\nabla_y\mathbf{n})^T}{2}\right]^2 \geq 0. \end{aligned} \tag{6.3.7}$$

From equation above we can conclude that

$$K_F \geq 4\frac{fb^2}{A_2+A_1}+4\frac{fb^2}{A_2} \quad \text{and} \quad K_F \geq 9\frac{f_s^2}{A_1+A_2}. \tag{6.3.8}$$

Equations (6.3.8) and (6.3.4) establish two constraints which must satisfy in order to maintain thermodynamic stability.

6.4 Flexo-electro-mechanical coupling in NLCE under small deformation and large electric field and large nematic reorientation

In order to simplify the theory, we will use small strain assumption to simplify the theory. As it was discussed in the introductory section, nematic dielectric sometimes are made of densely cross linked polymer network which does not undergo large deformation. In this case, we can relax large deformation assumption in order to simplify equations. However, the linearization process have to be done in a rigorous way which does not ignore some coupling features of the material such as electro-mechanical coupling due to the Maxwell stress. Therefore, here we present a linear theory for electro-mechanical behavior of a nematic dielectric including effects of flexoelectricity. As optical energy is highly nonlinear, we assume there is no opto-mechanical coupling and

$$\mathcal{F}^{\text{opt}} = 0. \tag{6.4.1}$$

Thus, we use elastic energy densities (6.2.9) and (6.2.11) in this section. Moreover, we assume the isotropic to nematic transition of the material will not lead to a large deformation. We replace the material constant a, used in Eqs.(6.2.10) and (6.2.12), with the material constant γ such that $a^{1/3} = \gamma + 1$ and $|\gamma| \ll 1$. Using Taylor series expansion we

have

$$(\mathbf{F_n}\mathbf{F_n}^T)^{-1} = (1+\gamma)\mathbf{I} - 3\gamma\mathbf{n}\otimes\mathbf{n} + 3\gamma^2\mathbf{n}\otimes\mathbf{n} + o(\gamma^2) \tag{6.4.2}$$

and $$(\mathbf{F}^T_{\mathbf{N}_a}\mathbf{F}_{\mathbf{N}_a})^{-1} = (1+\gamma)\mathbf{I} - 3\gamma\mathbf{N}_a\otimes\mathbf{N}_a + 3\gamma^2\mathbf{N}_a\otimes\mathbf{N}_a + o(\gamma^2). \tag{6.4.3}$$

Let $\mathbf{u} : V_R \to \mathbb{R}^3$ be the deformation ($\nabla\mathbf{u} = \mathbf{F} - \mathbf{I}$). Assuming small deformation ($|\nabla\mathbf{u}| \sim \varepsilon \ll 1$) we can present linear form of the elastic energies densities (6.2.9) and (6.2.11) as

$$W^{\text{elast}} = \frac{\partial W^{\text{elast}}}{\partial\mathbf{F}}\Big|_{\mathbf{F}=\mathbf{I}} : \nabla\mathbf{u} + \nabla\mathbf{u} : \frac{\partial^2 W^{\text{elast}}}{\partial\mathbf{F}\partial\mathbf{F}}\Big|_{\mathbf{F}=\mathbf{I}} \nabla\mathbf{u} + o(\varepsilon^2), \tag{6.4.4}$$

and $$W^{\text{anis}} = \frac{\partial W^{\text{anis}}}{\partial\mathbf{F}}\Big|_{\mathbf{F}=\mathbf{I}} : \nabla\mathbf{u} + \nabla\mathbf{u} : \frac{\partial^2 W^{\text{anis}}}{\partial\mathbf{F}\partial\mathbf{F}}\Big|_{\mathbf{F}=\mathbf{I}} \nabla\mathbf{u} + o(\varepsilon^2). \tag{6.4.5}$$

Substituting Eqs.(6.4.2), (6.4.3), (6.2.9) and (6.2.11) into (6.4.4) and (6.4.5), we obtain following linear dimensionless elastic energies

$$W^{\text{elast}} = |\mathbf{E}_d - \mathbf{E}^*(\mathbf{n})|^2 + \frac{1}{2}\kappa\left(\text{Tr}(\mathbf{E})\right)^2 + o(\varepsilon^2, \varepsilon\gamma, \gamma^2) \tag{6.4.6}$$

and $$W^{\text{anis}} = \mu_\beta|\mathbf{E}_d - \mathbf{E}^*(\mathbf{N}_a)|^2 + o(\varepsilon^2, \varepsilon\gamma, \gamma^2), \tag{6.4.7}$$

where

$$\mathbf{E} = \frac{\nabla\mathbf{u} + (\nabla\mathbf{u})^T}{2}, \qquad \mathbf{E}_d = \mathbf{E} - \frac{1}{3}\text{Tr}\mathbf{E} \quad \text{and} \quad \mathbf{E}^*(\mathbf{n}) = \frac{3\gamma}{2}\left(\mathbf{n}\otimes\mathbf{n} - \frac{1}{3}\mathbf{I}\right). \tag{6.4.8}$$

It should be mentioned that dimensionless form of all energy densities presented in this section have been obtained by dividing the dimensional form the energy density by shear modulus of the material. The linear form of the dimensionless Frank elasticity energy terms is given as

$$W^{\text{Frank}} = \frac{1}{2}K_F J|\nabla\mathbf{n}\mathbf{F}^{-1}|^2 = \frac{1}{2}K_F|\nabla\mathbf{n}|^2 + \boldsymbol{\sigma}^{\text{EL}} : \nabla\mathbf{u} + o(\varepsilon), \tag{6.4.9}$$

where

$$\boldsymbol{\sigma}^{\text{EL}} = \frac{1}{2}K_F|\nabla\mathbf{n}|^2\mathbf{I} - K_F(\nabla\mathbf{n})^T\nabla\mathbf{n}. \tag{6.4.10}$$

In addition electrical the electric part of the energy U^{ee} given in the Eq.(6.2.8) can be written in the following linear dimensionless fashion

$$\phi[\widetilde{\mathbf{P}},\mathbf{n}]=\int_{V_R}\frac{1}{2J}\widetilde{\mathbf{P}}\cdot\mathbb{A}_{\mathbf{n}}\widetilde{\mathbf{P}}=\int_{V_R}\frac{1}{2}\widetilde{\mathbf{P}}\cdot\mathbb{A}_{\mathbf{n}}\widetilde{\mathbf{P}}-\int_{V_R}\frac{1}{2}\widetilde{\mathbf{P}}\cdot\mathbb{A}_{\mathbf{n}}\widetilde{\mathbf{P}}(\nabla\cdot\mathbf{u})+o(\varepsilon). \tag{6.4.11}$$

Using divergence theorem, the electric energy term $\mathcal{E}^{\text{elect}}$ given in the Eq.(6.2.20) can be written in following dimensionless fashion

$$\begin{aligned}\mathcal{E}^{\text{elect}}&=\int_{V_R}\frac{1}{2}J|\mathbf{F}^{-T}\nabla\xi|^2+\int_{\Gamma_D}\xi_b(-J\mathbf{C}^{-1}\nabla\xi+\mathbf{F}^{-1}\widetilde{\mathbf{P}})\cdot\boldsymbol{\nu}_R\\&=\int_{V_R}\left(-\frac{1}{2}J|\mathbf{F}^{-T}\nabla\xi|^2+\mathbf{F}^{-T}\nabla\xi\cdot\widetilde{\mathbf{P}}\right).\end{aligned} \tag{6.4.12}$$

Using Taylor series expansion, we have

$$\mathcal{E}^{\text{elect}}=\int_{V_R}\left[-\frac{1}{2}|\nabla\xi|^2+\nabla\xi\cdot\widetilde{\mathbf{P}}+\boldsymbol{\sigma}'^{\text{MW}}:\nabla\mathbf{u}\right]+o(\varepsilon), \tag{6.4.13}$$

where

$$\boldsymbol{\sigma}'^{\text{MW}}=-\frac{1}{2}|\nabla\xi|^2\mathbf{I}+(-\nabla\xi)\otimes(-\nabla\xi+\widetilde{\mathbf{P}}). \tag{6.4.14}$$

Similarly, we can linearize flexoelectric energy terms as

$$\mathcal{F}^{\text{flexo}}=\int_{V_R}\widetilde{\mathbf{P}}\cdot\mathbf{p}^{\text{flexo}}+\boldsymbol{\sigma}^{\text{flexo}}:\nabla\mathbf{u}+o(\varepsilon), \tag{6.4.15}$$

where

$$\mathbf{p}^{\text{flexo}}=-f_s(\nabla\cdot\mathbf{n})\mathbf{n}+f_b(\nabla\mathbf{n})^T\mathbf{n}-f_b(\nabla\mathbf{n})\mathbf{n} \tag{6.4.16}$$

$$\text{and}\quad\boldsymbol{\sigma}^{\text{flexo}}=f_s(\widetilde{\mathbf{P}}\cdot\mathbf{n})(\nabla\mathbf{n})^T-f_b(\nabla\mathbf{n})^T\mathbf{n}\otimes\widetilde{\mathbf{P}}+f_b(\nabla\mathbf{n})^T\widetilde{\mathbf{P}}\otimes\mathbf{n}. \tag{6.4.17}$$

Finally, we can express total free energy for the regime of small deformations as

$$\begin{aligned}\mathcal{F}^{\text{tot}}[\mathbf{u},\mathbf{n},\mathbf{P}]=\int_{V_R}\Big[&|\mathbf{E}_d-\mathbf{E}^*(\mathbf{n})|^2+\frac{1}{2}\kappa\left(\text{Tr}(\mathbf{E})\right)^2+\mu_\beta|\mathbf{E}_d-\mathbf{E}^*(\mathbf{N}_a)|^2+\frac{1}{2}K_F|\nabla\mathbf{n}|^2\\&+(\boldsymbol{\sigma}^{\text{EL}}+\boldsymbol{\sigma}^{\text{flexo}}+\boldsymbol{\sigma}^{\text{MW}}):\nabla\mathbf{u}+\frac{1}{2}\widetilde{\mathbf{P}}\cdot\mathbb{A}_{\mathbf{n}}\widetilde{\mathbf{P}}-\frac{1}{2}|\nabla\xi|^2+\nabla\xi\cdot\widetilde{\mathbf{P}}+\widetilde{\mathbf{P}}\cdot\mathbf{p}^{\text{flexo}}\Big]-\int_{S_N}\mathbf{t}_a\cdot\mathbf{u},\end{aligned} \tag{6.4.18}$$

where $\mathbf{t}_a$ is the applied dimensionless traction which is work conjugate of the dimensionless displacement $\mathbf{u}$ and

$$\boldsymbol{\sigma}^{\mathrm{MW}} = \boldsymbol{\sigma}'^{\mathrm{MW}} - \frac{1}{2}\left(\widetilde{\mathbf{P}} \cdot \mathbb{A}_{\mathbf{n}}\widetilde{\mathbf{P}}\right)\mathbf{I}. \tag{6.4.19}$$

The equilibrium state of the system is an admissible state which minimizes the free energy (6.4.18), satisfies boundary conditions and the Maxwell equation. The linear dimensionless Maxwell equation is given as

$$\nabla\cdot\Big[-J\mathbf{C}^{-1}\nabla\xi + \mathbf{F}^{-1}\widetilde{\mathbf{P}}\Big] = \nabla\cdot\Big[-\left((1+\mathrm{Tr}\mathbf{E})\,\mathbf{I} - 2\mathbf{E}\right)\nabla\xi + (\mathbf{I}-\nabla\mathbf{u})\widetilde{\mathbf{P}} + o(\varepsilon)\Big] = 0. \tag{6.4.20}$$

Using standard calculus of variation, the weak form of the equations can be obtained as

$$\begin{aligned}
&\frac{\mathrm{d}}{\mathrm{d}\delta}\mathcal{F}^T[\mathbf{u}+\delta\mathbf{u}_1, \mathbf{n}+\delta\mathbf{n}_1, \widetilde{\mathbf{P}}+\delta\widetilde{\mathbf{P}}_1]\Big|_{\delta=0} = \int_{V_R}\Bigg\{ \\
&\widetilde{\mathbf{P}}_1 \cdot \Big[\left(\mathbf{I} - (\nabla\mathbf{u})^T\right)\nabla\xi + (1-\nabla\cdot\mathbf{u})\,\mathbb{A}_{\mathbf{n}}\widetilde{\mathbf{P}} + \mathbf{p}^{\mathrm{flexo}} + \mathbf{p}_1^{\mathrm{flexo}}\Big] + \\
&\nabla\mathbf{u}_1 : \Big[2(\mathbf{E}_d - \mathbf{E}^*(\mathbf{n})) + \kappa\mathrm{Tr}(\mathbf{E})\mathbf{I} + 2\mu_\beta(\mathbf{E}_d - \mathbf{E}^*(\mathbf{N}_a)) + \boldsymbol{\sigma}^{\mathrm{EL}} + \boldsymbol{\sigma}^{\mathrm{flexo}} + \boldsymbol{\sigma}^{\mathrm{MW}}\Big] + \\
&\mathbf{n}_1 \cdot \Big[-6\gamma(\mathbf{E}_d - \mathbf{E}^*(\mathbf{n}))\mathbf{n} + \mathbf{n}_1^{\mathrm{flexo}} + \mathbf{n}_2^{\mathrm{flexo}} + A_1(1-\nabla\cdot\mathbf{u})(\widetilde{\mathbf{P}}\cdot\mathbf{n})\widetilde{\mathbf{P}} - 2\lambda_{\mathbf{n}}\mathbf{n}\Big] + \\
&\nabla\mathbf{n}_1 : \Big[K_F(1+\mathrm{Tr}(\mathbf{E}))\nabla\mathbf{n} - 2K_F(\nabla\mathbf{n})\mathbf{E} + \mathbf{m}_1^{\mathrm{flexo}} + \mathbf{m}_2^{\mathrm{flexo}}\Big]\Bigg\} - \int_{S_N}\mathbf{t}_a\cdot\mathbf{u}_1 = 0,
\end{aligned} \tag{6.4.21}$$

where

$$\mathbf{p}_1^{\mathrm{flexo}} = f_s\left((\nabla\mathbf{n})^T : \nabla\mathbf{u}\right)\mathbf{n} - f_b(\nabla\mathbf{u})^T(\nabla\mathbf{n})^T\mathbf{n} + f_b(\nabla\mathbf{u})(\nabla\mathbf{n})\mathbf{n}, \tag{6.4.22}$$

$$\mathbf{n}_1^{\mathrm{flexo}} = -f_s(\nabla\cdot\mathbf{n})\widetilde{\mathbf{P}} + f_b(\nabla\mathbf{n})\widetilde{\mathbf{P}} - f_b(\nabla\mathbf{n})^T\widetilde{\mathbf{P}}, \tag{6.4.23}$$

$$\mathbf{n}_2^{\mathrm{flexo}} = f_s\left(\nabla\mathbf{n} : (\nabla\mathbf{u})^T\right)\widetilde{\mathbf{P}} - f_b\nabla\mathbf{n}(\nabla\mathbf{u})\widetilde{\mathbf{P}} + f_b(\nabla\mathbf{u})^T(\nabla\mathbf{n})^T\widetilde{\mathbf{P}}, \tag{6.4.24}$$

$$\mathbf{m}_1^{\mathrm{flexo}} = -f_s(\mathbf{n}\cdot\widetilde{\mathbf{P}})\mathbf{I} + f_b\mathbf{n}\otimes\widetilde{\mathbf{P}} - f_b\widetilde{\mathbf{P}}\otimes\mathbf{n}, \tag{6.4.25}$$

and $$\mathbf{m}_2^{\mathrm{flexo}} = f_s(\widetilde{\mathbf{P}}\cdot\mathbf{n})(\nabla\mathbf{u})^T - f_b\mathbf{n}\otimes(\nabla\mathbf{u})\widetilde{\mathbf{P}} + f_b(\widetilde{\mathbf{P}})\otimes(\nabla\mathbf{u})\mathbf{n}. \tag{6.4.26}$$

Here, we have avoided presenting the details of the variational procedure. Reader is referred to earlier sections and the reference [97] for more details. The equilibrium equations of the

system is obtained as

$$\nabla \cdot \Big[-\left((1 + \mathrm{Tr}\mathbf{E})\,\mathbf{I} - 2\mathbf{E} \right) \nabla \xi + (\mathbf{I} - \nabla \mathbf{u}) \widetilde{\mathbf{P}} \Big] = 0, \tag{6.4.27}$$

$$\left(\mathbf{I} - (\nabla \mathbf{u})^T \right) \nabla \xi + (1 - \nabla \cdot \mathbf{u})\, \mathbb{A}_{\mathbf{n}} \widetilde{\mathbf{P}} + \mathbf{p}^{\text{flexo}} + \mathbf{p}_1^{\text{flexo}} = \mathbf{0}, \tag{6.4.28}$$

$$\nabla \cdot \Big[2(\mathbf{E}_d - \mathbf{E}^*(\mathbf{n}))\mathbf{n} + \kappa \mathrm{Tr}(\mathbf{E})\mathbf{I} + 2\mu_\beta(\mathbf{E}_d - \mathbf{E}^*(\mathbf{N}_a)) + \boldsymbol{\sigma}^{\text{EL}} + \boldsymbol{\sigma}^{\text{flexo}} + \boldsymbol{\sigma}^{\text{MW}} \Big] = \mathbf{0}, \tag{6.4.29}$$

$$\nabla \cdot \Big[K_F(1 + \mathrm{Tr}(\mathbf{E}))\nabla \mathbf{n} - 2K_F(\nabla \mathbf{n})\mathbf{E} + \mathbf{m}_1^{\text{flexo}} + \mathbf{m}_2^{\text{flexo}} \Big] \tag{6.4.30}$$

and $$- \Big[-6\gamma(\mathbf{E}_d - \mathbf{E}^*(\mathbf{n}))\mathbf{n} + \mathbf{n}_1^{\text{flexo}} + \mathbf{n}_2^{\text{flexo}} + A_1(1 - \nabla \cdot \mathbf{u})(\widetilde{\mathbf{P}} \cdot \mathbf{n})\widetilde{\mathbf{P}} - 2\lambda_{\mathbf{n}}\mathbf{n} \Big] = \mathbf{0},$$

and the boundary conditions are given as

$$\mathbf{u} = \mathbf{u}_b \qquad \text{on} \quad S_D, \tag{6.4.31}$$

$$\boldsymbol{\nu}_R \cdot \Big[2(\mathbf{E}_d - \mathbf{E}^*(\mathbf{n})) + \kappa \mathrm{Tr}(\mathbf{E})\mathbf{I} + 2\mu_\beta(\mathbf{E}_d - \mathbf{E}^*(\mathbf{N}_a)) + \boldsymbol{\sigma}^{\text{EL}} + \boldsymbol{\sigma}^{\text{flexo}} + \boldsymbol{\sigma}^{\text{MW}} \Big] = \mathbf{t}_a \qquad \text{on} \quad S_N, \tag{6.4.32}$$

$$\boldsymbol{\nu}_R \cdot \Big[-\left((1 + \mathrm{Tr}\mathbf{E})\,\mathbf{I} - 2\mathbf{E} \right) \nabla \xi + (\mathbf{I} - \nabla \mathbf{u}) \widetilde{\mathbf{P}} \Big] = 0 \qquad \text{on} \quad \Gamma_N, \tag{6.4.33}$$

$$\xi = \xi_b \qquad \text{on} \quad \Gamma_D \tag{6.4.34}$$

and $$\boldsymbol{\nu}_R \cdot \Big[K_F(1 + \mathrm{Tr}(\mathbf{E}))\nabla \mathbf{n} - 2K_F(\nabla \mathbf{n})\mathbf{E} + \mathbf{m}_1^{\text{flexo}} + \mathbf{m}_2^{\text{flexo}} \Big] = \mathbf{0} \qquad \text{on} \quad \partial V_R. \tag{6.4.35}$$

6.5 Liquid Crystal Elastomers with Viscous Dissipation - Non-equilibrium processes

Here in this section, we construct a model to describe behavior of LCEs undergoing dissipative processes. We ignore photo-mechanical coupling ($\mathcal{F}^{\text{opt}} = 0$). It has been shown that viscoelastic properties of the LCEs may impact their behavior [277]. Thus, it is important to model LCE as a dissipative solid. Recently, Xu and Huo [287] used the continuum model given by Zhang et al. [290], which was originally based on dissipation principle for viscoelastic solids with micro order, and extended it to dielectric LCEs to study Fréedericksz transition. Here, we extend Ericksen-Leslie liquid crystal dynamic theory to dielectric LCEs. There are alternative versions of this theory available in the literature [260, 343, 261, 344, 345]. We have mostly relied on the versions of the theory available in the references [344] and [346].

As it will be shown later, it will be instructive to present formulation in the current configuration instead of reference undeformed configuration. We assume dead load $\widetilde{\mathbf{t}}$: $\partial V \to \mathbb{R}^3$ has been applied on the surface of the LCE ∂V. In addition, we identify power conjugate of time derivative of nematic director ($\frac{\mathrm{d}\mathbf{n}}{\mathrm{d}t}$) as $\mathbf{s} : \partial V \to \mathbb{R}^3$ and refer it as director stress vector. In the case of liquid crystals, the director field and local optical property of liquid crystals can quickly respond to and be controlled by the external electrical circuit which is the fundamental basis of the LCD technology. We are therefore motivated to consider the dynamical response of the director field under the application of a transient voltage $\xi_b = \xi_b(\mathbf{x}, t)$. For a thermodynamically consistent model, we identify the rate of work done by the external stimuli as

$$\dot{W} = \int_{\partial V} \left(\dot{\mathbf{y}} \cdot \widetilde{\mathbf{t}} + \dot{\mathbf{n}} \cdot \mathbf{s} \right) - \int_{\partial V_R} \xi_b \dot{\widetilde{\mathbf{D}}} \cdot \boldsymbol{\nu}_R, \tag{6.5.1}$$

where $\boldsymbol{\nu}_R$ (resp. $\boldsymbol{\nu}$) is the unit normal to the surface in the reference (resp. current) configuration. It should be mentioned that throughout these notes superposed dot denote total differentiation with respect to time. We identify energy potential $\psi(\mathbf{y}, \mathbf{n}, \mathbf{p})$ such that

total internal energy of the system U is expressed as

$$U = \int_V \psi(\nabla \mathbf{y}, \mathbf{n}, \nabla_y \mathbf{n}, \mathbf{p}) + \mathcal{E}^{\text{elect}}, \tag{6.5.2}$$

where $\mathcal{E}^{\text{elect}}$ is given as.

$$\mathcal{E}^{\text{elect}} = \int_V \frac{1}{2}\epsilon_0 |\nabla_y \xi|^2. \tag{6.5.3}$$

Therefore, rate of energy dissipation is expressed as

$$\begin{aligned} \dot{D} &= \dot{W} - \dot{U} - \frac{\mathrm{d}}{\mathrm{d}t}\int_V \frac{1}{2}\rho_0 |\dot{\mathbf{y}}|^2 \\ &= \int_{\partial V} \left(\dot{\mathbf{y}} \cdot \widetilde{\mathbf{t}} + \dot{\mathbf{n}} \cdot \mathbf{s}\right) - \int_{\partial V_R} \xi_b \dot{\tilde{\mathbf{D}}} \cdot \boldsymbol{\nu}_R - \dot{U} + \int_V \dot{\mathbf{y}} \cdot \boldsymbol{\iota}, \end{aligned} \tag{6.5.4}$$

where ρ_0 is the denity of the material and $\boldsymbol{\iota} = -\rho_0 \dot{\mathbf{v}}$ is the inertial force and $\mathbf{v}$ is the velocity. It is important to note that the LCE material is assumed to be incompressible and as a result density remains constant.

6.5.1 Balance laws for linear and angular momentum

We establish balance laws for linear and angular momentum by appealing to the frame-indifference priniple which states that physical laws are independent of the frame of reference. Suppose all the points $\mathbf{y}$ in the ambient space in which body V is evolving is represented using frame O. Upon a change in the frame $O \to O^*$ the spatial points $\mathbf{y}$ are maped to the spacial points $\mathbf{y}^*$ such that

$$\mathbf{y}^* = \mathbf{Q}(t)\mathbf{y} + \mathbf{c}(t), \tag{6.5.5}$$

where $\mathbf{Q}(t)$ is a rotation and $c(t)$ is a spatial point at each fixed time t. Superposed * is used to denote transformation due to change in the frame of reference. It is easily seen that velocity $\dot{\mathbf{y}}$ is transformed to

$$\dot{\mathbf{y}}^* = \mathbf{Q}\dot{\mathbf{y}} + \dot{\mathbf{Q}}\mathbf{y} + \dot{\mathbf{c}}. \tag{6.5.6}$$

We further assume traction $\widetilde{\mathbf{t}}$, nematic director $\mathbf{n}$, polarization $\mathbf{p}$, director stress vector $\mathbf{s}$ and inertial force $\boldsymbol{\iota}$ are frame-indifference [347]

$$\widetilde{\mathbf{t}}^* = \mathbf{Q}\widetilde{\mathbf{t}}, \qquad \mathbf{n}^* = \mathbf{Q}\mathbf{n}, \qquad \mathbf{p}^* = \mathbf{Q}\mathbf{p}, \qquad \mathbf{s}^* = \mathbf{Q}\mathbf{s}, \qquad \boldsymbol{\iota}^* = \mathbf{Q}\boldsymbol{\iota}. \tag{6.5.7}$$

We assume rate of energy dissipation, rate of change of internal energy and the energy balance relation given in the Eq.(6.5.4) are frame-indifferent

$$\dot{D} = \int_{\partial V} \left(\dot{\mathbf{y}}^* \cdot \widetilde{\mathbf{t}}^* + \dot{\mathbf{n}}^* \cdot \mathbf{s}^* \right) - \int_{\partial V_R} \xi_b \dot{\widetilde{\mathbf{D}}} \cdot \boldsymbol{\nu}_R - \dot{U} + \int_V \dot{\mathbf{y}}^* \cdot \boldsymbol{\iota}^*. \tag{6.5.8}$$

Substituting (6.5.6) and (6.5.7) into Eq.(6.5.8) we have

$$\begin{aligned} \dot{D} = &\int_{\partial V} \left((\dot{\mathbf{y}} + \mathbf{Q}^T\dot{\mathbf{Q}}\mathbf{y} + \mathbf{Q}^T\dot{\mathbf{c}}) \cdot \widetilde{\mathbf{t}} + (\dot{\mathbf{n}} + \mathbf{Q}^T\dot{\mathbf{Q}}\mathbf{n}) \cdot \mathbf{s} \right) + \int_{\partial V_R} \xi_b \dot{\widetilde{\mathbf{D}}} \cdot \boldsymbol{\nu}_R - \dot{U} \\ &+ \int_V ((\dot{\mathbf{y}} + \mathbf{Q}^T\dot{\mathbf{Q}}\mathbf{y} + \mathbf{Q}^T\dot{\mathbf{c}})) \cdot \boldsymbol{\iota}, \end{aligned} \tag{6.5.9}$$

where $\mathbf{Q}^T\dot{\mathbf{Q}}$ is skew and as a result there exist a vector of angular velocity $\boldsymbol{\zeta}$ such that $\mathbf{Q}^T\dot{\mathbf{Q}} = \boldsymbol{\zeta}\times$. Since relation $c(t)$ is arbitrary, we can replace $\mathbf{Q}^T\dot{\mathbf{c}}$ with $\dot{\mathbf{c}}$ and rewrite the equation above as

$$\begin{aligned} \dot{D} = &\int_{\partial V} \left(\dot{\mathbf{y}} \cdot \widetilde{\mathbf{t}} + \dot{\mathbf{c}} \cdot \widetilde{\mathbf{t}} + \mathbf{n} \cdot \mathbf{s} + \boldsymbol{\zeta} \cdot (\mathbf{y} \times \widetilde{\mathbf{t}}) + \boldsymbol{\zeta} \cdot (\mathbf{n} \times \mathbf{s}) \right) \\ &- \int_{\partial V_R} \xi_b \dot{\widetilde{\mathbf{D}}} \cdot \boldsymbol{\nu}_R - \dot{U} + \int_V \left(-\dot{\mathbf{y}} \cdot \rho_0 \dot{\mathbf{v}} - \dot{\mathbf{c}} \cdot \rho_0 \dot{\mathbf{v}} - \boldsymbol{\zeta} \cdot (\mathbf{y} \times \rho_0 \dot{\mathbf{v}}) \right). \end{aligned} \tag{6.5.10}$$

As it was mentioned earlier the rate of energy dissipation should not change by changeing frame of reference and the equation (6.5.10) must hold for any arbitrary $\boldsymbol{\zeta}$ and $\boldsymbol{c}(t)$. Therefore, we can obtain the balannce laws for linear and angular momentum by subtracting Eq.(6.5.10) from (6.5.4).

$$\int_V \rho_0 \dot{\mathbf{v}} = \int_{\partial V} \widetilde{\mathbf{t}} \tag{6.5.11}$$

$$\text{and} \qquad \int_V \mathbf{y} \times \rho_0 \dot{\mathbf{v}} = \int_{\partial V} \left(\mathbf{y} \times \widetilde{\mathbf{t}} + \mathbf{n} \times \mathbf{s} \right). \tag{6.5.12}$$

Using tetrahedron arguments [348, 346, 347], we can define tensor fields $\boldsymbol{\sigma}$ and $\mathbf{S}$ such that

$$\widetilde{\mathbf{t}} = \boldsymbol{\sigma}\boldsymbol{\nu} \quad \text{and} \qquad \mathbf{s} = \mathbf{S}\boldsymbol{\nu}. \tag{6.5.13}$$

The differential form of balance laws are obtained by substituting Eq.(6.5.13) in Eqs.(6.5.12) and (6.5.11) and using divergence theorem:

$$\nabla_y \cdot \boldsymbol{\sigma} = \rho_0 \dot{\mathbf{v}}, \qquad \text{or} \qquad \sigma_{ij,j} = \rho_0 \dot{v}_i, \tag{6.5.14}$$

$$\mathbb{E} : \Big(\boldsymbol{\sigma}^T + \nabla_y \cdot (\mathbf{n} \otimes \mathbf{S})\Big) = \mathbf{0}, \qquad \text{or} \qquad E_{ijk}\sigma_{kj} + (E_{ijk} n_j S_{kl})_{,l} = 0, \tag{6.5.15}$$

where $\mathbb{E}$ is the Levi-Civita tensor.

6.5.2 Constitutive relations

We use second law of thermodynamics and frame-indifference principle in order to obtain constitutive relations required to describe dissipative motion of LCEs. The constitutive relations should postulated in a way that satisfies following relation

$$\dot{D} = \dot{W} - \dot{U} \geq 0. \tag{6.5.16}$$

Assuming material is incompressible and using Eq.(6.5.2), reate of change of internal energy is expressed as

$$\dot{U} = \int_V \dot{\psi}(\nabla \mathbf{y}, \mathbf{n}, \nabla_y \mathbf{n}, \mathbf{p}) + \dot{\mathcal{E}}^{\text{elect}}. \tag{6.5.17}$$

Note that the energy density functional $\psi(\nabla \mathbf{y}, \mathbf{n}, \nabla_y \mathbf{n}, \mathbf{p})$ has been defined in the current configuration. The rate of change of energy density functional is given as

$$\dot{\psi}(\nabla \mathbf{y}, \mathbf{n}, \nabla_y \mathbf{n}, \mathbf{p}) = \frac{\partial \psi}{\partial \mathbf{F}} : \dot{\mathbf{F}} + \frac{\partial \psi}{\partial \mathbf{n}} \cdot \dot{\mathbf{n}} + \frac{\partial \psi}{\partial \nabla_y \mathbf{n}} : \dot{\overline{\nabla_y \mathbf{n}}} + \frac{\partial \psi}{\partial \mathbf{p}} \cdot \dot{\mathbf{p}}, \tag{6.5.18}$$

where $\dot{\mathbf{F}} = \mathbf{L}\mathbf{F}$ and $\mathbf{L} = \nabla_y \mathbf{v}$ is th velocity gradient tensor. Also, it is strightforward to show that

$$\dot{\overline{\nabla_y \mathbf{n}}} = \nabla_y \dot{\mathbf{n}} - (\nabla_y \mathbf{n})\mathbf{L}. \tag{6.5.19}$$

Substituting Eq.(6.5.19) into Eq.(6.5.20), we have

$$\dot{\psi}(\nabla \mathbf{y}, \mathbf{n}, \nabla_y \mathbf{n}, \mathbf{p}) = \left[\frac{\partial \psi}{\partial \mathbf{F}}\mathbf{F}^T - \frac{\partial \psi}{\partial \nabla_y \mathbf{n}}(\nabla_y \mathbf{n})^T\right] : \mathbf{L} + \frac{\partial \psi}{\partial \mathbf{n}} \cdot \dot{\mathbf{n}} + \frac{\partial \psi}{\partial \nabla_y \mathbf{n}} : \nabla_y \dot{\mathbf{n}} + \frac{\partial \psi}{\partial \mathbf{p}} \cdot \dot{\mathbf{p}}. \quad (6.5.20)$$

In addition, the rate of change of the electric energy is expresse as (see Appendix)

$$\dot{\mathcal{E}}^{\text{elect}} = \int_V \left(\boldsymbol{\sigma}^{\text{MW}} : \mathbf{L} + \nabla_y \xi \cdot \dot{\mathbf{p}}\right) - \int_{\partial V_R} \xi \dot{\tilde{\mathbf{D}}} \cdot \boldsymbol{\nu}_R, \quad (6.5.21)$$

where

$$\boldsymbol{\sigma}^{\text{MW}} = (-\nabla_y \xi) \otimes (-\epsilon_0 \nabla_y \xi + \mathbf{p}) - (\frac{\epsilon_0}{2}|\nabla_y \xi|^2 - \nabla_y \xi \cdot \mathbf{p})\mathbf{I}. \quad (6.5.22)$$

Moreover, by substituting Eq.(6.5.13) into (6.5.1) we have

$$\begin{aligned} \dot{W} &= \int_V [\boldsymbol{\sigma} : \mathbf{L} + \dot{\mathbf{y}} \cdot (\nabla_y \cdot \boldsymbol{\sigma}) + \mathbf{S} : \nabla_y \dot{\mathbf{n}} + (\nabla_y \cdot \mathbf{S}) \cdot \dot{\mathbf{n}}] - \int_{\partial V_R} \xi_b \dot{\tilde{\mathbf{D}}} \cdot \boldsymbol{\nu}_R \\ &= \int_V [\boldsymbol{\sigma} : \mathbf{L} - \dot{\mathbf{y}} \cdot \boldsymbol{\iota} + \mathbf{S} : \nabla_y \dot{\mathbf{n}} + (\nabla_y \cdot \mathbf{S}) \cdot \dot{\mathbf{n}}] - \int_{\partial V_R} \xi_b \dot{\tilde{\mathbf{D}}} \cdot \boldsymbol{\nu}_R. \end{aligned} \quad (6.5.23)$$

Using Eqs.(6.5.4), (6.5.20), (6.5.21) (6.5.23), We can express rate of energy dissipation as

$$\begin{aligned} \dot{D} = \int_V &\left(\boldsymbol{\sigma} - \boldsymbol{\sigma}^{\text{MW}} - \frac{\partial \psi}{\partial \mathbf{F}}\mathbf{F}^T + \frac{\partial \psi}{\partial \nabla_y \mathbf{n}}\right) : \mathbf{L} \\ &+ \left(\mathbf{S} - \frac{\partial \psi}{\partial \nabla_y \mathbf{n}}\right) : \nabla_y \dot{\mathbf{n}} + \left((\nabla_y \cdot \mathbf{S}) - \frac{\partial \psi}{\partial \mathbf{n}}\right) \cdot \dot{\mathbf{n}} \\ &+ \left(-\frac{\partial \psi}{\partial \mathbf{p}} - \nabla_y \xi\right) \cdot \dot{\mathbf{p}} \geq 0 \end{aligned} \quad (6.5.24)$$

We introduce potential Φ^{visc} such that

$$\dot{D} = \int_V \Phi^{\text{visc}}(\mathbf{L}, \mathbf{n}, \dot{\mathbf{n}}), \quad (6.5.25)$$

where $\Phi^{\text{visc}} \geq 0$ for any $(\mathbf{L}, \mathbf{n}, \dot{\mathbf{n}}) \in \mathbb{R}^{3\times 3} \times S^2 \times \mathbb{R}^3$. We have assumed that Φ^{visc} is independent of gradient of director angular velocity. Also, $\Phi^{\text{visc}}(\mathbf{0}, \mathbf{n}, \mathbf{0}) = 0$ for any $\mathbf{n} \in S^2$. Therefore, we assume following form for potential Φ^{visc}

$$\Phi^{\text{visc}}(\mathbf{L}, \mathbf{n}, \dot{\mathbf{n}}) = \boldsymbol{\tau} : \mathbf{L} + \hat{\mathbf{s}} \cdot \dot{\mathbf{n}}, \quad (6.5.26)$$

where $\boldsymbol{\tau}$ and $\hat{\mathbf{s}}$ are referred as viscous stress tesor and viscous couple stress vector, respectively. Therefore, the sufficient condition to satisfy Eq.(6.5.24) is to have

$$\boldsymbol{\sigma} = \boldsymbol{\sigma}^{\mathrm{MW}} + \frac{\partial \psi}{\partial \mathbf{F}}\mathbf{F}^T - \frac{\partial \psi}{\partial \nabla_y \mathbf{n}} - \lambda_p \mathbf{I} + \boldsymbol{\tau}, \tag{6.5.27}$$

$$\mathbf{S} = \frac{\partial \psi}{\partial \nabla_y \mathbf{n}}, \tag{6.5.28}$$

$$(\nabla_y \cdot \mathbf{S}) - \frac{\partial \psi}{\partial \mathbf{n}} - \lambda_{\mathbf{n}} \mathbf{n} = \mathbf{0} \tag{6.5.29}$$

$$\text{and} \qquad \frac{\partial \psi}{\partial \mathbf{p}} + \nabla_y \xi = \mathbf{0}. \tag{6.5.30}$$

In order to complete the theory, we need to provide constitutive relations for $\boldsymbol{\tau}$ and $\hat{\mathbf{s}}$. It is physically reasonable to assume $\boldsymbol{\tau}$ and $\hat{\mathbf{s}}$ are frame in-different

$$\boldsymbol{\tau}^* = \mathbf{Q}\boldsymbol{\tau}\mathbf{Q}^T \qquad \text{and} \qquad \hat{\mathbf{s}}^* = \mathbf{Q}\hat{\mathbf{s}}. \tag{6.5.31}$$

In addition, dissipation potential Φ^{visc} is independent of frame of reference. Thus,

$$\Phi^{\mathrm{visc}}(\mathbf{L}^*, \mathbf{n}^*, \dot{\mathbf{n}}^*) = \Phi^{\mathrm{visc}}(\mathbf{L}, \mathbf{n}, \dot{\mathbf{n}}) \tag{6.5.32}$$

$$\text{and} \qquad \boldsymbol{\tau}^* : \mathbf{L}^* + \hat{\mathbf{s}}^* \cdot \dot{\mathbf{n}}^* = \boldsymbol{\tau} : \mathbf{L} + \hat{\mathbf{s}} \cdot \dot{\mathbf{n}}. \tag{6.5.33}$$

From (6.5.5) and , we have $\mathbf{L}^* = \mathbf{Q}\mathbf{L}\mathbf{Q}^T + \dot{\mathbf{Q}}\mathbf{Q}^T$ and $\dot{\mathbf{n}}^* = \mathbf{Q}\dot{\mathbf{n}} + \dot{\mathbf{Q}}\mathbf{n}$. Therefore, we can rewrite Eq.(6.5.33) as

$$\boldsymbol{\tau} : \boldsymbol{\Omega} + \hat{\mathbf{s}} \cdot \boldsymbol{\Omega}\mathbf{n} = 0, \tag{6.5.34}$$

where $\boldsymbol{\Omega} = \dot{\mathbf{Q}}\mathbf{Q}^T$ is an arbitrary skew tensor. Since $\dot{\mathbf{n}} \cdot \mathbf{n} = 0$, we can determine viscous couple stress vector in terms of viscous stress tensor:

$$\mathbb{E} : \boldsymbol{\tau}^T = \hat{\mathbf{s}} \times \mathbf{n}, \qquad \text{or} \qquad E_{ijk}\tau_{kj} = E_{ijk}\hat{s}_j n_k. \tag{6.5.35}$$

Let $\mathbf{D} = \frac{1}{2}(\mathbf{L}+\mathbf{L}^T)$ and $\mathbf{W} = \frac{1}{2}(\mathbf{L}-\mathbf{L}^T)$ be symmetric and skew part of velocity gradient tensor. We identify co-rotational rate of change of nematic director $\mathring{\mathbf{n}}$ as

$$\mathring{\mathbf{n}} = \dot{\mathbf{n}} - \mathbf{W}\mathbf{n}. \tag{6.5.36}$$

In contrast to rate of change of nematic director $\dot{\mathbf{n}}$, co-rotational rate of change of nematic director is frame in-different ($\mathring{\mathbf{n}}^* = \mathbf{Q}\mathring{\mathbf{n}}$). Substituting Eq.(6.5.36) into Eq.(6.5.26) and using Eq.(6.5.34), we have

$$\Phi^{\text{visc}}(\mathbf{L}, \mathbf{n}, \dot{\mathbf{n}}) = \boldsymbol{\tau} : \mathbf{D} + \hat{\mathbf{s}} \cdot \mathring{\mathbf{n}}. \tag{6.5.37}$$

In order to proceed further with the theory, we need to make constitutive assumption for the viscous stress $\boldsymbol{\tau}$. From Eq.(6.5.26), we can conclude $\boldsymbol{\tau} = \boldsymbol{\tau}(\mathbf{L}, \mathbf{n}, \dot{\mathbf{n}})$. Moreover, since rigid body rotation does not contribute to viscous stress and energy dissipatopn, we can conclude that

$$\boldsymbol{\tau} = \boldsymbol{\tau}(\mathbf{D}, \mathbf{n}, \mathring{\mathbf{n}}). \tag{6.5.38}$$

In addition, viscous stress should necessarily satisfy objectivity principle

$$\boldsymbol{\tau}(\mathbf{Q}\mathbf{D}\mathbf{Q}^T, \mathbf{Q}\mathbf{n}, \mathbf{Q}\mathring{\mathbf{n}}) = \mathbf{Q}\boldsymbol{\tau}(\mathbf{D}, \mathbf{n}, \mathring{\mathbf{n}})\mathbf{Q}^T. \tag{6.5.39}$$

Also, transverse symmetry of nematic liquid crystal elastomers requires constitutive realation of viscous stress to be invariant under reflactions within plane containing nematic director $\mathbf{n}$. Consistent with experimental observations for liquid crystals [346], we assume following form for the viscous stress

$$\boldsymbol{\tau} = \mathbb{A}_{\mathbf{n}} + \mathbb{B}_{\mathbf{n}} \cdot \mathring{\mathbf{n}} + \mathbb{C}_{\mathbf{n}} : \mathbf{D}, \qquad \text{or} \qquad \tau_{ij} = (A_{\mathbf{n}})_{ij} + (B_{\mathbf{n}})_{ijk}\mathring{n}_k + (\mathbb{C}_{\mathbf{n}})_{ijkl}D_{kl}. \tag{6.5.40}$$

As it has been noted by Stewart [346], tensors $\mathbb{A}_{\mathbf{n}}$, $\mathbb{B}_{\mathbf{n}}$ and $\mathbb{C}_{\mathbf{n}}$ which satisfy transversely isotropic symmetry and also objectivity condition (6.5.39) can be expressed in terms of linear combination of products of $\mathbf{n}$ and $\mathbf{I} - \mathbf{n} \otimes \mathbf{n}$:

$$(A_{\mathbf{n}})_{ij} = \mu_1\delta_{ij} + \mu_2 n_i n_j, \tag{6.5.41}$$

$$(B_{\mathbf{n}})_{ijk} = \mu_3\delta_{ij}n_k + \mu_4\delta_{jk}n_i + \mu_5\delta_{ki}n_j \tag{6.5.42}$$

and
$$\begin{aligned}(C_{\mathbf{n}})_{ijkl} = {} & \mu_6\delta_{ij}\delta_{kl} + \mu_7\delta_{ik}\delta_{jl} + \mu_8\delta_{il}\delta_{jk} + \mu_9\delta_{ij}n_k n_p \\ & + \mu_{10}\delta_{jk}n_i n_l + \mu_{11}\delta_{ik}n_j n_l + \mu_{12}\delta_{il}n_j n_k \\ & + \mu_{13}\delta_{jp}n_i n_k + \mu_{14}\delta_{kp}n_i n_j + \mu_{15}n_i n_j n_k n_l.\end{aligned} \tag{6.5.43}$$

We can simplify expressions above using the fact that $\mathbf{D} = \mathbf{D}^T$, $\mathrm{Tr}(\mathbf{D}) = 0$ and $\mathbf{n} \cdot \mathring{n} = 0$. Thus, we have

$$\begin{aligned}\tau_{ij} &= (\mu_1 + \mu_9 n_k D_{kl} n_l)\delta_{ij} + (\mu_2 + \alpha_1 n_k D_{kl} n_l) n_i n_j \\ &+ \alpha_2 \mathring{n}_i n_j + \alpha_3 \mathring{n}_j n_i + \alpha_4 D_{ij} + \alpha_5 n_j A_{ik} n_k + \alpha_6 n_i A_{jk} n_k,\end{aligned} \tag{6.5.44}$$

$$\hat{s}_i = \gamma_1 \mathring{n}_i + \gamma_2 D_{ij} n_j, \tag{6.5.45}$$

$$\begin{aligned}\dot{D} =& \mu_2 n_i D_{ij} n_j + \alpha_1 (n_i D_{ij} n_j)^2 + (\alpha_2 + \alpha_3 + \gamma_2)\mathring{n}_i D_{ij} n_j \\ & \alpha_4 D_{ij} D_{ij} + (\alpha_5 + \alpha_6) n_i D_{ij} D_{jk} n_k + \gamma_1 \mathring{n}_i \mathring{n}_i \geq 0,\end{aligned} \tag{6.5.46}$$

$$\begin{aligned}&\alpha_1 = \mu_{15}, \quad \alpha_2 = \mu_5, \quad \alpha_3 = \mu_4, \quad \alpha_4 = \mu_7 + \mu_8, \quad \alpha_5 = \mu_{11} + \mu_{12}, \quad \alpha_6 = \mu_{10} + \mu_{13}, \\ &\gamma_1 = \alpha_3 - \alpha_2, \quad \gamma_2 = \alpha_6 - \alpha_5 \quad \text{and} \quad \mu_2 = 0.\end{aligned} \tag{6.5.47}$$

6.6 Finite Element Implementation

In this section, we develop finite element solution for coupled problem presented earlier. We aim to present a straightforward approach which will enable us to solve aforementioned system of equations without using any commercial packages. As the Eq. 6.2.46 is linear with respect to polarization and it is easier to express boundary condition in terms of electric potential, we determine polarization in terms of electric potential and will consider electric potential as our unknown field instead of polarization. The weak form of the equations are

given as

$$\int_{V_R} \nabla w_1 \cdot \widetilde{\mathbf{D}} = 0, \tag{6.6.1}$$

$$\int_{V_R} \nabla \mathbf{w}_2 : \left[\boldsymbol{\Sigma} + \boldsymbol{\Sigma}^{\text{anis}} + \boldsymbol{\Sigma}^{\text{EL}} + \boldsymbol{\Sigma}^{\text{MW}} + \boldsymbol{\Sigma}^{\text{flexo}} - \lambda_p J\mathbf{F}^{-T}\right] = \int_{S_N} \widetilde{\mathbf{t}}_a \cdot \mathbf{w}_2, \tag{6.6.2}$$

$$\int_{V_R} \nabla \mathbf{w}_3 : \left[K_F J \nabla \mathbf{n}\mathbf{F}^{-1}\mathbf{F}^{-T} + \mathbf{m}^{\text{flexo}}\right]$$
$$+ \int_{V_R} \mathbf{w}_3 \cdot \left[a_2 \mathbf{F}\mathbf{F}^T\mathbf{n} + A_1(\mathbf{n}\cdot\widetilde{\mathbf{P}})\frac{\widetilde{\mathbf{P}}}{J} + \mathbf{n}^{\text{flexo}} + \frac{\partial W^{\text{opt}}}{\partial \mathbf{n}} - 2\lambda_{\mathbf{n}}\mathbf{n}\right] = 0, \tag{6.6.3}$$

$$\int_{V_R} w_4\left(\frac{\partial(W^{\text{opt}} + W^{\text{elast}} + W^{\text{anis}})}{\partial Q}\right) = 0, \tag{6.6.4}$$

$$\int_{V_R} w_5(\mathbf{n}\cdot\mathbf{n} - 1) = 0, \tag{6.6.5}$$

and
$$\int_{V_R} w_6(\det\mathbf{F} - 1) = 0. \tag{6.6.6}$$

where $(w_1, w_2, w_3, w_4, w_5, w_6) \in \mathcal{W}$ and

$$\mathcal{W} := \{(w_1, \mathbf{w}_2, \mathbf{w}_3, w_4, w_5) \in H^1(V_R;\mathbb{R}) \times H^1(V_R;\mathbb{R}^3) \times H^1(V_R;\mathbb{R}^3)$$
$$\times L_2(V_R;\mathbb{R}) \times L_2(V_R;\mathbb{R}) \times L_2(V_R;\mathbb{R}) | w_1 = 0 \quad \text{on} \quad \Gamma_D, \quad \mathbf{w}_2 = \mathbf{0} \quad \text{on} \quad S_D\}. \tag{6.6.7}$$

We use open source FEA package FeniCS to solve above system of equations. We use Taylor-Hood element for this coupled nonlinear problem where we use we use quadratic interpolation for displacement, and linear interpolation for electric potential, nematic director, order parameter and Lagrange multipliers. A similar setting has been successfully used by Luo and Calderer [26] to study behavior of LCE materials. We will compare and validate results of our model with the results presented by Luo and Calderer [26].

6.7 Asymptotic theories for homogeneous LCE

Though the Euler-Lagrange equations obtained at the end of Section 6.4 presumably form a well-posed system for $(\mathbf{n}, \mathbf{y}, \mathbf{p})$, these general nonlinear differential systems are not amenable to explicit solution, hindering the predictive capability of the model. In practice, the loading conditions (i.e., the prescribed boundary conditions) and material constants are such that the responses of the LCE body is in a particular regime that can be well

approximated by a simplified asymptotic theory. We therefore consider some particular regimes delineated by relevant dimensionless parameters and the associated asymptotic theories. Strictly speaking, different asymptotic regimes should be precisely described by some relevant dimensionless parameters of material constants and loading conditions. However, nontrivial asymptotic theories can be more conveniently derived by directly assuming the relative scales of the state variables. Therefore, we present linear theory for NLCEs presented in the section 6.4 and establish asymptotic theories for these materials.

6.7.1 Asymptotic scalings

Similar to previous section, we use dimensionless form of the equations. Let ε_i $(i = 1, 2, 3)$ be the orders of magnitude of $(\nabla\mathbf{n}, \nabla\mathbf{u}, \mathbf{P})$:

$$|\nabla\mathbf{n}| \propto \varepsilon_1, \qquad |\nabla\mathbf{u}| \propto \varepsilon_2 \quad \text{and} \quad |\mathbf{p}| \propto \varepsilon_3,$$

and for an integer index $\alpha = (\alpha_1, \alpha_2, \alpha_3) \in \mathbb{Z}^3$, denote by $\varepsilon^\alpha = \varepsilon_1^{\alpha_1}\varepsilon_2^{\alpha_2}\varepsilon_3^{\alpha_3}$. Formally, we expand the dimensionless total free energy as

$$\mathcal{F}^T = \sum_\alpha F^{(\alpha)}[\mathbf{u}, \mathbf{n}, \mathbf{P}], \tag{6.7.1}$$

where $F^{(\alpha)}[\mathbf{u},\mathbf{n},\mathbf{P}]$ are the leading order terms of free energy and obtained by direct calculation as

$$F^{(2,0,0)}[\mathbf{n}] = \int_{V_R} \frac{1}{2} K_F |\nabla \mathbf{n}|^2, \tag{6.7.2}$$

$$F^{(2,1,0)}[\mathbf{n},\mathbf{u}] = \int_{V_R} \sigma^{\mathrm{EL}} : \nabla \mathbf{u}, \tag{6.7.3}$$

$$F^{(0,2,0)}[\mathbf{n},\mathbf{u}] = \int_{V_R} \frac{1}{2} \left(\nabla \mathbf{u} - \mathbf{E}^*(\mathbf{n})\right) : \mathbb{C} \left(\nabla \mathbf{u} - \mathbf{E}^*(\mathbf{n})\right) + \mu_\beta |\mathbf{E}_d - \mathbf{E}^*(\mathbf{N}_a)|^2, \tag{6.7.4}$$

$$F^{(0,0,2)}[\mathbf{n},\mathbf{P}] = \int_{V_R} -\frac{1}{2}|\nabla \xi|^2 + \frac{1}{2}\mathbf{P}\cdot \mathbb{A}_{\mathbf{n}}\mathbf{P} - \frac{1}{2}|\nabla \xi|^2 + \nabla \xi \cdot \mathbf{P}, \tag{6.7.5}$$

$$F^{(0,1,2)}[\mathbf{n},\mathbf{u},\mathbf{P}] = \int_{V_R} \nabla \mathbf{u} : \boldsymbol{\sigma}^{\mathrm{MW}}, \tag{6.7.6}$$

$$F^{(1,0,1)}[\mathbf{n},\mathbf{P}] = \int_{V_R} \mathbf{P} \cdot \mathbf{p}^{\mathrm{flexo}} \tag{6.7.7}$$

$$\text{and} \qquad F^{(1,1,1)}[\mathbf{n},\mathbf{u},\mathbf{P}] = \int_{V_R} \nabla \mathbf{u} : \boldsymbol{\sigma}^{\mathrm{flexo}}. \tag{6.7.8}$$

For brevity, we use $\mathbf{P}$ instead of $\widetilde{\mathbf{P}}$ in this section. Also, $\mathbb{C}$ is the dimensionless stiffness tensor of the material which is defined as dimensional elastic stiffness divided by shear modulus of the material. Depending on the relationship of the actual materials properties and loading conditions, the system in certain asymptotic regimes could be well approximated by simplified theories. Below we discuss separately about the possible nontrivial asymptotic regimes and associated theories for LCEs.

Liquid crystals ($\mathbb{C} \sim 0, \quad \mu_\beta \sim 0$)

In this regime, it is clear that the LCE behaves more similar to "liquid" crystal instead of behaving like a solid. Therefore, it is much more convenient to use Eulerian description. It is worth noting that we do not assume deformation is small in this regime but we neglect the regular elasticity energy terms from the free energy. The free energy in this regime is expressed as

$$\mathcal{F}[\mathbf{p},\mathbf{n}] = \int_V \frac{1}{2} K_F |\nabla_y \mathbf{n}|^2 + \frac{1}{2}\mathbf{p}\cdot \mathbb{A}_{\mathbf{n}}\mathbf{p} - \frac{1}{2}|\nabla_y \xi|^2 + \nabla_y \xi \cdot \mathbf{p} + \mathbf{p}\cdot \tilde{\mathbf{p}}^{\mathrm{flexo}}, \tag{6.7.9}$$

where

$$\tilde{\mathbf{p}}^{\text{flexo}} = -f_s(\nabla_y \cdot \mathbf{n})\mathbf{n} + f_b(\nabla_y \mathbf{n})^T \mathbf{n} - f_b(\nabla_y \mathbf{n})\mathbf{n}. \tag{6.7.10}$$

It should be mentioned that flexoelectric coefficients and Frank elasticity coefficient are size dependent coefficients. The flexoelectric coefficient is linearly proportional to inverse of the characteristic length of the material but the Frank elasticity depends linearly on the square of inverse of size scale (see Eq.(6.2.28)). Depending on the value of flexoelectric coefficients, we can divide this regime into two different categories by either including or excluding flexoelectric terms in the theory:

1. Let f_b and $f_s \to 0$. As a result, we neglect the flexoelectric term in the energy functional (6.7.9). The Euler-Lagrange equation for energy functional (6.7.9) along with the Maxwell equation forms a system of equations which gives equilibrium state of the system

$$\nabla_y \cdot (-K_F \nabla_y \mathbf{n}) - (\Delta\epsilon \nabla_y \xi \otimes \nabla_y \xi + \lambda_{\mathbf{n}} \mathbf{I})\, \mathbf{n} = \mathbf{0} \quad \text{in} \quad V, \tag{6.7.11}$$

$$\nabla_y \cdot (-\mathbb{D}_{\mathbf{n}} \nabla_y \xi) = 0 \quad \text{in} \quad V, \tag{6.7.12}$$

$$\mathbf{p} = -\mathbb{A}_{\mathbf{n}}^{-1} \nabla_y \xi \quad \text{in} \quad V, \tag{6.7.13}$$

$$-K_F \nabla_y \mathbf{n} \cdot \boldsymbol{\nu} = \mathbf{0} \quad \text{on} \quad \partial V, \tag{6.7.14}$$

$$-\mathbb{D}_{\mathbf{n}} \nabla_y \xi \cdot \boldsymbol{\nu} = \mathbf{0} \quad \text{on} \quad \Gamma_N \tag{6.7.15}$$

$$\text{and} \qquad \xi = \xi_b \quad \text{on} \quad \Gamma_D, \tag{6.7.16}$$

where $\Delta\epsilon = \epsilon_c - \epsilon_a$.

Remark #1:Qualitatively, the effect of electric field on the director field can be more conveniently seen by inserting Eq.(6.7.13) into (6.7.9) and rewriting the total free energy as

$$\begin{aligned} \mathcal{F}[\mathbf{p}, \mathbf{n}] &= \int_V \frac{1}{2} K_F |\nabla_y \mathbf{n}|^2 - \frac{1}{2} \mathbb{D}_{\mathbf{n}} \nabla_y \xi \cdot \nabla_y \xi \\ &= \int_V \frac{1}{2} K_F |\nabla_y \mathbf{n}|^2 - \epsilon_a |\nabla_y \xi|^2 - \Delta\epsilon (\mathbf{n} \cdot \nabla_y \xi)^2. \end{aligned} \tag{6.7.17}$$

Therefore, if $\Delta\epsilon > 0$ (resp. $\Delta\epsilon < 0$), i.e. $\epsilon_c > \epsilon_a$ (resp. $\epsilon_c < \epsilon_a$), the director field

tends to align with (resp. prependicular to) the electric field $-\nabla_y \xi$.

Remark #2: If $\Delta\epsilon \to 0$ or $K_F \gg A_1$ then the Frank elasticity tem in the energy functional (6.7.9) has the major impact and all other terms can be neglected. Therefore, nematic director can be determined solving following equation

$$\nabla_y \cdot (-K_F \nabla_y \mathbf{n}) - \lambda_{\mathbf{n}} \mathbf{n} = \mathbf{0} \qquad \text{in} \quad V \tag{6.7.18}$$

$$\text{and} \qquad -K_F \nabla_y \mathbf{n} \cdot \boldsymbol{\nu} = \mathbf{0} \qquad \text{on} \quad \partial V. \tag{6.7.19}$$

If we denote the solution of above equation with $\mathbf{n}^*$, the electric field in this case can be detirmined solving

$$\nabla_y \cdot (-\mathbb{D}_{\mathbf{n}^*} \nabla_y \xi) = 0 \qquad \text{in} \quad V. \tag{6.7.20}$$

2. Let $f_b \neq 0$ or $f_s \neq 0$. In this case, we need to take into account all the terms in the Eq.(6.7.9). Using standard calculus of variation and minimizing energy with respect

to polarization and nematic director we have

$$\begin{aligned}
&\nabla_y \cdot (-K_F \nabla_y \mathbf{n} - \tilde{\mathbf{m}}_1^{\text{flexo}}) + \tilde{\mathbf{n}}_1^{\text{flexo}} \\
&+ \left[-\Delta\epsilon \left(\nabla_y \xi + \tilde{\mathbf{p}}^{\text{flexo}} \right) \otimes \left(\nabla_y \xi + \tilde{\mathbf{p}}^{\text{flexo}} \right) + \lambda_{\mathbf{n}} \mathbf{I} \right] \mathbf{n} = \mathbf{0} \qquad \text{in} \quad V,
\end{aligned} \tag{6.7.21}$$

$$\nabla_y \cdot \left(-\mathbb{D}_{\mathbf{n}} \nabla_y \xi - \mathbb{A}_{\mathbf{n}}^{-1} \tilde{\mathbf{p}}^{\text{flexo}} \right) = 0 \qquad \text{in} \quad V, \tag{6.7.22}$$

$$\mathbf{p} = -\mathbb{A}_{\mathbf{n}}^{-1} \nabla_y \xi - \mathbb{A}_{\mathbf{n}}^{-1} \tilde{\mathbf{p}}^{\text{flexo}} \qquad \text{in} \quad V, \tag{6.7.23}$$

$$(-K_F \nabla_y \mathbf{n} - \tilde{\mathbf{m}}_1^{\text{flexo}}) \cdot \boldsymbol{\nu} = \mathbf{0} \qquad \text{on} \quad \partial V, \tag{6.7.24}$$

$$\left(-\mathbb{D}_{\mathbf{n}} \nabla_y \xi - \mathbb{A}_{\mathbf{n}}^{-1} \tilde{\mathbf{p}}^{\text{flexo}} \right) \cdot \boldsymbol{\nu} = \mathbf{0} \qquad \text{on} \quad \Gamma_N \tag{6.7.25}$$

$$\text{and} \qquad \xi = \xi_b \qquad \text{on} \quad \Gamma_D, \tag{6.7.26}$$

where

$$\tilde{\mathbf{n}}_1^{\text{flexo}} = -f_s (\nabla_y \cdot \mathbf{n}) \mathbf{p} + f_b \nabla_y \mathbf{n} \mathbf{p} - f_b (\nabla_y \mathbf{n})^T \mathbf{p} \tag{6.7.27}$$

$$\text{and} \qquad \tilde{\mathbf{m}}_1^{\text{flexo}} = -f_s (\mathbf{n} \cdot \bar{\mathbf{p}}) \mathbf{I} + f_b \mathbf{n} \otimes \mathbf{p} - f_b \mathbf{p} \otimes \mathbf{n}. \tag{6.7.28}$$

Remark #3: If $K_F \gg A_1$ (or $\Delta\epsilon \to 0$), $K_F \gg |f_b|$ and $K_f \gg |f_b|$, then nematic director can be determined independent of polarization solving following system of equations

$$\nabla_y \cdot (-K_F \nabla_y \mathbf{n}) - \lambda_{\mathbf{n}} = \mathbf{0} \qquad \text{in} \quad V \tag{6.7.29}$$

$$\text{and} \qquad -K_F \nabla_y \mathbf{n} \cdot \boldsymbol{\nu} = \mathbf{0} \qquad \text{on} \quad \partial V. \tag{6.7.30}$$

Let $\mathbf{n}^*$ be the solution of equation above then the electric field in this case can be

detirmined solving

$$\nabla_y \cdot \left(-\mathbb{D}_{\mathbf{n}^*} \nabla_y \xi - \mathbb{A}_{\mathbf{n}^*}^{-1} \tilde{\mathbf{p}}^{*\text{flexo}}\right) = 0 \qquad \text{in} \quad V, \tag{6.7.31}$$

where $\tilde{\mathbf{p}}^{*\text{flexo}}$ is the $\tilde{\mathbf{p}}^{\text{flexo}}$ for $\mathbf{n} = \mathbf{n}^*$.

Negligible Frank elasticity and flexoelectricity ($K_F \sim 0$, $f_b \sim 0$ and $f_s \sim 0$)

In this regime, the LCE behaves as a complex multi-variant solid. Depending on the strength of electrical coupling, there are different separate regimes. It is worth mentioning that the thermodynamic stability condition discussed earlier will require flexoelectric coefficients to be zero if the Frank elasticity coefficient is zero.

1. Let $\varepsilon_3 \ll \varepsilon_2$. In this regime, the energy due to electrical interaction is negligible compared with the regular and Frank elasticity. Therefore, the electric field would not influence the director field or elastic fields. However, the director field does depend on elastic fields and hence the electrical properties, particular, the optical refraction index, can be actively controlled by mechanical loadings. The equlibrium state in this case can be determined minimizing energy functional while ignoring the electrical contributions

$$\mathcal{F}[\mathbf{F}, \mathbf{n}] = \int_{V_R} \frac{1}{2} J^{-2/3} (\mathbf{F}\mathbf{F}^T) : (\mathbf{F}_{\mathbf{n}} \mathbf{F}_{\mathbf{n}}^T)^{-1} + \frac{1}{2}\kappa (J-1)^2 + \frac{\mu_\beta}{2} J^{-2/3} (\mathbf{F}^T\mathbf{F}) : (\mathbf{F}_{\mathbf{N}_a}^T \mathbf{F}_{\mathbf{N}_a})^{-1}. \tag{6.7.32}$$

Having the equilibrium state of deformation and nematic director, the equilibrium electric field and polarization can be determined minimizing energy functional with respect to polarization and using the Maxwell equation.

$$\min_{\mathbf{P}} \left[\int_{V_R} \frac{1}{2J} \mathbf{P} \cdot \mathbb{A}_{\mathbf{n}} \mathbf{P} - \frac{1}{2} |\mathbf{F}^{-T} \nabla \xi|^2 + \mathbf{F}^{-T} \nabla \xi \cdot \mathbf{P} \right]. \tag{6.7.33}$$

Using standard calculus of variation, the equilibrium for the electric field and polar-

ization is obtained as

$$\nabla \cdot \Big(-J\mathbf{F}^{-1}\mathbb{D}_{\mathbf{n}}\mathbf{F}^{-T}\nabla\xi\Big) = 0 \qquad \text{in} \quad V_R, \tag{6.7.34}$$

$$\mathbf{P} = -J\mathbb{A}_{\mathbf{n}}^{-1}\mathbf{F}^{-T}\nabla\xi \qquad \text{in} \quad V_R, \tag{6.7.35}$$

$$\Big(-J\mathbf{F}^{-1}\mathbb{D}_{\mathbf{n}}\mathbf{F}^{-T}\nabla\xi\Big)\cdot\boldsymbol{\nu}_R = \mathbf{0} \qquad \text{on} \quad \Gamma_N^c \tag{6.7.36}$$

$$\text{and} \qquad \xi = \xi_b \qquad \text{on} \quad \Gamma_D^c. \tag{6.7.37}$$

Remark #4: For the case of small deformations ($\varepsilon_3 \ll \varepsilon_2 \ll 1$), the linearized forms of energy functionals and the Maxwell equations can be used to determine the equilibrium state of the system. The linearized form of energy functional (6.7.32) is expressed as

$$\mathcal{F}[\nabla\mathbf{u},\mathbf{n}] = F^{(0,2,0)}[\mathbf{n},\mathbf{u}] = \int_{V_R}\frac{1}{2}\left(\nabla\mathbf{u}-\mathbf{E}^*(\mathbf{n})\right):\mathbb{C}\left(\nabla\mathbf{u}-\mathbf{E}^*(\mathbf{n})\right)+\mu_\beta|\mathbf{E}_d-\mathbf{E}^*(\mathbf{N}_a)|^2. \tag{6.7.38}$$

Also, polarization and electric field can be obtained by

$$\min_{\mathbf{P}}\Big[\int_{V_R}\frac{1}{2}\mathbf{P}\cdot\mathbb{A}_{\mathbf{n}}\mathbf{P}-\frac{1}{2}|\nabla\xi|^2+\nabla\xi\cdot\mathbf{P}+\boldsymbol{\sigma}^{\mathrm{MW}}:\nabla\mathbf{u}\Big]. \tag{6.7.39}$$

$$\Big(\mathbf{I}-(\nabla\mathbf{u})^T\Big)\nabla\xi+(1-\nabla\cdot\mathbf{u})\,\mathbb{A}_{\mathbf{n}}\mathbf{P} = \mathbf{0} \qquad \text{in} \quad V_R, \tag{6.7.40}$$

$$\nabla\cdot\left[-\left((1+\mathrm{Tr}\mathbf{E})\,\mathbf{I}-2\mathbf{E}\right)\nabla\xi+(\mathbf{I}-\nabla\mathbf{u})\mathbf{P}\right] = 0 \qquad \text{in} \quad V_R, \tag{6.7.41}$$

$$\left[-\left((1+\mathrm{Tr}\mathbf{E})\,\mathbf{I}-2\mathbf{E}\right)\nabla\xi+(\mathbf{I}-\nabla\mathbf{u})\mathbf{P}\right]\cdot\boldsymbol{\nu}_R = \mathbf{0} \qquad \text{on} \quad \Gamma_N \tag{6.7.42}$$

$$\text{and} \qquad \xi = \xi_b \qquad \text{on} \quad \Gamma_D. \tag{6.7.43}$$

It should be mentioned that we have not ignored terms containing gradient of deformation to include coupling between deformation and electric field.

Remark #5: If $\varepsilon_3 \ll \varepsilon_2$ and the Frank elasticity and flexoelectric coefficients are negligible but non-zero and if major contribution of electric terms come from the flexoelectric effect one could update Eq.(6.7.34) to include contribution of flexoelectric

effect

$$\nabla \cdot \left(-J\mathbf{F}^{-1}\mathbb{D}_{\mathbf{n}}\mathbf{F}^{-T}\nabla\xi - \mathbf{F}^{-1}\mathbb{A}_{\mathbf{n}}^{-1}\widetilde{\mathbf{P}}^{\text{flexo}} \right) = 0 \qquad \text{in} \quad V_R. \tag{6.7.44}$$

2. Let $\varepsilon_2 \sim \delta, \quad \varepsilon_3 \sim \delta^{1/2}$ and $\delta \ll 1$. In this regime, the electrical energy dominates the elastic contribution. Therefore, the director field is completely determined by the electric field. One way coupling, two sequential minimization to determine the equilibrium state. The leading order term in the energy functional is $F^{(0,0,2)}$ which should be minimized with respect to polarization and nematic director

$$\min_{\mathbf{P},\mathbf{n}} F^{(0,0,2)}. \tag{6.7.45}$$

The Euler-Lagrange equations are given as

$$(\mathbf{P} \otimes \mathbf{P})\mathbf{n} = \lambda_{\mathbf{n}}\mathbf{n} \qquad \text{in} \quad V_R \tag{6.7.46}$$

$$\text{and} \qquad \nabla\xi + \mathbb{A}_{\mathbf{n}}\mathbf{P} = 0 \qquad \text{in} \quad V_R. \tag{6.7.47}$$

From (6.7.46) we can coclude that $\lambda_{\mathbf{n}} = |\mathbf{P}|^2$ and

$$\mathbf{n} \parallel \mathbf{P} \qquad \text{or} \qquad \mathbf{n} \perp \mathbf{P}. \tag{6.7.48}$$

As a result, the local electric field is determined using the linearized Maxwell equation:

$$\begin{cases} \nabla \cdot (-\epsilon_c \nabla\xi) = 0 \qquad \text{if} \quad \mathbf{n} \parallel \mathbf{P} \\ \text{and} \qquad \nabla \cdot (-\epsilon_a \nabla\xi) = 0 \qquad \text{if} \quad \mathbf{n} \perp \mathbf{P}. \end{cases} \tag{6.7.49}$$

By solving the Maxwell equation and director fields and electric field are obtained. The solution for director field is denoted by $\mathbf{n}^*$. Then, we can proceed solution and determine the displacement at the equilibrium state of the system by minimizing

$(F^{(0,2,0)}[\mathbf{n}^*, \mathbf{u}] + F^{(0,1,2)}[\mathbf{n}^*, \mathbf{u}])$. The assocoated Euler-Lagrange equation is given by

$$\nabla \cdot \left[\mathbb{C}\nabla \mathbf{u} - 2\mathbf{E}^*(\mathbf{n}) + 2\mu_\beta \left(\mathbf{E}_d - \mathbf{E}^*(\mathbf{N}_a) \right) + \boldsymbol{\sigma}^{\mathrm{MW}} \right] = \mathbf{0}. \tag{6.7.50}$$

3. Let $\varepsilon_2 \sim \varepsilon_3 \sim \delta$ and $\delta \ll 1$. We can solve the coupled minimization problem for ($\mathbf{u}$, $\mathbf{n}, \mathbf{P}$) subject to the linearized Maxwell equation

$$\min_{\mathbf{u},\mathbf{n},\mathbf{P}} \{ F^{(0,2,0)}[\mathbf{n}, \mathbf{u}] + F^{(0,0,2)}[\mathbf{n}, \mathbf{P}] \}. \tag{6.7.51}$$

The variations with respect to $\mathbf{u}$ and $\mathbf{n}$ simply gives following the Euler-Lagrange equations

$$\nabla \cdot [\mathbb{C}\nabla \mathbf{u} - 2\mathbf{E}^*(\mathbf{n}) + 2\mu_\beta \left(\mathbf{E}_d - \mathbf{E}^*(\mathbf{N}_a) \right)] = \mathbf{0} \qquad \text{in} \quad V_R, \tag{6.7.52}$$

$$-6\gamma(\mathbf{E}_d - \mathbf{E}^*(\mathbf{n}))\mathbf{n} - \Delta\epsilon(\mathbf{n} \cdot \nabla\xi)\nabla\xi + \lambda_{\mathbf{n}}\mathbf{n} = \mathbf{0} \qquad \text{in} \quad V_R, \tag{6.7.53}$$

$$\nabla\xi + \mathbb{A}_{\mathbf{n}}\mathbf{P} = \mathbf{0} \qquad \text{in} \quad V_R, \tag{6.7.54}$$

$$\nabla \cdot (-\mathbb{D}_{\mathbf{n}}\xi) = 0 \qquad \text{in} \quad V_R, \tag{6.7.55}$$

$$[\mathbb{C}\nabla \mathbf{u} - 2\mathbf{E}^*(\mathbf{n}) + 2\mu_\beta \left(\mathbf{E}_d - \mathbf{E}^*(\mathbf{N}_a) \right)] \cdot \boldsymbol{\nu}_R = \mathbf{0} \qquad \text{on} \quad \partial S_N \tag{6.7.56}$$

$$\text{and} \qquad (-\mathbb{D}_{\mathbf{n}}\xi) \cdot \boldsymbol{\nu}_R = \mathbf{0} \qquad \text{on} \quad \Gamma_N. \tag{6.7.57}$$

Competition between Frank elasticity and regular elasticity ($K_F \sim \mathbb{C} \sim 1$)

Competition between Frank elasticity of LC, elastic forces and electric field. There are multiple distinct asymptotic regimes

1. Let $\varepsilon_2 \sim \delta$, $\varepsilon_1 \sim \varepsilon_3 \sim \delta^{1/2}$ and $\delta \ll 1$. The leading energy terms in (6.7.1) arise from electric energy and Frank elasticity (instead of regular elasticity). Physically, it corresponds to the energy associated with the applied electric field (or voltage) is significantly larger than that of deformations. The corresponding governing equations can be obtained from the variational principles subject to the constraint arise from

the Maxwell equation

$$\min_{\mathbf{P},\mathbf{n}}\{F^{(2,0,0)} + F^{(0,0,2)} + F^{(1,0,1)}\}. \tag{6.7.58}$$

The governing equations for nematic directors and polarization is obtained using standard calculus of variation

$$\begin{aligned}
&\nabla\cdot\left(-K_F\nabla\mathbf{n} - \mathbf{m}_1^{\text{flexo}}\right) + \mathbf{n}_1^{\text{flexo}} \\
&- \left[\Delta\epsilon\left(\nabla\xi + \mathbf{p}^{\text{flexo}}\right)\otimes\left(\nabla\xi + \mathbf{P}^{\text{flexo}}\right) + \lambda_{\mathbf{n}}\mathbf{I}\right]\mathbf{n} = \mathbf{0} \qquad \text{in} \quad V_R, \qquad (6.7.59)\\
&\mathbb{A}_{\mathbf{n}}\mathbf{P} + \nabla\xi + \mathbf{p}^{\text{flexo}} = \mathbf{0} \qquad \text{in} \quad V_R, \qquad (6.7.60)\\
&\nabla\cdot\left(-\mathbb{D}_{\mathbf{n}}\nabla\xi - \mathbb{A}_{\mathbf{n}}^{-1}\mathbf{p}^{\text{flexo}}\right) = \mathbf{0} \qquad \text{in} \quad V_R, \qquad (6.7.61)\\
&\left(-K_F\nabla\mathbf{n} - \mathbf{m}_1^{\text{flexo}}\right)\cdot\boldsymbol{\nu}_R = \mathbf{0} \qquad \text{on} \quad \partial V_R, \qquad (6.7.62)\\
&\left(-\mathbb{D}_{\mathbf{n}}\nabla\xi - \mathbb{A}_{\mathbf{n}}^{-1}\mathbf{p}^{\text{flexo}}\right)\boldsymbol{\nu}_R = \mathbf{0} \qquad \text{on} \quad \Gamma_N \qquad (6.7.63)
\end{aligned}$$

$$\text{and} \qquad \xi = \xi_b \qquad \text{on} \quad \Gamma_D. \tag{6.7.64}$$

System of equation above is a closed system for the nematic director and electric potential and polarization. Having the solution for $\mathbf{n}$, $\mathbf{P}$ and ξ, we can minimize the remaining energy terms in the (6.7.1) ($F^{(0,2,0)} \sim F^{(2,1,0)} \sim F^{(0,1,2)} \sim F^{(1,1,1)} \sim \delta^2$) to determine the displacement. The corresponding Euler-Lagrange equation for this minimization is given as

$$\nabla\cdot\left(\mathbb{C}\nabla\mathbf{u} - 2\mathbf{E}^*(\mathbf{n}) + 2\mu_\beta\left(\mathbf{E}_d - \mathbf{E}^*(\mathbf{N}_a)\right) + \boldsymbol{\sigma}^{\text{EL}} + \boldsymbol{\sigma}^{\text{MW}} + \boldsymbol{\sigma}^{\text{flexo}}\right) = \mathbf{0} \qquad \text{in} \quad V_R \tag{6.7.65}$$

and

$$\boldsymbol{\nu}_R\cdot\left(\mathbb{C}\nabla\mathbf{u} - 2\mathbf{E}^*(\mathbf{n}) + 2\mu_\beta\left(\mathbf{E}_d - \mathbf{E}^*(\mathbf{N}_a)\right) + \boldsymbol{\sigma}^{\text{EL}} + \boldsymbol{\sigma}^{\text{MW}} + \boldsymbol{\sigma}^{\text{flexo}}\right) = \mathbf{0} \qquad \text{on} \quad S_N. \tag{6.7.66}$$

Remark #5: It is obvious that flexoelectric terms can be ignored if flexoelectric coefficients are small compare to other material properties.

2. Let $\varepsilon_2 \sim \varepsilon_3 \sim \delta, \varepsilon_1 \sim \delta^{1/2}$ and assume flexoelectricity is negligible. The leading energy terms arise from Frank elasticity. Physically, it corresponds to the energy associated with the applied electric field (or voltage)is significantly larger than energies associated with deformations and Frank elasticity.The corresponding governing equations can be obtained from the variational principles:

$$\min_{\mathbf{n}} \left[F^{(2,0,0)}[\mathbf{n}] \right]. \tag{6.7.67}$$

Immediately, we find that the director field necessarily satisfies

$$K_F \Delta \mathbf{n} + \lambda_{\mathbf{n}} \mathbf{n} = 0 \qquad \text{in} \quad V. \tag{6.7.68}$$

The remaining energy terms in (6.7.1) are led by $F^{(0,2,0)}[\mathbf{n}, \mathbf{u}] \sim F^{(2,1,0)}[\mathbf{n}, \mathbf{u}] \sim F^{(0,0,2)}[\mathbf{n}, \mathbf{P}] \sim \delta^2$. Upon minimizing again over admissible set of displacements and polarizations and using the Maxwell equation, we obtain the governing equations for $\mathbf{u}$ and $\mathbf{P}$.

$$\nabla \xi + \mathbb{A}_{\mathbf{n}} \mathbf{P} = \mathbf{0} \qquad \text{in} \quad V_R, \tag{6.7.69}$$

$$\nabla \cdot (-\mathbb{D}_{\mathbf{n}} \xi) = 0 \qquad \text{in} \quad V_R \tag{6.7.70}$$

and

$$\nabla \cdot (\mathbb{C} \nabla \mathbf{u} - 2\mu \mathbf{E}^*(\mathbf{n}) + 2\mu_\beta (\mathbf{E}_d - \mathbf{E}^*(\mathbf{N}_a)) + \boldsymbol{\sigma}_{\mathrm{EL}}) = \mathbf{0} \qquad \text{in} \quad V_R. \tag{6.7.71}$$

3. Let $\varepsilon_3 \ll \varepsilon_1 \sim \varepsilon_2 \sim \delta \ll 1$ and assume flexoelectricity is negligible. The energy functional (6.7.1) is led by $F^{(2,0,0)}[\mathbf{n}] \sim F^{(0,2,0)}[\mathbf{n}, \mathbf{u}] \sim \delta^2$. Therefore, nematic director and deformation can be obtained by the minimization of these two energy terms

$$\min_{\mathbf{n},\mathbf{u}} \{ F^{(2,0,0)}[\mathbf{n}] + F^{(0,2,0)}[\mathbf{n}, \mathbf{u}] \}. \tag{6.7.72}$$

The corresponding Euler-Lagrange equations is expressed as

$$\nabla \cdot (\mathbb{C}\nabla \mathbf{u} - 2\mathbf{E}^*(\mathbf{n}) + 2\mu_\beta (\mathbf{E}_d - \mathbf{E}^*(\mathbf{N}_a))) = \mathbf{0} \quad \text{in} \quad V_R, \tag{6.7.73}$$

$$\nabla \cdot (-K_F \nabla \mathbf{n}) - 6\gamma \mathbf{E}^*(\mathbf{n}) + \lambda_{\mathbf{n}} = \mathbf{0} \quad \text{in} \quad V_R, \tag{6.7.74}$$

$$\boldsymbol{\nu}_R \cdot (\mathbb{C}\nabla \mathbf{u} - 2\mathbf{E}^*(\mathbf{n}) + 2\mu_\beta (\mathbf{E}_d - \mathbf{E}^*(\mathbf{N}_a))) = \mathbf{0} \quad \text{in} \quad S_N \tag{6.7.75}$$

$$\text{and} \quad \boldsymbol{\nu}_R \cdot (-K_F \nabla \mathbf{n}) = \mathbf{0} \quad \text{in} \quad \partial V_R. \tag{6.7.76}$$

The Euler-Lagrange equations above form a closed system in order to determine nematic director and deformation. Then, the polarzation and electric field can be determined minimizing the leading order terms of the remaining of the energy functional and by using the Maxwell equation. The corresponding equations are given as

$$\mathbb{A}_{\mathbf{n}}\mathbf{P} + \nabla \xi = \mathbf{0} \quad \text{in} \quad V_R \tag{6.7.77}$$

$$\text{and} \quad \nabla(-\mathbb{D}_{\mathbf{n}} \nabla \xi) = 0 \quad \text{in} \quad V_R. \tag{6.7.78}$$

6.8 Results and Discussion

6.8.1 Analytical results for bending induced flexoelectric effect in NLCEs

It was discussed that director reorientation can lead to a flexoelectric effect. As flexoelectric effect depends on the gradient of nematic field and strain gradient may induce a non-uniform arrangement of nematic director, strain gradient may lead to a flexoelectric effect in LCEs. The simplest way to induce strain gradient inside a material is by applying bending deformation to the material. Thus, in this section, we study bending induced flexoelectric effect using an analytical approach. The theoretical studies on the bending deformation of LCEs exists in the literature [349, 350, 331, 351, 328, 333, 352]. However, these studies mostly focus on the actuation induced in response to external stimuli [328] or overall response of the LCE [352]. There have been little attention on the director reorientation in bending deformation of LCEs [353, 354] and there is no study on the bending induced

flexoelectric response of the material. Recently, Liu et al. [355] studied pure bending deformation of LCEs using four different constitutive laws and showed that, depending on the constitutive equation used, there may be two different solutions for any given bending angle and there is a critical bending angle on which a $\pi/2$ rotation of nematic director is reported from one solution to another. Here, in this section, we use the formulation presented earlier to study pure bending deformation of LCEs and possible director reorientation predicted using constitutive relations given in Eqs.(6.2.15) and (6.2.16). We also use the asymptotic theories presented earlier to present analytical solution for bending induced flexoelectric behavior of the LCE.

We have presented the solution for the bending deformation of dielectric elastomers and electret materials in our earlier work [178]. Here, we extend our earlier work to study bending problem of LCEs. We use the same notation as the one given in [178] and avoid presenting all the details. Reader is referred to this reference for more detailed derivation.

Figure 6.4a shows the LCE with thickness $2H$ and the length $2L$ in the undeformed configuration. Similar to what was mentioned earlier, we continue using dimensionless quantities. We have used thickness as the characteristic length and we have dropped over bar from all dimensionless quantities for brevity. We use Cartesian coordinate system $\{\mathbf{e}_X,\mathbf{e}_Y,\mathbf{e}_Z\}$ to denote material points in the reference configuration and a cylindrical coordinate system $\{\mathbf{e}_r,\mathbf{e}_\theta,\mathbf{e}_z\}$ is used to denote spatial points. In response to applied bending moment M , the LCE undergoes a pure plane strain bending deformation (Figures 6.4b and 6.4c) such that any points initially located in the plane with normal $\mathbf{e}_X$ (resp. $\mathbf{e}_Y$) is mapped to a point located in a plane with normal $\mathbf{e}_r$ (resp. $\mathbf{e}_\theta$). Also, we set $\mathbf{N}_a = \mathbf{e}_X$. Assuming the material is incompressible ($\det\mathbf{F} = 1$), the deformation and the deformation gradient tensor is obtained as [103]

$$r = \sqrt{2AX + B}, \qquad \theta = \frac{Y}{A} \tag{6.8.1}$$

$$\text{and} \qquad \mathbf{F} = \frac{A}{r}\mathbf{e}_r \otimes \mathbf{e}_X + \frac{r}{A}\mathbf{e}_\theta \otimes \mathbf{e}_Y + \mathbf{e}_z \otimes \mathbf{e}_Z, \tag{6.8.2}$$

where A and B are unknown constants. We identify $r_1 = r(X = -H)$, $r_2 = r(X = H)$ and $\alpha = \theta(Y = L)$ (see Fig. 6.4). We assume the effect the Frank elasticity coeffieient and

flexoelectric coefficients are small and their effect on the deformation is negligible. Thus, we use the scaling given in the section 6.7.1. Minimizing energy functional (6.7.32) with respect to $\mathbf{n}$ yields

$$\mathbf{F}\mathbf{F}^T\mathbf{n} = \lambda_{\mathbf{n}}\mathbf{n}. \tag{6.8.3}$$

Substituting Eq.(6.8.2) into Eq.(6.8.3), we obtain two solutions for nematic director

$$\begin{cases} \mathbf{n} = \quad \mathbf{e}_\theta & \text{Case 1,} \\ \mathbf{n} = \quad \mathbf{e}_r & \text{Case 2.} \end{cases} \tag{6.8.4}$$

Throughout this paper, we refer to first solution as *case 1* and the second solution *case 2*. Note that $\mathbf{N}_a = \mathbf{e}_X$ and the anisotropy behavior of the material tends to keep nematic directors align with the thickness direction. The bending deformation creates strain a long the axis of the material (beam) and it may be energetically favorable for the nematic directors to reorient toward axis of the beam. The case 1 (shown in Fig. 6.4b) represents the situation in which nematic directors have rotated toward the axis of the beam while no reorientation is reported according to case 2 (shown in Fig. 6.4c). It is important to note that both solutions represent a uniform arrangement of nematic directors throughout the material. Liu et al. [355] also obtained similar uniform solutions using different constitutive relations. The reason for this behavior is that non-uniform arrangment of the nematic director induces shear deformation in the material. However, shear deformation is not allowed based on the kinematic constraint used in this work and work done by Liu [355] (see Eq.(6.8.1)). Therefore, the solution obtained using these models might not match experimental results. We will use FEA model in the next sections in order to obtain more realistic results.

From (6.8.4), we have

$$\begin{cases} \nabla\mathbf{n} = -\frac{1}{A}\mathbf{e}_r \otimes \mathbf{e}_Y & \text{Case 1,} \\ \nabla\mathbf{n} = \frac{1}{A}\mathbf{e}_\theta \otimes \mathbf{e}_Y & \text{Case 2.} \end{cases} \tag{6.8.5}$$

Substituting Eqs.(6.8.4), (6.8.5) and (6.8.2) into (6.2.37), the flexoelectric polarization is

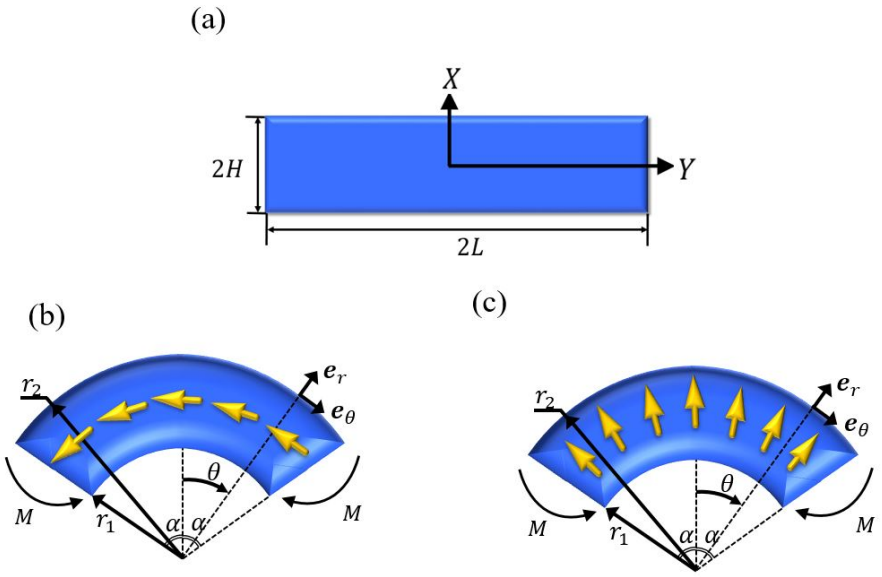

Figure 6.4: Schematic of the LCE under bending deformation. The gold arrows show the direction of nematic directors. (a) Undeformed isotropic configuration. (b) Deformed configuration with $\mathbf{n} = \mathbf{e}_\theta$ (case 1). (c) Deformed configuration with $\mathbf{n} = \mathbf{e}_r$ (case 2).

obtained as

$$\begin{cases} \widetilde{\mathbf{P}}^{\text{flexo}} = -\frac{f_b r}{A^2}\mathbf{e}_r & \text{Case 1,} \\ \\ \widetilde{\mathbf{P}}^{\text{flexo}} = -\frac{f_s}{r}\mathbf{e}_r & \text{Case 2.} \end{cases} \tag{6.8.6}$$

The Eq. 6.8.6 illustrates that the flexoelectric effect predicted in the case 1 is based on f_b effects which is due to bending reorientation of the nematic directors. On the contrary, the flexoelectric effect predicted in the case 2 is based on f_s effects which is due to splay reorientation of the nematic directors. We impose open circuit electric boundary condition for all the surfaces ($\widetilde{\mathbf{D}} \cdot \boldsymbol{\nu}_R = 0$) for all the surfaces and determine the flexoelectric effect generated electric field inside the material by substituting Eq.(6.8.6) into Eq.(6.7.44) and

$$\begin{cases} -\nabla\xi = -\frac{f_b(\epsilon_a - 1)}{A\epsilon_a}\mathbf{e}_X & \text{Case 1,} \\ \\ -\nabla\xi = -\frac{A f_s(\epsilon_c - 1)}{r^2\epsilon_c}\mathbf{e}_X & \text{Case 2.} \end{cases} \tag{6.8.7}$$

Now, we need to determine which solutions between case 1 and case 2 are energetically favorable. Therefore, we need to fully solve the problem for unknowns A and B and then

determine the free energy for each case. We introduce $\mathbf{\Sigma}^T$ as

$$\mathbf{\Sigma}^T = \mathbf{\Sigma} + \mathbf{\Sigma}^{\text{anis}} = \Sigma^T_{rX}\mathbf{e}_r \otimes \mathbf{e}_X + \Sigma^T_{\theta Y}\mathbf{e}_\theta \otimes \mathbf{e}_Y + \Sigma^T_{zZ}\mathbf{e}_z \otimes \mathbf{e}_Z, \tag{6.8.8}$$

where Σ^T_{rX}, $\Sigma^T_{\theta Y}$ and Σ^T_{zZ} can be obtained substituting Eq.(6.8.2) into Eqs.(6.2.40) and (6.2.41). Minimization of the energy functional Eq.(6.7.32) with respect to the deformation gives

$$\frac{\mathrm{d}}{\mathrm{d}X}\left(\Sigma^T_{rX} - \lambda_p \frac{r}{A}\right) - \frac{1}{A}\left(\Sigma^T_{\theta Y} - \lambda_p \frac{A}{r}\right) = 0. \tag{6.8.9}$$

Solving the Eq.(6.8.9) for the Lagrange multiplier λ_p, we have

$$\begin{cases} \lambda_p = a^{1/3}\frac{A^2}{2r^2}(1 + \frac{\mu_\beta}{a}) - a^{-2/3}\frac{r^2}{2A^2}(1 + a\mu_\beta) + C_1 \quad \text{Case 1,} \\ \\ \lambda_p = a^{-2/3}\frac{A^2}{2r^2}(1 + \mu_\beta) - a^{1/3}\frac{r^2}{2A^2}(1 + \mu_\beta) + C_1 \quad \text{Case 2,} \end{cases} \tag{6.8.10}$$

where C_1 is the integration constant and can simply be determined from free traction boundary condition on the surface $X = -H$,

$$\Sigma^T_{rX} - \lambda_p \frac{r}{A}\bigg|_{X=-H} = 0. \tag{6.8.11}$$

We identify two unknown constants λ_b and κ_b as

$$\lambda_b = \frac{r_2 - r_1}{2H} \qquad \text{and} \qquad \kappa_b = \frac{r_2 - r_1}{r_1}. \tag{6.8.12}$$

It is clear that λ_b is a measure for change of the thickness during bending deformation and κ_b is a dimensionless measure for the curvature. The unknowns A and B can be expressed in terms of λ_b and κ_b as

$$A = \frac{H\lambda_b^2(2 + \kappa_b)}{\kappa_b} \qquad \text{and} \qquad B = \frac{2H^2\lambda_b^2\,(2 + \kappa_b(2 + \kappa_b))}{\kappa_b^2}. \tag{6.8.13}$$

The only two unknowns at this point are λ_b and κ_b. The free traction boundary condition

on the surface $X = H$ is used to determine λ_b in terms of κ_b:

$$\begin{cases} \lambda_b^4 = \frac{16(1+a\mu_\beta)(1+\kappa_b)^2}{(2+\kappa_b)^4(a+\mu_\beta)} & \text{Case 1,} \\ \lambda_b^4 = \frac{16a(1+\kappa_b)^2}{(2+\kappa_b)^4} & \text{Case 2.} \end{cases} \tag{6.8.14}$$

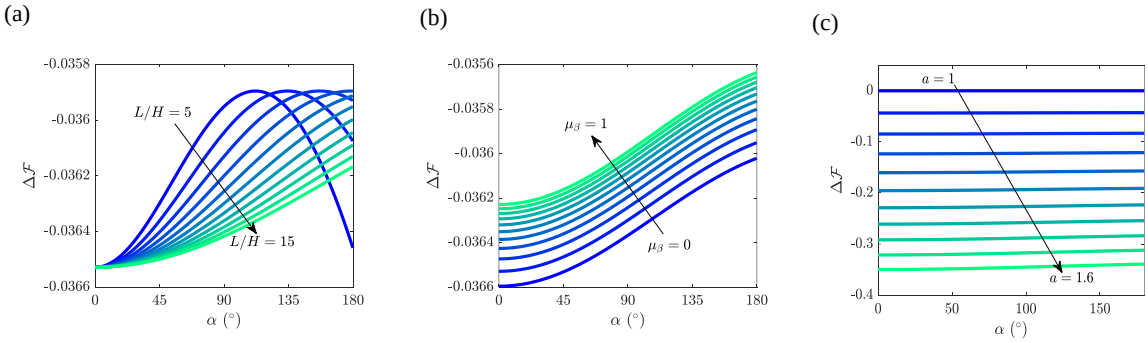

Figure 6.5: The difference of free energy obtained using case 1 and case 2 versus bending angle for different (a) aspect ratios L/H, (b) the material property μ_β and (c) the material property a.

At this point, the only unknown is the dimensionless curvature κ_b. The relationship between the applied bending moment M and the curvature κ_b can be simply established using traction boundary condition on the surface $Y = \pm L$. We can also determine the relationship between bending angle α and curvature κ_b from the relation $A = \frac{L}{\alpha}$ and the first of (6.8.13). Therefore, all quantities can be written in terms of the bending angle α.

In order to determine which one of two cases are more energetically favorable, we calculate free energy using the relation (6.7.32). The difference between the value of the free energy of obtained based on solution given in the case 1 and the value of the free energy obtained based on solution given in the case 2 ($\Delta\mathcal{F} = \mathcal{F}_{\text{case 1}} - \mathcal{F}_{\text{case 2}}$) has been plotted in the Fig. 6.5. The negative values of the free energy difference $\Delta\mathcal{F}$ means that the case 1 has lower energy and therefore energetically favorable. It is seen that always case 1 has the lower energy disregarding the material or geometrical parameters used. Therefore, according to this energy functional and setting used, bending deformation of the LCE always will lead to a $\pi/2$ director reorientation. Also, we conclude that the electric field generated in the material is determined from case 1 which is given as $-\nabla\xi = -f_b(\epsilon_a - 1)/(A\epsilon_a)\mathbf{e}_X$.

It is important to note again that these theoretical results is based on the assumption that no shear deformation will be observed in the LCE under bending deformation. Therefore, this model and models like this [355] can not accurately predict the behavior of LCEs under bending deformation.

6.8.2 Analytical results for opto-flexoelectric behavior of the LCE.

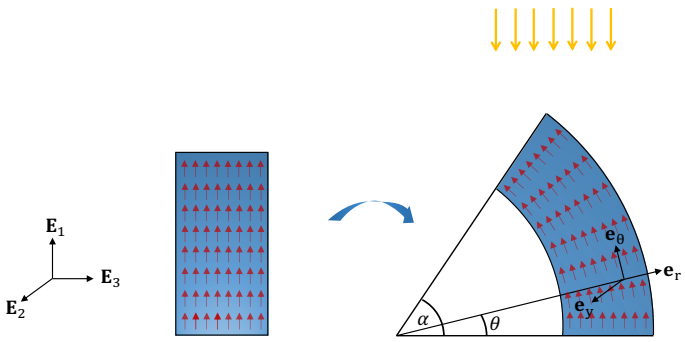

Figure 6.6: Schematic of the deformation of the body subject to the light.

In this section we probe the possibility of simplified analytical results for the coupled opto-flexoelectric boundary value problem. The energy of the system is given in Eq.(6.2.7). We assume polarized light irradiated from top of the material (Fig. 6.6). The body deforms as the nematic directors rotate as shown in Figure 6.6. Assuming a form of deformation as $\bar{\mathbf{x}} = r(\bar{Z})\mathbf{e}_r(\theta) + Y\mathbf{e}_y$ in which

$$\begin{cases} \theta = \theta(\bar{X}) = \alpha\bar{X} + \beta, \\ y = \bar{Y}, \\ \qquad r = r(\bar{Z}) \end{cases} \tag{6.8.15}$$

and α, β and $r(\bar{Z})$ are to be obtained. The deformation gradient is given as

$$\mathbf{F} = \alpha r(\bar{Z})\mathbf{e}_\theta \otimes \mathbf{e}_1 + \mathbf{e}_y \otimes \mathbf{e}_2 + r'(\bar{Z})\mathbf{e}_r \otimes \mathbf{e}_3. \tag{6.8.16}$$

Let the profile of nematic directors in reference and current configurations be

$$\mathbf{n}_0 = \mathbf{e}_3, \qquad \mathbf{n}(\theta) = \mathbf{e}_\theta. \tag{6.8.17}$$

We are interested in a scaling in which the Frank elasticity and the optical energy are dominant. Therefore, the problem becomes

$$\min_{\mathbf{n}(\theta)} \left[\int_{V_R} W^{\text{Frank}}[\nabla \mathbf{n}, \mathbf{y}] + W^{\text{opt}}[Q, \mathbf{n}] \right]. \tag{6.8.18}$$

After linearization, minimizing the above mentioned equation with respect to the nematic directiors gives α as follows

$$\alpha = \sqrt{\frac{10}{3} + \frac{5\bar{K}_F \mu (I_0(Q-1)-3)^3}{9 f I_0 Q \mu_n \left(Q^2 J_n((f-1)I_0(Q-1)+3) + G[Q](I_0(Q-1)-3)\right)}}, \tag{6.8.19}$$

where $G[Q] = g^{-1}(Q) - Q\log[Z(Q)]$. Upon linearization of (6.3(c)) (first EL) which is

$$\frac{\partial}{\partial Q}\left(W^{\text{elast}}[Q, \mathbf{n}, \mathbf{y}] + W^{\text{opt}}[Q, \mathbf{n}]\right), \tag{6.8.20}$$

we can have a good approximation of the state variable Q as $Q \simeq 0.6$.

After we implement the effect of the light on the deformation of the system, for simplicity, we eliminate the energy associated with the light in the subsequent system and just implement the effect of it in the profile of the nematic directors. Assuming $\epsilon_1 \sim \epsilon_2 \gg \epsilon_3$ we can ignore the higher order effects and the problem reduces to

$$\begin{cases} \nabla \cdot \left(\boldsymbol{\Sigma} + \boldsymbol{\Sigma}^{\text{anis}} + \boldsymbol{\Sigma}^{\text{elast}} - \lambda_p J \mathbf{F}^{-T}\right) = \mathbf{0}, \\ \mathbf{n} \cdot \mathbf{n} = 1, \\ \text{and} \qquad \det\mathbf{F} = 1 \end{cases} \tag{6.8.21}$$

subject to

$$\begin{aligned} &\theta(X)\big|_{X=0} = 0 \\ \text{and} \qquad &\Big(\boldsymbol{\Sigma} + \boldsymbol{\Sigma}^{\text{anis}} + \boldsymbol{\Sigma}^{\text{elast}} - \lambda_p J\mathbf{F}^{-T}\Big)\cdot\mathbf{e}_3\Big|_{Z=0,1} = \mathbf{0}, \end{aligned} \tag{6.8.22}$$

where

$$\begin{aligned} &\boldsymbol{\Sigma} = a_1(Q)\left(\alpha r(Z)\mathbf{e}_\theta\otimes\mathbf{e}_1 + \mathbf{e}_y\otimes\mathbf{e}_2 + r'(Z)\mathbf{e}_r\otimes\mathbf{e}_3\right) + a_2(Q)\alpha r(Z)\mathbf{e}_\theta\otimes\mathbf{e}_1, \\ &\boldsymbol{\Sigma}^{\text{anis}} = \\ &\mu^{\text{anis}}\left[a_1(Q)\left(\alpha r(Z)\mathbf{e}_\theta\otimes\mathbf{e}_1 + \mathbf{e}_y\otimes\mathbf{e}_2 + r'(Z)\mathbf{e}_r\otimes\mathbf{e}_3\right) + a_2(Q)\alpha r(Z)\mathbf{e}_\theta\otimes\mathbf{e}_1\right] \\ \text{and} \qquad &\boldsymbol{\Sigma}^{\text{elast}} = \frac{K_F}{2}\left(-\frac{1}{\alpha(r(Z))^3}\mathbf{e}_\theta\otimes\mathbf{e}_1 + \frac{1}{(r(Z))^2}\mathbf{e}_y\otimes\mathbf{e}_2 + \frac{1}{r'(Z)(r(Z))^2}\mathbf{e}_r\otimes\mathbf{e}_3\right). \end{aligned}$$

From $(6.8.22)_1$ we infer $\beta = 0$ and the normalization constraint on $(6.8.21)_2$ is already satisfied due to the nature of the suggested solution in (6.8.17). Substituting (6.8.16) in $(6.8.21)_3$ we reach to

$$\alpha r(Z)r'(Z) = 1 \rightarrow r(Z) = \sqrt{\frac{2Z}{\alpha} + \zeta}, \tag{6.8.23}$$

where ζ is to be obtained. Substituting (6.8.16),(6.8.17), (6.8.23) and (6.8.23), into $(6.8.21)_1$ we obtain a differential equation involving λ_p which results in

$$\lambda_p(Z) = -\frac{1}{\alpha}(\mu^{\text{anis}} + 1)\left(\alpha^2\left(a_1(Q) + a_2(Q)\right)Z - \frac{a_1(Q)}{2\alpha\zeta + 4Z}\right)c_1. \tag{6.8.24}$$

The remaining unknowns c_1 and ζ can be obtained by imposing $(6.8.22)_2$ in the boundaries.

The next step is to obtain the electric potential and polarization profile. The boundary value problem is reduced to:

$$\begin{cases} \quad \mathbf{F}^{-T}\nabla\xi + \frac{1}{J}\mathbb{A}_{\mathbf{n}}\tilde{\mathbf{P}} + \tilde{\tilde{\mathbf{P}}}^{\text{flexo}} = 0, \\ \text{and} \quad \nabla\cdot\left(-J\mathbf{C}^{-1}\nabla\xi + \mathbf{F}^{-1}\tilde{\mathbf{P}}\right) = 0, \end{cases} \tag{6.8.25}$$

subject to the boundary condition

$$\widetilde{\mathbf{D}} \cdot \nu = 0, \tag{6.8.26}$$

where ν is the unit vector normal to the boundaries in the reference configuration and

$$\tilde{\mathbf{P}}^{\text{flexo}} = \frac{f_b}{r(Z)} \mathbf{e}_r. \tag{6.8.27}$$

Let the electric potential varies only in r direction, i.e. $\xi = \xi(r)$. Substituting (6.8.27) into $(6.8.25)_1$ and $(6.8.25)_2$, eliminating $\tilde{\mathbf{P}}$ and solving for $\xi(r)$ we obtain:

$$\xi = \gamma_1 \log[r] + \gamma_2, \tag{6.8.28}$$

where $\gamma_i (i = 1, 2)$ are to be obtained. Then the polarization is obtained as

$$\tilde{\mathbf{P}} = -\frac{1}{A_2 r(Z)} \left(\gamma_1 + f_b\right) \mathbf{e}_r. \tag{6.8.29}$$

γ_1 is obtained by imposing (6.8.26) as $\gamma_1 = -\frac{f_b}{1+A_2}$. Also, γ_2 is a constant of no consequence therefore we set $\gamma_2 = 0$.

Figure 6.7 shows the profile of the normalized electric potential for different size scaling.

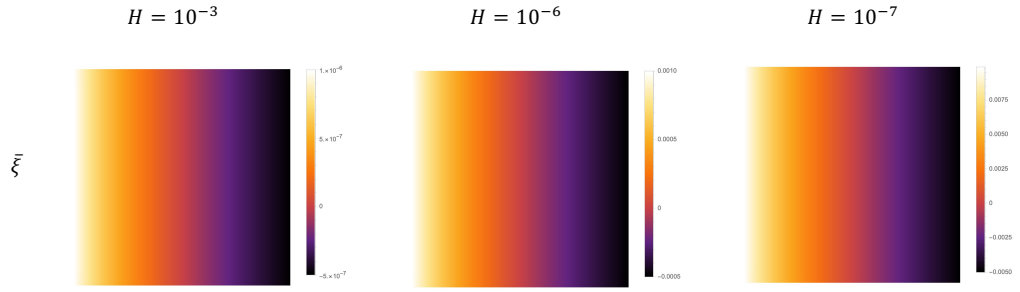

Figure 6.7: The electric potential distribution for different scaling factors.

6.8.3 FEA results for LCE film under stretch

The stretch deformation of a nematic LCE sheet is a well known problem which have been widely investigated experimentally [356, 357, 358] and theoretically [359, 360, 361, 362].

Experimental observation of stress-strain relationship for a clamped nematic LCE sheet under stretch reveals a *semi-soft* behavior. The semi-soft behavior means that stress-strain diagram is composed of three different parts [357, 358, 361]. Initially, the material shows a hard response under small strains in which nematic directors do not rotate. As strain increases a soft response is observed accompanied by the reorientation nematic directors. Finally, once nematic directors are all aligned along the direction of maximum stretch, a hard response is observed. The theoretical prediction based on the model presented by Bladon, Terentjev, and Warner(BTW) [347] were able to predict formation of stripe domain instability but they were unable to capture initial hard response and showed an ideally soft response. However, Conti and coworkers [361] used the free energy presented by Verwey, Warner, and Terentjev (VWT) and successfully captured formation of stripe domains and semi-soft behavior of LCEs. Luo and Calderer [26] added Oseen-Frank energy expression to BTW energy and predicted a semi-soft behavior for LCE using Finite Element Analysis. Their results did not show formation of stripe domains as they used relatively large Frank elasticity coefficient. Also, the mesh size they used were too coarse to capture formation of stripe domains. Here, in this section, we have used the free energy proposed by DeSimone [263] along with FEA framework explained earlier to study flexoelectric behavior of NLCEs under stretch deformation. We also have included effects of Frank elasticity because the focus of our work is flexoelectric behavior in nematic LCEs and the flexoelectric effect is considerable at small scales where the Frank elasticity effect is also considerable. We do not perform stability analysis and we do not report formation of stripe domain instabilities. We believe at small scales Frank elasticity terms penalizes rotation of nematic directors and avoids creation of stripe domains. Also, even if stripe domains form, we do not believe it will impact our general conclusions about flexoelectric behavior of nematic elastomers. Comprehensive stability analysis of nematic LCEs under electro-mechanical loading is the subject of our future research.

Figure 6.8 shows schematics of the two dimensional sample simulated. In the reference state, the sample is in the isotropic state where the deformation is zero all over the sample. After energy minimization in the initial state and in absence of any external loading, the sample is transformed into nematic state where all nematic directors are aligned along

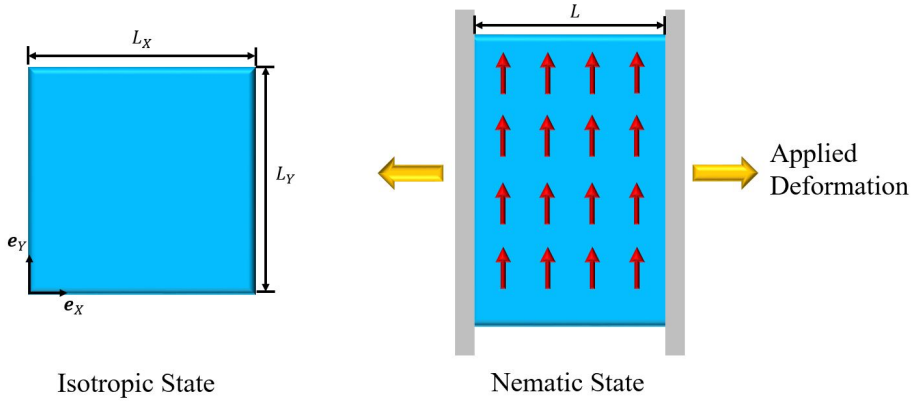

Figure 6.8: Schematics of simulated specimen in clamp pulling numerical experiment. The system is relaxed to nematic state and then the boundary conditions are applied.

one random direction. We have chosen Y-direction as this random direction(Fig. 6.8). In the next step and in order to simulate clamp pulling experiment, we have constrained the deformation along Y-direction and the direction of nematic director on both vertical surfaces of the specimen to stay the same as the values observed in the nematic state and in absence of any external loading on both vertical surfaces of the specimen. Then, we begin to pull the specimen from both left and right end by applying uniform deformation ΔL along X-direction.

Validation of FEA code

In the first stage of our analysis and in order to validate our FEA code, we set electrical terms to zero and assume $a_1 = 1$ and $a_2 = -0.4$ in Eq.(6.2.18). Also, we set $\bar{\mu}_\beta = 0$, $\bar{\mu} = 2$, $\bar{K}_F = 0.03$. The simulated specimen has the dimensions of $L_X = 1/\sqrt{0.5}$ and $L_Y = 1$ (see Fig. 6.8). By doing so, our model reduces to one presented in [26]. Due to symmetry we will simulate upper right quarter of the figure and we will impose exact boundary conditions imposed in [26]. Figure 6.9 shows our results and results presented in [26] for the deformed configurations of LCE under different strain along with direction of nematic directors and contours of BTW energy. It is seen that our results exactly match to the ones presented by Luo and Calderer [26].

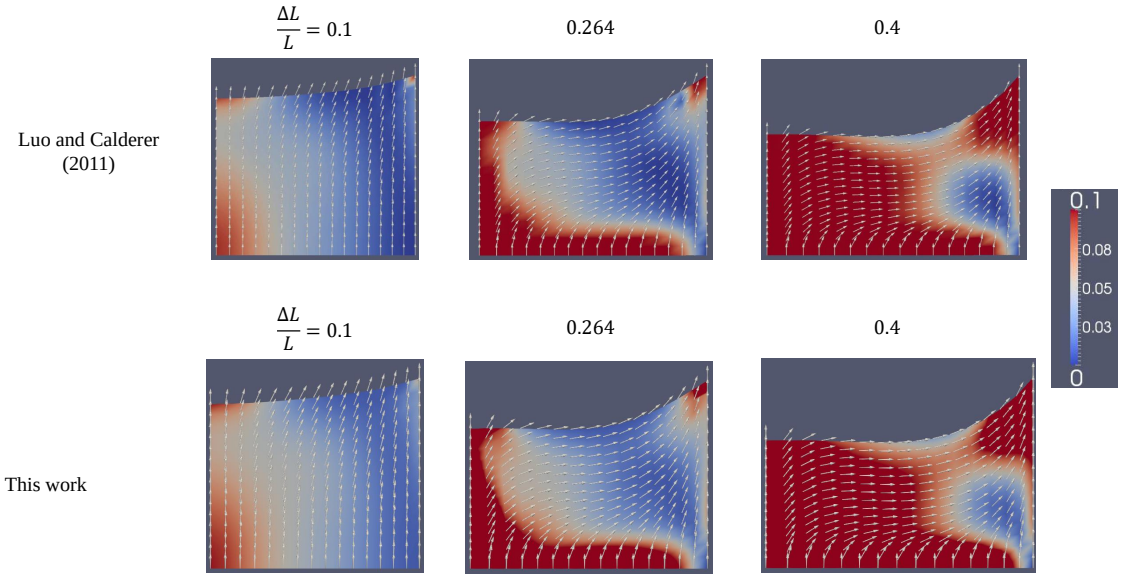

Figure 6.9: Comparison of BTW energy contours, deformation and direction of nematic director between current study and the FEA results presented by [26]

Size effect on the semi-soft response of the material

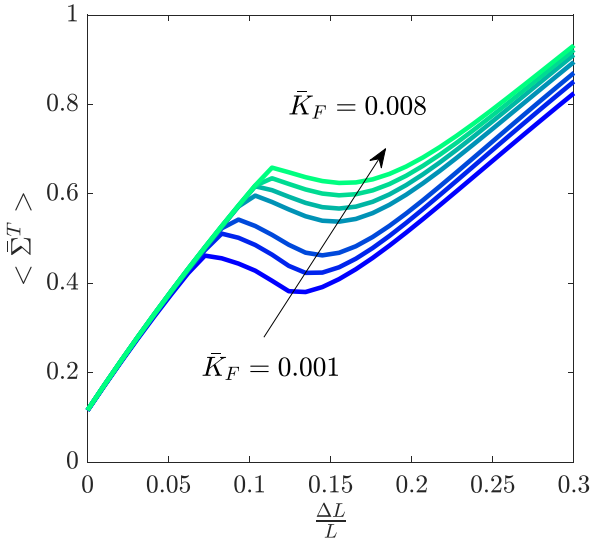

Figure 6.10: The effect of the Frank elasticity coefficient on the semi-soft behavior of the LCE under clamp-puling deformation.

In addition to validation of our results, we investigate effects of the Frank elasticity on the stress-strain behavior of NLCE. The stress-strain diagram for different values of $\bar{K}_F$ has been plotted in Fig. 6.10 where stress values plotted is the average normal stress along X

direction and we have set $\bar{\mu}_\beta = 0.5$. It is seen that we are able to capture semi-soft behavior of the material. As it is expected, increase in the $\bar{K}_F$ penalizes rotation of nematic director and delays soft behavior of the material. It should be mentioned that although the Frank elasticity coefficient K_F itself is a material property and it is constant but the effect it has is size dependent and as size changes $\bar{K}_F$ also changes. This graph shows that stress strain response of LCE does depend on the sample size.

Flexoelectric response of LCE sheet under uni-axial stretch

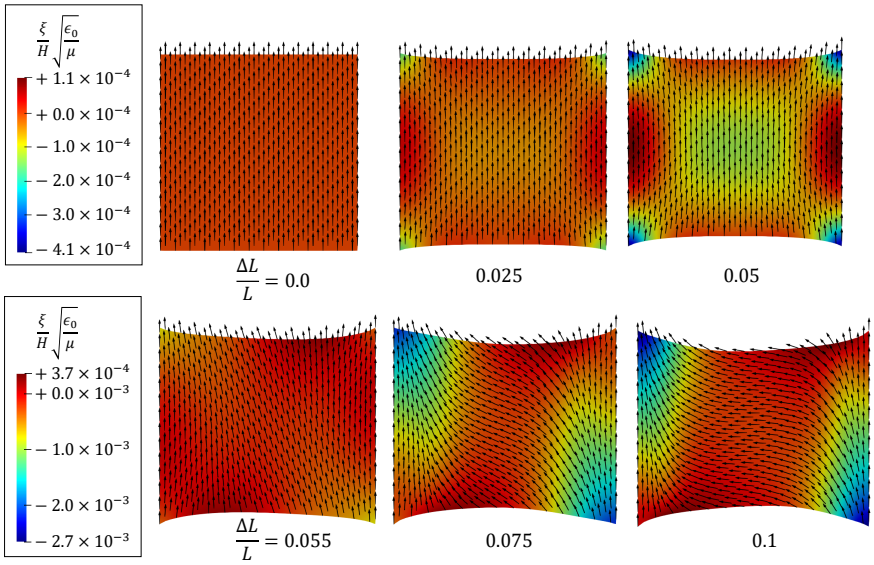

Figure 6.11: Contours of dimensionless electric potential shown in the deformed configuration under different stretch values. The black arrows show the direction of nematic directors.

As it was shown earlier, the rotation of nematic director is observed in clamp-puling experiment. As flexoelectric behavior of LCEs depends on the rotation of director, then one could expect observation of a flexoelectric effect under clamp-puling experiment of LCE at small size scale. Therefore, we will include effects of electrical terms by setting $\bar{\epsilon}_a = 2.26$, $\bar{\epsilon}_a = 4.52$, $\bar{f}_b = 0.001$ and $\bar{f}_s = 0.002$. We will comment further on the values of flexoelectric coefficient later but the magnitude of these values will not impact our qualitative conclusion in this section. The film is under open circuit condition ($\widetilde{\mathbf{D}} \cdot \mathbf{N} = 0$) on all surfaces. Without loss of generality, we set electric potential on the point $(L_X/2, 0)$ to zero in order to ease numerical convergence. Figure 6.11 shows contours of dimensionless electric potential

plotted in the deformed configuration for different values of applied deformation. Also, the direction of nematic directors have been plotted with black arrows. It is seen that in the earlier stages of deformation, the rotation of nematic directors is negligible and generated electric potential due to flexoelectric effect is also negligible. As strain increases, the gradient of nematic director field becomes larger and an electric potential difference becomes obvious along the specimen. However, the electric potential difference is symmetric in all steps of loading. Our calculation showed the volume average of dimensionless electric field in both X and Y directions remains zero in all steps of loading. From this, we can conclude that the flexoelectric effect may be present in the clamp-puling experiment if conducted in small scale. However, it will not be measurable as the average electric field will be zero. Here, we did not report formation of strip domains but we still believe the conclusion made in this section can be extended to the case in which strip domains is formed. As strip domains are symmetric, the generated electric potential difference also will be symmetric and the overall electric field will be zero.

6.8.4 FEA results for flexoelectric effect in bending deformation of LCE

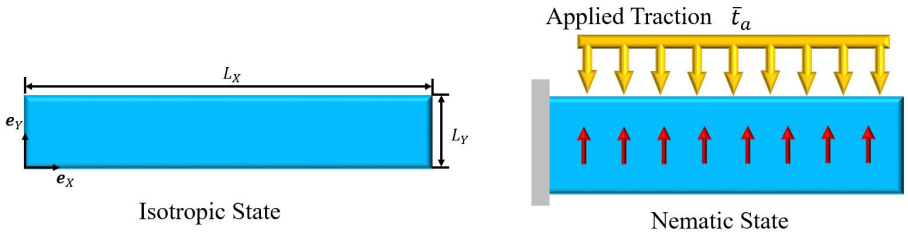

Figure 6.12: The schematic of the sample simulated. We apply boundary conditions in the nematic state.

As flexoelectric effect in LCEs is result existence of non-zero gradient of nematic director fields and bending is one way to create non-uniform deformation and consequently non-zero gradient of nematic director field, we investigate bending deformation of NLCEs in this section. Photo induced bending deformation of NLCEs have been widely studied. However, almost all these studies do not include director field reorientation in bending deformation. In addition, plate theories have been developed for NLCEs [353, 363, 364] that can be used to study bending deformation of LCEs. However, as these models average out variations

along the thickness directions they are not suitable for studying flexoelectric effect under bending deformation. Here, we will use the formulation developed earlier along with FEA in order to study flexoelectric effect in bending deformation on of LCEs. We have used the free energy proposed by DeSimone [263] by setting $a_1 = a^{1/3}$ and $a_2 = -a^{1/3}\frac{a-1}{a}$. Unless other wise stated we have assumed $a = 1.05$, $\mu = 30$ KPa, $K_F = 10^{-11}$ J/m, $\epsilon_a = 2.26$, $\epsilon_c = 4.52$ and $\mu_\beta = 0.1\mu$. The size scale is set to be $H = 10^{-6}$ m. As discussed in the paper, the maximum value of the flexoelectric coefficient depends on the value of Frank elasticity term. The order of flexoelectric coefficient for LCEs is expected to be in the order of $1/\epsilon_0$ pC/m [306]. Therefore, we have set $f_b\epsilon_0 = f_s\epsilon_0 = 1$ pC/N. We also identify volume average sign as $< \cdot >= \frac{1}{V}\int_V \cdot$ which will be used in this section to plot average electric field and average polarization generated in the material in response to bending.

The schematics of simulated samples is shown in Fig. 6.12. Similar to what mentioned earlier for stretch simulation, we apply boundary conditions on the material in nematic state. We assume $\mathbf{N}_a = \mathbf{e}_Y$ and let the system relax from isotropic state to nematic state and then we constrain deformation and nematic director direction on the left end side of the material(see Fig. 6.12). In order to create bending deformation, a dimensionless traction $\bar{\mathbf{t}}_a = -\bar{t}_a\mathbf{e}_Y$ is applied on the top surface of the material. We will use this setting in our FEA code and investigate bending induced flexoelectric effect in this section.

Bending and splay flexoelectric effect

Based on the formulation presented in this paper, rotation of nematic director will lead to flexoelectric effect in LCEs. Two types of rotation has been considered in the flexoelectric formulation: bending rotation characterized by f_b and splay rotation characterized by f_s. We should note the difference between bending rotation of nematic director and bending deformation of material itself. Here, we have used same sign for both effects and we have used same positive values for the both in order to ease the interpretation of the underlying physics behind the flexoelectric effect in LCEs. Our results show that both bending and splay rotations may occur under bending deformation.

Figure 6.13 shows average dimensionless electric field versus applied traction in presence and absence of each one of bending or splay flexoelectric effects. It is shown that the average

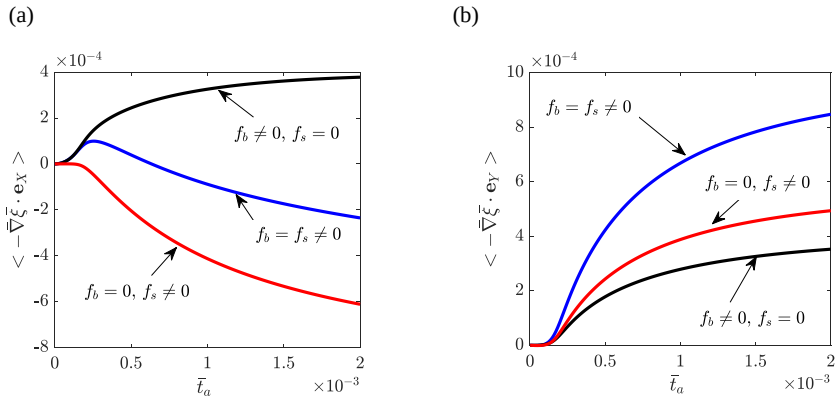

Figure 6.13: Average dimensionless electric field along X (a) and Y (b) directions versus applied traction in presence and absence of bending and splay flexoelectric effects.

electric field along X direction is not negligible compare to average electric field generated along Y direction specially under small loading ($\bar{t}_a < 0.1$) where the major flexoelectric effect observed is an electric field generated along axis direction (X direction). This electric field is the result of bending rotation of nematic directors (f_b flexoelectric effect). Figure 6.13a shows that f_b flexoelectric effect will lead to generation of average electric field with positive value along the axis direction of the material (X direction) for all stages of loading while f_s flexoelectric effect generates negative electric field along the X direction. Therefore, there is a competition between two effects. The f_b flexoelectric effect is leading under small deformation and the f_s flexoelectric effect will take over under large deformations. Therefor, Fig. 6.13a shows that, in presence of both f_b and f_s effects, as loading increases the average electric field in X direction increases and peaks at a positive value and then it begins to decrease toward negative values and finally becomes increasingly negative. However, Fig. 6.13b shows both f_b and f_s effect will lead to a positive electric field along the thickness direction and these two effects intensify each other and electric field in Y direction always increases as loading increases. It is important to note that we have assumed positive values for both f_b and f_s. If these two coefficients had opposite signs, we would see competition along Y direction instead of X direction.

The effect of material parameter a in flexoelectric effect

Figure 6.14 also shows the effect of material parameter a in the bending induced flexoelectric behavior of the material. The magnitude of the material parameter a determines the magnitude of strain induced in the material as a result of alignment or rotation of nematic directors. For prolate nematic elastomers a is always greater than one. Under small strain assumption, the magnitude of a is close to 1 while it could be larger for large deformations. DeSimone and coworkers used value of 1.05 in the reference [365] and value of 1.88 in the reference [366].

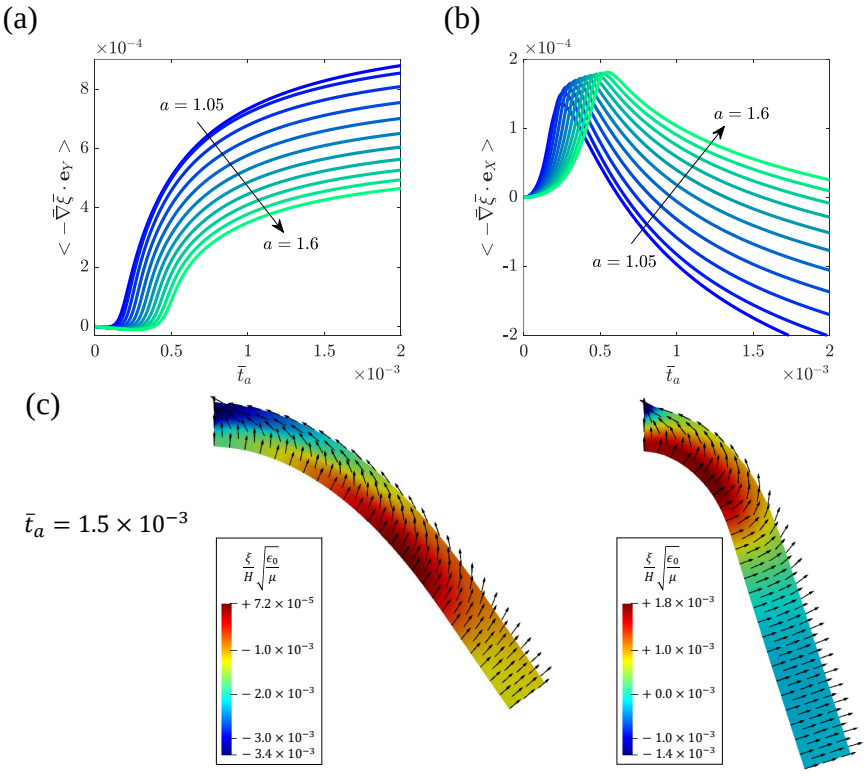

Figure 6.14: Electric potential and average electric field generated in the material under bending deformation. (a) Average electric field in Y direction versus applied traction for different values of material parameter a. (b) Average electric field in X direction versus applied traction for different values of material parameter a. (c) Contours of dimensionless electric potential for two different materials one with $a = 1.05$ shown on the left side and one with $a = 1.6$ shown on the right side ($\bar{t}_a = 1.5 \times 10^{-3}$ for both). Black arrows show the direction of nematic directors.

Here, we have plotted average electric field along X and Y directions in Figures 6.14a

and 6.14b for values of a from 1.05 to 1.6. It is seen that as this material parameter increases, the flexoelectric effect becomes weaker. The reason for this behavior can be investigated in the Fig. 6.14c where contours of dimensionless electric potential and direction of nematic directors has been plotted on the deformed configuration of two materials one with $a = 1.05$ (left) and one with $a = 1.6$ (right), both under the same bending load. In order to interpret these figures we should note that the nematic director tend to rotate toward principle stretch direction in order to reduce elastic part of free energy W^{elast}. However, there are two factors which tend to avoid rotation of nematic director. The first factor is related to bending deformation of the material. Under bending deformation, the principle stretch direction is perpendicular to thickness direction both above and below the neutral axis. The rotation of nematic director toward principle stretch direction creates tension while external load tend to compress material points below the neutral axis. Therefore, external load opposes rotation of nematic director in the areas below neutral axis which is under compression. This explains the reason that, for the point located near surface $Y = 0$ in the on deformed configuration, nematic directors have remained more or less parallel to the thickness in Fig. 6.14c. The second factor is the anisotropic part of energy $W^{\text{anisotropy}}$ which is minimized if nematic directors are parallel to the thickness direction of the material. The W^{elast} energy reduction induced due to rotation of nematic directors should overcome energy increase in $W^{\text{anisotropy}}$ in order to observe rotation of nematic directors with respect to material points. This energy barrier against rotation is larger if the material parameter a is larger. Therefore, the flexoelectric effect is weaker in the materials with larger a. It is worthwhile to note that $W^{\text{anisotropy}}$ will not restrict rotation of material points itself. Therefore, it does not restrict nematic director gradient induced as a result of rotation of material points. It means that it does not restrict f_b flexoelectric effect while restricting f_s flexoelectric effect. This is consistent with the behavior observed in the 6.14b where it is seen that for the material with small values of a the average electric field in X direction is negative while the opposite is true for the material with large a. This shows that increase in the value of the material parameter a may change flexoelectric mechanism from splay induced flexoelectric effect to bending induced flexoelectric effect in LCEs.

Size effect in bending

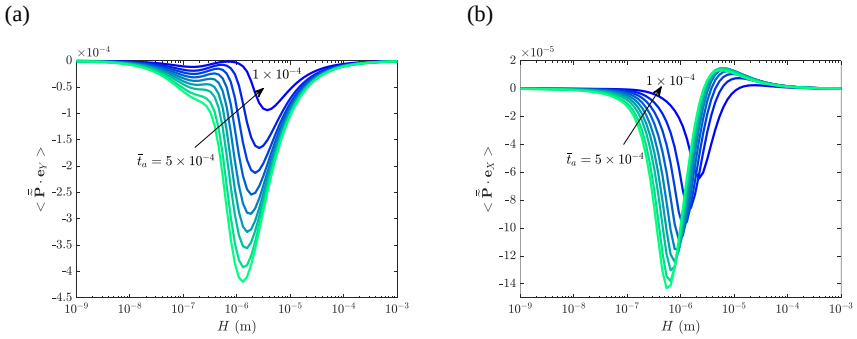

Figure 6.15: Size effect in bending deformation induced flexoelectric effect. (a) Average polarization field along X direction versus characteristic length for materials under different magnitude of loading. (b) Average polarization field along Y direction versus characteristic length for materials under different magnitude of loading.

It is well known that the flexoelectric effect is a size dependent effect. The flexoelectricity of solids is often considerable at small nanosize scales while this effect is negligible at larger size scales [80]. Therefore, it is important to study the effect of size scale on flexoelectricity in LCEs. The average polarization along X and Y directions versus characteristic length of the material has been plotted in Fig. 6.15a and Fig. 6.15b, respectively. Both figures show similar trend where the flexoelectric effect is negligible in large size scales. As the characteristic length becomes smaller the polarization becomes larger and the flexoelectric effect reaches a maximum at around characteristic length $H \approx 10^{-6}$. As the characteristic length further decrease the flexoelectric effect becomes smaller. The exact characteristic length in which bending deformation induced polarization reaches its maximum depends on the value of applied traction (Fig. 6.15).

The reduction of flexoelectric effect with decrease of size scale is against common notion of flexoelectricity in solids. This is because different mechanism of flexoelectricity in LCEs compare to conventional solids.The flexoelectricity in nematic LCEs is due to existence of gradient in the nematic director field while in conventional solids strain gradient induces flexoelectricity. For a given strain in a solid, as size scale of the solid decreases its strain gradient increases linearly and the flexoelectric effect increases as a result. The same is true

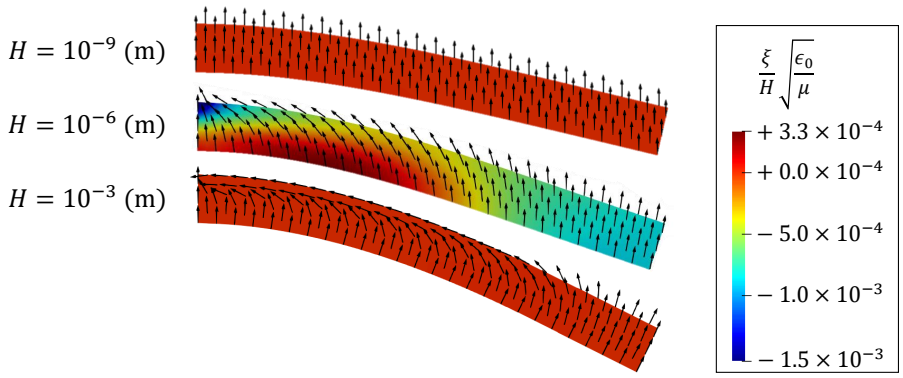

Figure 6.16: Contours dimensionless electric field and direction of nematic director for three materials in three different size scale.

for a given nematic director field. However, the difference between the two is because of the effect of Frank elasticity. Formulation earlier showed that flexoelectric effect is linearly proportional to the inverse of characteristic length and the effect of Frank elasticity is quadratically proportional to the inverse of characteristic length. At very small size scale, Frank elasticity term becomes a major constraint which tends to keep nematic directors uniform and avoids exhibition of the flexoelectric effect. To better show this effect consider Fig. 6.16 where contours of dimensionless electric field and direction of nematic directors has been plotted in the deformed configuration of three materials at three different size scales. The applied dimensionless loading is the same between these three materials. For $H = 10^{-3}$m, the gradient of nematic field has not led to any flexoelectric effect and electric potential iz zero everywhere. Both flexoelectric effect and the Frank elasticity effect are negligible at this large size scale. As size scale gets smaller to $H = 10^{-6}$m, an electric potential difference is observed across the material which shows flexoelectricity is important at this size scale. For size scale $H = 10^{-}6$, no gradient in the nematic field is reported. This is because the Frank elasticity effect is so large that penalizes any gradient in the nematic director field. Therefore, no flexoelectric effect is reported at this size scale disregarding how large flexoelectric coefficients may be.

6.8.5 FEA results for opto-flexoelectric effect in NLCEs

It is well known that nematic LCEs containing azobenzene molecules can exhibit a large reversible photo induced strain [242]. Disregarding the photothermal effect which are not subject of current work and the discussion on this topic can be found elsewhere (see reviews [317, 318, 319]), light illumination to a photo responsive LCE can lead to two kind of deformation, the first is the photo-induced phase transition and the second is the photo-induced reorientation of nematic directors [316]. Photo-induced phase transition is due absorption of photon by azobenzene which lead to trans–cis photoisomerization, the disturbance of the orientational order and transformation of the material from nematic to isotropic state [237]. The light induced reorientation effect, also known as the Weigert Effect [322], is a result of repeated trans–cis–trans isomerization cycles in response to polarized light irradiation [323]. Although experimental studies have studied photo-induced reorientation in nematic liquid crystal polymers [324, 325, 326], most theoretical studies have not considered light polarization direction dependent light induced reorientation effects [327, 328, 329, 330, 331, 332, 333]. Recently, Bai and Bhattacharya [336] used free energy developed by [337] studied photomechanical coupling in a photoactive LCE under both light illumination and mechanical stress. They studied effect of light polarization direction on the reorientation of nematic directors. Here, we have used the same free energy and coupled it with electricity to study light induced flexoelectric effect.

Here, we use formulation presented earlier and FEA model described in order to investigate opto-electric effect in LCEs. Unless other wise stated we have assumed $a = 1.05$, $\mu = 30$ KPa, $K_F = 10^{-11}$ J/m, $\epsilon_a = 2.26$, $\epsilon_c = 4.52$, $f_b\epsilon_0 = f_s\epsilon_0 = 1$ pC/N and $\mu_\beta = \mu$. The size scale is set to be $H = 10^{-6}$ m. We further assume $\bar{J_n} = 5$, $f = \frac{1}{6}$ and $\mu_n = 20\mu$. For simplicity, we assume light intensity in the material is obtained using so-called Beer-Lambert law as follows

$$I = I_0 \exp\left(\frac{X_2 - H}{d_p}\right). \tag{6.8.30}$$

In order to ease interpretation of results, we assume $d_p = 0.1H$. We also set $I_0 = 0.5$. It should be mentioned that the exact profile of the light and light intensity in each position in the material depends on the texture of the material. The polarization direction of light

beam can be modified using polarizer. Also, penetration depth of the material can be modified by addition of scattering particles such as microspheres [367] or intralipid fat [368], or absorbing particles such as black ink to the solution of the material. Detailed description of manufacturing process of the material is out of scope of current work.

Similar to what mentioned earlier for the stretch and bending simulations, we set boundary conditions on the nematic state. Assuming $\mathbf{N}_a = \mathbf{e}_Y$, we relax the system and then constrain the deformation and nematic directors on the bottom surface (Fig. 6.17).

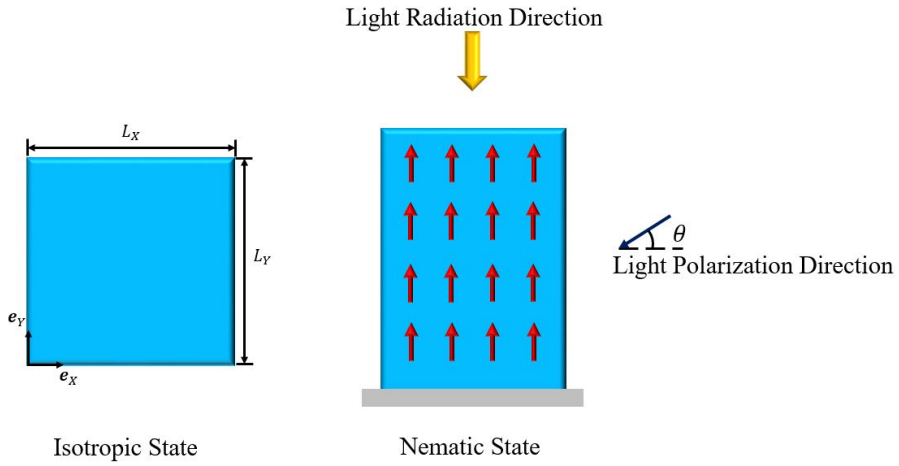

Figure 6.17: Schematic of the specimen simulated for opto-flexoelectric analysis. The boundary conditions are applied in the nematic state.

Effect of polarization direction of light on opto-flexoelectric effect

The contours of dimensionless electric potential along with direction of nematic director is plotted in the Fig. 6.18 for material under light with different polarization directions. We identify polarization direction of the material with θ. Initially, we have set $\theta = 0$. As nematic director tend to remain perpendicular to polarization direction, no deformation and flexoelectric effect is observed in this case. In the next step in our FEA analysis, we start increasing θ with step size of one degree where we observe a reorientation of nematic directors takes place. Fig. 6.18 shows as θ increases the reorientation of nematic directors increases and as a result the flexoelectric effect becomes stronger and deformation becomes larger. The maximum director reorientation is reported on the region of the material which is close to top surface and has higher light intensity.

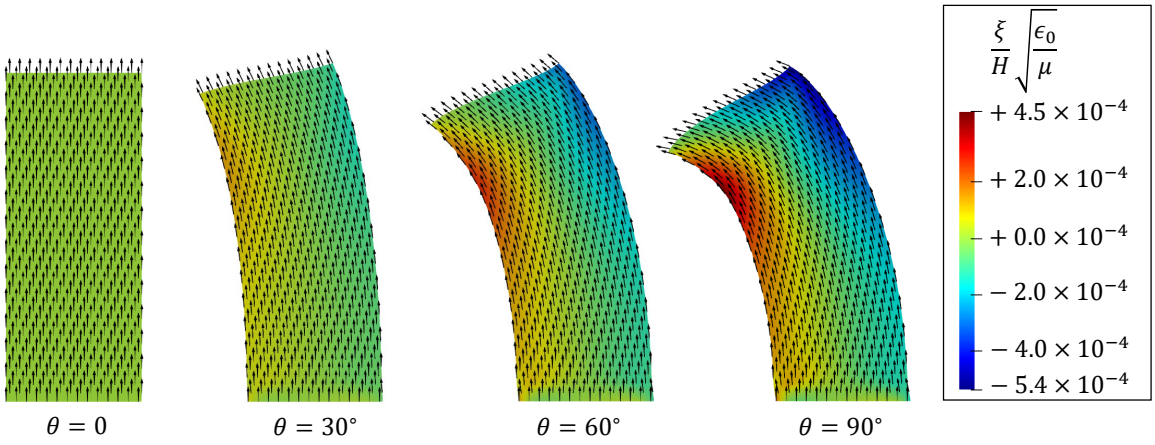

Figure 6.18: Contours of dimensionless electric potential for material under polarized light irradiation with different polarization direction. The black arrows show the direction of nematic directors.

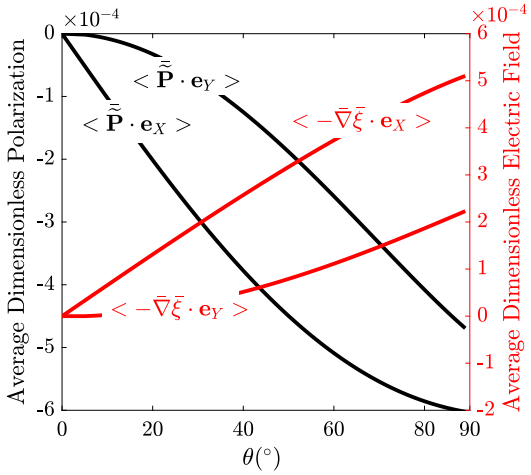

Figure 6.19: Average dimensionless polarization and electric field induced in the material as result of polarized light irradiation with different polarization directions.

Average dimensionless polarization and dimensionless electric field versus light polarization direction in both X and Y directions have been plotted in the Fig. 6.19. Fig. 6.19 also shows that flexoelectric effect becomes stronger as θ increases. Also, this figure shows that light induced electric field and polarization is not negligible in X or Y directions.

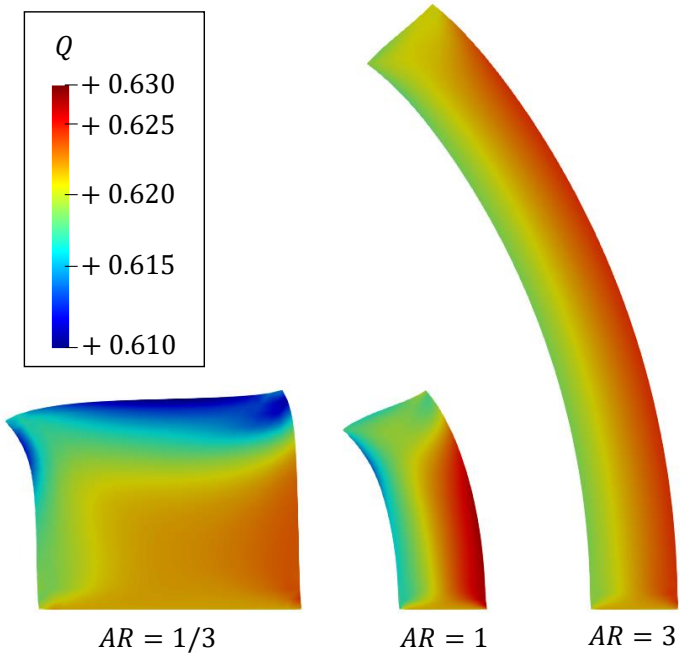

Figure 6.20: Contours of order parameter Q for material with different aspect ratio (AR) under polarized light with $\theta = \pi/4$.

Effect of the material aspect ratio

The effect of materials aspect ratio on the light induced deformation along with distribution of order parameter Q is shown in the Fig. 6.20 where aspect ratio is defined as Ł$_x/L_y$ (see Fig. 6.17). Figure 6.20 shows that the light induced deformation in materials with smaller AR looks more like shear deformation and in the materials with larger AR looks more like bending. Also, contours of order parameter shows that the variation of order parameter in the material is small and material is far from transformation to isotropic phase in which $Q = 0$. This is because light intensity used in this section has been deliberately chose to be small to avoid phase transition.

Size effect in opto-flexoelectric behavior of the material

The size effect in light induced flexoelectric effect in LCEs is studied in Figs. 6.21 and 6.22. Figure 6.21 shows at larger size scales opto-flexoelectric effect is negligible. As size

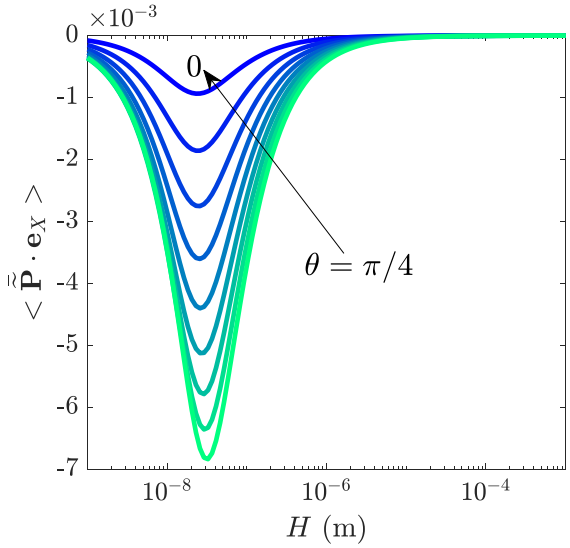

Figure 6.21: Average dimensionless polarization along X direction versus characteristic length of the material for photoactive LCE under light irradiation with different polarization directions.

Figure 6.22: Contours of dimensionless electric potential for materials with different characteristic length under polarized light with $\theta = \pi/4$.

scale decreases, the light induced polarization increases until it peaks at size scale close to 5×10^{-8} and then again it decreases with further reduction in the value of size scale. This trend is similar to what mentioned earlier for bending induced flexoelectric effect. Figure 6.21 shows that for size scale $H = 10^{-3}$ light induced rotation of nematic directors has not led to any flexoelectric effect because nematic director gradient is not small enough at this

size scale. Also, figure 6.21 shows that for smaller size scales of $H = 10^{-6}$ and $H = 5 \times 10^{-6}$ the distribution of nematic director is similar to distribution observed in the size scale $H = 10^{-3}$ but flexoelectric effect is larger because gradient of nematic director is larger at this size scale. However, figure 6.21 shows that there is no nematic director gradient and flexoelectric effect for the $H = 10^{-9}$ because the Frank elasticity effect becomes so large that it avoids observance of any gradient in the nematic director field. In general, the reason for behavior observed in these two graph is that flexoelectric effect is linearly proportional to inverse of characteristic length of the material and the Frank elasticity effect is quadratically proportional to inverse of characteristic length of the material.

6.9 Concluding Remarks

A nonlinear coupled energy formulation for Nematic Liquid Crystal Elastomers (NLCEs) was presented considering effects of photomechanical coupling and flexoelectricity. In addition, we used scaling regimes to present simplified linear theories which can be used to investigate behavior of LCEs.We employed finite element analysis to investigate flexoelectric effect and photoflexoelectric effect in NLCEs. We investigated size effects and showed there is an optimum size scale in which flexoelectric effect and photoflexoelectric is optimum. Moreover, we showed that both bending and splay reorientation of nematic director can lead to emergence of flexoelectric effect and these two contribution may intensity or weaken each other depending on the loading and material properties. Moreover, we showed that a simple stretch of nematic sheet may lead to polarization of material but as the deformation is symmetric the average polarization is negligible.

6.10 Appendix

6.10.1 Derivation for the rate of change of electric energy

Here in this section we present a derivation for the rate of change of electric energy considering polarization and deformation as two independent variables. We relax constraint of incompressibility in order to obtain the general form of the Maxwell stress. In order to

proceed this derivation we need following relation which is obtained by multiplying the Maxwell equation (6.2.2) by ξ and using divergence theorem:

$$\int_V \epsilon_0 \nabla_y \xi \cdot \nabla_y \xi = \int_V \nabla_y \xi \cdot \mathbf{p} - \int_{\partial V} \xi \mathbf{d} \cdot \boldsymbol{\nu}. \tag{6.10.1}$$

Similarly, multiplying the Maxwell equation with $\dot{\xi}$ and using divergence theorem, we obtain following relation which later will be needed in order to determine rate of change of electric energy:

$$\int_V \epsilon_0 \nabla_y \dot{\xi} \cdot \nabla_y \xi = \int_V \nabla_y \dot{\xi} \cdot \mathbf{p} - \int_{\partial V} \dot{\xi} \mathbf{d} \cdot \boldsymbol{\nu}. \tag{6.10.2}$$

Using Eq.(6.10.1), the rate of change of electric energy can be written as

$$\dot{\mathcal{E}}^{\text{elect}} = \frac{\mathrm{d}}{\mathrm{d}t} \int_V \frac{1}{2} \epsilon_0 |\nabla_y \xi|^2 = \frac{\mathrm{d}}{\mathrm{d}t} \int_V \frac{1}{2} \nabla_y \xi \cdot \mathbf{p} - \frac{\mathrm{d}}{\mathrm{d}t} \int_{\partial V} \frac{1}{2} \xi \mathbf{d} \cdot \boldsymbol{\nu}. \tag{6.10.3}$$

Using Raynolds Transport theorem, we can rewrite equation (6.10.3) as

$$\dot{\mathcal{E}}^{\text{elect}} = \frac{1}{2} \int_V \left[\dot{\overline{\nabla_y \xi}} \cdot \mathbf{p} + \nabla_y \xi \cdot \dot{\mathbf{p}} + \nabla_y \xi \cdot \mathbf{p} (\nabla_y \cdot \mathbf{v}) \right] - \frac{\mathrm{d}}{\mathrm{d}t} \int_{\partial V} \frac{1}{2} \xi \mathbf{d} \cdot \boldsymbol{\nu}. \tag{6.10.4}$$

The rate of change of electric field can be expanded as

$$\dot{\overline{\nabla_y \xi}} = \nabla_y \dot{\xi} - \mathbf{L}^T \nabla_y \xi. \tag{6.10.5}$$

Thus, Eq.(6.10.4) is wtirren as

$$\dot{\mathcal{E}}^{\text{elect}} = \frac{1}{2} \int_V \left[\nabla_y \dot{\xi} \cdot \mathbf{p} - \mathbf{L}^T \nabla_y \xi \cdot \mathbf{p} + \nabla_y \xi \cdot \dot{\mathbf{p}} + \nabla_y \xi \cdot \mathbf{p} (\nabla_y \cdot \mathbf{v}) \right] - \frac{\mathrm{d}}{\mathrm{d}t} \int_{\partial V} \frac{1}{2} \xi \mathbf{d} \cdot \boldsymbol{\nu}. \tag{6.10.6}$$

Since our independent variable is polization, we need to determin the first term on the right hand side of Eq.(6.10.6) in terms of $\dot{\mathbf{p}}$. Thus, using Raynolds Transport theorem and

(6.10.5) we have

$$\begin{aligned}\dot{\mathcal{E}}^{\text{elect}} &= \frac{\mathrm{d}}{\mathrm{d}t}\int_V \frac{1}{2}\epsilon_0|\nabla_y\xi|^2 \\ &= \int_V \left[\epsilon_0\left(\nabla_y\dot{\xi} - \mathbf{L}^T\nabla_y\xi\right)\cdot\nabla_y\xi + \frac{\epsilon_0}{2}|\nabla_y\xi|^2(\nabla_y\cdot\mathbf{v})\right] \\ &= \int_V \left[\nabla_y\dot{\xi}\cdot\mathbf{p} - \epsilon_0\mathbf{L}^T\nabla_y\xi\cdot\nabla_y\xi + \frac{\epsilon_0}{2}|\nabla_y\xi|^2(\nabla_y\cdot\mathbf{v})\right] - \int_{\partial V}\dot{\xi}\mathbf{d}\cdot\boldsymbol{\nu},\end{aligned} \tag{6.10.7}$$

where we have used Eq.(6.10.2) to derive last equality. Now, by subtracting Eq.(6.10.7) from (6.10.6) we have

$$\begin{aligned}&\frac{1}{2}\int_V \nabla_y\dot{\xi}\cdot\mathbf{p} = \\ &\int_V \left[-\frac{1}{2}\mathbf{L}^T\nabla_y\xi\cdot\mathbf{p} + \frac{1}{2}\nabla_y\xi\cdot\dot{\mathbf{p}} + \frac{1}{2}\nabla_y\xi\cdot\mathbf{p}(\nabla_y\cdot\mathbf{v}) + \epsilon_0\mathbf{L}^T\nabla_y\xi\cdot\nabla_y\xi - \frac{\epsilon_0}{2}|\nabla_y\xi|^2(\nabla_y\cdot\mathbf{v})\right] \\ &+ \int_{\partial V}\dot{\xi}\mathbf{d}\cdot\boldsymbol{\nu} - \frac{\mathrm{d}}{\mathrm{d}t}\int_{\partial V}\frac{1}{2}\xi\mathbf{d}\cdot\boldsymbol{\nu}.\end{aligned} \tag{6.10.8}$$

By substituting Eq.(6.10.8) into Eq.(6.10.6), the rate of change of internal energy is obtained as

$$\dot{\mathcal{E}}^{\text{elect}} = \int_V \left(\boldsymbol{\sigma}^{\text{MW}} : \mathbf{L} + \nabla_y\xi\cdot\dot{\mathbf{p}}\right) - \int_{\partial V_R}\xi\dot{\tilde{\mathbf{D}}}\cdot\boldsymbol{\nu}_R, \tag{6.10.9}$$

where

$$\boldsymbol{\sigma}^{\text{MW}} = (-\nabla_y\xi)\otimes(-\epsilon_0\nabla_y\xi + \mathbf{p}) - (\frac{\epsilon_0}{2}|\nabla_y\xi|^2 - \nabla_y\xi\cdot\mathbf{p})\mathbf{I} \tag{6.10.10}$$

References

[1] X. Zhang, P. Pondrom, L. Wu, and G. Sessler, "Vibration-based energy harvesting with piezoelectrets having high d 31 activity," *Applied Physics Letters*, vol. 108, no. 19, p. 193903, 2016.

[2] Q. Guo, G. Cao, and I. Shen, "Measurements of piezoelectric coefficient d33 of lead zirconate titanate thin films using a mini force hammer," *Journal of Vibration and Acoustics*, vol. 135, no. 1, 2013.

[3] G. S. Neugschwandtner, R. Schwödiauer, S. Bauer-Gogonea, S. Bauer, M. Paajanen, and J. Lekkala, "Piezo-and pyroelectricity of a polymer-foam space-charge electret," *Journal of Applied Physics*, vol. 89, no. 8, pp. 4503–4511, 2001.

[4] W. Jing and F. Fang, "A flexible multiferroic composite with high self-biased magnetoelectric coupling," *Composites Science and Technology*, vol. 153, pp. 145–150, 2017.

[5] A. Lima, N. Pereira, R. Policia, C. Ribeiro, V. Correia, S. Lanceros-Mendez, and P. Martins, "All-printed multilayer materials with improved magnetoelectric response," *Journal of Materials Chemistry C*, vol. 7, no. 18, pp. 5394–5400, 2019.

[6] X. Hu, Y. Che, Z. Zhang, Q.-D. Shen, and B. Chu, "Bifeo3–batio3/p (vdf-trfe) multifunctional polymer nanocomposites," *ACS Applied Electronic Materials*, vol. 3, no. 2, pp. 743–751, 2021.

[7] Y. Zong, T. Zheng, P. Martins, S. Lanceros-Mendez, Z. Yue, and M. J. Higgins, "Cellulose-based magnetoelectric composites," *Nature communications*, vol. 8, no. 1, pp. 1–8, 2017.

[8] V. Andrade, A. Amirov, D. Yusupov, B. Pimentel, N. Barroca, A. Pires, J. Belo, A. Pereira, M. Valente, and J. Araújo, "Multicaloric effect in a multiferroic composite

of gd 5 (si, ge) 4 microparticles embedded into a ferroelectric pvdf matrix," *Scientific reports*, vol. 9, no. 1, pp. 1–10, 2019.

[9] D. M. Correia, P. Martins, M. Tariq, J. M. Esperança, and S. Lanceros-Méndez, "Low-field giant magneto-ionic response in polymer-based nanocomposites," *Nanoscale*, vol. 10, no. 33, pp. 15747–15754, 2018.

[10] J. Jin, F. Zhao, K. Han, M. Haque, L. Dong, and Q. Wang, "Multiferroic polymer laminate composites exhibiting high magnetoelectric response induced by hydrogen-bonding interactions," *Advanced functional materials*, vol. 24, no. 8, pp. 1067–1073, 2014.

[11] Z. Fang, S. Lu, F. Li, S. Datta, Q. Zhang, and M. El Tahchi, "Enhancing the magnetoelectric response of metglas/polyvinylidene fluoride laminates by exploiting the flux concentration effect," *Applied Physics Letters*, vol. 95, no. 11, p. 112903, 2009.

[12] S. Reis, N. Castro, M. P. Silva, V. Correia, J. G. Rocha, P. Martins, and S. Lanceros-Mendez, "Fabrication and characterization of high-performance polymer-based magnetoelectric dc magnetic field sensors devices," *IEEE Transactions on Industrial Electronics*, vol. 64, no. 6, pp. 4928–4934, 2017.

[13] M. Silva, S. Reis, C. Lehmann, P. Martins, S. Lanceros-Mendez, A. Lasheras, J. Gutiérrez, and J. Barandiarán, "Optimization of the magnetoelectric response of poly (vinylidene fluoride)/epoxy/vitrovac laminates," *ACS applied materials & interfaces*, vol. 5, no. 21, pp. 10912–10919, 2013.

[14] A. Lasheras, J. Gutiérrez, S. Reis, D. Sousa, M. Silva, P. Martins, S. Lanceros-Mendez, J. Barandiarán, D. Shishkin, and A. Potapov, "Energy harvesting device based on a metallic glass/pvdf magnetoelectric laminated composite," *Smart Materials and Structures*, vol. 24, no. 6, p. 065024, 2015.

[15] A. Kulkarni, K. Meurisch, I. Teliban, R. Jahns, T. Strunskus, A. Piorra, R. Knöchel, and F. Faupel, "Giant magnetoelectric effect at low frequencies in polymer-based thin film composites," *Applied Physics Letters*, vol. 104, no. 2, p. 022904, 2014.

[16] X. He, J. Qiu, Y. Long, Q. Chang, Z. Hu, H. Liu, W. Hu, Y. She, and X. Tang, "Giant zero-biased flexible magnetoelectric laminate composites for wearable magnetic sensor," *Ceramics International*, vol. 44, pp. S100–S103, 2018.

[17] X. Mu, H. Zhang, C. Zhang, S. Yang, J. Xu, Y. Huang, J. Xu, Y. Zhang, Q. Li, and X. Wang, "Poly (vinylidene fluoride-trifluoroethylene)/cobalt ferrite composite films with a self-biased magnetoelectric effect for flexible ac magnetic sensors," *Journal of Materials Science*, vol. 56, no. 16, pp. 9728–9740, 2021.

[18] P. Martins, A. Lasheras, J. Gutiérrez, J. M. Barandiarán, I. Orue, and S. Lanceros-Méndez, "Optimizing piezoelectric and magnetoelectric responses on cofe2o4/p (vdf-trfe) nanocomposites," *Journal of Physics D: Applied Physics*, vol. 44, no. 49, p. 495303, 2011.

[19] P. Martins, X. Moya, L. Phillips, S. Kar-Narayan, N. Mathur, and S. Lanceros-Mendez, "Linear anhysteretic direct magnetoelectric effect in ni0. 5zn0. 5fe2o4/poly (vinylidene fluoride-trifluoroethylene) 0-3 nanocomposites," *Journal of Physics D: Applied Physics*, vol. 44, no. 48, p. 482001, 2011.

[20] Y. Feng, Y. Zhang, J. Sheng, T. Zhang, Q. Chi, Q. Chen, and W. Fei, "Multiferroic properties and magnetic anisotropy in p (vdf-trfe) composites with oriented cofe2o4 nanofibers," *The Journal of Physical Chemistry C*, vol. 125, no. 16, pp. 8840–8852, 2021.

[21] L. Zhou, Q. Fu, D. Zhou, Z. Zheng, Y. Hu, W. Luo, Y. Tian, C. Wang, F. Xue, and X. Tang, "Self-assembled core-shell cofe2o4@ batio3 particles loaded p (vdf-hfp) flexible films with excellent magneto-electric effects," *Applied Physics Letters*, vol. 111, no. 3, p. 032903, 2017.

[22] S. Reis, M. Silva, N. Castro, V. Correia, J. Gutierrez, A. Lasheras, S. Lanceros-Mendez, and P. Martins, "Optimized anisotropic magnetoelectric response of fe61. 6co16. 4si10. 8b11. 2/pvdf/fe61. 6co16. 4si10. 8b11. 2 laminates for ac/dc magnetic field sensing," *Smart Materials and Structures*, vol. 25, no. 5, p. 055050, 2016.

[23] D. Li, X.-M. Zhao, H.-X. Zhao, Y.-P. Ren, L.-S. Long, and L.-S. Zheng, "Room-temperature magnetoelectric response in molecular–ionic ferroelectric-based magnetoelectric composites," *physica status solidi (RRL)–Rapid Research Letters*, vol. 14, no. 3, p. 1900644, 2020.

[24] P. Yang, S. Peng, X. B. WU, J. G. Wan, and J. Zhu, "Magnetoelectric study in terfenol-d/pfnt laminate composite," *Integrated Ferroelectrics - INTEGR FERROELECTRICS*, vol. 99, pp. 86–92, 06 2008.

[25] R. Zhao, Y. Kim, S. A. Chester, P. Sharma, and X. Zhao, "Mechanics of hard-magnetic soft materials," *Journal of the Mechanics and Physics of Solids*, vol. 124, pp. 244–263, 2019.

[26] C. Luo and M.-C. Calderer, "Numerical study of liquid crystal elastomers by a mixed finite element method," *European Journal of Applied Mathematics*, vol. 23, no. 1, pp. 121–154, 2012.

[27] B. Mazzolai and V. Mattoli, "Generation soft," *Nature*, vol. 536, no. 7617, pp. 400–401, 2016.

[28] S. Bauer, S. Bauer-Gogonea, I. Graz, M. Kaltenbrunner, C. Keplinger, and R. Schwödiauer, "25th anniversary article: a soft future: from robots and sensor skin to energy harvesters," *Advanced Materials*, vol. 26, no. 1, pp. 149–162, 2014.

[29] Z. Suo, "Mechanics of stretchable electronics and soft machines," *Mrs Bulletin*, vol. 37, no. 3, pp. 218–225, 2012.

[30] H.-T. Lin, G. G. Leisk, and B. Trimmer, "Goqbot: a caterpillar-inspired soft-bodied rolling robot," *Bioinspiration & biomimetics*, vol. 6, no. 2, p. 026007, 2011.

[31] Y. Sugiyama and S. Hirai, "Crawling and jumping by a deformable robot," *The International journal of robotics research*, vol. 25, no. 5-6, pp. 603–620, 2006.

[32] B. Zhang, Y. Fan, P. Yang, T. Cao, and H. Liao, "Worm-like soft robot for complicated tubular environments," *Soft robotics*, vol. 6, no. 3, pp. 399–413, 2019.

[33] C. Ahn, X. Liang, and S. Cai, "Bioinspired design of light-powered crawling, squeezing, and jumping untethered soft robot," *Advanced Materials Technologies*, vol. 4, no. 7, p. 1900185, 2019.

[34] G. Gu, J. Zou, R. Zhao, X. Zhao, and X. Zhu, "Soft wall-climbing robots," *Science Robotics*, vol. 3, no. 25, p. eaat2874, 2018.

[35] S. Huang, Y. Liu, Y. Zhao, Z. Ren, and C. F. Guo, "Flexible electronics: stretchable electrodes and their future," *Advanced Functional Materials*, vol. 29, no. 6, p. 1805924, 2019.

[36] R. Landers, A. Pfister, U. Hübner, H. John, R. Schmelzeisen, and R. Mülhaupt, "Fabrication of soft tissue engineering scaffolds by means of rapid prototyping techniques," *Journal of materials science*, vol. 37, no. 15, pp. 3107–3116, 2002.

[37] S. Laflamme, M. Kollosche, J. Connor, and G. Kofod, "Soft capacitive sensor for structural health monitoring of large-scale systems," *Structural Control and Health Monitoring*, vol. 19, no. 1, pp. 70–81, 2012.

[38] J.-H. Low, I. Delgado-Martinez, and C.-H. Yeow, "Customizable soft pneumatic chamber–gripper devices for delicate surgical manipulation," *Journal of Medical Devices*, vol. 8, no. 4, 2014.

[39] J. K. Liu, O. N. Gottfried, C. D. Cole, W. R. Dougherty, and W. T. Couldwell, "Porous polyethylene implant for cranioplasty and skull base reconstruction," *Neurosurgical focus*, vol. 16, no. 3, pp. 1–5, 2004.

[40] H.-R. Lim, H. S. Kim, R. Qazi, Y.-T. Kwon, J.-W. Jeong, and W.-H. Yeo, "Advanced soft materials, sensor integrations, and applications of wearable flexible hybrid electronics in healthcare, energy, and environment," *Advanced Materials*, vol. 32, no. 15, p. 1901924, 2020.

[41] J. Kim, J. W. Kim, H. C. Kim, L. Zhai, H.-U. Ko, and R. M. Muthoka, "Review of soft actuator materials," *International Journal of Precision Engineering and Manufacturing*, vol. 20, no. 12, pp. 2221–2241, 2019.

[42] R. Kaltseis, C. Keplinger, R. Baumgartner, M. Kaltenbrunner, T. Li, P. Mächler, R. Schwödiauer, Z. Suo, and S. Bauer, "Method for measuring energy generation and efficiency of dielectric elastomer generators," *Applied Physics Letters*, vol. 99, no. 16, p. 162904, 2011.

[43] G. Buchberger, R. Schwödiauer, and S. Bauer, "Flexible large area ferroelectret sensors for location sensitive touchpads," *Applied Physics Letters*, vol. 92, no. 12, p. 123511, 2008.

[44] F. Carpi, D. De Rossi, R. Kornbluh, R. E. Pelrine, and P. Sommer-Larsen, *Dielectric elastomers as electromechanical transducers: Fundamentals, materials, devices, models and applications of an emerging electroactive polymer technology.* Elsevier, 2011.

[45] D. Yang, M. S. Verma, J.-H. So, B. Mosadegh, C. Keplinger, B. Lee, F. Khashai, E. Lossner, Z. Suo, and G. M. Whitesides, "Buckling pneumatic linear actuators inspired by muscle," *Advanced Materials Technologies*, vol. 1, no. 3, 2016.

[46] C. Dagdeviren, B. D. Yang, Y. Su, P. L. Tran, P. Joe, E. Anderson, J. Xia, V. Doraiswamy, B. Dehdashti, and X. Feng, "Conformal piezoelectric energy harvesting and storage from motions of the heart, lung, and diaphragm," *Proceedings of the National Academy of Sciences*, vol. 111, no. 5, pp. 1927–1932, 2014.

[47] J. Huang, S. Shian, Z. Suo, and D. R. Clarke, "Maximizing the energy density of dielectric elastomer generators using equi-biaxial loading," *Advanced Functional Materials*, vol. 23, no. 40, pp. 5056–5061, 2013.

[48] S. Yang, X. Zhao, and P. Sharma, "Avoiding the pull-in instability of a dielectric elastomer film and the potential for increased actuation and energy harvesting," *Soft Matter*, vol. 13, pp. 4552–4558, 2017.

[49] T. Kelly, B. M. Ghadi, S. Berg, and H. Ardebili, "In situ study of strain-dependent ion conductivity of stretchable polyethylene oxide electrolyte," *Scientific reports*, vol. 6, p. 20128, 2016.

[50] F. Carpi, S. Bauer, and D. De Rossi, "Stretching dielectric elastomer performance," *Science*, vol. 330, no. 6012, pp. 1759–1761, 2010.

[51] J. A. Rogers, T. Someya, and Y. Huang, "Materials and mechanics for stretchable electronics," *Science*, vol. 327, no. 5973, pp. 1603–1607, 2010.

[52] P. Muralt, R. Polcawich, and S. Trolier-McKinstry, "Piezoelectric thin films for sensors, actuators, and energy harvesting," *MRS bulletin*, vol. 34, no. 9, pp. 658–664, 2009.

[53] S. Trolier-McKinstry and P. Muralt, "Thin film piezoelectrics for mems," *Journal of Electroceramics*, vol. 12, no. 1-2, pp. 7–17, 2004.

[54] S. B. Long, E. B. Campbell, and R. MacKinnon, "Voltage sensor of kv1. 2: structural basis of electromechanical coupling," *Science*, vol. 309, no. 5736, pp. 903–908, 2005.

[55] N. Murayama, K. Nakamura, H. Obara, and M. Segawa, "The strong piezoelectricity in polyvinylidene fluroide (pvdf)," *Ultrasonics*, vol. 14, no. 1, pp. 15–24, 1976.

[56] C. Keplinger, T. Li, R. Baumgartner, Z. Suo, and S. Bauer, "Harnessing snap-through instability in soft dielectrics to achieve giant voltage-triggered deformation," *Soft Matter*, vol. 8, no. 2, pp. 285–288, 2012.

[57] L. Tian, *Effective behavior of dielectric elastomer composites (dissertation).* PhD thesis, California Institute of Technology, Pasadena, CA, 2007.

[58] L. Tian, L. Tevet-Deree, and K. Bhattacharya, "Dielectric elastomer composites," *Journal of the Mechanics and Physics of Solids*, vol. 60, no. 1, pp. 181–198, 2012.

[59] X. Zhao and Z. Suo, "Electrostriction in elastic dielectrics undergoing large deformation," *Journal of Applied Physics*, vol. 104, no. 12, p. 123530, 2008.

[60] S. J. A. Koh, T. Li, J. Zhou, X. Zhao, W. Hong, J. Zhu, and Z. Suo, "Mechanisms of large actuation strain in dielectric elastomers," *Journal of Polymer Science Part B: Polymer Physics*, vol. 49, no. 7, pp. 504–515, 2011.

[61] S. J. A. Koh, X. Zhao, and Z. Suo, "Maximal energy that can be converted by a dielectric elastomer generator," *Applied Physics Letters*, vol. 94, no. 26, p. 262902, 2009.

[62] S. Bauer, R. Gerhard-Multhaupt, and G. M. Sessler, "Ferroelectrets: Soft electroactive foams for transducers," 2004.

[63] G. Neugschwandtner, R. Schwödiauer, M. Vieytes, S. Bauer-Gogonea, S. Bauer, J. Hillenbrand, R. Kressmann, G. Sessler, M. Paajanen, and J. Lekkala, "Large and broadband piezoelectricity in smart polymer-foam space-charge electrets," *Applied Physics Letters*, vol. 77, no. 23, pp. 3827–3829, 2000.

[64] G. Neugschwandtner, R. Schwödiauer, S. Bauer-Gogonea, and S. Bauer, "Large piezoelectric effects in charged, heterogeneous fluoropolymer electrets," *Applied Physics A: Materials Science & Processing*, vol. 70, no. 1, pp. 1–4, 2000.

[65] J. Hillenbrand and G. Sessler, "Dc-biased ferroelectrets with large piezoelectric d 33-coefficients," *Journal of applied physics*, vol. 103, no. 7, p. 074103, 2008.

[66] S. Orrego, K. Shoele, A. Ruas, K. Doran, B. Caggiano, R. Mittal, and S. H. Kang, "Harvesting ambient wind energy with an inverted piezoelectric flag," *Applied Energy*, vol. 194, pp. 212–222, 2017.

[67] C.-h. Yun, B. Watson, J. Friend, and L. Yeo, "A piezoelectric ultrasonic linear micromotor using a slotted stator," *IEEE transactions on ultrasonics, ferroelectrics, and frequency control*, vol. 57, no. 8, 2010.

[68] J. G. Smits, "Piezoelectric micropump with three valves working peristaltically," *Sensors and Actuators A: Physical*, vol. 21, no. 1-3, pp. 203–206, 1990.

[69] S. A. Rios, A. J. Fleming, and Y. K. Yong, "Miniature resonant ambulatory robot," *IEEE Robotics and Automation Letters*, vol. 2, no. 1, pp. 337–343, 2017.

[70] J. H. Yoo, J. I. Hong, and W. Cao, "Piezoelectric ceramic bimorph coupled to thin metal plate as cooling fan for electronic devices," *Sensors and Actuators A: Physical*, vol. 79, no. 1, pp. 8–12, 2000.

[71] S. Roundy and P. K. Wright, "A piezoelectric vibration based generator for wireless electronics," *Smart Materials and structures*, vol. 13, no. 5, p. 1131, 2004.

[72] M. J. Ramsay and W. W. Clark, "Piezoelectric energy harvesting for bio-mems applications," in *SPIE's 8th Annual International Symposium on Smart Structures and Materials*, pp. 429–438, International Society for Optics and Photonics, 2001.

[73] L. He, J. Lou, J. Du, and J. Wang, "Finite bending of a dielectric elastomer actuator and pre-stretch effects," *International Journal of Mechanical Sciences*, vol. 122, pp. 120–128, 2017.

[74] S.-B. Choi and G.-W. Kim, "Measurement of flexoelectric response in polyvinylidene fluoride films for piezoelectric vibration energy harvesters," *Journal of Physics D: Applied Physics*, vol. 50, no. 7, p. 075502, 2017.

[75] S. Baskaran, N. Ramachandran, X. He, S. Thiruvannamalai, H. J. Lee, H. Heo, Q. Chen, and J. Y. Fu, "Giant flexoelectricity in polyvinylidene fluoride films," *Physics Letters A*, vol. 375, no. 20, pp. 2082–2084, 2011.

[76] W. Ma and L. E. Cross, "Flexoelectricity of barium titanate," *Applied Physics Letters*, vol. 88, no. 23, p. 232902, 2006.

[77] J. Y. Fu, W. Zhu, N. Li, and L. E. Cross, "Experimental studies of the converse flexoelectric effect induced by inhomogeneous electric field in a barium strontium titanate composition," *Journal of Applied Physics*, vol. 100, no. 2, p. 024112, 2006.

[78] A. G. Petrov, "Electricity and mechanics of biomembrane systems: flexoelectricity in living membranes," *Analytica chimica acta*, vol. 568, no. 1, pp. 70–83, 2006.

[79] A. Todorov, A. Petrov, and J. Fendler, "First observation of the converse flexoelectric effect in bilayer lipid membranes," *The Journal of Physical Chemistry*, vol. 98, no. 12, pp. 3076–3079, 1994.

[80] F. Ahmadpoor and P. Sharma, "Flexoelectricity in two-dimensional crystalline and biological membranes," *Nanoscale*, vol. 7, no. 40, pp. 16555–16570, 2015.

[81] S. Krichen and P. Sharma, "Flexoelectricity: A perspective on an unusual electromechanical coupling," *Journal of Applied Mechanics*, vol. 83, no. 3, p. 030801, 2016.

[82] P. Yudin and A. Tagantsev, "Fundamentals of flexoelectricity in solids," *Nanotechnology*, vol. 24, no. 43, p. 432001, 2013.

[83] P. Zubko, G. Catalan, and A. K. Tagantsev, "Flexoelectric effect in solids," *Annual Review of Materials Research*, vol. 43, pp. 387–421, 2013.

[84] D. Lee and T. W. Noh, "Giant flexoelectric effect through interfacial strain relaxation," *Philosophical Transactions of the Royal Society of London A: Mathematical, Physical and Engineering Sciences*, vol. 370, no. 1977, pp. 4944–4957, 2012.

[85] T. D. Nguyen, S. Mao, Y.-W. Yeh, P. K. Purohit, and M. C. McAlpine, "Nanoscale flexoelectricity," *Advanced Materials*, vol. 25, no. 7, pp. 946–974, 2013.

[86] T. Q. Thai, T. Rabczuk, and X. Zhuang, "A large deformation isogeometric approach for flexoelectricity and soft materials," *Computer Methods in Applied Mechanics and Engineering*, 2018.

[87] H. Ghasemi, H. S. Park, and T. Rabczuk, "A multi-material level set-based topology optimization of flexoelectric composites," *Computer Methods in Applied Mechanics and Engineering*, vol. 332, pp. 47–62, 2018.

[88] R. A. Toupin, "The elastic dielectric," *Journal of Rational Mechanics and Analysis*, vol. 5, no. 6, pp. 849–915, 1956.

[89] A. C. Eringen and G. A. Maugin, *Electrodynamics of continua, Vol I and II*. Springer press, 1990.

[90] A. Dorfmann and R. Ogden, "Nonlinear electroelasticity," *Acta Mechanica*, vol. 174, no. 3-4, pp. 167–183, 2005.

[91] R. D. Mindlin, "Polarization gradient in elastic dielectrics," *International Journal of Solids and Structures*, vol. 4, no. 6, pp. 637–642, 1968.

[92] R. D. James and M. Wuttig, "Magnetostriction of martensite," *Philosophical Magazine A*, vol. 77, no. 5, pp. 1273–1299, 1998.

[93] R. M. McMeeking and C. M. Landis, "Electrostatic forces and stored energy for deformable dielectric materials," *Journal of Applied Mechanics*, vol. 72, no. 4, pp. 581–590, 2005.

[94] Z. Suo, X. Zhao, and W. H. Greene, "A nonlinear field theory of deformable dielectrics," *Journal of the Mechanics and Physics of Solids*, vol. 56, no. 2, pp. 467–486, 2008.

[95] Z. Suo, "Theory of dielectric elastomers," *Acta Mechanica Solida Sinica*, vol. 23, no. 6, pp. 549–578, 2010.

[96] Y. Xiao and K. Bhattacharya, "A continuum theory of deformable, semiconducting ferroelectrics," *Archive for Rational Mechanics and Analysis*, vol. 189, no. 1, pp. 59–95, 2008.

[97] L. Liu, "An energy formulation of continuum magneto-electro-elasticity with applications," *Journal of the Mechanics and Physics of Solids*, vol. 63, pp. 451–480, 2014.

[98] Q. Deng, L. Liu, and P. Sharma, "Electrets in soft materials: Nonlinearity, size effects, and giant electromechanical coupling," *Physical Review E*, vol. 90, no. 1, p. 012603, 2014.

[99] Q. Deng, L. Liu, and P. Sharma, "Flexoelectricity in soft materials and biological membranes," *Journal of the Mechanics and Physics of Solids*, vol. 62, pp. 209–227, 2014.

[100] L. Liu and P. Sharma, "Emergent electromechanical coupling of electrets and some exact relations—the effective properties of soft materials with embedded external charges and dipoles," *Journal of the Mechanics and Physics of Solids*, vol. 112, pp. 1–24, 2018.

[101] A. Mellinger, "Dielectric resonance spectroscopy: a versatile tool in the quest for better piezoelectric polymers," *IEEE Transactions on Dielectrics and Electrical Insulation*, vol. 10, no. 5, pp. 842–861, 2003.

[102] A. Meitzler, H. Tiersten, A. Warner, D. Berlincourt, G. Couqin, and F. Welsh III, "Ieee standard on piezoelectricity," 1988.

[103] R. Rivlin, "Large elastic deformations of isotropic materials. v. the problem of flexure," in *Proceedings of the Royal Society of London A: Mathematical, Physical and Engineering Sciences*, vol. 195, pp. 463–473, The Royal Society, 1949.

[104] G. Sessler and R. Gerhard-Multhaupt, "Electrets, morgan hill," 1999.

[105] F. Ahmadpoor, Q. Deng, L. Liu, and P. Sharma, "Apparent flexoelectricity in lipid bilayer membranes due to external charge and dipolar distributions," *Physical Review E*, vol. 88, no. 5, p. 050701, 2013.

[106] D. Berlincourt and H. Jaffe, "Elastic and piezoelectric coefficients of single-crystal barium titanate," *Physical Review*, vol. 111, no. 1, p. 143, 1958.

[107] S. Qu and Y. Yu, "Electromechanical coupling properties and stability analysis of ferroelectrets," *Journal of Applied Physics*, vol. 110, no. 4, p. 043525, 2011.

[108] Q. Deng, M. Kammoun, A. Erturk, and P. Sharma, "Nanoscale flexoelectric energy harvesting," *International Journal of Solids and Structures*, vol. 51, no. 18, pp. 3218–3225, 2014.

[109] D. Bigoni, M. Gei, and S. Roccabianca, "Bifurcation of elastic multilayers," in *Mathematical Methods and Models in Composites*, pp. 173–207, World Scientific, 2014.

[110] D. Trivedi, C. D. Rahn, W. M. Kier, and I. D. Walker, "Soft robotics: Biological inspiration, state of the art, and future research," *Applied bionics and biomechanics*, vol. 5, no. 3, pp. 99–117, 2008.

[111] K. Dong, X. Peng, and Z. L. Wang, "Fiber/fabric-based piezoelectric and triboelectric nanogenerators for flexible/stretchable and wearable electronics and artificial intelligence," *Advanced Materials*, vol. 32, no. 5, p. 1902549, 2020.

[112] A. Rafsanjani, Y. Zhang, B. Liu, S. M. Rubinstein, and K. Bertoldi, "Kirigami skins make a simple soft actuator crawl," *Science Robotics*, vol. 3, no. 15, p. eaar7555, 2018.

[113] M. Cianchetti, C. Laschi, A. Menciassi, and P. Dario, "Biomedical applications of soft robotics," *Nature Reviews Materials*, vol. 3, no. 6, pp. 143–153, 2018.

[114] A. L. Kholkin, N. A. Pertsev, and A. V. Goltsev, "Piezoelectricity and crystal symmetry," in *Piezoelectric and Acoustic Materials for Transducer Applications*, pp. 17–38, Springer, 2008.

[115] R. Newnham, V. Sundar, R. Yimnirun, J. Su, and Q. Zhang, "Electrostriction: nonlinear electromechanical coupling in solid dielectrics," *The Journal of Physical Chemistry B*, vol. 101, no. 48, pp. 10141–10150, 1997.

[116] N. Sharma, R. Maranganti, and P. Sharma, "On the possibility of piezoelectric nanocomposites without using piezoelectric materials," *Journal of the Mechanics and Physics of Solids*, vol. 55, no. 11, pp. 2328–2350, 2007.

[117] M. Majdoub, P. Sharma, and T. Cagin, "Enhanced size-dependent piezoelectricity and elasticity in nanostructures due to the flexoelectric effect," *Physical Review B*, vol. 77, no. 12, p. 125424, 2008.

[118] M. Majdoub, P. Sharma, and T. Çağin, "Erratum: Enhanced size-dependent piezoelectricity and elasticity in nanostructures due to the flexoelectric effect [phys. rev. b 77, 125424 (2008)]," *Physical Review B*, vol. 79, no. 11, p. 119904, 2009.

[119] R. Mbarki, N. Baccam, K. Dayal, and P. Sharma, "Piezoelectricity above the curie temperature? combining flexoelectricity and functional grading to enable high-temperature electromechanical coupling," *Applied Physics Letters*, vol. 104, no. 12, p. 122904, 2014.

[120] P. Mohammadi, L. Liu, and P. Sharma, "A theory of flexoelectric membranes and effective properties of heterogeneous membranes," *Journal of Applied Mechanics*, vol. 81, no. 1, 2014.

[121] B. Wang, S. Yang, and P. Sharma, "Flexoelectricity as a universal mechanism for energy harvesting from crumpling of thin sheets," *Physical Review B*, vol. 100, no. 3, p. 035438, 2019.

[122] M. Grasinger, K. Mozaffari, and P. Sharma, "Flexoelectricity in soft elastomers and the molecular mechanisms underpinning the design and emergence of giant flexoelectricity," *Proceedings of the National Academy of Sciences*, vol. 118, no. 21, 2021.

[123] A. Abdollahi, C. Peco, D. Millan, M. Arroyo, and I. Arias, "Computational evaluation of the flexoelectric effect in dielectric solids," *Journal of Applied Physics*, vol. 116, no. 9, p. 093502, 2014.

[124] A. Abdollahi, N. Domingo, I. Arias, and G. Catalan, "Converse flexoelectricity yields large piezoresponse force microscopy signals in non-piezoelectric materials," *Nature communications*, vol. 10, no. 1, pp. 1–6, 2019.

[125] X. Tian, J. Sladek, V. Sladek, Q. Deng, and Q. Li, "A collocation mixed finite element method for the analysis of flexoelectric solids," *International Journal of Solids and Structures*, vol. 217, pp. 27–39, 2021.

[126] Q. Deng, S. Lv, Z. Li, K. Tan, X. Liang, and S. Shen, "The impact of flexoelectricity on materials, devices, and physics," *Journal of Applied Physics*, vol. 128, no. 8, p. 080902, 2020.

[127] A. K. Tagantsev and P. V. Yudin, *Flexoelectricity in solids: from theory to applications*. World Scientific, 2016.

[128] Q. Deng, L. Liu, and P. Sharma, "A continuum theory of flexoelectricity," in *Flexoelectricity in Solids: From Theory to Applications*, pp. 111–167, World Scientific, 2017.

[129] X. Zhang, J. Hillenbrand, and G. M. Sessler, "Piezoelectric d 33 coefficient of cellular polypropylene subjected to expansion by pressure treatment," *Applied physics letters*, vol. 85, no. 7, pp. 1226–1228, 2004.

[130] G. Sessler and J. Hillenbrand, "Electromechanical response of cellular electret films," in *10th International Symposium on Electrets (ISE 10). Proceedings (Cat. No. 99 CH36256)*, pp. 261–264, IEEE, 1999.

[131] S. Bauer, S. Bauer-Gogonea, M. Dansachmuller, I. Graz, H. Leonhartsberger, H. Salhofer, and R. Schwodiauer, "Modern electrets," in *IEEE Symposium on Ultrasonics, 2003*, vol. 1, pp. 370–376, IEEE, 2003.

[132] R. Kacprzyk, A. Dobrucki, and J. Gajewski, "Double-layer electret transducer," *Journal of electrostatics*, vol. 39, no. 1, pp. 33–40, 1997.

[133] J. Hillenbrand and G. Sessler, "Piezoelectricity in cellular electret films," *IEEE Transactions on Dielectrics and Electrical Insulation*, vol. 7, no. 4, pp. 537–542, 2000.

[134] G. M. Sessler and J. E. West, "Foil-electret microphones," *The Journal of the Acoustical Society of America*, vol. 40, no. 6, pp. 1433–1440, 1966.

[135] S. Gong, J. Zhang, C. Wang, K. Ren, and Z. L. Wang, "A monocharged electret nanogenerator-based self-powered device for pressure and tactile sensor applications," *Advanced Functional Materials*, vol. 29, no. 41, p. 1807618, 2019.

[136] S.-W. Cheng, T. Han, T.-Y. Huang, Y.-H. Chang Chien, C.-L. Liu, B. Z. Tang, and G.-S. Liou, "Novel organic phototransistor-based nonvolatile memory integrated with uv-sensing/green-emissive aggregation enhanced emission (aee)-active aromatic polyamide electret layer," *ACS applied materials & interfaces*, vol. 10, no. 21, pp. 18281–18288, 2018.

[137] Y. Zhang, J. Zhang, K. Suzuki, M. Sumita, K. Terayama, J. Li, Z. Mao, K. Tsuda, and Y. Suzuki, "Discovery of polymer electret material via de novo molecule generation and functional group enrichment analysis," *Applied Physics Letters*, vol. 118, no. 22, p. 223904, 2021.

[138] Y. Suzuki, "Recent progress in mems electret generator for energy harvesting," *IEEJ Transactions on Electrical and Electronic Engineering*, vol. 6, no. 2, pp. 101–111, 2011.

[139] Y. Suzuki, D. Miki, M. Edamoto, and M. Honzumi, "A mems electret generator with electrostatic levitation for vibration-driven energy-harvesting applications," *Journal of Micromechanics and Microengineering*, vol. 20, no. 10, p. 104002, 2010.

[140] J. Boland, Y.-H. Chao, Y. Suzuki, and Y. Tai, "Micro electret power generator," in *The Sixteenth Annual International Conference on Micro Electro Mechanical Systems, 2003. MEMS-03 Kyoto. IEEE*, pp. 538–541, IEEE, 2003.

[141] K. Kashiwagi, K. Okano, T. Miyajima, Y. Sera, N. Tanabe, Y. Morizawa, and Y. Suzuki, "Nano-cluster-enhanced high-performance perfluoro-polymer electrets for energy harvesting," *Journal of Micromechanics and Microengineering*, vol. 21, no. 12, p. 125016, 2011.

[142] A. Luo, Y. Xu, Y. Zhang, M. Zhang, X. Zhang, Y. Lu, and F. Wang, "Spray-coated electret materials with enhanced stability in a harsh environment for an mems energy harvesting device," *Microsystems & nanoengineering*, vol. 7, no. 1, pp. 1–9, 2021.

[143] A. H. Rahmati, S. Bauer, S. Yang, and P. Sharma, "Nonlinear bending deformation of soft electrets and prospects for engineering flexoelectricity and transverse (d_{31}) piezoelectricity," *Soft matter*, vol. 15, no. 1, pp. 127–148, 2019.

[144] Z. Alameh, Q. Deng, L. Liu, and P. Sharma, "Using electrets to design concurrent magnetoelectricity and piezoelectricity in soft materials," *Journal of Materials Research*, vol. 30, no. 1, pp. 93–100, 2015.

[145] K. Tan, X. Wen, Q. Deng, S. Shen, L. Liu, and P. Sharma, "Soft rubber as a magnetoelectric material—generating electricity from the remote action of a magnetic field," *Materials Today*, vol. 43, pp. 8–16, 2021.

[146] F. Darbaniyan, K. Dayal, L. Liu, and P. Sharma, "Designing soft pyroelectric and electrocaloric materials using electrets," *Soft matter*, vol. 15, no. 2, pp. 262–277, 2019.

[147] L. Tian, *Effective behavior of dielectric elastomer composites*. PhD thesis, California Institute of Technology, 2008.

[148] D. Cioranescu and P. Donato, *An introduction to homogenization*, vol. 17. Oxford university press Oxford, 1999.

[149] G. Milton, "The theory of composites (cambridge monographs on applied and computational mathematics) cambridge university press," *Cambridge, UK*, 2002.

[150] H. Hiroshi and T. Minoru, "Equivalent inclusion method for steady state heat conduction in composites," *International Journal of Engineering Science*, vol. 24, no. 7, pp. 1159–1172, 1986.

[151] S. Li and G. Wang, *Introduction to micromechanics and nanomechanics*. World Scientific Publishing Company, 2008.

[152] T. Mura, *Micromechanics of defects in solids*. Springer Science & Business Media, 2013.

[153] L. Liu, "Solutions to the eshelby conjectures," *Proceedings of the Royal Society A: Mathematical, Physical and Engineering Sciences*, vol. 464, no. 2091, pp. 573–594, 2008.

[154] J. D. Eshelby, "The determination of the elastic field of an ellipsoidal inclusion, and related problems," *Proceedings of the royal society of London. Series A. Mathematical and physical sciences*, vol. 241, no. 1226, pp. 376–396, 1957.

[155] P. Sharma and S. Ganti, "Size-dependent eshelby's tensor for embedded nano-inclusions incorporating surface/interface energies," *TRANSACTIONS-AMERICAN SOCIETY OF MECHANICAL ENGINEERS JOURNAL OF APPLIED MECHANICS*, vol. 71, no. 5, pp. 663–671, 2004.

[156] C. E. Rosenkilde, "Surface-energy tensors for ellipsoids," *Journal of Mathematical Physics*, vol. 8, no. 1, pp. 88–97, 1967.

[157] H. Schmid, "Multi-ferroic magnetoelectrics," *Ferroelectrics*, vol. 162, no. 1, pp. 317–338, 1994.

[158] N. A. Hill, "Why are there so few magnetic ferroelectrics?," 2000.

[159] K. Bhoi, H. Mohanty, M. F. Abdullah, D. K. Pradhan, S. N. Babu, A. Singh, P. Vishwakarma, A. Kumar, R. Thomas, and D. K. Pradhan, "Unravelling the nature of magneto-electric coupling in room temperature multiferroic particulate (pbfe 0.5 nb 0.5 o 3)–(co 0.6 zn 0.4 fe 1.7 mn 0.3 o 4) composites," *Scientific reports*, vol. 11, no. 1, pp. 1–17, 2021.

[160] C. W. Nan, M. Li, and J. H. Huang, "Calculations of giant magnetoelectric effects in ferroic composites of rare-earth–iron alloys and ferroelectric polymers," *Physical Review B*, vol. 63, no. 14, p. 144415, 2001.

[161] C. W. Nan, M. Li, X. Feng, and S. Yu, "Possible giant magnetoelectric effect of ferromagnetic rare-earth–iron-alloys-filled ferroelectric polymers," *Applied Physics Letters*, vol. 78, no. 17, pp. 2527–2529, 2001.

[162] J. Ryu, S. Priya, A. V. Carazo, K. Uchino, and H.-E. Kim, "Effect of the magnetostrictive layer on magnetoelectric properties in lead zirconate titanate/terfenol-d laminate composites," *Journal of the American Ceramic Society*, vol. 84, no. 12, pp. 2905–2908, 2001.

[163] J. Ryu, A. V. Carazo, K. Uchino, and H.-E. Kim, "Magnetoelectric properties in piezoelectric and magnetostrictive laminate composites," *Japanese Journal of Applied Physics*, vol. 40, no. 8R, p. 4948, 2001.

[164] S. Dong, J.-F. Li, and D. Viehland, "Ultrahigh magnetic field sensitivity in laminates of terfenol-d and pb (mg 1/3 nb 2/3) o 3–pbtio 3 crystals," *Applied Physics Letters*, vol. 83, no. 11, pp. 2265–2267, 2003.

[165] G. Srinivasan, E. Rasmussen, and R. Hayes, "Magnetoelectric effects in ferrite-lead zirconate titanate layered composites: The influence of zinc substitution in ferrites," *Physical Review B*, vol. 67, no. 1, p. 014418, 2003.

[166] S. Dong, J. Zhai, N. Wang, F. Bai, J. Li, D. Viehland, and T. A. Lograsso, "Fe–ga/ pb (mg 1/ 3 nb 2/ 3) o 3–pb ti o 3 magnetoelectric laminate composites," *Applied Physics Letters*, vol. 87, no. 22, p. 222504, 2005.

[167] J. Zhai, S. Dong, Z. Xing, J. Li, and D. Viehland, "Giant magnetoelectric effect in metglas/polyvinylidene-fluoride laminates," *Applied Physics Letters*, vol. 89, no. 8, p. 083507, 2006.

[168] H. Palneedi, D. Maurya, L. D. Geng, H.-C. Song, G.-T. Hwang, M. Peddigari, V. Annapureddy, K. Song, Y. S. Oh, and S.-C. Yang, "Enhanced self-biased magnetoelectric coupling in laser-annealed pb (zr, ti) o3 thick film deposited on ni foil," *ACS applied materials & interfaces*, vol. 10, no. 13, pp. 11018–11025, 2018.

[169] S. Kopyl, R. Surmenev, M. Surmeneva, Y. Fetisov, and A. Kholkin, "Magnetoelectric effect: principles and applications in biology and medicine–a review," *Materials Today Bio*, vol. 12, p. 100149, 2021.

[170] M. Nair, R. Guduru, P. Liang, J. Hong, V. Sagar, and S. Khizroev, "Externally controlled on-demand release of anti-hiv drug using magneto-electric nanoparticles as carriers," *Nature communications*, vol. 4, no. 1, pp. 1–8, 2013.

[171] T. Nguyen, J. Gao, P. Wang, A. Nagesetti, P. Andrews, S. Masood, Z. Vriesman, P. Liang, S. Khizroev, and X. Jin, "In vivo wireless brain stimulation via non-invasive and targeted delivery of magnetoelectric nanoparticles," *Neurotherapeutics*, pp. 1–16, 2021.

[172] S. Ribeiro, C. Ribeiro, E. O. Carvalho, C. R. Tubio, N. Castro, N. Pereira, V. Correia, A. C. Gomes, and S. Lanceros-Meéndez, "Magnetically activated electroactive microenvironments for skeletal muscle tissue regeneration," *ACS Applied Bio Materials*, vol. 3, no. 7, pp. 4239–4252, 2020.

[173] Y. Kim, H. Yuk, R. Zhao, S. A. Chester, and X. Zhao, "Printing ferromagnetic domains for untethered fast-transforming soft materials," *Nature*, vol. 558, no. 7709, pp. 274–279, 2018.

[174] Y. Kim, G. A. Parada, S. Liu, and X. Zhao, "Ferromagnetic soft continuum robots," *Science Robotics*, vol. 4, no. 33, 2019.

[175] S. Gong, J. Zhang, C. Wang, K. Ren, and Z. Wang, "A monocharged electret nanogenerator-based self-powered device for pressure and tactile sensor applications," *Advanced Functional Materials*, p. 1807618, 01 2019.

[176] K. Tan, X. Wen, Q. Deng, S. Shen, L. Liu, and P. Sharma, "Soft rubber as a magneto-electric material—generating electricity from the remote action of a magnetic field," *Materialstoday*, 2020.

[177] P. Martins and S. Lanceros-MenNdez, "Polymer-based magnetoelectric materials," *Advanced Functional Materials*, vol. 23, no. 27, pp. 3371–3385, 2013.

[178] A. H. Rahmati, S. Yang, S. Bauer, and P. Sharma, "Nonlinear bending deformation of soft electrets and prospects for engineering flexoelectricity and transverse (d 31) piezoelectricity," *Soft matter*, vol. 15, no. 1, pp. 127–148, 2019.

[179] X. Wen, D. Li, K. Tan, Q. Deng, and S. Shen, "Flexoelectret: An electret with a tunable flexoelectriclike response," *Physical review letters*, vol. 122, no. 14, p. 148001, 2019.

[180] X. Gong, K. Tan, Q. Deng, and S. Shen, "Athermal shape memory effect in magnetoactive elastomers," *ACS applied materials & interfaces*, vol. 12, no. 14, pp. 16930–16936, 2020.

[181] A. Logg, K.-A. Mardal, and G. Wells, *Automated solution of differential equations by the finite element method: The FEniCS book*, vol. 84. Springer Science & Business Media, 2012.

[182] P. Martins, Y. V. Kolen'ko, J. Rivas, and S. Lanceros-Mendez, "Tailored magnetic and magnetoelectric responses of polymer-based composites," *ACS applied materials & interfaces*, vol. 7, no. 27, pp. 15017–15022, 2015.

[183] C.-W. Nan, M. Bichurin, S. Dong, D. Viehland, and G. Srinivasan, "Multiferroic magnetoelectric composites: Historical perspective, status, and future directions," *Journal of applied physics*, vol. 103, no. 3, p. 1, 2008.

[184] M. Fiebig, "Revival of the magnetoelectric effect," *Journal of physics D: applied physics*, vol. 38, no. 8, p. R123, 2005.

[185] I. A. Osaretin and R. G. Rojas, "Theoretical model for the magnetoelectric effect in magnetostrictive/piezoelectric composites," *Physical Review B*, vol. 82, no. 17, p. 174415, 2010.

[186] M. Vopson, Y. Fetisov, G. Caruntu, and G. Srinivasan, "Measurement techniques of the magneto-electric coupling in multiferroics," *materials*, vol. 10, no. 8, p. 963, 2017.

[187] S. Chen, R. Huang, and K. Ravi-Chandar, "Linear and nonlinear poroelastic analysis of swelling and drying behavior of gelatin-based hydrogels," *International Journal of Solids and Structures*, 2020.

[188] D. Garcia-Gonzalez and C. M. Landis, "Magneto-diffusion-viscohyperelasticity for magneto-active hydrogels: rate dependences across time scales," *Journal of the Mechanics and Physics of Solids*, p. 103934, 2020.

[189] M. Bibes and A. Barthélémy, "Towards a magnetoelectric memory," *Nature materials*, vol. 7, no. 6, pp. 425–426, 2008.

[190] V. Annapureddy, H. Palneedi, G.-T. Hwang, M. Peddigari, D.-Y. Jeong, W.-H. Yoon, K.-H. Kim, and J. Ryu, "Magnetic energy harvesting with magnetoelectrics: an emerging technology for self-powered autonomous systems," *Sustainable Energy & Fuels*, vol. 1, no. 10, pp. 2039–2052, 2017.

[191] R. Guduru, P. Liang, C. Runowicz, M. Nair, V. Atluri, and S. Khizroev, "Magnetoelectric nanoparticles to enable field-controlled high-specificity drug delivery to eradicate ovarian cancer cells," *Scientific reports*, vol. 3, no. 1, pp. 1–8, 2013.

[192] S. Dong, J.-M. Liu, S.-W. Cheong, and Z. Ren, "Multiferroic materials and magnetoelectric physics: symmetry, entanglement, excitation, and topology," *Advances in Physics*, vol. 64, no. 5-6, pp. 519–626, 2015.

[193] G. Catalan and J. F. Scott, "Physics and applications of bismuth ferrite," *Advanced materials*, vol. 21, no. 24, pp. 2463–2485, 2009.

[194] N. Spaldin and R. Ramesh, "Advances in magnetoelectric multiferroics," *Nature Materials*, vol. 18, pp. 203–212, 03 2019.

[195] T. Lottermoser, T. Lonkai, U. Amann, D. Hohlwein, J. Ihringer, and M. Fiebig, "Magnetic phase control by an electric field," *Nature*, vol. 430, no. 6999, pp. 541–544, 2004.

[196] Y. Wang, J. Hu, Y. Lin, and C.-W. Nan, "Multiferroic magnetoelectric composite nanostructures," *NPG Asia Materials*, vol. 2, no. 2, pp. 61–68, 2010.

[197] A. P. Pyatakov and A. K. Zvezdin, "Magnetoelectric and multiferroic media," *Physics-Uspekhi*, vol. 55, no. 6, p. 557, 2012.

[198] Y. Tokura, S. Seki, and N. Nagaosa, "Multiferroics of spin origin," *Reports on Progress in Physics*, vol. 77, no. 7, p. 076501, 2014.

[199] M. Fiebig, T. Lottermoser, D. Meier, and M. Trassin, "The evolution of multiferroics," *Nature Reviews Materials*, vol. 1, no. 8, pp. 1–14, 2016.

[200] W. Eerenstein, N. Mathur, and J. F. Scott, "Multiferroic and magnetoelectric materials," *nature*, vol. 442, no. 7104, pp. 759–765, 2006.

[201] Y. Zhou, D. Maurya, Y. Yan, G. Srinivasan, E. Quandt, and S. Priya, "Self-biased magnetoelectric composites: An overview and future perspectives," *Energy Harvesting and Systems*, vol. 3, 07 2015.

[202] J. Ma, J. Hu, Z. Li, and C.-W. Nan, "Recent progress in multiferroic magnetoelectric composites: from bulk to thin films," *Advanced materials*, vol. 23, no. 9, pp. 1062–1087, 2011.

[203] X. Liang, H. Chen, and N. X. Sun, "Magnetoelectric materials and devices," *APL Materials*, vol. 9, no. 4, p. 041114, 2021.

[204] F. Narita and M. Fox, "A review on piezoelectric, magnetostrictive, and magnetoelectric materials and device technologies for energy harvesting applications," *Advanced Engineering Materials*, vol. 20, no. 5, p. 1700743, 2018.

[205] J.-M. Hu, C.-G. Duan, C.-W. Nan, and L.-Q. Chen, "Understanding and designing magnetoelectric heterostructures guided by computation: progresses, remaining questions, and perspectives," *NPJ Computational Materials*, vol. 3, no. 1, pp. 1–21, 2017.

[206] Z. Chu, M. PourhosseiniAsl, and S. Dong, "Review of multi-layered magnetoelectric composite materials and devices applications," *Journal of Physics D: Applied Physics*, vol. 51, no. 24, p. 243001, 2018.

[207] S. Malley, S. Newacheck, and G. Youssef, "Additively manufactured multifunctional materials with magnetoelectric properties," *Additive Manufacturing*, p. 102239, 2021.

[208] D. K. Pradhan, S. Kumari, and P. D. Rack, "Magnetoelectric composites: Applications, coupling mechanisms, and future directions," *Nanomaterials*, vol. 10, no. 10, p. 2072, 2020.

[209] Y. Bitla and Y.-H. Chu, "Development of magnetoelectric nanocomposite for soft technology," *Journal of Physics D: Applied Physics*, vol. 51, no. 23, p. 234006, 2018.

[210] C. Dagdeviren, B. D. Yang, Y. Su, P. L. Tran, P. Joe, E. Anderson, J. Xia, V. Doraiswamy, B. Dehdashti, and X. Feng, "Conformal piezoelectric energy harvesting and storage from motions of the heart, lung, and diaphragm," *Proceedings of the National Academy of Sciences*, vol. 111, no. 5, pp. 1927–1932, 2014.

[211] J. Peng, I. Witting, N. Geisendorfer, M. Wang, M. Chang, A. Jakus, C. Kenel, X. Yan, R. Shah, and G. Snyder, "3d extruded composite thermoelectric threads for flexible energy harvesting," *Nature communications*, vol. 10, no. 1, pp. 1–8, 2019.

[212] B. Shi, Z. Li, and Y. Fan, "Implantable energy-harvesting devices," *Advanced Materials*, vol. 30, no. 44, p. 1801511, 2018.

[213] M. de Cea, A. Atabaki, and R. Ram, "Energy harvesting optical modulators with sub-attojoule per bit electrical energy consumption," *Nature communications*, vol. 12, no. 1, pp. 1–9, 2021.

[214] V. Bhavanasi, V. Kumar, K. Parida, J. Wang, and P. S. Lee, "Enhanced piezoelectric energy harvesting performance of flexible pvdf-trfe bilayer films with graphene oxide," *ACS applied materials & interfaces*, vol. 8, no. 1, pp. 521–529, 2016.

[215] L. Lu, W. Ding, J. Liu, and B. Yang, "Flexible pvdf based piezoelectric nanogenerators," *Nano Energy*, p. 105251, 2020.

[216] H. Liu, J. Zhong, C. Lee, S.-W. Lee, and L. Lin, "A comprehensive review on piezoelectric energy harvesting technology: Materials, mechanisms, and applications," *Applied Physics Reviews*, vol. 5, no. 4, p. 041306, 2018.

[217] C. Chang, V. H. Tran, J. Wang, Y.-K. Fuh, and L. Lin, "Direct-write piezoelectric polymeric nanogenerator with high energy conversion efficiency," *Nano letters*, vol. 10, no. 2, pp. 726–731, 2010.

[218] S. Mandal, G. Sreenivasulu, V. Petrov, and G. Srinivasan, "Flexural deformation in a compositionally stepped ferrite and magnetoelectric effects in a composite with piezoelectrics," *Applied Physics Letters*, vol. 96, no. 19, p. 192502, 2010.

[219] S. Mandal, S. Gollapudi, V. Petrov, and G. Srinivasan, "Magnetization-graded multiferroic composite and magnetoelectric effects at zero bias," *Phys. Rev. B*, vol. 84, 07 2011.

[220] J. Zhang, L. Ping, Y. Wen, H. Wei, and C. Lu, "Giant self-biased magnetoelectric response with obvious hysteresis in layered homogeneous composites of negative magnetostrictive material samfenol and piezoelectric ceramics," *Applied Physics Letters*, vol. 103, no. 20, p. 1062, 2013.

[221] E. Lage, C. Kirchhof, V. Hrkac, L. Kienle, and D. Meyners, "Exchange biasing of magnetoelectric composites," *Nature Materials*, vol. 11, no. 6, pp. 523–529, 2012.

[222] Z. Alameh, Q. Deng, L. Liu, and P. Sharma, "Using electrets to design concurrent magnetoelectricity and piezoelectricity in soft materials," *Journal of Materials Research*, vol. 30, pp. 93–100, 01 2014.

[223] K. Tan, X. Wen, X. Gong, Q. Deng, and S. Shen, "Diversifying temporal responses of magnetoactive elastomers," *Materials Research Express*, vol. 7, no. 4, 2020.

[224] A. Apte, K. Mozaffari, F. S. Samghabadi, J. A. Hachtel, L. Chang, S. Susarla, J. C. Idrobo, D. C. Moore, N. R. Glavin, and D. Litvinov, "2d electrets of ultrathin moo2 with apparent piezoelectricity," *Advanced Materials*, vol. 32, no. 24, p. 2000006, 2020.

[225] F. Mushtaq, H. Torlakcik, Q. Vallmajo-Martin, E. C. Siringil, J. Zhang, C. Röhrig, Y. Shen, Y. Yu, X.-Z. Chen, and R. Müller, "Magnetoelectric 3d scaffolds for enhanced bone cell proliferation," *Applied Materials Today*, vol. 16, pp. 290–300, 2019.

[226] Y. Zhang, S. Chen, Z. Xiao, X. Liu, C. Wu, K. Wu, A. Liu, D. Wei, J. Sun, and L. Zhou, "Magnetoelectric nanoparticles incorporated biomimetic matrix for wireless electrical stimulation and nerve regeneration," *Advanced Healthcare Materials*, p. 2100695, 2021.

[227] M. Dong, X. Wang, X.-Z. Chen, F. Mushtaq, S. Deng, C. Zhu, H. Torlakcik, A. Terzopoulou, X.-H. Qin, and X. Xiao, "3d-printed soft magnetoelectric microswimmers for delivery and differentiation of neuron-like cells," *Advanced Functional Materials*, vol. 30, no. 17, p. 1910323, 2020.

[228] X. Zhang, J. Ai, Z. Ma, Y. Yin, R. Zou, and B. Su, "Liquid metal based stretchable magnetoelectric films and their capacity for mechanoelectrical conversion," *Advanced Functional Materials*, vol. 30, no. 45, p. 2003680, 2020.

[229] X. Zhang, J. Ai, R. Zou, and B. Su, "Compressible and stretchable magnetoelectric sensors based on liquid metals for highly sensitive, self-powered respiratory monitoring," *ACS Applied Materials & Interfaces*, vol. 13, no. 13, pp. 15727–15737, 2021.

[230] Z. Alameh, S. Yang, Q. Deng, and P. Sharma, "Emergent magnetoelectricity in soft materials, instability, and wireless energy harvesting," *Soft Matter*, vol. 14, no. 28, pp. 5856–5868, 2018.

[231] D. L. Henann, S. A. Chester, and K. Bertoldi, "Modeling of dielectric elastomers: Design of actuators and energy harvesting devices," *Journal of the Mechanics and Physics of Solids*, vol. 61, no. 10, pp. 2047–2066, 2013.

[232] X. Zhao and Z. Suo, "Method to analyze programmable deformation of dielectric elastomer layers," *Applied Physics Letters*, vol. 93, no. 25, p. 251902, 2008.

[233] I. Babuška, "Error-bounds for finite element method," *Numerische Mathematik*, vol. 16, no. 4, pp. 322–333, 1971.

[234] F. Brezzi, "On the existence, uniqueness and approximation of saddle-point problems arising from lagrangian multipliers," *Publications mathématiques et informatique de Rennes*, no. S4, pp. 1–26, 1974.

[235] M. Fortin and F. Brezzi, *Mixed and hybrid finite element methods*. New York: Springer-Verlag, 1991.

[236] N. Bouklas, C. M. Landis, and R. Huang, "A nonlinear, transient finite element method for coupled solvent diffusion and large deformation of hydrogels," *Journal of the Mechanics and Physics of Solids*, vol. 79, pp. 21–43, 2015.

[237] M. Warner and E. M. Terentjev, *Liquid crystal elastomers*, vol. 120. Oxford university press, 2007.

[238] K. M. Herbert, H. E. Fowler, J. M. McCracken, K. R. Schlafmann, J. A. Koch, and T. J. White, "Synthesis and alignment of liquid crystalline elastomers," *Nature Reviews Materials*, pp. 1–16, 2021.

[239] D. L. Thomsen, P. Keller, J. Naciri, R. Pink, H. Jeon, D. Shenoy, and B. R. Ratna, "Liquid crystal elastomers with mechanical properties of a muscle," *Macromolecules*, vol. 34, no. 17, pp. 5868–5875, 2001.

[240] H. E. Fowler, P. Rothemund, C. Keplinger, and T. J. White, "Liquid crystal elastomers with enhanced directional actuation to electric fields," *Advanced Materials*, vol. 33, no. 43, p. 2103806, 2021.

[241] A. Kaiser, M. Winkler, S. Krause, H. Finkelmann, and A. M. Schmidt, "Magnetoactive liquid crystal elastomer nanocomposites," *Journal of materials chemistry*, vol. 19, no. 4, pp. 538–543, 2009.

[242] H. Finkelmann, E. Nishikawa, G. Pereira, and M. Warner, "A new opto-mechanical effect in solids," *Physical Review Letters*, vol. 87, no. 1, p. 015501, 2001.

[243] Q. He, Z. Wang, Y. Wang, A. Minori, M. T. Tolley, and S. Cai, "Electrically controlled liquid crystal elastomer–based soft tubular actuator with multimodal actuation," *Science advances*, vol. 5, no. 10, p. eaax5746, 2019.

[244] M. T. Brannum, A. M. Steele, M. C. Venetos, L. T. Korley, G. E. Wnek, and T. J. White, "Light control with liquid crystalline elastomers," *Advanced Optical Materials*, vol. 7, no. 6, p. 1801683, 2019.

[245] C. Ferrantini, J. M. Pioner, D. Martella, R. Coppini, N. Piroddi, P. Paoli, M. Calamai, F. S. Pavone, D. S. Wiersma, and C. Tesi, "Development of light-responsive liquid crystalline elastomers to assist cardiac contraction," *Circulation research*, vol. 124, no. 8, pp. e44–e54, 2019.

[246] T. Turiv, J. Krieger, G. Babakhanova, H. Yu, S. V. Shiyanovskii, Q.-H. Wei, M.-H. Kim, and O. D. Lavrentovich, "Topology control of human fibroblast cells monolayer by liquid crystal elastomer," *Science Advances*, vol. 6, no. 20, p. eaaz6485, 2020.

[247] S. Iseki, "Liquid crystalline elastomer precursor and liquid crystalline elastomer," Feb. 28 2019. US Patent App. 16/070,555.

[248] S. W. Ula, N. A. Traugutt, R. H. Volpe, R. R. Patel, K. Yu, and C. M. Yakacki, "Liquid crystal elastomers: an introduction and review of emerging technologies," *Liquid Crystals Reviews*, vol. 6, no. 1, pp. 78–107, 2018.

[249] C. Ohm, M. Brehmer, and R. Zentel, "Liquid crystalline elastomers as actuators and sensors," *Advanced materials*, vol. 22, no. 31, pp. 3366–3387, 2010.

[250] M. Chanda and S. K. Roy, *Plastics technology handbook*. CRC press, 2006.

[251] F. Brömmel, D. Kramer, and H. Finkelmann, "Preparation of liquid crystalline elastomers," *Liquid Crystal Elastomers: Materials and Applications*, pp. 1–48, 2012.

[252] P.-G. De Gennes and J. Prost, *The physics of liquid crystals*. No. 83, Oxford university press, 1993.

[253] P. J. Collings, *Liquid crystals: nature's delicate phase of matter*. Princeton University Press, 2002.

[254] P. Oswald and P. Pieranski, *Nematic and cholesteric liquid crystals: concepts and physical properties illustrated by experiments*. CRC press, 2005.

[255] A. Bailly-Reyre and H. T. Diep, "Nematic and smectic phases: Dynamics and phase transition," *Symmetry*, vol. 12, no. 9, p. 1574, 2020.

[256] T. J. White and D. J. Broer, "Programmable and adaptive mechanics with liquid crystal polymer networks and elastomers," *Nature materials*, vol. 14, no. 11, pp. 1087–1098, 2015.

[257] P. Bladon, E. Terentjev, and M. Warner, "Transitions and instabilities in liquid crystal elastomers," *Physical Review E*, vol. 47, no. 6, p. R3838, 1993.

[258] J. Biggins, M. Warner, and K. Bhattacharya, "Elasticity of polydomain liquid crystal elastomers," *Journal of the Mechanics and Physics of Solids*, vol. 60, no. 4, pp. 573–590, 2012.

[259] D. R. Anderson, D. E. Carlson, and E. Fried, "A continuum-mechanical theory for nematic elastomers," *Journal of Elasticity*, vol. 56, no. 1, pp. 33–58, 1999.

[260] J. L. Ericksen, "Conservation laws for liquid crystals," *Transactions of the Society of Rheology*, vol. 5, no. 1, pp. 23–34, 1961.

[261] F. M. Leslie, "Some constitutive equations for liquid crystals," *Archive for Rational Mechanics and Analysis*, vol. 28, no. 4, pp. 265–283, 1968.

[262] Y.-C. Chen and E. Fried, "Uniaxial nematic elastomers: constitutive framework and a simple application," *Proceedings of the Royal Society A: Mathematical, Physical and Engineering Sciences*, vol. 462, no. 2068, pp. 1295–1314, 2006.

[263] A. DeSimone and L. Teresi, "Elastic energies for nematic elastomers," *The European Physical Journal E*, vol. 29, no. 2, pp. 191–204, 2009.

[264] V. Agostiniani and A. DeSimone, "Ogden-type energies for nematic elastomers," *International Journal of Non-Linear Mechanics*, vol. 47, no. 2, pp. 402–412, 2012.

[265] H. Zhou and K. Bhattacharya, "Accelerated computational micromechanics and its application to polydomain liquid crystal elastomers," *Journal of the Mechanics and Physics of Solids*, vol. 153, p. 104470, 2021.

[266] R. Zentel, "Shape variation of cross-linked liquid-crystalline polymers by electric fields," *Liquid Crystals*, vol. 1, no. 6, pp. 589–592, 1986.

[267] Y. Yusuf, J.-H. Huh, P. Cladis, H. R. Brand, H. Finkelmann, and S. Kai, "Low-voltage-driven electromechanical effects of swollen liquid-crystal elastomers," *Physical Review E*, vol. 71, no. 6, p. 061702, 2005.

[268] X. Zhao and Z. Suo, "Theory of dielectric elastomers capable of giant deformation of actuation," *Physical review letters*, vol. 104, no. 17, p. 178302, 2010.

[269] N. Cohen, K. Dayal, and G. deBotton, "Electroelasticity of polymer networks," *Journal of the Mechanics and Physics of Solids*, vol. 92, pp. 105–126, 2016.

[270] D.-H. Kim, N. Lu, Y. Huang, and J. A. Rogers, "Materials for stretchable electronics in bioinspired and biointegrated devices," *MRS bulletin*, vol. 37, no. 3, pp. 226–235, 2012.

[271] Z. S. Davidson, H. Shahsavan, A. Aghakhani, Y. Guo, L. Hines, Y. Xia, S. Yang, and M. Sitti, "Monolithic shape-programmable dielectric liquid crystal elastomer actuators," *Science advances*, vol. 5, no. 11, p. eaay0855, 2019.

[272] T. Guin, H. E. Hinton, E. Burgeson, C. C. Bowland, L. T. Kearney, Y. Li, I. Ivanov, N. A. Nguyen, and A. K. Naskar, "Tunable electromechanical liquid crystal elastomer actuators," *Advanced Intelligent Systems*, vol. 2, no. 7, p. 2000022, 2020.

[273] K. Urayama, S. Honda, and T. Takigawa, "Deformation coupled to director rotation in swollen nematic elastomers under electric fields," *Macromolecules*, vol. 39, no. 5, pp. 1943–1949, 2006.

[274] K. Urayama, "Selected issues in liquid crystal elastomers and gels," *Macromolecules*, vol. 40, no. 7, pp. 2277–2288, 2007.

[275] D. Corbett and M. Warner, "Deformation and rotations of free nematic elastomers in response to electric fields," *Soft Matter*, vol. 5, no. 7, pp. 1433–1439, 2009.

[276] A. Fukunaga, K. Urayama, T. Takigawa, A. DeSimone, and L. Teresi, "Dynamics of electro-opto-mechanical effects in swollen nematic elastomers," *Macromolecules*, vol. 41, no. 23, pp. 9389–9396, 2008.

[277] D. Corbett and M. Warner, "Electromechanical elongation of nematic elastomers for actuation," *Sensors and Actuators A: Physical*, vol. 149, no. 1, pp. 120–129, 2009.

[278] A. C. Eringen, "A unified continuum theory for electrodynamics of polymeric liquid crystals," *International Journal of Engineering Science*, vol. 38, no. 9-10, pp. 959–987, 2000.

[279] A. M. Menzel, H. Pleiner, and H. R. Brand, "Response of prestretched nematic elastomers to external fields," *The European Physical Journal E*, vol. 30, no. 4, pp. 371–377, 2009.

[280] E. Terentjev, M. Warner, R. Meyer, and J. Yamamoto, "Electromechanical fredericks effects in nematic gels," *Physical Review E*, vol. 60, no. 2, p. 1872, 1999.

[281] R. Diaz-Calleja, P. Llovera-Segovia, E. Riande, and A. Quijano López, "Mechanic and electromechanic effects in biaxially stretched liquid crystal elastomers," *Applied Physics Letters*, vol. 102, no. 5, p. 052901, 2013.

[282] R. Díaz-Calleja and P. Díaz-Boïls, "Electromechanical behaviour of biaxially stretched nematic liquid single crystal elastomers," *International Journal of Non-Linear Mechanics*, vol. 64, pp. 26–32, 2014.

[283] R. D. Calleja, P. Díaz-Boïls, P. Llovera-Segovia, and A. Quijano, "On the nonlinear behaviour of nematic single crystal elastomers under biaxial mechanic and electrical force fields," *The European Physical Journal E*, vol. 37, no. 7, pp. 1–13, 2014.

[284] A. Menzel and H. Brand, "Instabilities in nematic elastomers in external electric and magnetic fields," *The European Physical Journal E*, vol. 26, no. 3, pp. 235–249, 2008.

[285] O. Müller and H. Brand, "Undulation versus frederiks instability in nematic elastomers in an external electric field," *The European Physical Journal E*, vol. 17, no. 1, pp. 53–62, 2005.

[286] E. Terentjev, M. Warner, and P. Bladon, "Orientation of nematic elastomers and gels by electric fields," *Journal de Physique II*, vol. 4, no. 4, pp. 667–676, 1994.

[287] Y. Xu and Y. Huo, "Continuum modeling of the nonlinear electro-opto-mechanical coupling and solid fréedericksz transition in dielectric liquid crystal elastomers," *International Journal of Solids and Structures*, vol. 219, pp. 198–212, 2021.

[288] Y. Xu, Y. Zhang, and Y. Huo, "Electromechanical deformation of dielectric nematic elastomers accompanied by the rotation of mesogens," *International Journal of Mechanical Sciences*, p. 107061, 2022.

[289] G. Pampolini and N. Triantafyllidis, "Continuum electromechanical theory for nematic continua with application to freedericksz instability," *Journal of Elasticity*, vol. 132, no. 2, pp. 219–242, 2018.

[290] Y. Zhang, C. Xuan, Y. Jiang, and Y. Huo, "Continuum mechanical modeling of liquid crystal elastomers as dissipative ordered solids," *Journal of the Mechanics and Physics of Solids*, vol. 126, pp. 285–303, 2019.

[291] R. B. Meyer, "Piezoelectric effects in liquid crystals," *Physical Review Letters*, vol. 22, no. 18, p. 918, 1969.

[292] W. Helfrich, "Inherent bounds to the elasticity and flexoelectricity of liquid crystals," *Molecular Crystals and Liquid Crystals*, vol. 26, no. 1-2, pp. 1–5, 1974.

[293] A. Buka and N. Éber, *Flexoelectricity in liquid crystals: theory, experiments and applications*. World Scientific, 2013.

[294] A. Emelyanenko and M. Osipov, "Theoretical model for the discrete flexoelectric effect and a description for the sequence of intermediate smectic phases with increasing periodicity," *Physical Review E*, vol. 68, no. 5, p. 051703, 2003.

[295] J. H. Adler, T. J. Atherton, T. R. Benson, D. Emerson, and S. P. MacLachlan, "Energy minimization for liquid crystal equilibrium with electric and flexoelectric effects," *SIAM Journal on Scientific Computing*, vol. 37, no. 5, pp. S157–S176, 2015.

[296] J. Harden, B. Mbanga, N. Éber, K. Fodor-Csorba, S. Sprunt, J. T. Gleeson, and A. Jakli, "Giant flexoelectricity of bent-core nematic liquid crystals," *Physical review letters*, vol. 97, no. 15, p. 157802, 2006.

[297] Y. Xiang, H.-Z. Jing, Z.-D. Zhang, W.-J. Ye, M.-Y. Xu, E. Wang, P. Salamon, N. Éber, and Á. Buka, "Tunable optical grating based on the flexoelectric effect in a bent-core nematic liquid crystal," *Physical Review Applied*, vol. 7, no. 6, p. 064032, 2017.

[298] X. Jiang, W. Huang, and S. Zhang, "Flexoelectric nano-generator: Materials, structures and devices," *Nano Energy*, vol. 2, no. 6, pp. 1079–1092, 2013.

[299] J. Prost and J. Marcerou, "On the microscopic interpretation of flexoelectricity," *Journal de Physique*, vol. 38, no. 3, pp. 315–324, 1977.

[300] D. L. Cheung, S. J. Clark, and M. R. Wilson, "Calculation of flexoelectric coefficients for a nematic liquid crystal by atomistic simulation," *The Journal of chemical physics*, vol. 121, no. 18, pp. 9131–9139, 2004.

[301] P. Kumar, Y. Marinov, H. Hinov, U. S. Hiremath, C. Yelamaggad, K. Krishnamurthy, and A. Petrov, "Converse flexoelectric effect in bent-core nematic liquid crystals," *The Journal of Physical Chemistry B*, vol. 113, no. 27, pp. 9168–9174, 2009.

[302] H. Takezoe and Y. Takanishi, "Bent-core liquid crystals: their mysterious and attractive world," *Japanese journal of applied physics*, vol. 45, no. 2R, p. 597, 2006.

[303] P. Rudquist and S. Lagerwall, "On the flexoelectric effect in nematics," *Liquid crystals*, vol. 23, no. 4, pp. 503–510, 1997.

[304] J. Harden, M. Chambers, R. Verduzco, P. Luchette, J. T. Gleeson, S. Sprunt, and A. Jákli, "Giant flexoelectricity in bent-core nematic liquid crystal elastomers," *Applied Physics Letters*, vol. 96, no. 10, p. 102907, 2010.

[305] M. Chambers, R. Verduzco, J. T. Gleeson, S. Sprunt, and A. Jakli, "Flexoelectricity of a calamitic liquid crystal elastomer swollen with a bent-core liquid crystal," *Journal of Materials Chemistry*, vol. 19, no. 42, pp. 7909–7913, 2009.

[306] C. P. Rajapaksha, M. Gunathilaka, S. Narute, H. Albehaijan, C. Piedrahita, P. Paudel, C. Feng, B. Lüssem, T. Kyu, and A. Jákli, "Flexo-ionic effect of ionic liquid crystal elastomers," *Molecules*, vol. 26, no. 14, p. 4234, 2021.

[307] A. Menzel, *Nonlinear macroscopic description of liquid crystalline elastomers in external fields*. PhD thesis, 2008.

[308] A. M. Menzel and H. R. Brand, "Cholesteric elastomers in external mechanical and electric fields," *Physical Review E*, vol. 75, no. 1, p. 011707, 2007.

[309] K. Kumar, C. Knie, D. Bléger, M. A. Peletier, H. Friedrich, S. Hecht, D. J. Broer, M. G. Debije, and A. P. Schenning, "A chaotic self-oscillating sunlight-driven polymer actuator," *Nature communications*, vol. 7, no. 1, pp. 1–8, 2016.

[310] C. Li, Y. Liu, X. Huang, and H. Jiang, "Direct sun-driven artificial heliotropism for solar energy harvesting based on a photo-thermomechanical liquid-crystal elastomer nanocomposite," *Advanced Functional Materials*, vol. 22, no. 24, pp. 5166–5174, 2012.

[311] H. Yu and T. Ikeda, "Photocontrollable liquid-crystalline actuators," *Advanced Materials*, vol. 23, no. 19, pp. 2149–2180, 2011.

[312] C. Van Oosten, K. Harris, C. Bastiaansen, and D. Broer, "Glassy photomechanical liquid-crystal network actuators for microscale devices," *The European Physical Journal E*, vol. 23, no. 3, pp. 329–336, 2007.

[313] M. Camacho-Lopez, H. Finkelmann, P. Palffy-Muhoray, and M. Shelley, "Fast liquid-crystal elastomer swims into the dark," *Nature materials*, vol. 3, no. 5, pp. 307–310, 2004.

[314] R. C. Verpaalen, M. Pilz da Cunha, T. A. Engels, M. G. Debije, and A. P. Schenning, "Liquid crystal networks on thermoplastics: reprogrammable photo-responsive actuators," *Angewandte Chemie International Edition*, vol. 59, no. 11, pp. 4532–4536, 2020.

[315] M. Pilz da Cunha, S. Ambergen, M. G. Debije, E. F. Homburg, J. M. den Toonder, and A. P. Schenning, "A soft transporter robot fueled by light," *Advanced Science*, vol. 7, no. 5, p. 1902842, 2020.

[316] X. Pang, J.-a. Lv, C. Zhu, L. Qin, and Y. Yu, "Photodeformable azobenzene-containing liquid crystal polymers and soft actuators," *Advanced Materials*, vol. 31, no. 52, p. 1904224, 2019.

[317] L. Dong and Y. Zhao, "Photothermally driven liquid crystal polymer actuators," *Materials Chemistry Frontiers*, vol. 2, no. 11, pp. 1932–1943, 2018.

[318] Y. Shang, J. Wang, T. Ikeda, and L. Jiang, "Bio-inspired liquid crystal actuator materials," *Journal of Materials Chemistry C*, vol. 7, no. 12, pp. 3413–3428, 2019.

[319] H. K. Bisoyi, A. M. Urbas, and Q. Li, "Soft materials driven by photothermal effect and their applications," *Photoactive Functional Soft Materials: Preparation, Properties, and Applications*, pp. 1–44, 2019.

[320] M. L. Dunn, "Photomechanics of mono-and polydomain liquid crystal elastomer films," *Journal of applied physics*, vol. 102, no. 1, p. 013506, 2007.

[321] T. Ube and T. Ikeda, "Photomobile polymer materials with complex 3d deformation, continuous motions, self-regulation, and enhanced processability," *Advanced Optical Materials*, vol. 7, no. 16, p. 1900380, 2019.

[322] F. Weigert, "Uber einen neuen effekt der strahlung in lichtempfindlichen schichten," *Verh. Dtsch. Phys. Ges.*, vol. 21, pp. 479–491, 1919.

[323] T. Ube and T. Ikeda, "Photomobile polymer materials with crosslinked liquid-crystalline structures: molecular design, fabrication, and functions," *Angewandte Chemie International Edition*, vol. 53, no. 39, pp. 10290–10299, 2014.

[324] U. Hrozhyk, S. Serak, N. Tabiryan, T. J. White, and T. J. Bunning, "Bidirectional photoresponse of surface pretreated azobenzene liquid crystal polymer networks," *Optics Express*, vol. 17, no. 2, pp. 716–722, 2009.

[325] T. J. White, S. V. Serak, N. V. Tabiryan, R. A. Vaia, and T. J. Bunning, "Polarization-controlled, photodriven bending in monodomain liquid crystal elastomer cantilevers," *Journal of Materials Chemistry*, vol. 19, no. 8, pp. 1080–1085, 2009.

[326] C. Luo, C. Chung, C. M. Yakacki, K. Long, and K. Yu, "Real-time alignment and reorientation of polymer chains in liquid crystal elastomers," *ACS Applied Materials & Interfaces*, 2021.

[327] L. Jin, Y. Yan, and Y. Huo, "A gradient model of light-induced bending in photochromic liquid crystal elastomer and its nonlinear behaviors," *International Journal of Non-Linear Mechanics*, vol. 45, no. 4, pp. 370–381, 2010.

[328] M. Warner and L. Mahadevan, "Photoinduced deformations of beams, plates, and films," *Physical Review Letters*, vol. 92, no. 13, p. 134302, 2004.

[329] Y. Zhang and Y. Huo, "First order shear strain beam theory for spontaneous bending of liquid crystal polymer strips," *International Journal of Solids and Structures*, vol. 136, pp. 168–185, 2018.

[330] M. Warner, C. D. Modes, and D. Corbett, "Curvature in nematic elastica responding to light and heat," *Proceedings of the Royal Society A: Mathematical, Physical and Engineering Sciences*, vol. 466, no. 2122, pp. 2975–2989, 2010.

[331] Y. Lin, L. Jin, and Y. Huo, "Quasi-soft opto-mechanical behavior of photochromic liquid crystal elastomer: Linearized stress–strain relations and finite element simulations," *International Journal of Solids and Structures*, vol. 49, no. 18, pp. 2668–2680, 2012.

[332] D. Corbett and M. Warner, "Linear and nonlinear photoinduced deformations of cantilevers," *Physical review letters*, vol. 99, no. 17, p. 174302, 2007.

[333] Y. You, C. Xu, S. Ding, and Y. Huo, "Coupled effects of director orientations and boundary conditions on light induced bending of monodomain nematic liquid crystalline polymer plates," *Smart materials and structures*, vol. 21, no. 12, p. 125012, 2012.

[334] P. Hogan, A. Tajbakhsh, and E. Terentjev, "Uv manipulation of order and macroscopic shape in nematic elastomers," *Physical Review E*, vol. 65, no. 4, p. 041720, 2002.

[335] L. Liu and P. R. Onck, "Enhanced deformation of azobenzene-modified liquid crystal polymers under dual wavelength exposure: A photophysical model," *Physical review letters*, vol. 119, no. 5, p. 057801, 2017.

[336] R. Bai and K. Bhattacharya, "Photomechanical coupling in photoactive nematic elastomers," *arXiv preprint arXiv:2002.04000*, 2020.

[337] D. Corbett and M. Warner, "Nonlinear photoresponse of disordered elastomers," *Physical review letters*, vol. 96, no. 23, p. 237802, 2006.

[338] A. DeSimone, "Electro-mechanical response of nematic elastomers: an introduction," in *Mechanics and Electrodynamics of Magneto-and Electro-elastic Materials*, pp. 231–266, Springer, 2011.

[339] T. H. Ware, J. S. Biggins, A. F. Shick, M. Warner, and T. J. White, "Localized soft elasticity in liquid crystal elastomers," *Nature communications*, vol. 7, no. 1, pp. 1–7, 2016.

[340] A. DeSimone, "Nematic elastomers: modelling, analysis, and numerical simulations," in *Poly-, Quasi-and Rank-One Convexity in Applied Mechanics*, pp. 241–264, Springer, 2010.

[341] F. C. Frank, "I. liquid crystals. on the theory of liquid crystals," *Discussions of the Faraday Society*, vol. 25, pp. 19–28, 1958.

[342] S. J. Elston, "Flexoelectricity in nematic domain walls," *Physical Review E*, vol. 78, no. 1, p. 011701, 2008.

[343] F. M. Leslie, "Some constitutive equations for anisotropic fluids," *The Quarterly Journal of Mechanics and Applied Mathematics*, vol. 19, no. 3, pp. 357–370, 1966.

[344] F. M. Leslie, "Theory of flow phenomena in liquid crystals," in *Advances in liquid crystals*, vol. 4, pp. 1–81, Elsevier, 1979.

[345] F. M. Leslie, "Continuum theory for nematic liquid crystals," *Continuum Mechanics and Thermodynamics*, vol. 4, no. 3, pp. 167–175, 1992.

[346] I. W. Stewart, *The static and dynamic continuum theory of liquid crystals: a mathematical introduction*. Crc Press, 2019.

[347] M. E. Gurtin, E. Fried, and L. Anand, *The mechanics and thermodynamics of continua*. Cambridge University Press, 2010.

[348] D. C. Leigh, *Nonlinear continuum mechanics: an introduction to the continuum physics and mathematical theory of the nonlinear mechanical behavior of materials*. McGraw-Hill, 1968.

[349] D. Corbett, C. Van Oosten, and M. Warner, "Nonlinear dynamics of optical absorption of intense beams," *Physical Review A*, vol. 78, no. 1, p. 013823, 2008.

[350] C. Fu, Y. Xu, F. Xu, and Y. Huo, "Light-induced bending and buckling of large-deflected liquid crystalline polymer plates," *International Journal of Applied Mechanics*, vol. 8, no. 07, p. 1640007, 2016.

[351] C. Modes, M. Warner, C. Van Oosten, and D. Corbett, "Anisotropic response of glassy splay-bend and twist nematic cantilevers to light and heat," *Physical Review E*, vol. 82, no. 4, p. 041111, 2010.

[352] T. J. Pence, "Soft elastic bending response of a nematic elastomer described by a microstructurally relaxed free energy," *Continuum Mechanics and Thermodynamics*, vol. 18, no. 5, pp. 281–304, 2006.

[353] Y. Liu, W. Ma, and H.-H. Dai, "On a consistent finite-strain plate model of nematic liquid crystal elastomers," *Journal of the Mechanics and Physics of Solids*, vol. 145, p. 104169, 2020.

[354] Y. Xu, Y. Zhang, and Y. Huo, "Electric-field induced deformation and bending in nematic elastomer strips with orientation gradient," *International Journal of Solids and Structures*, vol. 202, pp. 243–259, 2020.

[355] Y. Liu, W. Ma, and H.-H. Dai, "Bending-induced director reorientation of a nematic liquid crystal elastomer bonded to a hyperelastic substrate," *Journal of Applied Physics*, vol. 129, no. 10, p. 104701, 2021.

[356] J. Küupfer and H. Finkelmann, "Liquid crystal elastomers: Influence of the orientational distribution of the crosslinks on the phase behaviour and reorientation processes," *Macromolecular chemistry and physics*, vol. 195, no. 4, pp. 1353–1367, 1994.

[357] I. Kundler and H. Finkelmann, "Strain-induced director reorientation in nematic liquid single crystal elastomers," *Macromolecular rapid communications*, vol. 16, no. 9, pp. 679–686, 1995.

[358] J. Küpfer and H. Finkelmann, "Nematic liquid single crystal elastomers," *Die Makromolekulare Chemie, Rapid Communications*, vol. 12, no. 12, pp. 717–726, 1991.

[359] G. Verwey, M. Warner, and E. Terentjev, "Elastic instability and stripe domains in liquid crystalline elastomers," *Journal de Physique II*, vol. 6, no. 9, pp. 1273–1290, 1996.

[360] L. Golubović and T. Lubensky, "Nonlinear elasticity of amorphous solids," *Physical review letters*, vol. 63, no. 10, p. 1082, 1989.

[361] S. Conti, A. DeSimone, and G. Dolzmann, "Semisoft elasticity and director reorientation in stretched sheets of nematic elastomers," *Physical Review E*, vol. 66, no. 6, p. 061710, 2002.

[362] B. L. Mbanga, F. Ye, J. V. Selinger, and R. L. Selinger, "Modeling elastic instabilities in nematic elastomers," *Physical Review E*, vol. 82, no. 5, p. 051701, 2010.

[363] L. A. Mihai and A. Goriely, "A plate theory for nematic liquid crystalline solids," *Journal of the Mechanics and Physics of Solids*, vol. 144, p. 104101, 2020.

[364] V. Agostiniani and A. DeSimone, "Rigorous derivation of active plate models for thin sheets of nematic elastomers," *Mathematics and Mechanics of Solids*, vol. 25, no. 10, pp. 1804–1830, 2020.

[365] A. DeSimone, A. DiCarlo, and L. Teresi, "Critical voltages and blocking stresses in nematic gels," *The European Physical Journal E*, vol. 24, no. 3, pp. 303–310, 2007.

[366] M. Arroyo and A. DeSimone, "Shape control of active surfaces inspired by the movement of euglenids," *Journal of the Mechanics and Physics of Solids*, vol. 62, pp. 99–112, 2014.

[367] M. Firbank, M. Oda, and D. T. Delpy, "An improved design for a stable and reproducible phantom material for use in near-infrared spectroscopy and imaging," *Physics in Medicine & Biology*, vol. 40, no. 5, p. 955, 1995.

[368] S. T. Flock, S. L. Jacques, B. C. Wilson, W. M. Star, and M. J. van Gemert, "Optical properties of intralipid: a phantom medium for light propagation studies," *Lasers in surgery and medicine*, vol. 12, no. 5, pp. 510–519, 1992.